THESIS APPROVAL

GRADUATE SCHOOL, KASETSART UNIVERSITY

Doctor of Engineering (Chemical Engineering)
DEGREE

Chemical Engineering
FIELD

Chemical Engineering
DEPARTMENT

TITLE: Modeling and Simulation of Hydrodynamics, and Heat and Mass Transfer in a Down-Flow Circulating Fluidized Bed Reactor

NAME: Mr. Parinya Khongprom

THIS THESIS HAS BEEN ACCEPTED BY

THESIS ADVISOR
(Associate Professor Sunun Limtrakul, D.Sc.)

THESIS-CO ADVISOR
(Associate Professor Terdthai Vatanatham, Ph.D.)

DEPARTMENT HEAD
(Associate Professor Apinya Duangchan, Ph.D.)

APPROVED BY THE GRADUATE SCHOOL ON

DEAN
(Associate Professor Gunjana Theeragool, D.Agr.)

THESIS

MODELING AND SIMULATION OF HYDRODYNAMICS, AND HEAT AND MASS TRANSFER IN A DOWN-FLOW CIRCULATING FLUIDIZED BED REACTOR

PARINYA KHONGPROM

A Thesis Submitted in Partial Fulfillment of
the Requirements for the Degree of
Doctor of Engineering (Chemical Engineering)
Graduate School, Kasetsart University
2011

Parinya Khongprom 2011: Modeling and Simulation of Hydrodynamics, and Heat and Mass Transfer in a Down-Flow Circulating Fluidized Bed Reactor. Doctor of Engineering (Chemical Engineering), Major Field: Chemical Engineering, Department of Chemical Engineering. Thesis Advisor: Associate Professor Sunun Limtrakul, D.Sc. 254 pages.

The hydrodynamics and heat and mass transfer behavior in a down-flow circulating fluidized bed (downer reactor) were studied using the two-fluid model and the discrete element method (DEM) model. In studies of hydrodynamics and mixing behavior in a downer reactor by the two-fluid model, it was found that both gas and solids flows approximated an ideal plug flow behavior. The gas phase flow behavior reaches higher levels of attainment to ideal plug flow patterns than that of the solids phase. The correlations of the axial gas and solids Peclet numbers as a function of the operating conditions and the physical properties of gas and solids particles in the system were proposed. In addition, the two-fluid model was used for predicting the performance of CO_2 removal in a circulating fluidized bed. It was found that the CO_2 concentration in the downer reactor was much more uniform than that in the riser reactor. However, the conversion in the downer is lower than that in the riser because of lower solids fraction in the downer. Finally, DEM was developed to investigate the heat and mass transfer in a catalytic cracking downer reactor. The simulation of the catalytic cracking downer reactor exhibits the almost uniform temperature and concentration distributions in the lateral direction. In addition, the gasoline mass fraction, which is the desired product, increases with increasing cracking temperature, solids circulation rate and decreasing of superficial gas velocity. However, the gasoline product undergoes further cracking to yield more gaseous products at very high inlet temperature.

____________________ _______________________ _____/_____/_____

Student's signature Thesis Advisor's signature

ACKNOWLEDGEMENTS

I owe my deepest gratitude to my advisor, Assoc. Prof. Dr. Sunun Limtrakul for her useful supervision and guidance. I am also greatly indebted to Assoc. Prof. Dr. Therdthai Vatanatham, Prof. P.A. Ramachandran, and Prof. Dimitry Gidaspow, who as my co-advisors, in helping me to broaden my view and knowledge. In addition, they give the guidance, comments, discussions and invaluable suggestions throughout this project.

I deeply thank to the Kasetsart University Research and Development Institute (KURDI), Department of Chemical Engineering, Kasetsart University, and Thailand Research Fund (TRF) under the Research Career Development Project and the Royal Golden Jubilee Ph.D. Program for financial support.

Additional thanks to all of my friends from Phatthalung school, especially Mr. Mongkol Bumrungdee, Mr. Prachaya Muangsong and Ms. Panida Chantrarakran and my friends from Kasetsart University, especially Ms. Rungthip Berphan, Ms. Nattha Thanoomboon, Ms. Pattharaporn Kladthong and Mr. Uthane Nanthapoonsub for their technical support and helping me balance school with a little fun. In addition, I would like to thank Mr. Kiattichai Wadaugsorn for proofreading this thesis book.

Lastly, I would like to express my sincere and deepest grateful to my parents for their unconditional support and encouragement to pursue my interests.

Parinya Khongprom
April 2011

TABLE OF CONTENTS

Page

LIST OF TABLES

Table **Page**

LIST OF FIGURES

LIST OF FIGURES (Continued)

Figure **Page**

LIST OF FIGURES **(Continued)**

Figure **Page**

LIST OF FIGURES (Continued)

LIST OF FIGURES (Continued)

LIST OF FIGURES (Continued)

Figure **Page**

LIST OF FIGURES (Continued)

LIST OF FIGURES (Continued)

LIST OF FIGURES (Continued)

Figure **Page**

Appendix Figure

LIST OF ABBREVIATIONS

a = Specific surface area (m^{-1})

$\vec{a}$ = Acceleration vector (m/s^2)

c = Concentration (kmol/m^3)

C = Concentration (kg/m^3)

C_0 = Heavy oil mass concentration at the inlet (kg/m^3)

C_D = Drag coefficient (-)

C_{fr} = Friction coefficient (-)

C_{max} = Maximum concentration (kg/m^3)

C_p = Heat catacity (kJ/kg.K)

$\widehat{C}_{p,g}$ = Heat capacity of gas mixture (kJ/kg.K)

C_{step} = Step concentration (kg/m^3)

C_μ = Turbulence model constant (-)

D = Axial dispersion coefficient (m^2/s)

D_{im} = Diffusivity coefficient of species *i* in the gas mixture (m^2/s)

d_s = Particle diameter (m)

D_T = Reactor diameter (m)

E = Residence time distribution function (1/s)

e_s = Restitution coefficient between particles (-)

E_θ = Normalized residence time distribution (-)

F = Cumulative residence time distribution function (-)

$\vec{f}_C$ = Contact force (N)

$\vec{f}_D$ = Fluid force (N)

$\vec{f}_p$ = Drag force of fluid on particle (N)

$\vec{f}_{total}$ = Total force acting on the particle (N)

$\vec{g}$ = Gravity acceleration (m/s^2)

g_0 = Radial distribution function (-)

G_k = Production of turbulent kinetic energy (kg/m.s^3)

G_s = Solids circulation rate (kg/m^2.s)

h = Heat transfer coefficient (W/m^2.K)

H = Height (m)

LIST OF ABBREVIATIONS (Continued)

I = Moment of inertia of the particle (kg.m^2)
$\bar{\bar{I}}$ = Unit tensor (-)
$\vec{J}$ = Mass flux (kg/m^2 .s)
j_h = j factor (-)
k = Turbulent kinetic energy (m^2/s^2)
K = Mass transfer between phases (1/s)
k' = Kinetic rate constant (m^6/kg.kg$_{cat}$.s, 2nd order; m^3/kg$_{cat}$.s, 1st order)
K_F = Overall mass transfer coefficient (m/s)
k_g = Mass transfer coefficient between phases (m/s)
k_r = Reaction rate constant
$k_{stif,nor}$ = Normal stiffness of the spring (N/m)
$k_{stif,tan}$ = Tangential stiffness of the spring (N/m)
k_Θ = Diffusion coefficient of granular temperature (kg/m.s)
L = Length (m)
m = Mass (kg)
M = Molecular weight (g/mol)
Nu = Nusselt number (-)
p = Pressure (Pa)
Pe = Peclet number (-)
Pe_m = Peclet number for mass transfer (-)
Pr = Prandtl number (-)
R = The universal gas constant (0.08205 atm.m^3/kmol.K)
r = Radial position (m)
Re = Reynolds number (-)
Sc = Schmidt number (-)
t = Time (s)
T = Temperature (K)
$\vec{T}$ = Torque (N.m)
t_m = Mean time (s)
u = Velocity (m/s)

LIST OF ABBREVIATIONS (Continued)

U = Superficial velocity (m/s)

v = Volumetric solids to gas ratio (-)

V = Volume of the particle (m^3)

W = Weight of catalyst (kg)

w_i = Mass fraction of component i in gas phase (-)

$w_{i,s}$ = Mass fraction of component i in solid phase (-)

Y_i = Mole fraction of species i (-)

z = Dimensionless axial position (-)

$-\Delta H$ = Heat of reaction (J/kg)

Greek letters

α = Volume fraction (-)

$\vec{\alpha}$ = Angular acceleration vector (rad/s^2)

$\alpha_{s,max}$ = Solids volume fraction at maximum packing (-)

β = Momentum transfer coefficient (kg/s.m^3)

$\vec{\delta}$ = Particle displacement (m)

ε = Turbulent dissipation rate (m^2/s^3)

γ = Collisional dissipation of solid fluctuating energy (kg/m.s^3)

κ_p = Conductivity of the fluctuating energy (kg/m.s)

λ_g = Gas thermal conductivity (kW/m.K)

λ_s = Solids bulk viscosity

μ = Viscosity (kg/m.s)

μ_t = Turbulent viscosity (kg/m.s)

η = Ratio between the Lagragian integral time scale and the characteristic particle relaxation time (-)

η_{damp} = Damping coefficient (N.s/m)

$\vec{\omega}$ = Angular velocity (rad/s)

ρ = Density (kg/m^3)

τ = Stress tensor (Pa)

LIST OF ABBREVIATIONS **(Continued)**

θ = Dimensionless time (-)
Θ = Granular temperature (m^2/s^2)

Subscripts

b = Bubble phase
cl = Cloud phase
e = Emulsion phase
g = Gas phase
m = Mixture phase
mf = Minimum fluidized bed
n = Gas phase (n=1), main solids phase (n=2), and tracer solids phase (n=3)
nor = Normal direction
p = Solids phase
q = Gas, main solids, and tracer solids phases
s = Solids phase
tan = Tangential direction
t = Tracer solids phase
tu = Turbulence

MODELING AND SIMULATION OF HYDRODYNAMICS, AND HEAT AND MASS TRANSFER IN A DOWN-FLOW CIRCULATING FLUIDIZED BED REACTOR

INTRODUCTION

Circulating fluidized beds (CFBs) are highly effective reactors for gas-solid reaction systems. These reactors have been widely used in various applications, including catalytic cracking, calcination operation, polyethylene production, and combustion of a variety of fuels, since they offer many advantages such as high throughput rates and thorough gas-solid contact leading to excellent heat and mass transfers. Conventionally, CFBs have been designed with the entrance of the reactor located at the bottom end, where the gas and solids meet and flow upward to the exit at the top of the reactor. Therefore, these reactors are called risers. In spite of their advantages, the riser reactors suffer from significant solids back mixing, in some applications. The solids back mixing reduces selectivity and irregular distribution of the desired product. A downer is a new type of CFBs, which gas and solid particles are fed at the top section of the reactor. Gas and particles flow downward along the direction of gravity. According to this set up, a more uniform radial solids distribution (Yang *et al.*, 1991; Wang *et al.*, 1992; Cao *et al.*, 1994; Bolkan, 2003; Chen and Li, 2004) and a narrow residence time distribution can be achieved (Wang *et al.*, 1992; Zhu *et al.*, 1995; Wei and Zhu, 1996; Lehner and Wirth, 1999a; Wu *et al.*, 2010; Zhao *et al.*, 2010a). These advantages make the downer reactor the most attractive reactor for a fast reaction with an intermediate as a desired product such as the catalytic cracking of hydrocarbons. The fluid catalytic cracking (FCC) units convert heavy oil to lighter products. Major FCC products are gasoline, diesel fuel, and light gases which are used for the production of petrochemical. This reaction is an endothermic reaction and requires a short contact time in order to reduce over cracking. A little increase in selectivity or yield of gasoline is very important to the process. Several studies revealed that a downer reactor can improve the selectivity or yield of desired products over a riser reactor (Bolkan *et al.*, 1994; Deng *et al.*, 2002a, 2002b; Abul-Hamayel, 2004; Wu *et al.*, 2009, 2010). The downer reactor shows a large potential for improving the yield of the FCC process due to the less axial back-mixing of gas and solids (Zhu *et al.*, 1995) and flatter radial distributions of velocity profile (Cao *et al.*, 1994; Deng *et al.*, 2002a) and solids volume fraction profile (Yang *et al.*, 1991; Bolkan *et al.*, 2003).

The design, optimization, and scale-up of the downer reactors require a more precise with a quantitative understanding of the flow behavior in the system. Mixing characteristics are the key parameters in this regard, since some simpler models based on axial dispersion can be applied if the parameters are estimated and correlated. Practically, the downer reactors have been used as heterogeneous catalytic reactors, where the solids phase might be the catalyst or active species while the reactants and products are usually in gaseous form, such as in a catalytic cracking reaction. Thus, the understanding of both gas and solids mixing is necessary for the accurate evaluation of the reactor performance and good reactor design. Several researchers studied gas and solids mixing in the downers. However, no systematic study has been carried out to assess the mixing behavior of both gas and solids phases in the same system. In particular, no tie-up of computational flow models with virtual tracer studies exists.

Since experimental approaches to directly measure the hydrodynamics behavior in the fluidized beds, such as optical fiber probe (Zhang *et al.*, 1999; Ball and Zhu, 2001; Magnusson *et al.*, 2005; Qi *et al.*, 2008), dual optical density probe, and laser Doppler velocimeter system (Wang *et al.*, 1998; Zhang *et al.*, 2003a) are quite difficult techniques with high cost of equipment, meanwhile a numerical simulation approach can provide a powerful tool to investigate the local phenomena in these reactors. Thus many researchers applied numerical approaches to study the flow behavior in the fluidized beds. Previously, the performance of fluidized bed reactors has numerically been investigated using a simple model such as the two-region model (Davidson and Harrison, 1963; Kunii and Levenspiel, 1991). In this model, the reactor consists of two distinct zones, the bubble phase and the emulsion phase. The model is based on many parameters and many simplifications. The two-fluid model with kinetic theory of granular flow has been developed to investigate the flow behavior in a fluidized bed reactor with high particle loading (Anderson and Jackson, 1967; Kuiper *et al.*, 1992; Gidaspow, 1994; Khongprom *et al.*, 2008). In this model, the particles are treated as a continuum as in the gas phase. The behavior of each phase is characterized by its own conservation equations, which are linked through interphase exchange coefficients. The kinetic theory of granular flow is used for calculating the fluid properties of solids phase. Recently, many researchers (Tsuji *et al.*, 1992; Tsuji *et al.*, 1993; Limtrakul *et al.*, 2003, 2008) presented the discrete particle simulation in a fluidized bed based on the physical properties of particle in the bed using the Discrete Element Method (DEM). In the DEM model, the motion of individual particle is obtained from the calculation of the contact force acting on each particle. The contact force is calculated from analogy to a spring, dash-pot, and friction slider system which was first proposed by Cundall and Strack (1979). Furthermore, this model can be combined with mass transfer and chemical reaction (Limtrakul *et al.*, 2004). This combined model can be predicted the hydrodynamics and the concentrations in gas and particle phases. The simulation results from this combined model show good agreement with the experimental results and are in better agreement than the results obtained from the one-dimensional model. The DEM model was further developed for studying the polymerization in fluidized bed reactor by combining this model with mass and heat transfers (Kaneko *et al.*, 1999; Limtrakul *et al.*, 2006). The DEM model can be calculated the local concentration and local temperature throughout the bed. Recently, Wu *et al.* (2010) developed the DEM model incorporated with heat transfer sub-model and chemical reaction to simulate gas-solid reacting flows in fluid catalytic cracking (FCC) process. However, they assumed gas-solids reaction as a homogeneous reaction. The mass transfer mechanism in the heterogeneous catalytic reaction is more complicate. Thus a more realistic mass transfer model is needed for this complicate system.

The objective of the present study is to systematically analyze of the axial dispersion of gas and solids in a downer reactor using a two-fluid model based on the kinetic theory of granular flow as a basis for flow. The hydrodynamics behavior was compared with experimental data obtained from literature. The residence time distribution (RTD) was then computed using virtual tracers and compared with the available experimental results. The effects of operating conditions (superficial gas velocity, solids circulation rate) and particle properties (particle density, particle diameter) on the mixing behavior were addressed. Moreover, the hydrodynamics and reactor performance of a downer and a riser reactor was studied using the two-fluid model. The heat and mass and transfer in a downer was also studied using the DEM models. The DEM model was developed by coupling with heat and mass transfer and catalytic cracking reaction. The simulation models can predict the hydrodynamics, the overall conversion, temperature, and product distribution in the reactor under various operating conditions. The DEM model was applied in a FORTRAN code, while the two-fluid model with the kinetic theory for the particle phase was performed using FLUENT software.

OBJECTIVES

The two-fluid model and the discrete element method (DEM) model were developed to study the hydrodynamics, heat and mass transfer in a circulating fluidized bed reactor. The scopes of this research work are

1. To develop the two-fluid model for studying the hydrodynamics, mixing behavior and mass transfer in a circulating fluidized bed reactor. The details of this section are

1.1 The hydrodynamics behavior in a downer reactor was studied. The effects of operating condition and particle properties on the hydrodynamics were addressed.

1.2 The axial mixing of gas and particle in a downer reactor was studied. The effects of operating condition and particle properties on the mixing behavior were addressed.

1.3 The flow behavior and CO_2 removal performance were studied in a circulating fluidized bed including a riser and downer. The hydrodynamics and CO_2 removal performance in a downer were compared with those in a riser at various operating conditions and particle properties.

2. To develop the discrete element method (DEM) model for simulation of the hydrodynamics and heat and mass transfer in a downer reactor. The details of this study are explained as follows.

2.1 The hydrodynamics and heat and mass transfer in a downer reactor was studied. The catalytic cracking of heavy oil was chosen as a case study.

2.2 The effect of operating condition on the performance of the catalytic cracking downer was studied.

LITERATURE REVIEW

1. Downer reactor

In recent years, a new type of CFB reactors, the downer has been developed. In the downer, the gas and solids phases enter the reactor at the top section, allowing the gas-solids mixture to flow co-current downward along the direction of gravity as shown in Figure 1. This set up leads to desirable hydrodynamics qualities such as more uniform flow and better control of fluid-solids contact times. Furthermore, the low residence time and less mixing of particles from different layer lead to plug flow characteristic (Bai *et al.*, 1991; Wang *et al.*, 1992; Kimm *et al.*, 1996; Cheng *et al.*, 1999; Zhang *et al.*, 1999; Ball and Zhu, 2001; Limtrakul *et al.*, 2008). Therefore a downer reactor is suitable for fast reaction with an intermediate as a desired product such as fluidized catalytic cracking reaction (Liu *et al.*, 2006) and combustion of a biomass (Wang *et al.*, 1992).

2. Hydrodynamics behavior in a downer

The hydrodynamics behavior in a downer reactor is the key parameters for reactor design and operations. Several researchers have been studied in this research field. Zhang *et al.* (1999) studied the axial distributions of the local solids holdup using a fiber optical solids concentration probe and a series of pressure transducers. The result showed that the cross-sectional average particle velocity increases rapidly in the first section of the downer column. This is due to the high drag caused by the large initial difference between gas and particle velocities. After that the acceleration is slow down and finally the particle velocity approaches a constant further down the column. As a result, the solids holdup profile decreases sharply in the first section in the downer column, then gradually decreases and approaches a constant further down the reactor.

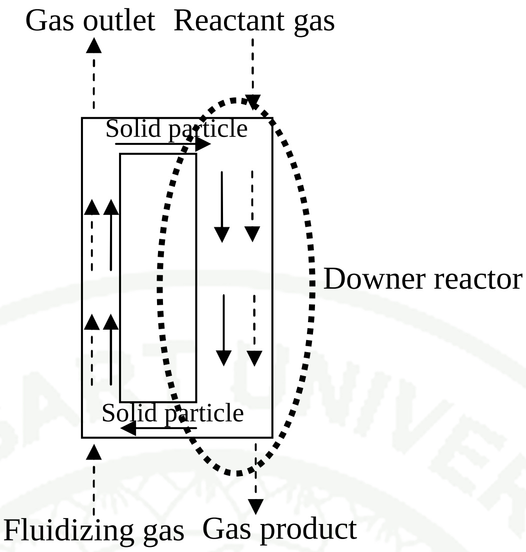

Figure 1 Simple configuration downer reactor.

Normally, the radial profiles of local solids fraction at different axial positions were obtained through an optical fiber or a dual optical density probe (Bai *et al.*, 1991; Wang *et al.*, 1992; Herbert *et al.*, 1995; Wei and Zhu, 1996; Zhang *et al.*, 1999; Zhang *et al.*, 2003a, 2003b). The radial profile of solids fraction near the entrance of a downer reactor is fluctuation up and down because of the distributor effect. Further down the column, the radial solids distribution is more flat. The peak of solids concentration decreases with increasing distance from a downer entrance. In addition, the radial solids distribution in a downer is more uniform than that in a riser (Yang *et al.*, 1991; Bolkan *et al.*, 2003).

There are many studies on the radial particle velocity but the results reported by difference researchers are not consistent with each other as well. The radial profiles of particle velocity obtained by Bai *et al.* (1991), Yang *et al.* (1991), and Wang *et al.* (1992) show a slowly increasing trend in the core region and a small peak at r/R = 0.85-0.96. In 1995, Herbert *et al.* found that, the particle velocity profiles have a flat core (r/R < 0.6) and a decreasing trend in the wall region under low gas velocity conditions. In a small downer diameter, the radial particle velocity profile shows a parabolic shape with the maximum at the center. Due to the diameter of downer is too small (0.05 m) so the wall-effect-layer could cover up to 80% of the whole radius of the reactor. This leaves little area for the core and thus leads to a radial profile of parabolic type shape. However, the radial distribution of particle velocity in a downer is found to be more uniform than that in a riser (Cao *et al.*, 1994; Deng *et al.*, 2002a).

3. Gas and solids mixing in a fluidized bed

The mixing characteristics are the key parameters for the design, optimization, and scale up of a downer reactor. Thus several experimental methods have been developed to study gas and solids mixing in the downers, as summarized in Table 1. However, no systematic study has been carried out to assess the mixing behavior of both gas and solids phases in the same system.

4. Mass transfer in fluidized bed

Practically, fluidized bed reactors are used as a chemical reactor. Thus the mass transfer behavior is the crucial information for reactor design, optimization, and reactor performance predictions. The characteristic of gas-solids mass transfer in a CFB downer was experimentally studied using the adsorption of CO_2 tracer method (Luo *et al.*, 2007). The operating conditions such as solids circulation rate and gas velocity have complicated effects on the gas-solids mass transfer coefficient. The empirical correlation for calculating the overall mass transfer coefficient, K_F is as follow:

$$Pe_m = \frac{U_g}{K_F aL} = 0.000185\,\mathrm{Re}^{0.618}\, v^{-0.983} \tag{1}$$

where Pe_m is a Peclet number of mass transfer, U_g the superficial gas velocity, a the specific surface area of adsorbent, L the total height of downer reactor, Re the particle Reynolds number, and v the volumetric solids to gas ratio, which obtained from

Table 1 Experimental study of mixing behavior in a downer reactor.

Reference	**Method**	**Dispersion**	**ID (mm)**	**H (m)**	**Dp (µm)**	**Density (kg/m^3)**	**Ug (m/s)**	**Gs (kg/m^{2}s)**
Wei *et al.* (1994b)	Phosphor tracer technique	Axial solids Radial solids	140	7.6	54	1 710	2.3-9.0	5-60
Wei and Zhu (1996)	Phosphor tracer technique	Axial solids	140	7.2	54,1 810	1 710-1 473	2.6-8.0	8-80
Bang *et al.* (1999)	He tracer technique	Radial gas	100	3.5	64,164	3 120	1.6-4.5	0-40
Brust and Wirth (2004)	Argon tracer technique	Axial gas	150	8.6	85	-	1-6	25-60
Huang *et al.* (2006)	Phosphor tracer technique	Axial solids Radial solids	418	6.5	69.2	1 520	2.9-5.8	50-150
Luo *et al.* (2007)	CO_2 tracer technique	Axial gas	33	2.81	337	1 270	0.31-1.6	1.5-9.9

$$v = \frac{G_s}{\left(U_g \rho_s\right)} = \frac{u_s\left(1-\alpha_g\right)}{\left(U_g \alpha_g\right)} \tag{2}$$

Several models have been developed to predict mass transfer in a fluidized bed reactor. Toomey and Johnstone (1952) proposed a simple model, called Two-phase model, which consists of a rising bubble phase and a stagnant emulsion at minimum fluidizing condition. This model was further improved for predicting the performance of various fluidized bed regimes (Partridge and Rowe, 1966; Kato and Wen, 1969; Fryer and Potter, 1976; Kunii and Levenspiel, 1990). This model assumes gas phase behave like an ideal plug flow. The material balances in a bubble, cloud and emulsion for a first order kinetic reaction are:

$$u_b \frac{dC_b}{dz} = -C_b \alpha_b k \; - K_{bc}\left(C_b - C_{cl}\right) \tag{3}$$

$$u_e \frac{dC_e}{dz} = -C_e \alpha_e k_r + K_{ce}\left(C_{cl} - C_e\right) \tag{4}$$

$$C_{cl}\alpha_{cl}k_r + K_{ce}\left(C_{cl} - C_e\right) - K_{bc}\left(C_b - C_{cl}\right) = 0 \tag{5}$$

where C_b, C_e, C_{cl} are the reactant concentrations in a bubble, emulsion and cloud, respectively; z is the reactor height; k_r is the reaction rate constant; u_b and u_e are the bubble and gas velocities; $\alpha_b, \alpha_e, \alpha_{cl}$ are the volume fraction of bubble, emulsion, and cloud, respectively; K is the mass transfer coefficient between phase.

Recently, our research group (Boonsrirat *et al.*, 2001; Limtrakul *et al.*, 2004) successfully developed the DEM model by coupling with mass transfer, to study the performance of the reactive flow in the fluidized bed reactors. The catalyst is in solids phase while the reactants are in gas phase. The reaction is assumed to occur on the catalyst surface. The mass transfer coefficient between gas and solids phases, k_g is obtained from Fogler's correlation (Fogler, 1992)

$$k_{ig} = 0.4548\,\mathrm{Re}^{-0.4069}\left[\frac{D_{im}}{\alpha_g d_s}\left(\frac{\mu_g}{\rho_g D_{im}}\right)^{\frac{1}{3}}\mathrm{Re}\right] \qquad \text{when Re<10} \qquad (6)$$

$$k_{ig} = \left(\frac{0.765}{\mathrm{Re}^{0.82}}+\frac{0.365}{\mathrm{Re}^{0.386}}\right)\left[\frac{D_{im}}{\alpha_g d_s}\left(\frac{\mu_g}{\rho_g D_{im}}\right)^{\frac{1}{3}}\mathrm{Re}\right] \qquad \text{when Re} \geq 10 \qquad (7)$$

5. Heat transfer in fluidized bed

A clear understanding of heat transfer behaviors in CFBs may help to control the bed temperature and energy exchange during reaction. It is also necessary for the proper design of CFB reactors. Heat transfer between gas and solids flow in a CFB comprises mainly of three components: particle convection, gas convection and radiation. At low temperature, the radiation component can be neglected. Normally, particle convection is the primary heat transfer mechanism, given the large heat capacity of the solids, as compare to the gas. Gas convection may become importance when gas velocity is high and solids holdup is low. In 1999, Ma and Zhu experimentally studied the local heat transfer in a co-current down flow fluidized bed with FCC particles. The results showed that the radial and axial distributions of heat transfer in a downer were not the same as those in a riser. The heat transfer rate in the downer is closely related to the hydrodynamics. The average heat transfer coefficient decreases along the column as shown in Figure 2. This decreasing of the heat transfer coefficient is understandable because the average measured solids holdup also decreases from the top to the bottom. At the top of the bed, the average heat transfer coefficient increases with solids circulation rate or decreasing of gas velocity. The dilute region will lead to the gas convection becoming an important component, such as at the lower bed position where the heat transfer coefficients are higher at higher gas velocities under the same solids circulation rate. The local heat transfer rate also changes with radial position as shown in Figure 3, in the first acceleration section, the heat transfer coefficient is high and its radial distribution is very non-uniform.

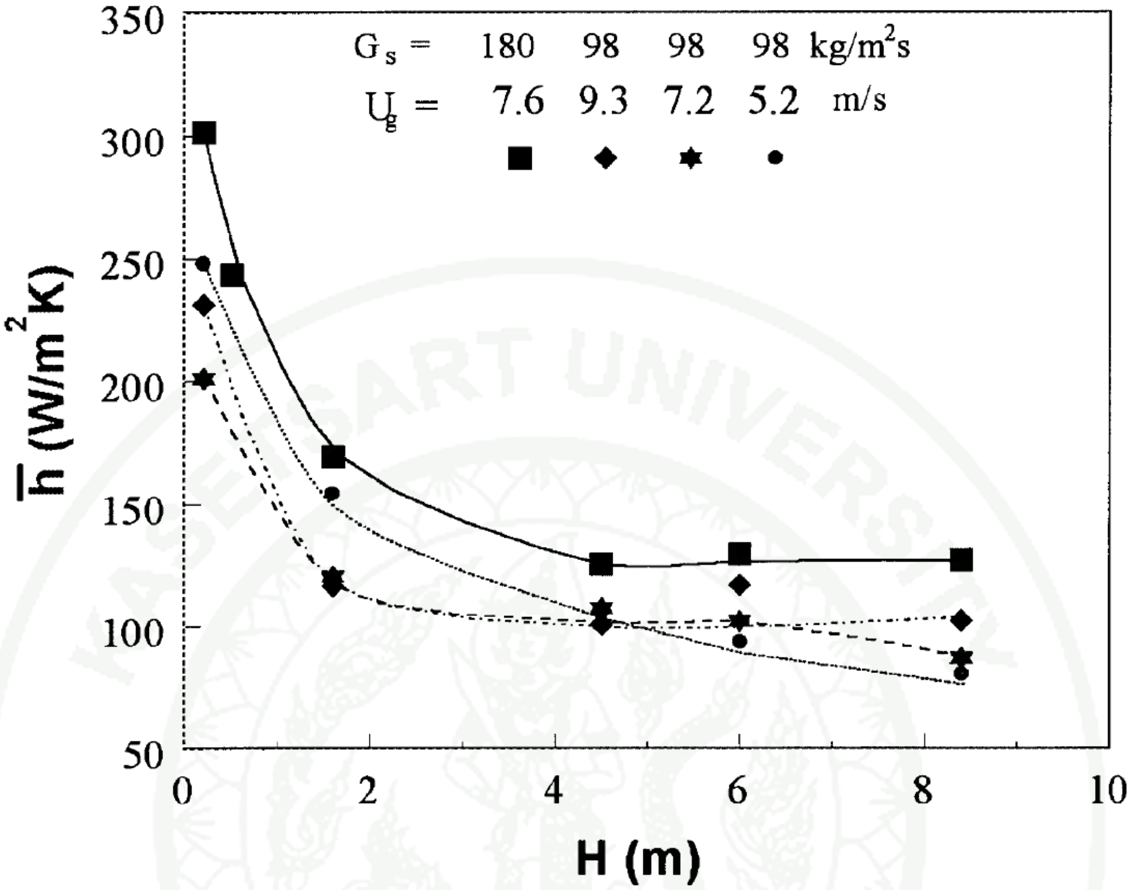

Figure 2 Axial distribution of the average heat transfer coefficient.

Source: Ma and Zhu (1999)

While it remains fairly constant in the central region of this section, the heat transfer coefficient increases dramatically to form a significant peak at $r/R \approx 0.85$-0.90, and then decreases toward the wall. Further down in the second acceleration section, this radial distribution becomes much more uniform and almost constant along the radial direction in the third section.

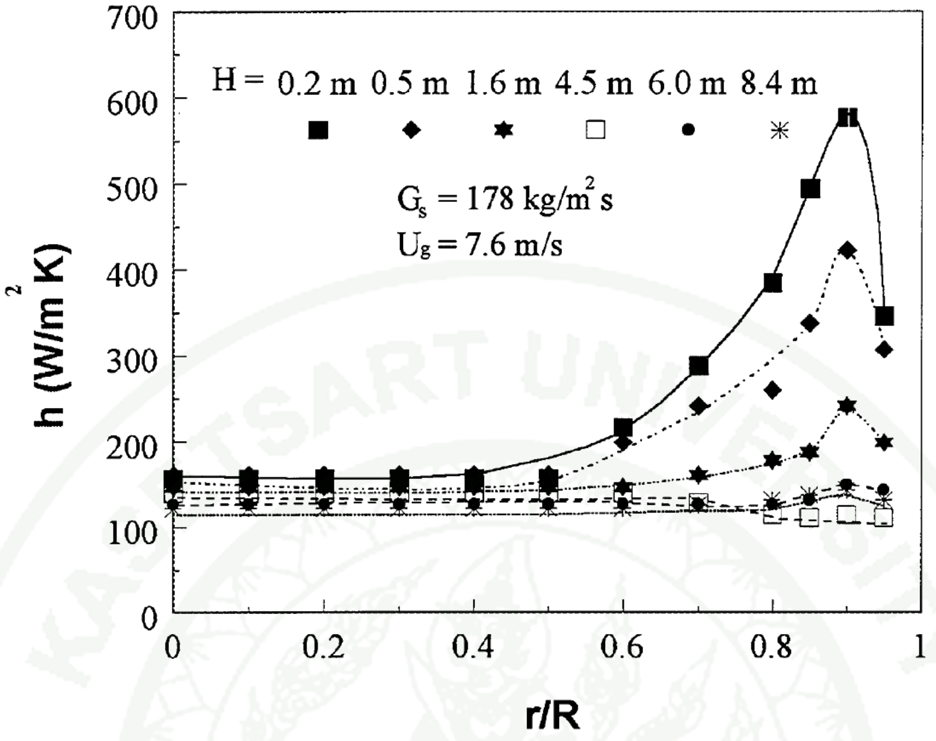

Figure 3 Radial distribution of the heat transfer coefficient in axial position.

Source: Ma and Zhu (1999)

The DEM model was implemented for investigating the local heat and mass transfers in the fluidized bed polymerization reactor (Kaneko *et al.*, 1999; Kladthong, 2005; Limtrakul *et al.*, 2006). The simulation was performed using a numerical code and incorporating the energy balance and the reaction rate. The heat transfer coefficient (*h*) is estimated by the following Ranz-Marshall equation:

$$Nu = 2.0 + 0.6\,\mathrm{Pr}^{1/3}\,\mathrm{Re}^{1/2} \tag{8}$$

where

$$Nu = hd_s / \lambda_g \tag{9}$$

$$\Pr = C_{p,g}\mu_g / \lambda_g \tag{10}$$

$$\mathrm{Re} = \rho_g d_s \left| u_s - u_g \right| / \mu_g \tag{11}$$

where λ_g is the thermal conductivity of the gas, $C_{p,g}$ the heat capacity of gas, μ_g the gas viscosity, and $\left| u_s - u_g \right|$ the gas-to-particle relative velocity.

The energy balance for gas phase

$$\frac{\partial(\alpha_g T_g)}{\partial t} + \frac{\partial(\alpha_g u_i T_g)}{\partial x_i} = \frac{Q_g}{\rho_g C_{p,g}} \tag{12}$$

where T_g is the gas temperature. Q_g is the heat transfer rate between particle and gas phases in a unit volume and is expressed by the following equation:

$$Q_g = \frac{6(1-\alpha_g)}{d_s}\left\langle h(T_s - T_g)\right\rangle \tag{13}$$

where h is the heat transfer coefficient between particle and gas phases, d_s the particle diameter, and T_s the temperature of the particle in the fluid cell.

The energy balance for a particle is given by the following equation:

$$V_s C_{p,s} \rho_s \frac{dT_s}{dt} = r_s(-\Delta H) - \left\{ h\left(T_s - T_g\right) S_s \right\} \tag{14}$$

where V_s is the volume of the particle, $C_{p,s}$ the specific heat of the solids, $-\Delta H$ the heat of polymerization, r_s the reaction rate on the catalyst surface, and S_s the external surface area of a particle.

6. Mathematical model

Computer capability has been recently developed to a great extent and thus Computational Fluid Dynamics (CFD) has become a powerful tool to study the flow behavior in fluidized beds. Two main approaches have been used to simulate flow behavior in fluidized beds: Eulerian-Lagragian and Eulerian-Eulerian approaches. An Eulerian-Lagragian approach such as the DEM model treats gas as a continuous phase while the movement of each particle in the system is calculated from Newton's second law of motion. An Eulerian-Eulerian approach such as the two-fluid model considers each phase as an interpenetrating continuum and uses the kinetic theory of granular flow as a model for particle scale interactions. The kinetic theory of granular flow is thus used for the calculation of the flow properties of the solids phase (solid pressure, solid viscosity, etc.). As a comparison of the two methods, the Eulerian-Lagragian approach is a time-consuming method for systems with a high amount of solids particles, such as fluidized bed reactors. Thus the Eulerian-Eulerian approach becomes an appropriate method for these reactors.

6.1 Discrete Element Method (DEM)

The DEM model was originally used to predict the behavior of soil. Cundall and Strack (1979) developed the DEM model for predicting the behavior of granular flow system. Many researchers further developed the DEM model to simulate gas-solids flow systems such as fluidized bed reactors. In DEM model, gas phase is considered as a continuous phase. The particle contact force is calculated with simple mechanism models of a spring, a dash-pot, and a friction slider.

6.1.1 Particle motion

The Newton's second law of motion is used for calculating the particle movement with includes the effects of gravitational force, contact force and fluid force. Both translational and rotational motions are considered in the equations of motion. The equations for the individual particle can be written as follows:

$$\vec{a} = \frac{\vec{f}_{total}}{m} + \vec{g} \tag{15}$$

$$\vec{\alpha} = \frac{\vec{T}}{I} \tag{16}$$

where $\vec{a}$ is the particle acceleration vector; m is the particle mass; $\vec{f}_{total}$ is the total of force acting on the particle; $\vec{g}$ is the gravity acceleration vector; $\vec{\alpha}$ is the angular acceleration vector; $\vec{T}$ is the net torque caused by the contact force and I is the moment of inertia of the particle. The force acting on each particle consists of the particle contact force ($\vec{f}_C$) and the force exerted by the surrounding fluid ($\vec{f}_D$) which can be written as:

$$\vec{f}_{total} = \vec{f}_C + \vec{f}_D \tag{17}$$

The new velocities and position of the particle after the time step Δt are given by:

$$\vec{u} = \vec{u}_{old} + \vec{a}\Delta t \tag{18}$$

$$\vec{\omega} = \vec{\omega}_{old} + \vec{\alpha}\Delta t \tag{19}$$

$$\vec{x} = \vec{x}_{old} + \vec{u}\Delta t \tag{20}$$

where Δt is the time step increment; and $\vec{x}$ is the position vector.

The soft particle model was used to calculate the particle contact force using a spring, dash pot, slider and other mechanical elements (Cundall and Strack, 1979). In estimating the contact force acting between two particles in DEM model, the contacting of two particles is allowed to overlap instead of the deforming. The estimation of the contact force using the analogy of a spring, a dash pot and a friction slider shows in Figure 4. The parameters of stiffness, dissipation and friction coefficients can be obtained from the physical properties of the particles such as Young's modulus, Poisson ratio and the coefficients of restitution. The details of the estimation of parameters were shown in the previous work (Tsuji *et al.*, 1992). The contact force can be separated into normal ($\vec{f}_{c,nor}$) and tangential ($\vec{f}_{c,\tan}$) directions as written in Eqs. (21) and (22), respectively.

$$\vec{f}_{c,nor} = -k_{stif,nor}\vec{\delta}_{nor} - \eta_{damp}\dot{\vec{\delta}}_{nor} \tag{21}$$

$$\vec{f}_{c,\tan} = -k_{stif,\tan}\vec{\delta}_{\tan} - \eta_{damp}\dot{\vec{\delta}}_{\tan} \tag{22}$$

if $\vec{f}_{c,\tan} > \mu_f \left| \vec{f}_{c,nor} \right|$ then

$$\vec{f}_{c,\tan} = -\mu_f \left| \vec{f}_{c,nor} \right| \tag{23}$$

where $\vec{\delta}_{nor}$ and $\vec{\delta}_{\tan}$ are the particle displacements in the normal and tangential directions, respectively; k_{stif} is the stiffness of the spring; and μ_f is the coefficient of viscous dissipation.

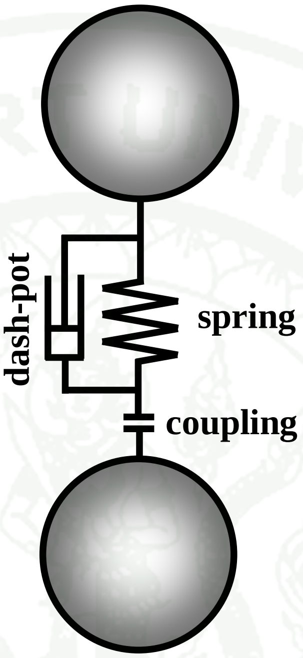

(a)

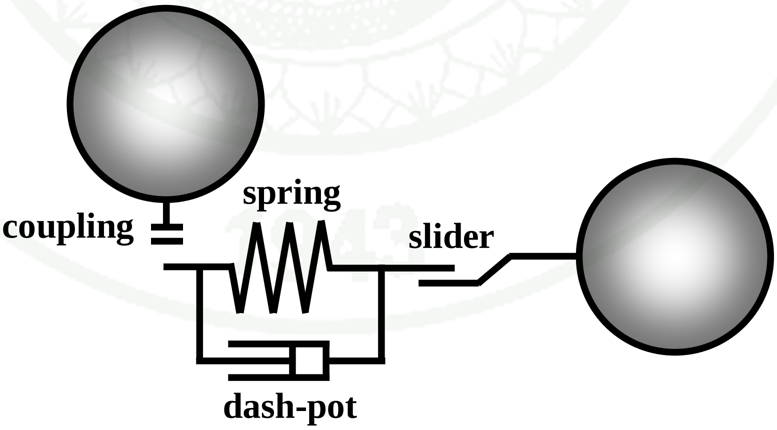

(b)

Figure 4 Models of contact force (a) the normal force, (b) the tangential force.

In the downer reactor, each particle contacts with many neighboring particles and/or walls. Thus the total contact force for the consideration particle *i* is obtained by the summation of all these contact forces, which can be written in Eqs. (24) and (25)

$$\vec{f}_{c,nor} = \sum_{j=1}^{N} \vec{f}_{c,nor,ij} \tag{24}$$

$$\vec{f}_{c,\tan} = \sum_{j=1}^{N} \vec{f}_{c,\tan,ij} \tag{25}$$

where *i* is the consideration particle and *j* are the adjacent particles and/or walls; *N* is the total number of adjacent particles/walls.

The force exerted by the surrounding fluid ($\vec{f}_D$) can be calculated from Ergun's equation (Tsuji *et al.*, 1992; Boonsrirat, 2001; Muangrat, 2001; Limtrakul *et al.*, 2002,2007; Thanomboon, 2005),

r direction :

$$\vec{f}_{Dr} = \frac{\pi d_s^3}{6}\left[\frac{\beta}{(1-\alpha_g)}(\vec{u}_{g,r} - \vec{u}_{s,r}) + (1-\alpha_g)\frac{\partial p}{\partial r}\right] \tag{26}$$

z direction :

$$\vec{f}_{Dz} = \frac{\pi d_s^3}{6}\left[\frac{\beta}{(1-\alpha_g)}(\vec{u}_{g,z} - \vec{u}_{s,z}) + (1-\alpha_g)\frac{\partial p}{\partial z}\right] \tag{27}$$

where $\vec{u}_{g,r}$ and $\vec{u}_{g,z}$ are fluid velocities in r and z directions respectively; $\vec{u}_{s,r}$ and $\vec{u}_{s,z}$ are the average particle velocities in r and z directions. The coefficient β depends on the void fraction (Ergun, 1952) as given by:

$$\beta = \frac{(1-\alpha_g)}{d_s \alpha_g^2}\left[150\frac{(1-\alpha_g)\mu}{d_s} + 1.75\rho\alpha_g\left|\vec{u}_s - \vec{u}_g\right|\right] \qquad \text{for } \varepsilon \le 0.8 \tag{28}$$

$$\beta = \frac{3}{4}C_D \frac{\left|\vec{u}_s - \vec{u}_g\right|\rho(1-\alpha_g)}{d_s}\alpha_g^{-2.7} \qquad \text{for } \varepsilon > 0.8 \tag{29}$$

which

$$C_D = 24\left(1 + 0.15\,\mathrm{Re}^{0.687}\right)/\mathrm{Re} \qquad \text{for } \mathrm{Re} \le 1000 \tag{30}$$

$$C_D = 0.43 \qquad \text{for } \mathrm{Re} > 1000 \tag{31}$$

$$\mathrm{Re} = \frac{\left|\vec{u}_s - \vec{u}_g\right|\rho\alpha_g d_s}{\mu} \tag{32}$$

where d_s is the diameter of particle.

6.1.2 Gas motion

The fluid motion is described by the equations of momentum conservation, as shown below.

Equation of momentum conservation can be expressed as follow:

$$\frac{\partial(\alpha_g \vec{u}_g)}{\partial t} + (\nabla \cdot \alpha_g \vec{u}_g \vec{u}_g) = -\frac{\nabla \alpha_g p}{\rho} + \vec{f}_p \tag{33}$$

where $\vec{u}_g$ is the fluid velocity vector, α_g the void fraction, ρ the density of gas, and p the pressure. The drag force of fluid on particle ($\vec{f}_p$) in Eq. (33) is given by

$$\vec{f}_p = \frac{\beta}{\rho}\left(\vec{u}_s - \vec{u}_g\right) \tag{34}$$

6.1.3 Equation of mass conservation

The concept of mass transfer mechanism is described in this section. The reactant in the bulk gas phase diffuses though the gas film surrounding the catalyst particles as seen in Figure 7 (c). The reaction takes place on the catalyst surface. The reaction rate depends on the reactant concentration in solids phase. The product diffuses from the catalyst surface to the bulk gas phase. The concentration distribution for component *i* in gas phase can be calculated from Eq. (35). This equation includes the terms of accumulation, convection, diffusion and mass transfer between phases.

$$\frac{\partial(\alpha_g C_i)}{\partial t} + \frac{1}{r}\frac{\partial(r\alpha_g u_r C_i)}{\partial r} + \frac{\partial(\alpha_g u_z C_i)}{\partial z} = \frac{1}{r}\frac{\partial}{\partial r}\left(r\frac{\partial(\alpha_g D_{im} C_i)}{\partial r}\right) + \frac{\partial}{\partial z}\left(\frac{\partial(\alpha_g D_{im} C_i)}{\partial z}\right) + \frac{6(1-\alpha_g)}{d_s}k_g\left(C_{i,s} - C_i\right) \tag{35}$$

where C_i and $C_{i,s}$ are the concentrations of species *i* in gas and solids phases, respectively; α_g is void fraction; D_{im} is diffusivity coefficient of species *i* in the gas mixture; d_s is the particle diameter; k_g is mass transfer coefficient between gas and solids phases.

The equation of mass conservation for component *i* in particle phase, which consists of accumulation term, mass transfer between phase term and generation term due to reaction, is written as follows:

$$\frac{\partial((1-\alpha_g)\rho_g C_{i,s})}{\partial t} = \frac{6(1-\alpha_g)}{d_s}\rho_g k_{ig}(C_i - C_{i,s}) + S_i \qquad (36)$$

where S_i is the mass source term due to reaction.

6.1.4 Equation of energy conservation

The heat transfer mechanism in gas phase is analogy to the mass transfer mechanism. Heat from hot gas was transferred from bulk gas phase to solids phase through the gas film surrounding the particles. This energy was used for endothermic catalytic cracking reaction in solids phase. The equation of energy conservation for gas phase describing the temperature distribution of gas phase is derived as:

$$\frac{\partial\left(\alpha_g \rho_g \hat{C}_{p,g} T_g\right)}{\partial t} + \nabla \cdot \left(\alpha_g \rho_g \vec{u} \hat{C}_{p,g} T_g\right) = \nabla \cdot \left(\alpha_g \lambda_g \nabla T_g\right) + \frac{6\left(1-\alpha_g\right)h}{d_s}\left(T_s - T_g\right) \qquad (37)$$

where $\hat{C}_{p,g}$ is the heat capacity of gas mixture; T_g and T_s are the temperatures of gas and particle phases, respectively; and h is the heat transfer coefficient between particles and gas phase.

The equation of energy conservation for particle phase is given by the following equation:

$$\frac{\partial\left(\left(1-\alpha_g\right)\rho_s C_{p,s} T_s\right)}{\partial t} = \frac{6\left(1-\alpha_g\right)h}{d_s}\left(T_g - T_s\right) + Q_s \tag{38}$$

where $C_{p,s}$ is the heat capacity of particles and Q_s is the heat source term. The first term of Eq. (38) represents the accumulation term. The second and the last terms are the heat transfer between phases and the source term due to the reaction, respectively.

6.2 Two-fluid model

The two-fluid model has been successfully developed to simulate the hydrodynamics behavior of fluidized beds (Ding and Gidaspow, 1990; Jiradilok *et al.*, 2006, 2007, 2008; Khongprom *et al.*, 2008; Rodriguez-Rojo and Cocero, 2009; Khongprom and Gidaspow, 2010). In addition, the two-fluid model has recently been developed for the extensive investigation of the flow behavior in a downer reactor, as summarized by Vaishali *et al.* (2008). Moreover, the two-fluid model has been used to study the mixing behavior in a gas–liquid system (van Baten and Krishna, 2001; Ekambara *et al.*, 2005; Talvy *et al.*, 2007; Moullec *et al.*, 2008).

The governing equations consist of a set of the conservation of mass, momentum and energy equations. The continuity equation for phase *i* (*i* = gas phase or solids phase) is written as

$$\frac{\partial}{\partial t}(\alpha_i \rho_i) + \nabla \cdot (\alpha_i \rho_i \vec{u}_i) = 0 \tag{39}$$

The conservation of momentum for the gas phase (g) yields

$$\frac{\partial}{\partial t}(\alpha_g \rho_g \vec{u}_g) + \nabla \cdot (\alpha_g \rho_g \vec{u}_g \vec{u}_g) = -\alpha_g \nabla p + \nabla \cdot \overset{=}{\tau}_g + \alpha_g \rho_g \vec{g} + \beta(\vec{u}_s - \vec{u}_g) \tag{40}$$

The conservation of momentum for the solid phase (s) is

$$\frac{\partial}{\partial t}(\alpha_s \rho_s \vec{u}_s) + \nabla \cdot (\alpha_s \rho_s \vec{u}_s \vec{u}_s) = -\alpha_s \nabla p - \nabla p_s + \nabla \cdot \overline{\overline{\tau}}_s + \alpha_s \rho_s \vec{g}$$

$$+ \beta(\vec{u}_g - \vec{u}_s) \tag{41}$$

where β is the inter phase momentum transfer coefficient.

The granular temperature for the solids phase is proportional to the kinetic energy of the random motion of the particles. The transport equation derived from the kinetic theory can be written in the form

$$\frac{3}{2}\left[\frac{\partial}{\partial t}(\rho_s \alpha_s \Theta_s) + \nabla \cdot (\rho_s \alpha_s \vec{u}_s \Theta_s)\right] = (-p_s \overline{\overline{I}} + \overline{\overline{\tau}}_s) : \nabla \vec{u}_s + \nabla \cdot (\kappa_{\Theta_s} \nabla \Theta_s)$$

$$- \gamma_{\Theta_s} + \phi_{gs} \tag{42}$$

The phase stress tensor of *i* phase is given by

$$\overline{\overline{\tau}}_i = \alpha_i \mu_i \left(\nabla \cdot u_i + \nabla \cdot u_i^T\right) + \alpha_i \left(\lambda_{s,i} - \frac{2}{3}\mu_i\right) \nabla \cdot u_i \overline{\overline{I}} \tag{43}$$

Solids pressure describes the change in the total momentum transport of the motion of particles and theirs interaction, which is expressed as

$$p_s = \alpha_s \rho_s \Theta_s + 2\rho_s (1 + e_{ss}) \alpha_s^2 g_{0,ss} \Theta_s \tag{44}$$

The radial distribution function is a correction factor that modifies the probability of collisions between particles when the solids phase becomes dense. This term is given by

$$g_{0,ss} = \left[1 - \left(\frac{\alpha_s}{\alpha_{s,\max}}\right)^{\frac{1}{3}}\right]^{-1} \tag{45}$$

The solids shear viscosity which consists of a collision term, a kinetic term, and a friction term is given by

$$\mu_s = \mu_{s,col} + \mu_{s,kin} + \mu_{s,fr} \tag{46}$$

The solids collisional part of solids shear viscosity is modeled as

$$\mu_{s,col} = \frac{4}{5}\alpha_s \rho_s d_s g_{0,ss}(1+e_{ss})\left(\frac{\Theta_s}{\pi}\right)^{1/2} \tag{47}$$

The kinetic viscosity from Syamlal and O’Brien (1993) is expressed as

$$\mu_{s,kin} = \frac{\alpha_s d_s \rho_s \sqrt{\Theta_s \pi}}{6(3-e_{ss})}\left[1 + \frac{2}{5}(1+e_{ss})(3e_{ss}-1)\alpha_s g_{0,ss}\right] \tag{48}$$

The solids frictional viscosity from Schaeffer’s expression is

$$\mu_{s,fr} = \frac{p_s \sin\phi}{2\sqrt{I_{2D}}} \tag{49}$$

The solids bulk viscosity, which accounts for the resistance of the solids phase to compression and expansion is expressed by (Lun *et al.*, 1984):

$$\lambda_s = \frac{4}{3}\alpha_s \rho_s d_s g_{0,ss}(1+e_{ss})\left(\frac{\Theta_s}{\pi}\right)^{1/2} \tag{50}$$

The diffusion coefficient of granular temperature (Syamlal and O’Brien, 1993) is given by

$$\kappa_{\Theta_s} = \frac{15 d_s \rho_s \alpha_s \sqrt{\Theta_s \pi}}{4(41-33\eta_\Theta)} \left[1 + \frac{12}{5}\eta_\Theta^2 \left(4\eta_\Theta - 3\right)\alpha_s g_{0,ss} + \frac{16}{15\pi}\left(41-33\eta_\Theta\right)\eta_\Theta \alpha_s g_{0,ss} \right] \qquad (51)$$

where

$$\eta_\Theta = \frac{1}{2}(1+e_{ss}) \qquad (52)$$

The collision dissipation of energy represents the rate of energy dissipation within the solids phase due to collision between particles (Lun *et al.*, 1984)

$$\gamma_{\Theta_s} = \frac{12(1-e_{ss}^2)g_{0,ss}}{d_s\sqrt{\pi}} \rho_s \alpha_s^2 \Theta_s^{3/2} \qquad (53)$$

The transfer of the kinetic energy from the solids phase to the gas phase is expressed by

$$\phi_{gs} = -3K_{\Theta,gs}\Theta_s \qquad (54)$$

MATERIALS AND METHODS

1. Equipment

1. The DEM model was carried out by a personal computer with RedHat Linux operating system. The FORTRAN code was adopted.
2. The two-fluid model was performed using FLUENT software.

2. Methodology

The hydrodynamics, heat and mass transfer in the downer reactor were predicted using the two-fluid model and the discrete element method (DEM). The methodology of this work was described below.

2.1 Hydrodynamics and axial gas and solids mixing in a downer reactor

The two-fluid model based on the kinetic theory of granular flow with k-ε turbulence model was developed to study the hydrodynamics and the axial dispersion of gas and particle in a downer reactor. In the two-fluid model, both gas and solids are considered as the continuous phases. The kinetic theory of granular flow was used to calculate the solids phase stress. The simulation was performed in a two-dimension. A downer reactor geometry is depicted in Figure 5(a). Such a reactor consists of a particle storage tank, distributor, downer section, in which both gas and particles flow co-currently downward in the gravitational direction, and a riser section, which is used to convey solids particles back to the storage tank. To simplify the problem, only the downer section was simulated. A 2-D computational domain of the downer reactor used in this study is shown in Figure 5(b). Its height and diameter are 7 and 0.14 m, respectively.

2.1.1 Simulation conditions

Air including nitrogen and oxygen was used as the fluidizing gas. At the inlet, velocity, fraction of each phase, and concentration of each species in gas phase were specified. The simulation conditions are summarized in Table 2.

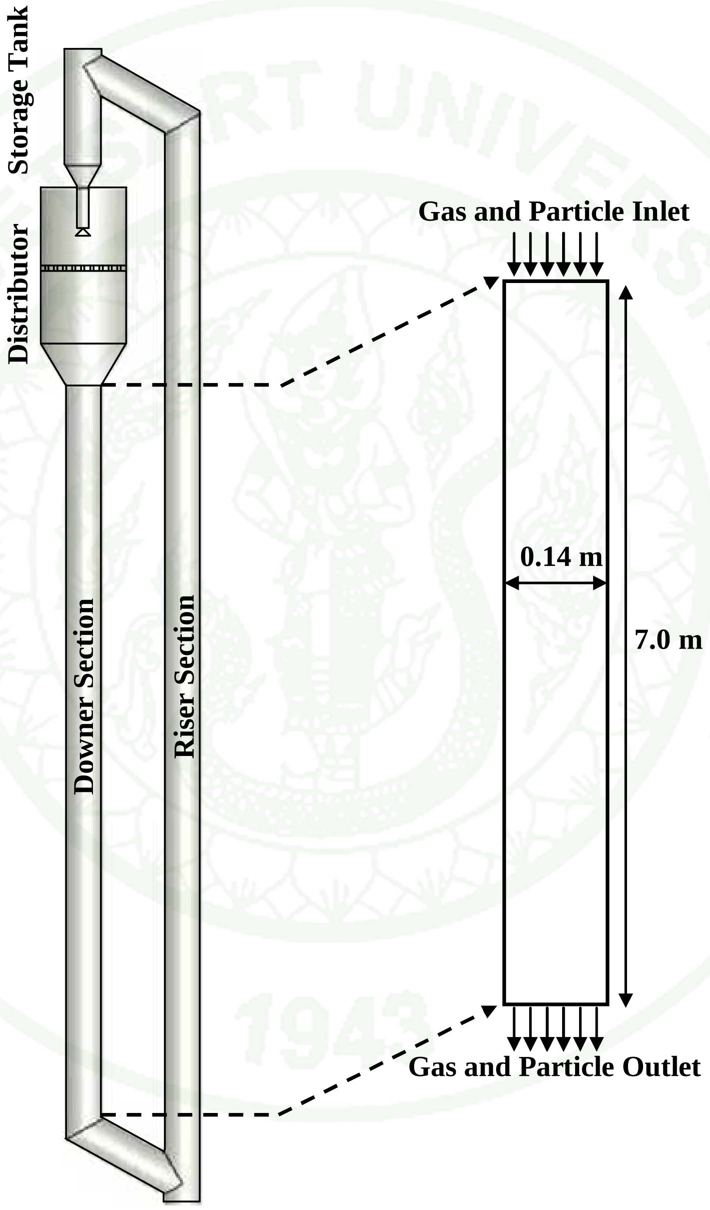

(a) (b)

Figure 5 Geometry of a downer reactor (a), and 2-D computational domain used for studying the axial mixing in a downer reactor (b).

Table 2 Simulation conditions for studying axial gas and solids mixing in a downer reactor.

Simulation case	Superficial gas velocity (m/s)	Solids circulation rate (kg/m^{2}s)	Particle diameter (μm)	Particle density (kg/m^3)
The effects of superficial gas velocity	2.00	31	54	1 545
	4.33			
	6.00			
	3.43	70	54	1 545
	4.33			
	6.10			
	7.50			
	8.50			
	9.50			
The effects of solids circulation rate	4.33	31	54	1 545
		70		
		110		
		150		
The effects of particle size	4.33	70	25	1 545
			54	
			75	
			100	
The effects of particle density	4.33	70	54	1 000
				1 545
				2 000
				2 500

2.1.2 Mathematical model

The hydrodynamics model based on the kinetic theory of granular flow coupling with k-ε turbulent model was used to predict flow behavior in a downer reactor. CFD simulation has been performed with the commercial software of FLUENT. The governing and constitutive equations are discussed below.

The continuity equation for phase q is expressed by

$$\frac{\partial}{\partial t}\left(\alpha_q \rho_q\right) + \nabla \cdot \left(\alpha_q \rho_q \vec{u}_q\right) = 0 \tag{55}$$

where the subscript q stands for gas, main solids, and tracer solids phases, α_q the volume fraction, ρ_q the density, and $\vec{u}_q$ the velocity vector.

The momentum equation for the gas phase g is given by

$$\frac{\partial}{\partial t}\left(\alpha_g \rho_g \vec{u}_g\right) + \nabla \cdot \left(\alpha_g \rho_g \vec{u}_g \vec{u}_g\right) = -\alpha_g \nabla p + \alpha_g \rho_g \vec{g} + \nabla \cdot \overline{\overline{\tau}}_g + \nabla \cdot \overline{\overline{\tau}}_{tu,g} + \sum_{n=1}^{N} \beta_{gn}\left(\vec{u}_n - \vec{u}_g\right) \tag{56}$$

n=1 for gas phase (g), n=2 for main solids phase (p), and n=3 for tracer solids phase (t), $\overline{\overline{\tau}}_g$ and $\overline{\overline{\tau}}_{tu,g}$ the viscous stress tensor and the Reynolds stress tensor, respectively, β_{gn} the interphase momentum transfer coefficient between the gas phase g and phase n, and N the total number of phases (N=3).

The momentum equation for the main solids phase p can be expressed as,

$$\frac{\partial}{\partial t}\left(\alpha_p\rho_p\vec{u}_p\right)+\nabla\cdot\left(\alpha_p\rho_p\vec{u}_p\vec{u}_p\right)=-\alpha_p\nabla p-\nabla p_p+\nabla\cdot\overline{\overline{\tau}}_p+\nabla\cdot\overline{\overline{\tau}}_{tu,p}+$$

$$\alpha_p\rho_p\vec{g}+\sum_{n=1}^{N}\beta_{pn}\left(\vec{u}_n-\vec{u}_p\right) \tag{57}$$

where p_p is the solids pressure of the main solids phase and β_{pn} the interphase momentum transfer coefficient between the main solids phase *p* and phase *n*.

The momentum equation for the tracer solids phase *t* can be written as,

$$\frac{\partial}{\partial t}\left(\alpha_t\rho_t\vec{u}_t\right)+\nabla\cdot\left(\alpha_t\rho_t\vec{u}_t\vec{u}_t\right)=-\alpha_t\nabla p-\nabla p_t+\nabla\cdot\overline{\overline{\tau}}_t+\nabla\cdot\overline{\overline{\tau}}_{tu,t}+\alpha_t\rho_t\vec{g}+$$

$$\sum_{n=1}^{N}\beta_{tn}\left(\vec{u}_n-\vec{u}_t\right) \tag{58}$$

where p_t is the solids pressure of the tracer solids phase and β_{tn} the interphase momentum transfer coefficient between the tracer solids phase *t* and phase *n*.

In accordance with the low solids concentration in this study, the Wen and Yu drag model (Wen and Yu, 1966) was used to calculate the interphase momentum transfer coefficient between the gas phase *g* and the solids phase *s*. The solids phases can be either main solids phase *p* or tracer solids phase *t* as follows:

$$\beta_{gs}=\frac{3}{4}\frac{\left(1-\alpha_g\right)\alpha_g}{d_s}\rho_g\left|\vec{u}_g-\vec{u}_s\right|C_D\alpha_g^{-2.65} \tag{59}$$

with

$$C_D=\frac{24}{\mathrm{Re}}\left(1+0.15\,\mathrm{Re}^{0.687}\right) \tag{60}$$

and

$$\mathrm{Re} = \frac{\rho_g \alpha_g \left|\vec{u}_g - \vec{u}_s\right| d_s}{\mu_g} \tag{61}$$

The interphase momentum transfer coefficient between the tracer solids phase *t* and the main solids phase *p* is calculated by means of the Syamlal–O'Brien symmetric model (Syamlal, 1987):

$$\beta_{tp} = \frac{3\left(1+e_s\right)\left(\frac{\pi}{2} + C_{fr,tp}\frac{\pi^2}{8}\right)\alpha_t \rho_t \alpha_p \rho_p \left(d_t + d_p\right)^2 g_{0,tp}}{2\pi\left(\rho_p d_p^3 + \rho_t d_t^3\right)}\left|\vec{u}_t - \vec{u}_p\right| \tag{62}$$

where e_s is the coefficient of restitution, $C_{fr,tp}$ the coefficient of friction between the tracer solids phase *t* and the main solids phase *p*, *d* the diameter of the particle, and $g_{0,tp}$ the radial distribution coefficient.

The granular temperature is proportional to the kinetic energy of the random motion of the particles. The granular temperature transport equations for the main solids phase *p* and the tracer solids phase *t* derived from the kinetic theory take the form (Ding and Gidaspow, 1990):

$$\frac{3}{2}\left[\frac{\partial}{\partial t}\left(\rho_s \alpha_s \Theta_s\right) + \nabla\cdot\left(\rho_s \alpha_s \vec{u}_s \Theta_s\right)\right] = \left(-p_s \overline{\overline{I}} + \overline{\overline{\tau}}_s\right) : \nabla \vec{u}_s + \nabla\cdot\left(k_{\Theta s}\nabla\Theta_s\right) - \gamma_{\Theta s} + \sum_{n=1}^{N}\phi_{ns} \tag{63}$$

where the subscript *s* stands for main solids phase *p* and tracer solids phase *t*. The first term on the right side of the equation represents the generation of energy by the solids stress tensor. The second and the third terms denote the diffusion and the collisional dissipation of energy, respectively. The last term represents the energy exchange between the solids phase *s* and phase *n*. The constitutive equations for closing the governing equations are summarized in Table 3.

Table 3 Constitutive equations for studying gas and solids mixing in a downer reactor.

Parameter	Equation
(a) Gas phase stress:	$\overline{\overline{\tau}}_g = \alpha_g \mu_g \left[\nabla \vec{u}_g + \left(\nabla \vec{u}_g\right)^T\right] - \frac{2}{3}\alpha_g \mu_g \left(\nabla \cdot \vec{u}_g\right)\overline{\overline{I}}$
(b) Solids phase stress:	$\overline{\overline{\tau}}_p = \alpha_p \mu_p \left[\nabla \vec{u}_p + \left(\nabla u_p\right)^T\right] - \alpha_p \left(\xi_p - \frac{2}{3}\mu_p\right)\nabla \cdot \vec{u}_p \overline{\overline{I}}$
(c) Reynolds stress:	$\overline{\overline{\tau}}_{tu,q} = \alpha_q \mu_{tu,q} \left[\nabla \vec{u}_q + \left(\nabla \vec{u}_q\right)^T\right] - \frac{2}{3}\alpha_q \left(\rho_q k_q + \rho_q \mu_{tu,q} \nabla \cdot \vec{u}_q\right)\overline{\overline{I}}$
(d) Collisional dissipation of solids fluctuating energy:	$\gamma_p = 3\left(1 - e^2\right)\alpha_p^2 \rho_p g_0 \Theta_p \left(\frac{4}{d_p}\sqrt{\frac{\Theta_p}{\pi}}\right)$
(e) Radial distribution function:	$g_0 = \left[1 - \left(\frac{\alpha_p}{\alpha_{p,\max}}\right)^{1/3}\right]^{-1}$
(f) Solids phase pressure:	$p_p = \alpha_p \rho_p \Theta_p \left[1 + 2 g_0 \alpha_p (1 + e_s)\right]$
(g) Solids phase shear viscosity:	$\mu_p = \frac{4}{5}\alpha_p \rho_p d_p g_0 (1 + e_s)\sqrt{\frac{\Theta_p}{\pi}} + \frac{10 \rho_p d_p \sqrt{\pi \Theta_p}}{96 (1 + e_s) g_0 \alpha_p}\left[1 + \frac{4}{5} g_0 \alpha_p (1 + e_s)\right]^2$
(h) Solids phase bulk viscosity:	$\xi_p = \frac{4}{3}\alpha_p \rho_p d_p g_0 (1 + e_s)\sqrt{\frac{\Theta_p}{\pi}}$

Table 3 (Continued)

Parameter	Equation
(i) Conductivity of the fluctuating energy:	$\kappa_p = \frac{150\rho_p d_p\sqrt{\Theta_p\pi}}{384(1+e_s)g_0}\left[1+\frac{6}{5}\alpha_p g_0(1+e_s)\right]^2 + 2\rho_p\alpha_p^2 d_p(1+e_s)g_0\sqrt{\frac{\Theta_p}{\pi}}$
(j) Momentum transfer coefficient between gas-solids phase (Wen and Yu, 1966):	$K_{gp} = \frac{3}{4}\frac{(1-\alpha_g)\alpha_g}{d_p}\rho_g\left\|\vec{u}_g-\vec{u}_p\right\|C_{D0}\alpha_g^{-2.65}$ where $C_{D0} = \frac{24}{\mathrm{Re}}\left(1+0.15\,\mathrm{Re}^{0.687}\right)$ and $\mathrm{Re} = \frac{\rho_g\alpha_g\left\|\vec{u}_g-\vec{u}_p\right\|d_p}{\mu_g}$
(k) Momentum transfer coefficient between solids-solids phase (Syamlal, 1987):	$\beta_{pq} = \frac{3(1+e_s)\left(\frac{\pi}{2}+C_{fr,pq}\frac{\pi^2}{8}\right)\alpha_q\rho_q\alpha_p\rho_p(d_q+d_p)^2 g_{0,pq}}{2\pi(\rho_p d_p^3+\rho_q d_q^3)}\left\|\vec{u}_p-\vec{u}_q\right\|$

The species transport equation of species *i* in the gas phase *g* can be represented in the following form:

$$\frac{\partial}{\partial t}\left(\rho_g\alpha_g Y_{i,g}\right)+\nabla\cdot\left(\rho_g\alpha_g\vec{u}_g Y_{i,g}\right)=-\nabla\cdot\alpha_g\vec{J}_{i,g} \tag{64}$$

This equation is used for monitoring the concentrations of nitrogen, oxygen, and carbon dioxide (as a gas tracer). $\vec{J}_{i,g}$ in Eq. (64), is the diffusion flux of species *i*, which arises due to concentration gradients. In turbulent flows, the mass diffusion flux can be formulated as follows:

$$\vec{J}_{i,g} = -\left(\rho_g D_{i,m} + \frac{\mu_{tu}}{Sc_{tu}} \right) \nabla Y_{i,g} \tag{65}$$

where $D_{i,m}$ is the diffusion coefficient for species *i* in the mixture and μ_{tu} the turbulent viscosity. The turbulent Schmidt number, Sc_{tu} is assumed constant as 0.7.

$$\mu_{tu} = \rho_g C_\mu \frac{k_g^2}{\varepsilon_g} \tag{66}$$

where C_μ is the turbulence model constant, k_g the turbulent kinetic energy of the gas phase g, and ε_g the turbulent dissipation rate of the gas phase g.

The standard *k*-ε turbulent model with per phase approach was used in this study. This approach solves the turbulent equations for each phase. The turbulent kinetic energy, *k* and turbulent dissipation rate, ε is obtained by solving Eqs. (67) and (68) respectively.

$$\frac{\partial}{\partial t}\left(\alpha_q \rho_q k_q\right) + \nabla \cdot \left(\alpha_q \rho_q \vec{u}_q k_q\right) = \nabla \cdot \left(\alpha_q \frac{\mu_{tu,q}}{\sigma_k} \nabla k_q \right) + \left(\alpha_q G_{k,q} - \alpha_q \rho_q \varepsilon_q\right) +$$
$$\sum_{n=1}^{N} K_{nq}\left(C_{nq} k_n - C_{qn} k_q\right) - \sum_{n=1}^{N} K_{nq}\left(\vec{u}_n - \vec{u}_q\right) \cdot \frac{\mu_{tu,n}}{\alpha_n \sigma_n} \nabla \alpha_n + \sum_{n=1}^{N} K_{nq}\left(\vec{u}_n - \vec{u}_q\right) \cdot \frac{\mu_{tu,q}}{\alpha_q \sigma_q} \nabla \alpha_q \tag{67}$$

and

$$\frac{\partial}{\partial t}\left(\alpha_q \rho_q \varepsilon_q\right) + \nabla \cdot \left(\alpha_q \rho_q \vec{u}_q \varepsilon_q\right) = \nabla \cdot \left(\alpha_q \frac{\mu_{tu,q}}{\sigma_\varepsilon} \nabla \varepsilon_q \right) + \frac{\varepsilon_q}{k_q} \left[C_{1\varepsilon} \alpha_q G_{k,q} - \right.$$

$$C_{2\varepsilon}\alpha_q\rho_q\varepsilon_q + C_{3\varepsilon}\left(\sum_{n=1}^{N}K_{nq}\left(C_{nq}k_n - C_{qn}k_q\right) - \sum_{n=1}^{N}K_{nq}\left(\vec{u}_n - \vec{u}_q\right)\frac{\mu_{tu,n}}{\alpha_n\sigma_n}\nabla\alpha_n + \right.$$

$$\left.\sum_{n=1}^{N}K_{nq}\left(\vec{u}_n - \vec{u}_q\right)\frac{\mu_{tu,q}}{\alpha_q\sigma_q}\nabla\alpha_q\right)\Bigg] \qquad (68)$$

where σ_k and σ_ε are the turbulent Prandtl numbers for the turbulent kinetic energy and the dissipation rate, respectively, and K_{nq} the turbulent interphase momentum transfer coefficient between phase n and phase q. The term C_{nq} is assumed constant as 2 and C_{qn} can be calculated as (Fluent User’s Guide, 2006):

$$C_{qn} = 2\left(\frac{\eta_{qn}}{1+\eta_{qn}}\right) \qquad (69)$$

where η_{qn} is the ratio between the Lagragian integral time scale and the characteristic particle relaxation time. The turbulent constants used in this study are summarized in Table 4.

Table 4 Turbulence model constant.

$C_{1\varepsilon}$	$C_{2\varepsilon}$	$C_{3\varepsilon}$	C_μ	σ_k	σ_ε
1.44	1.92	1.30	0.09	1.0	1.3

2.1.3 Numerical method

The governing equations were discretized by means of the finite volume method (Patankar, 1980). A first-order upwind scheme was applied as to differentiate the convection terms. The SIMPLE algorithm was used for the pressure-velocity coupling and correction. FLUENT CFD software was used in this case study. The grid independency was tested as shown in Figure 6. Both Figures 6(a) and

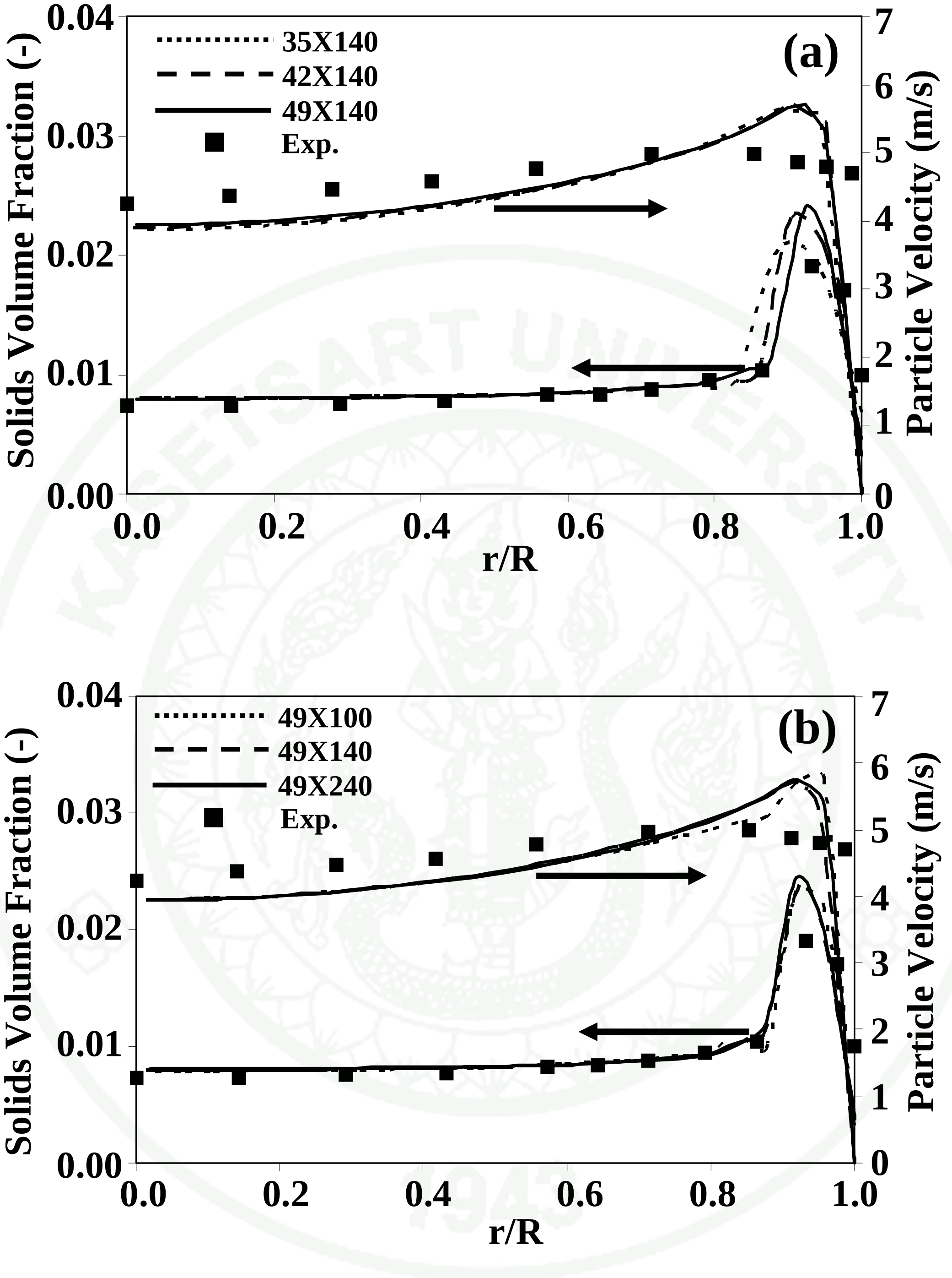

Figure 6 Time-averaged solids volume fraction and axial particle velocity with variation of (a) grid number in the radial direction, and (b) grid number in the axial direction.

(b) show the time-averaged solids volume fraction and particle velocity with the different grid number cases in the radial and axial directions, respectively. The predicted values were approximately the same for all the different grid number cases. Thus a rectangular grid system of 49×140, which offers a good precision and computational effort, was subsequently employed for all cases in this study. A convergence criterion of 10^{-5} for each scale residual component with 50 iterations per time step was used.

The developed model can predict the hydrodynamics behavior including the solids volume fraction and the gas and solids velocities. This information was compared with available experimental results (Wang *et at.*, 1992) and simulation results based on gas and solids turbulent ($k-\varepsilon-\Theta-k_p$) two fluid model (Cheng *et al.*, 1999) to verify the simulation models. The transient flow information of 3 phases can be obtained from the model and then used for studying the mixing behavior in the downer.

2.1.4 Residence time distributions (RTD)

The transient flow behavior in the downer was simulated. Solids and gas tracers were step injected to the reactor at the inlet after the flow behavior of both phases reached the steady state. The solids tracer and gas tracer transport was addressed by the application of Eqs. (58) and (64), respectively.

The physical properties of solids tracer are identical to those of the main solids particle. CO_2 was used as a gas tracer. The concentration of tracer in the feed is 5% by wt. for each phase to ensure the stability of the simulation and flow behavior. The outlet concentrations of solids and gas tracers were monitored as a function of time. The RTD data obtained from the simulation was fitted with the axial dispersion model to predict the mixing parameters in the downer.

For the step tracer input method, $F(t)$ is given by

$$F(t)=\frac{1}{C_{\max}}\left(C_{step}\left(t_i\right)\right) \tag{70}$$

For closed vessels, the relationship between the *F* and *E* curves is given by

$$F(t)=E(t)dt \tag{71}$$

and, on differentiating,

$$E(t)=\frac{dF(t)}{dt} \tag{72}$$

The normalized RTD function, E_θ is formulated as follows:

$$E_\theta = t_m E(t) \tag{73}$$

The mean residence time (t_m) is calculated as follows:

$$t_m = \frac{1}{C_{\max}}\int_0^{C_{\max}} tdC_{step} \tag{74}$$

The dispersion model, which was used to fit with the RTD data obtained from this simulation, is described in this sub section. The differential equation for the axial dispersion of each phase can be expressed as follows:

$$\frac{\partial C_t}{\partial \theta}=\left(\frac{1}{Pe}\right)\frac{\partial^2 C_t}{\partial z^2}-\frac{\partial C_t}{\partial z} \tag{75}$$

where C_t denotes a tracer concentration; $\theta(=\frac{t}{t_m})$ represents the dimensionless time; z represents a dimensionless axial position; and $Pe=\frac{uL}{D}$, refers to as the axial Peclet number; D denotes the axial dispersion coefficient. In case of $1/Pe < 0.01$, the solution of Eq. (75) is rendered as (Levenspiel, 1999):

$$E_\theta(\theta)=\frac{1}{2\sqrt{\pi(1/Pe)}}\exp\left[-\frac{(1-\theta)^2}{4(1/Pe)}\right] \tag{76}$$

The axial Peclet number is given to demonstrate the degree of mixing in the system. For an ideal mixed flow, the axial Peclet number needs to approximate zero. The ideal plug flow number needs to approach ∞. $E_\theta(\theta)$ obtained from this simulation was fitted with an analytical solution (Eq. (76)) to determine *Pe*.

2.2 Hydrodynamics and CO_2 removal performance in a circulating fluidized bed reactor

The two-fluid model based on the kinetic theory of granular flow was developed to study the CO_2 removal from flue gases using the circulating fluidized beds (CFB). The two-fluid model was coupled with mass transfer and a kinetic reaction model. The simulation was performed in two-dimension. In this section the effect of the riser feeding configuration on the reactor performance was studied. In addition, the hydrodynamics and reactor performance of a CO_2 capture in a downer and riser reactors were also compared.

Figure 7 shows two types of CFB configuration used in this study. Figure 7(a) shows the CFB system with solids feeding at one side wall of the riser. The CFB system consists of a riser section with a 3 m height and 0.6 m of a diameter. Flue gases were fed at the bottom of the riser section, while the solids sorbents were fed to the riser at the right side wall. The sorption reaction occurs in this riser section.

The treated flue gases and the solids sorbent were separated in the separator. The treated gases are exit from the system, while the solids sorbents were fed back to the riser through the storage tank and the stand pipe. Figure 7(b) shows the configuration of riser with bottom solids feed inlet. In this riser, both gas and solids sorbent were fed at the bottom inlet. Its height and diameter are the same as those of the riser section of CFB which are 3 and 0.6 m, respectively. Both gas and solids sorbent are injected at higher velocities at the center than near the wall. This inlet flow pattern can be obtained from the riser with a U-tube inlet (Miller and Gidaspow, 1992). The treated gas and solids sorbent are exit at the outlets on the top of reactor.

The performance of CO_2 capture in a downer and a riser were also studied. The geometries of these reactors were depicted in Figure 8. Both reactors have the same diameter and height which are 0.14 and 3 m, respectively. In the downer, flue gas with CO_2 rich and solids sorbent were fed from the top and exit at the bottom of the reactor. On the other hand, flue gas and solids sorbent were fed into the riser from the bottom and the exit located at the top of the reactor.

2.2.1 Simulation conditions

Initially, solids sorbents were filled in the CFB system with the height of 1.5 m with the solids volume fraction of 0.63. At the inlet of the riser, the gas velocity and composition of flue gases were specified. In the riser with bottom solids feed inlet, the system is empty at the initial condition. The velocity and solids volume fraction of both phases were specified at the inlet boundary. The inlet conditions used in this work are summarized in Table 5. The simulation conditions used for all cases are showed in Table 6. The simulation conditions used for studying the hydrodynamics and CO_2 sorption performance in a riser and a downer are summarized in Table 7.

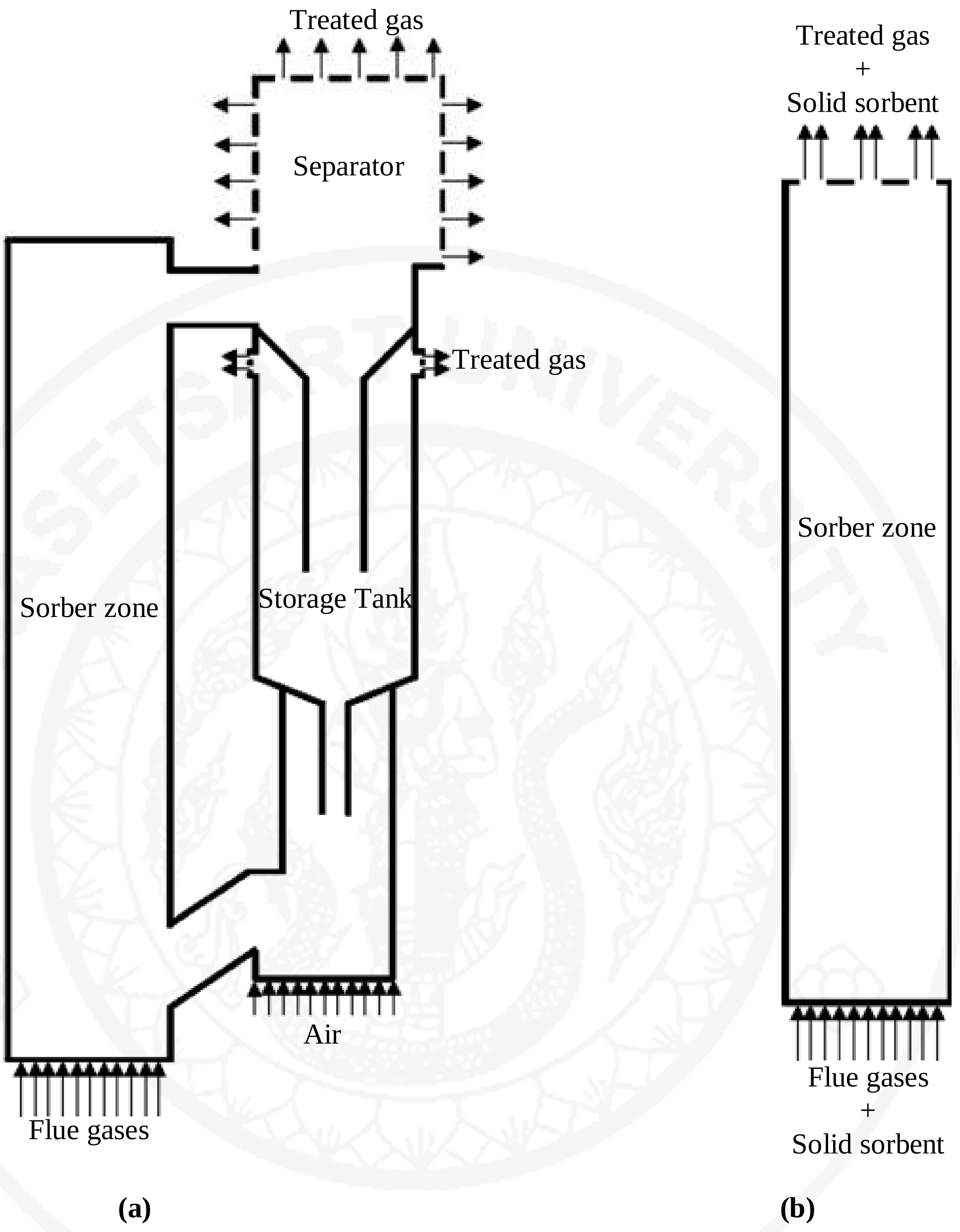

Figure 7 Reactor geometry used for CO_2 capture simulation; (a) CFB system, (b) riser with bottom feed inlet.

Table 5 Inlet conditions used for CO_2 capture simulation.

Operating parameters	Value
CFB	
- At the bottom of the riser section	
Inlet gas volume fraction	1.00
Inlet CO_2 species mole fraction	0.15
Inlet H_2O species mole fraction	0.15
Inlet air species mole fraction	0.70
- At the bottom of the downer section	
Inlet gas volume fraction	1.00
Inlet CO_2 species mole fraction	0.00
Inlet H_2O species mole fraction	0.00
Inlet air species mole fraction	1.00
Riser with bottom feed of gas and solids sorbent	
Inlet gas volume fraction	0.75
Inlet CO_2 species mole fraction	0.15
Inlet H_2O species mole fraction	0.15
Inlet air species mole fraction	0.70

Table 6 Simulation conditions used for CO_2 capture simulation.

Case	**Ug** (m/s)	$\boldsymbol{\rho_p}$ (kg/m^3)	**H** (m)	**Gs** (kg/m^{2}s)
- The comparison of CFB and riser with bottom feed inlet of gas and solids sorbent	1	1530	3	200
- The effect of reactor height	0.5	1530	3 4 5	200

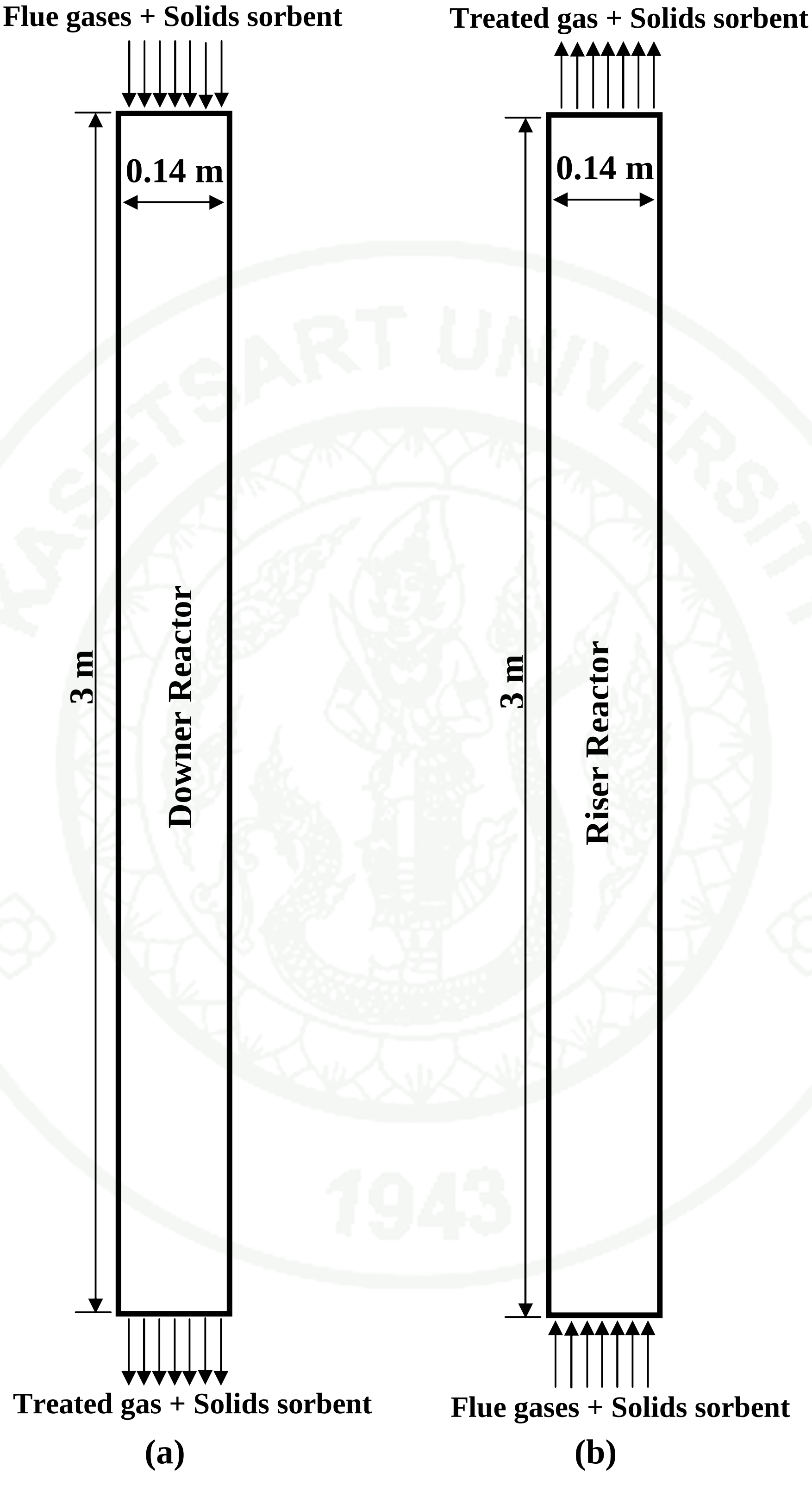

Figure 8 Reactor geometry used for CO_2 capture simulation (a) downer reactor, (b) riser reactor.

Table 7 Simulation conditions for studying CO_2 sorption in a downer and a riser.

Simulation case	Superficial gas velocity (m/s)	Solids circulation rate (kg/m^{2}s)	Particle diameter (μm)	Particle density (kg/m^3)
Based case	1.5	200	75	1 545
The effects of superficial gas velocity	1.0 1.5 2.0	200	75	1 545
The effects of solids circulation rate	1.5	150 200 250	75	1 545
The effects of particle size	1.5	200	25 50 75	1 545
The effects of particle density	1.5	200	75	1 545 2 000 2 500

2.2.2 Mathematical model

The two-fluid model based on kinetic theory of granular flow was adopted in this work. This model has been successfully applied to study the hydrodynamics, heat and mass in the fluidized bed by Gidaspow's research group (Ding and Gidaspow, 1990; Jiradilok *et al.*, 2006, 2007; Chalermsinsuwan *et al.*, 2009a, 2009b). Recently, Chalermsinsuwan *et al.* (2010) have been developed the two-fluid model for studying the CO_2 capture in the riser reactor. Their study revealed that the temperature rising just a few degree due to the high circulation rate. Thus the isothermal condition was assumed in this study. The governing equations, which consist of the continuity, momentum, species conservations and the equation of granular temperature conservation are summarized in Table 8. The constitutive equations are required to close the governing equations, which are summarized in Table 9. The standard k-ε turbulent model with per phase approach was used in this study. This approach solves the turbulent equations for each phase. The turbulent kinetic energy, k and turbulent dissipation rate, ε is obtained by solving Eqs. (67) and (68) respectively.

Table 8 Governing equations used for CO_2 capture simulation.

Governing Equation	**Equation**
(a) Conservation of mass for phase *q*:	$\frac{\partial}{\partial t}\left(\alpha_q\rho_q\right)+\nabla\cdot\left(\alpha_q\rho_q\vec{u}_q\right)=0$
(b) Conservation of momentum:	- Gas phase $\frac{\partial}{\partial t}\left(\alpha_g\rho_g\vec{u}_g\right)+\nabla\cdot\left(\alpha_g\rho_g\vec{u}_g\vec{u}_g\right)=-\alpha_g\nabla p+$ $\alpha_g\rho_g\vec{g}+\nabla\cdot\overline{\overline{\tau}}_g+\nabla\cdot\overline{\overline{\tau}}_{tu,g}+\sum_{n=1}^{N}\beta_{gn}\left(\vec{u}_n-\vec{u}_g\right)$ - Solids phase $\frac{\partial}{\partial t}\left(\alpha_p\rho_p\vec{u}_p\right)+\nabla\cdot\left(\alpha_p\rho_p\vec{u}_p\vec{u}_p\right)=-\alpha_p\nabla p-\nabla p_p+$ $\nabla\cdot\overline{\overline{\tau}}_p+\nabla\cdot\overline{\overline{\tau}}_{tu,p}+\alpha_p\rho_p\vec{g}+\sum_{n=1}^{N}\beta_{pn}\left(\vec{u}_n-\vec{u}_p\right)$
(c) Conservation of species *i* in phase *q*:	$\frac{\partial}{\partial t}\left(\rho_q\alpha_qY_{i,q}\right)+\nabla\cdot\left(\rho_q\alpha_q\vec{u}_qY_{i,q}\right)=-\nabla\cdot\alpha_q\vec{J}_{i,q}+R_{i,q}$
(d) Conservation of solid phase fluctuating energy:	$\frac{3}{2}\left[\frac{\partial}{\partial t}\left(\rho_s\alpha_s\Theta_s\right)+\nabla\cdot\left(\rho_s\alpha_s\vec{u}_s\Theta_s\right)\right]=\left(-p_s\overline{\overline{I}}+\overline{\overline{\tau}}_s\right):\nabla\vec{u}_s+$ $\nabla\cdot\left(k_{\Theta s}\nabla\Theta_s\right)-\gamma_{\Theta s}+\phi$

Table 9 Constitutive equations used for CO_2 capture simulation.

Parameter	**Equation**
(a) Gas phase stress:	$\overline{\overline{\tau}}_g = \alpha_g \mu_g \left[\nabla \vec{u}_g + \left(\nabla \vec{u}_g\right)^T\right] - \frac{2}{3}\alpha_g \mu_g \left(\nabla \cdot \vec{u}_g\right)\overline{\overline{I}}$
(b) Solids phase stress:	$\overline{\overline{\tau}}_s = \alpha_s \mu_s \left[\nabla \vec{u}_s + \left(\nabla \vec{u}_s\right)^T\right] - \alpha_s \left(\xi_s - \frac{2}{3}\mu_s\right)\nabla \cdot \vec{u}_s \overline{\overline{I}}$
(c) Collisional dissipation of solid fluctuating energy:	$\gamma_{\Theta s} = 3\left(1 - e_s^2\right)\alpha_s^2 \rho_s g_0 \Theta_s \left(\frac{4}{d_s}\sqrt{\frac{\Theta_s}{\pi}}\right)$
(d) Radial distribution function:	$g_0 = \left[1 - \left(\frac{\alpha_s}{\alpha_{s,\max}}\right)^{1/3}\right]^{-1}$
(e) Solids phase pressure:	$p_s = \alpha_s \rho_s \Theta_s \left[1 + 2 g_0 \alpha_s (1 + e_s)\right]$
(f) Solid phase shear viscosity:	$\mu_s = \frac{4}{5}\alpha_s \rho_s d_p g_0 (1+e)\sqrt{\frac{\theta}{\pi}} + \frac{10\rho_s d_p \sqrt{\pi\theta}}{96(1+e) g_0 \alpha_s}\left[1 + \frac{4}{5} g_0 \alpha_s (1+e)\right]^2$
(g) Solids phase bulk viscosity:	$\xi_s = \frac{4}{3}\alpha_s \rho_s d_s g_0 (1 + e_s)\sqrt{\frac{\Theta_s}{\pi}}$
(h) Conductivity of the fluctuating energy:	$\kappa_s = \frac{150\rho_s d_s \sqrt{\Theta_s \pi}}{384\left(1 + e_s\right) g_0}\left[1 + \frac{6}{5}\alpha_s g_0 \left(1 + e_s\right)\right]^2 + 2\rho_s \alpha_s^2 d_s \left(1 + e_s\right) g_0 \sqrt{\frac{\Theta_s}{\pi}}$

Table 9 (Continued)

Parameter	**Equation**
(i) Gas-solid phase interphase exchange coefficient:	- when $\varepsilon_g \le 0.80$: $\beta_{gs} = 150\dfrac{(1-\alpha_g)^2\mu_g}{\alpha_g d_p^2} + 1.75\dfrac{(1-\alpha_g)\rho_g\lvert v_g - v_s\rvert}{d_p}$ - when $\varepsilon_g > 0.80$: $\beta_{gs} = \dfrac{3}{4}\dfrac{(1-\alpha_g)\alpha_g}{d_p}\rho_g\lvert v_g - v_s\rvert C_{D0}\alpha_g^{-2.65}$ with $\mathrm{Re} = \dfrac{\rho_g\alpha_g\lvert u_g - u_s\rvert d_p}{\mu_g}$ and $\mathrm{Re} < 1000\text{: } C_{D0} = \dfrac{24}{\mathrm{Re}}\left(1 + 0.15\,\mathrm{Re}^{0.687}\right)$ $\mathrm{Re} \ge 1000\text{: } C_{D0} = 0.44$

2.2.3 Chemical reaction model

Gidaspow (1972) and Onischak and Gidaspow (1972) studied the kinetic reaction of CO_2 sorption by K_2CO_3 solids sorbent. In their studied, they neglected the effect of steam in the system. Thus they proposed the first order reaction with respect to CO_2 concentration and volume fraction of solids sorbent. Recently, Part *et al.* (2006) shows that the water vapor affects significantly to the sorption rate of CO_2. Thus this study modified the first reaction rate expression to account the effect of water vapor in the system. The process of CO_2 from wet flue gases removal follows the reversible reaction (Hirano *et al.*, 1995; Hayashi *et al.*, 1998),

$$K_2CO_3 + H_2O + CO_2 \leftrightarrow 2KHCO_3 \tag{77}$$

The reaction rate expression used in this present work is

$$r = -k_r C_{CO_2} C_{H_2O} \alpha_s \tag{78}$$

where k_r is the reaction rate constant. This reaction rate constant is calculated from Onischak and Gidaspow experimental data, which can be expressed follow the Arrhenius law,

$$k_r = 55.0 \exp(-(-3609)/RT_g) \tag{79}$$

where R is the universal gas constant and T_g is the gas temperature.

2.2.4 Numerical method

The finite volume method with a second-order upwind scheme was applied to differentiate the governing equations. The SIMPLE algorithm was used for the pressure-velocity coupling and correction. The grid size used in the study was shown in Table 10. A convergence criterion of 10^{-5} for each scale residual component with 50 iterations per time step was used. For the simulation in this study the commercial CFD code FLUENT was used.

Table 10 Parameters used for CO_2 capture simulation.

Parameter	Value
Effect of particle feeding inlet	
Grid size	
- CFB	Non-uniform grid
- Riser with bottom feed gas and solid	1 cm×3 cm
Time step	5×10^{-4} s
Comparison between downer and riser	
Grid size	
- Downer	0.33 cm × 2 cm
- Riser	0.33 cm × 2 cm
Time step	5×10^{-4} s

2.3 DEM modeling and simulation for catalytic cracking of heavy oil in a downer reactor

The DEM model was used to simulate the hydrodynamics, mass and heat transfer in a downer reactor. Movement of individual particle is evaluated by the Newton’s equation of motion which includes the effects of gravitational fore, fluid force and contact force. This contact force was calculated using the discrete element method (DEM). The DEM models the contact force by the simple concept of a spring, a dash-pot, and a friction slider which can be obtained from the physical properties of particle such as Young’s modulus, Poisson ratio. The equations of continuity, momentum, mass and heat were used to calculate the motion of gas, mass, and heat transfers in the downer. The motion of fluid, mass and heat transfers in gas phase were considered as two-dimension and axis-symmetry, meanwhile the particle movement was considered in 3-dimension. The simulation was carried out in a downer reactor. The geometry of the downer reactor is depicted in Figure 9 (a). The diameter and the height of the cylindrical downer reactor were 0.07 m and 5.5 m, respectively.

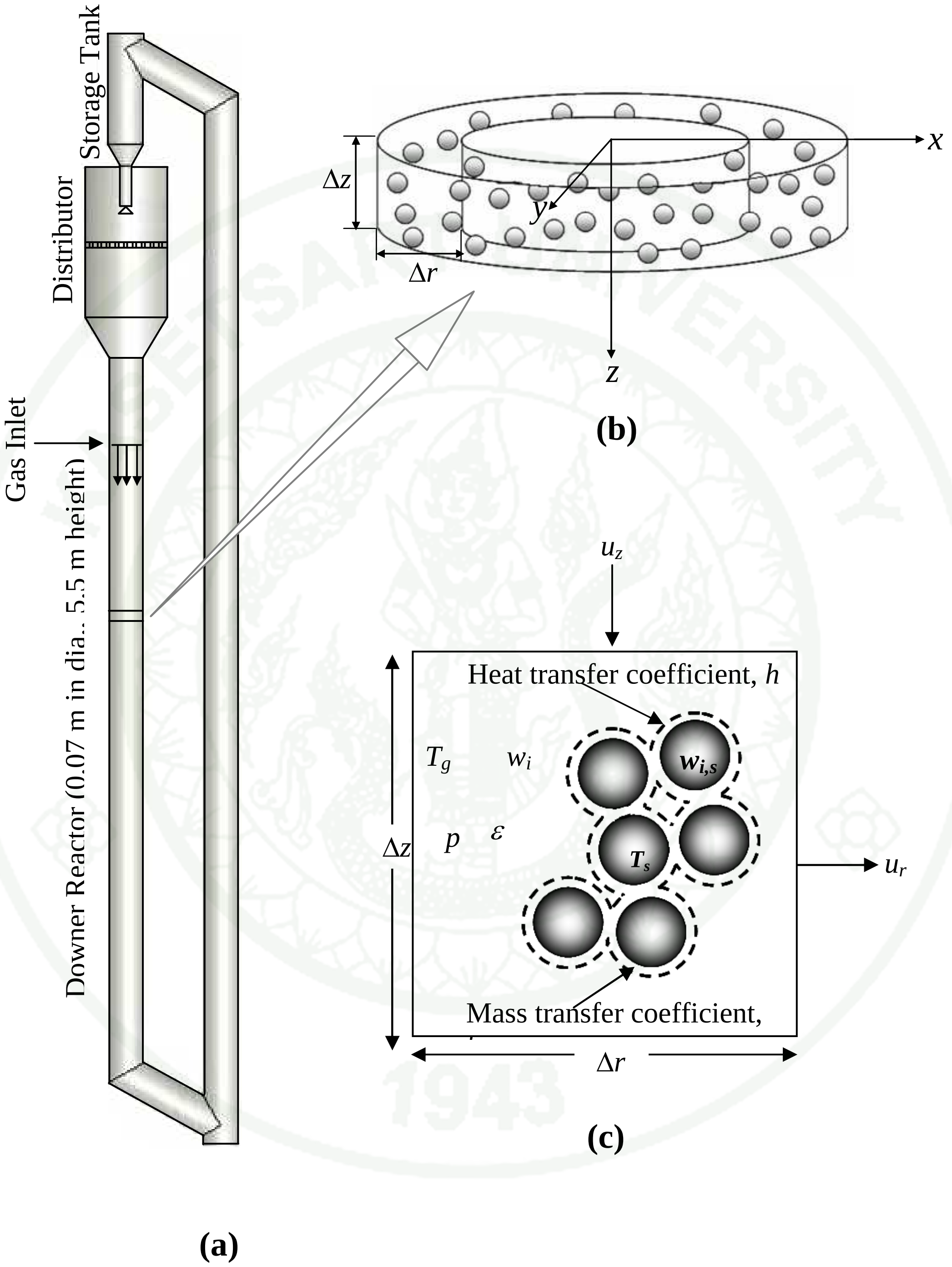

Figure 9 Geometry of a downer used for catalytic cracking simulation (a), particle movement for three-dimensional model (b), and fluid flow field for two-dimensional model (c).

2.3.1 Simulation conditions

Initially, catalyst particles were collected in the storage tank and flowed downward passing through the distributor before entering the downer reactor. The details of the distributor can be seen in Thanomboon (2005) and Limtrakul *et al.* (2008). The catalytic cracking of heavy oil over rare-earth metal exchanged Y-type (REY) zeolite was adopted. The chemical properties of fresh REY zeolite are shown in Songip *et al.* (1994). A four-lump kinetic model was chosen. The simulation conditions used in this work are shown in Table 11.

Table 11 Simulation conditions for studying catalytic cracking in a downer reactor.

Properties and Conditions	Values
Particle diameter (mm)	2.8
Particle density (kg/m^3)	1 500
Number of particles	40 000
Superficial gas velocity (m/s)	2.5,3.0,5.0
Solid flux (kg/m^{2}s)	25,37,65,75
Inlet temperature (K)	623,673,723
Coefficient of restitution	0.9
Coefficient of friction	0.3
Stiffness (N/m)	800
Inlet mass fraction;	
Heavy oil:Nitrogen	0.8:0.2

2.3.2 Mathematical modeling

Particle motion is considered in a three dimensional coordinate as shown in Figure 9(b). The movement of particles consists of translational and rotational motion, which can be calculated by Newton's second law of motion. The contact force between two particles was modeled by DEM model. The fluid flow domain was divided into small fluid cells in a two-dimensional coordinate as seen in Figure 9(c). The pressure, gas velocity, temperature and concentrations of each species are assumed to be uniform in each cell. The governing equations and the constitutive equations are summarized in Tables 12 and 13, respectively.

Table 12 Governing equation for catalytic cracking simulation.

Governing Equation	**Equation**
(a) Particle motion:	- Translational motion: $\vec{a} = \dfrac{\vec{f}}{m} + \vec{g}$ - Rotational motion: $\vec{\alpha} = \dfrac{\vec{T}}{I}$
(b) Gas motion:	$\dfrac{\partial\left(\alpha_g \rho_g \vec{u}\right)}{\partial t} + \left(\nabla \cdot \alpha_g \rho_g \vec{u}\vec{u}\right) = -\nabla \alpha_g p + \rho_g \vec{f}_p$
(c) Conservation of species for gas phase:	$\dfrac{\partial(\alpha_g \rho_g w_i)}{\partial t} + \nabla \cdot \left(\alpha_g \rho_g \vec{u} w_i\right) = \nabla \cdot \left(\alpha_g \rho_g D_{i,m} \nabla w_i\right) +$ $6\dfrac{\left(1-\alpha_g\right)}{d_s} \rho_g k_{ig} \left(w_{i,s} - w_i\right)$
(d) Conservation of species for solids phase:	$\dfrac{\partial(1-\varepsilon)\rho_g w_{i,s}}{\partial t} = \dfrac{6(1-\varepsilon)}{d_s} \rho_g k_{gs,i} (w_i - w_{i,s}) + (1-\varepsilon)\rho_s r_i'$
(e) Conservation of energy for gas phase:	$\dfrac{\partial\left(\alpha_g \rho_g \hat{C}_{p,g} T_g\right)}{\partial t} + \nabla \cdot \left(\alpha_g \rho_g \vec{u} \hat{C}_{p,g} T_g\right) = \nabla \cdot \left(\alpha_g \lambda_g \nabla T_g\right) +$ $\dfrac{6\left(1-\alpha_g\right)h}{d_s} \left(T_s - T_g\right)$
(f) Conservation of energy for solids phase:	$\dfrac{\partial\left(\left(1-\varepsilon\right)\rho_s C_{p,s} T_s\right)}{\partial t} = \dfrac{6\left(1-\varepsilon\right)h}{d_s} \left(T_g - T_s\right) + \left(1-\varepsilon\right)\rho_s \Delta H_A r_A'$

Table 13 Constitutive equations for catalytic cracking simulation.

Parameter	Equation
(a) Mass transfer coefficient (Fogler, 1992):	$k_{ig} = 0.4548\,\mathrm{Re}^{-0.4069}\left[\frac{D_{i,m}}{\alpha_g d_s}\left(\frac{\mu}{\rho_g D_{i,m}}\right)^{1/3}\mathrm{Re}\right]$ for, $\mathrm{Re} < 10$ $k_{ig} = \left(\frac{0.765}{\mathrm{Re}^{0.82}} + \frac{0.365}{\mathrm{Re}^{0.386}}\right)\left[\frac{D_{i,m}}{\alpha_g d_s}\left(\frac{\mu}{\rho_g D_{i,m}}\right)^{1/3}\mathrm{Re}\right]$ for, $\mathrm{Re} \geq 10$ where $\mathrm{Re} = \frac{\lvert\vec{u}_s - \vec{u}_g\rvert \rho_g \alpha_g d_s}{\mu}$
(b) Heat transfer coefficient (Palancz e*t al.*, 1983):	$h = \hat{C}_{p,g} U_0 \rho_g j_h \mathrm{Pr}^{-2/3}$ where $j_h = 5.70\,\mathrm{Re}_0^{-0.78}$ for $\mathrm{Re}_0 < 30$ $j_h = 1.77\,\mathrm{Re}_0^{-0.44}$ for $\mathrm{Re}_0 \geq 30$ and $\mathrm{Re}_0 = \frac{d_s U_0 \rho_g}{(1-\alpha_{g,mf})\mu}$ with $\alpha_{g,mf} = 0.586\zeta^{-0.72}\left[\frac{\mu^2}{\rho_g(\rho_s - \rho_g) g d_s^3}\right]^{0.029}\left(\frac{\rho_g}{\rho_s}\right)^{0.021}$

2.3.3 Kinetic model

A lumping method has been used to develop the kinetic model for catalytic cracking of hydrocarbon (Weekman, 1968, 1969; Wei and Kuo, 1969). In the lumping method, the chemical species are grouped into smaller groups according to their boiling point. Songip *et al.* (1994) proposed a four-lump model for catalytic cracking of heavy oil from waste plastics over REY zeolite. Figure 10 illustrates a reaction pathway for the four-lump kinetic model, which consists of heavy oil (A), gasoline (B), gas (C), and coke (D). The cracking of heavy oil followed a second-order kinetic with respect to the heavy oil mass fraction, whereas that of gasoline was expressed by first-order kinetics with respect to gasoline. Therefore, the reaction rate of heavy oil can be expressed as follows:

$$r'_A = -(k'_1 + k'_2 + k'_3)C_0^2 w_{A,s}^2 \tag{80}$$

$$r'_B = k'_1 C_0^2 w_{A,s}^2 - (k'_4 + k'_5)C_0 w_{B,s} \tag{81}$$

$$r'_C = k'_2 C_0^2 w_{A,s}^2 + k'_4 C_0 w_{B,s} \tag{82}$$

$$r'_D = k'_3 C_0^2 w_{A,s}^2 + k'_5 C_0 w_{B,s} \tag{83}$$

where C_0 is the mass concentration of heavy oil at the reactor inlet. The temperature dependence of kinetic rate constants follows the Arrhenius expression. The details kinetic constants, obtained from the experimental data (Songip *et al.*, 1994), are given in Table 14.

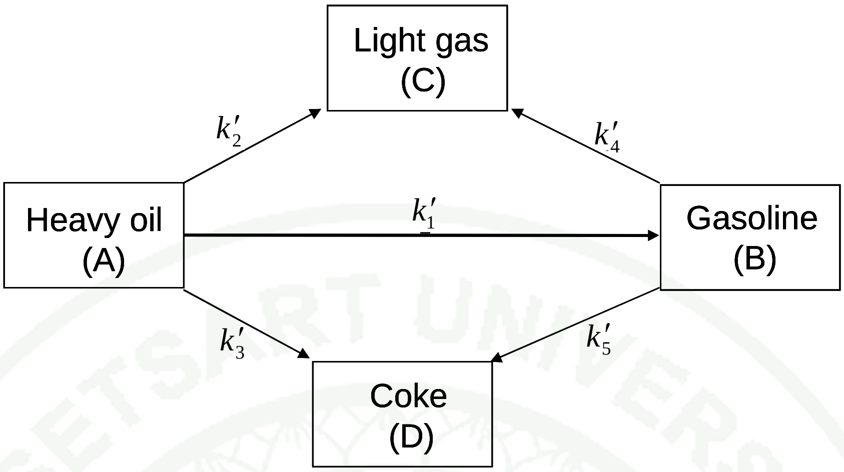

Figure 10 Four-lump kinetic model for heavy oil catalytic cracking reaction.

Table 14 Frequency factors and activation energies for heavy oil catalytic cracking reaction.

Second order reaction	k_0 ($m^6/kg.kg_{cat}.s$)	Ea (kJ/mol)
$A \xrightarrow{k_1'} B$	2,822	50.7
$A \xrightarrow{k_2'} C$	53,502	75.7
$A \xrightarrow{k_3'} D$	9.39×10^{-3}	18.5
First order reaction	k_0 ($m^3/kg_{cat}.s$)	Ea (kJ/mol)
$B \xrightarrow{k_4'} C$	1.17	35.1
$B \xrightarrow{k_5'} D$	8.00×10^{-2}	42.1

2.3.4 Numerical method

The finite difference method was applied for discretizing the partial differential equations of gas motion and mass and energy conservation. The central discretization scheme was used for diffusion term, while the upwind scheme was used for convection term. A semi-implicit method for pressure link equation (SIMPLE), developed by Patankar (1980), was adopted for correcting pressure and velocity. The simulation flow domain was divided into small cells as can be seen in Figure 9(c), which were smaller than the macroscopic behavior in the system, but larger than the particle size. In this present work, the cell size was selected to obtain realistic results within manageable computer time, which was 8.75×15.16 mm ($\Delta r \times \Delta z$). The computational program was performed in FORTRAN code.

RESULTS AND DISCUSSION

1. Hydrodynamics and axial gas and solids mixing in a downer reactor based on two-fluid model

1.1 Hydrodynamics behavior in a downer reactor

1.1.1 Flow development in a downer reactor

Flow development in the downer reactor can be classified into 3 regions which are the accelerating, the developing, and the fully developed zones. This flow development can be clearly explained using the axial distributions of solids volume fraction, gas, and solids velocities (Figure 11). In the accelerating zone, particles are accelerated by gravitational and drag forces due to high gas velocity. This leads to sharp increases in particle velocity. Thus the solids volume fraction rapidly decreases. In the developing zone, particles start to move faster than gas phase. The drag force becomes to resist the particle movement. Thus the particle velocity slightly increases resulting in a gradually decreasing of solids volume fraction. When the drag force and the gravitational force are in balanced, the gas and particle velocities are almost constant. This causes a constant solids volume fraction profile. Thus the fully developed region is achieved.

The developing of gas and particle velocities profiles in the radial direction is shown in Figure 12. Near the entrance region, both gas and particle velocities show a parabolic profile. Gas velocity is higher than solids velocity. Further down the column, the radial profiles of both gas and particle show almost constant in the center region with a slight increasing trend near the wall region. In addition, gas velocity is lower than solids velocity. In the fully developed region, gas and particle velocities in the center region show an increasing towards the wall and a peak near the wall region, which can also be observed in experimental study (Qian *et al.*, 2004). A high density peak of solids volume fraction near the wall region causes the reduction of the effective drag force acting on gas and solids particle in this region. Thus both gas and solids particle in this region tend to move downward with high acceleration. For this reason, the radial profiles of gas and particle velocities show the trend corresponding to an increasing from the center towards the wall and a maximum velocity in the near wall region.

1.1.2 Effect of operating conditions on the hydrodynamics behavior

The effects of superficial gas velocity and solids circulation rate on the solids volume fraction in the radial direction in the fully developed region are shown in Figures 13 and 14, respectively. Theses profiles show an almost uniform solids volume fraction in the center region and a high density peak slightly away from the wall, which is a typical characteristic behavior in a downer reactor. These simulation results are similar with those obtained by many previous studies (Bai *et al.*, 1991; Yang *et al.*, 1991; Wang *et al.*, 1992; Herbert *et al.*, 1994; Wei *et al.*, 1997; Yang *et al.*, 1998; Cheng *et al.*, 1999; Lehner and Wirth, 1999a, b; Zhang *et al.*, 2003a). A high density peak of solids volume fraction in the radial direction is the results of a net movement of particles in the center region towards the wall and a net movement of particles away from the wall. In the center region, particles tend to move away from the center toward the wall to conserve energy because of a larger drag force acting on the particles. According to friction between the gas-solids suspension and the bed wall, the particles near the wall region tend to move away from the bed wall to reduce energy losing. In addition, the solids volume fraction distribution in the fully developed region increases with decreasing superficial gas velocity, and/or increasing solids circulation rate, as observed by previous investigators (Nova *et al.*, 2004; Limtrakul *et al.*, 2008; Qi *et al.*, 2008). As increasing superficial gas velocity increases the particle velocity (see Figure 17) which results in lower solids volume fraction.

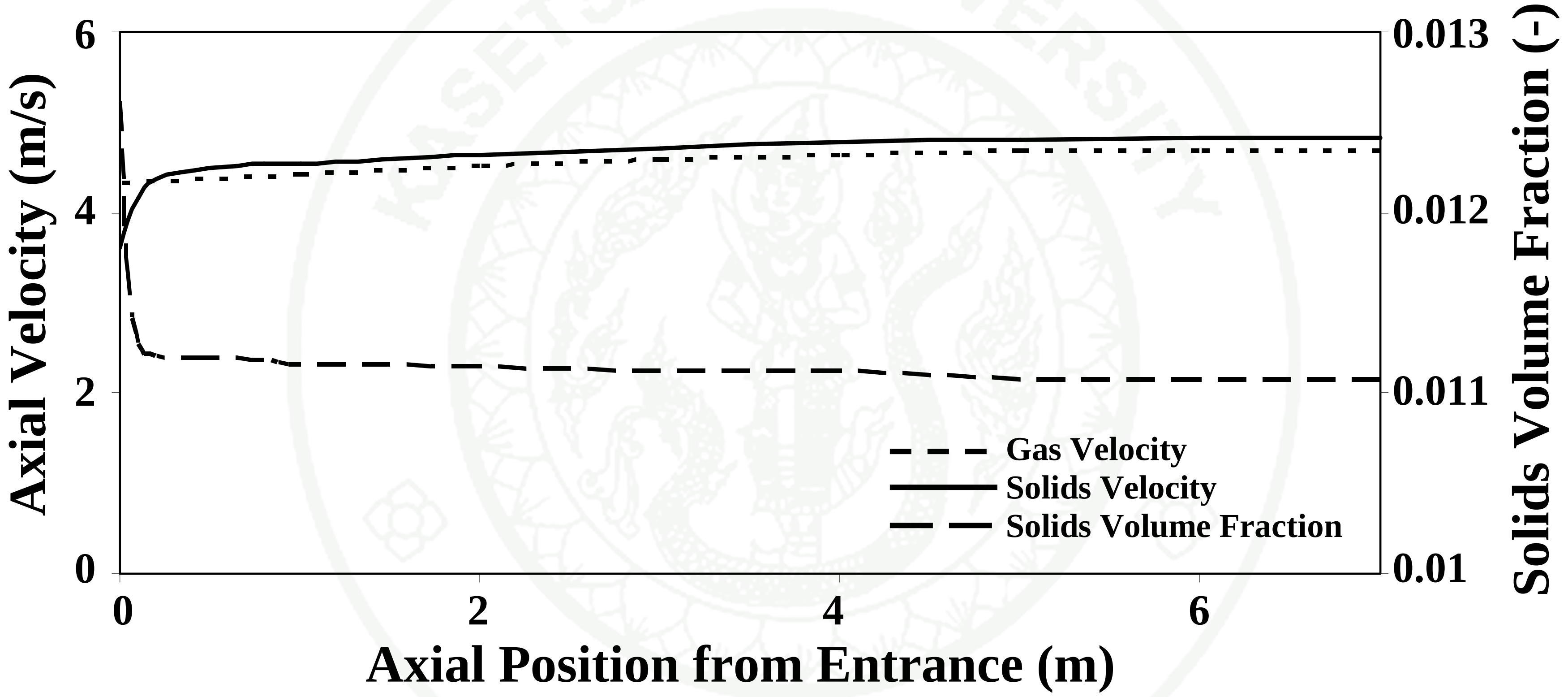

Figure 11 Axial flow development in a downer reactor at U_g = 4.33 m/s and G_s = 70 kg/m^{2}s.

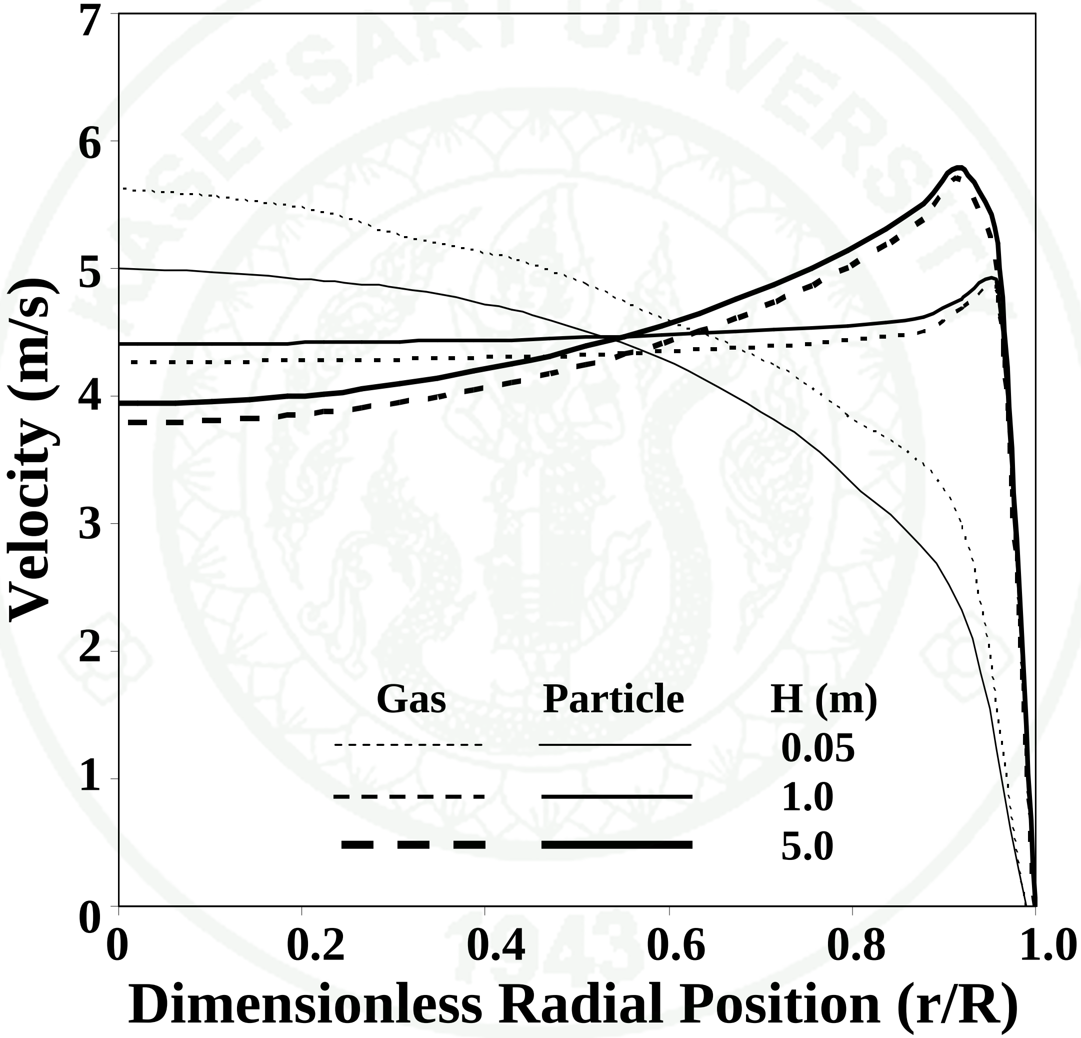

Figure 12 Gas and solids velocities developing in the downer reactor at various axial positions at U_g = 4.33 m/s and G_s = 70 kg/m^{2}s.

Figure 15 shows the effect of the superficial gas velocity on the solids volume fraction distribution in the axial direction. This figure shows that the axial distributions of the solids volume fraction obtained from various superficial gas velocities have the same trend. The solids volume fraction rapidly decreases in the accelerating zone and eventually approaching the constant value in the fully developed region. In addition, an increasing superficial gas velocity causes a consistent decrease in solids volume fraction at any axial position. The effect of the solids circulation rate (Gs) on the axial distribution of solids volume fraction is illustrated in Figure 16. As expected, the solids volume fraction decreases with decreasing the solids circulation rate. At low Gs, the solids volume fraction distribution is almost constant along the downer height. At high Gs, the solids volume fraction profiles shows a high non uniform in axial direction which dramatically decreases in the entrance region. Increasing Gs also extends the developing region.

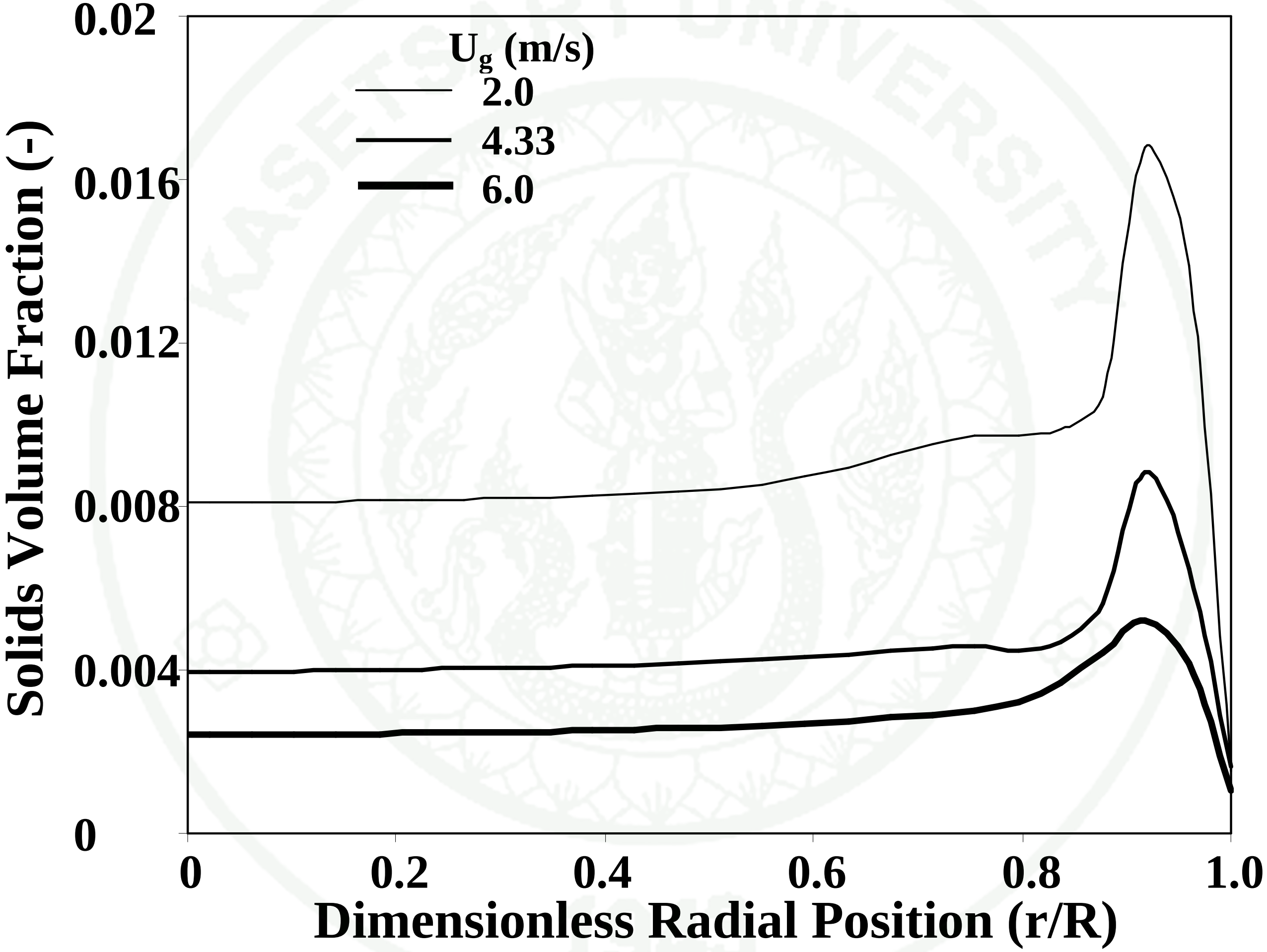

Figure 13 Effect of superficial gas velocity on the solids volume fraction in the radial direction at the solids circulation rate of 31 kg/m^{2}s.

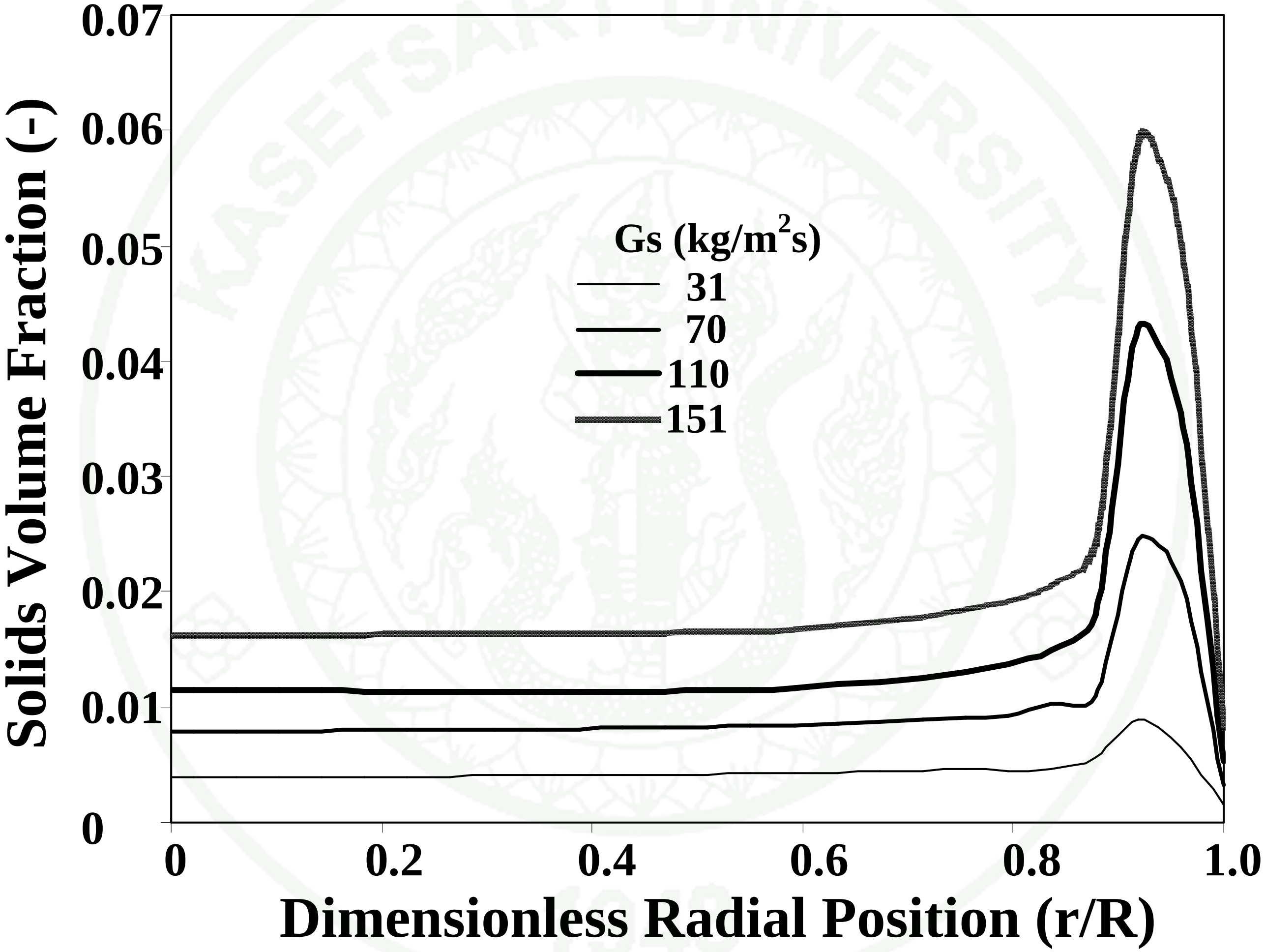

Figure 14 Effects of solids circulation rate on the solids volume fraction in the radial direction.

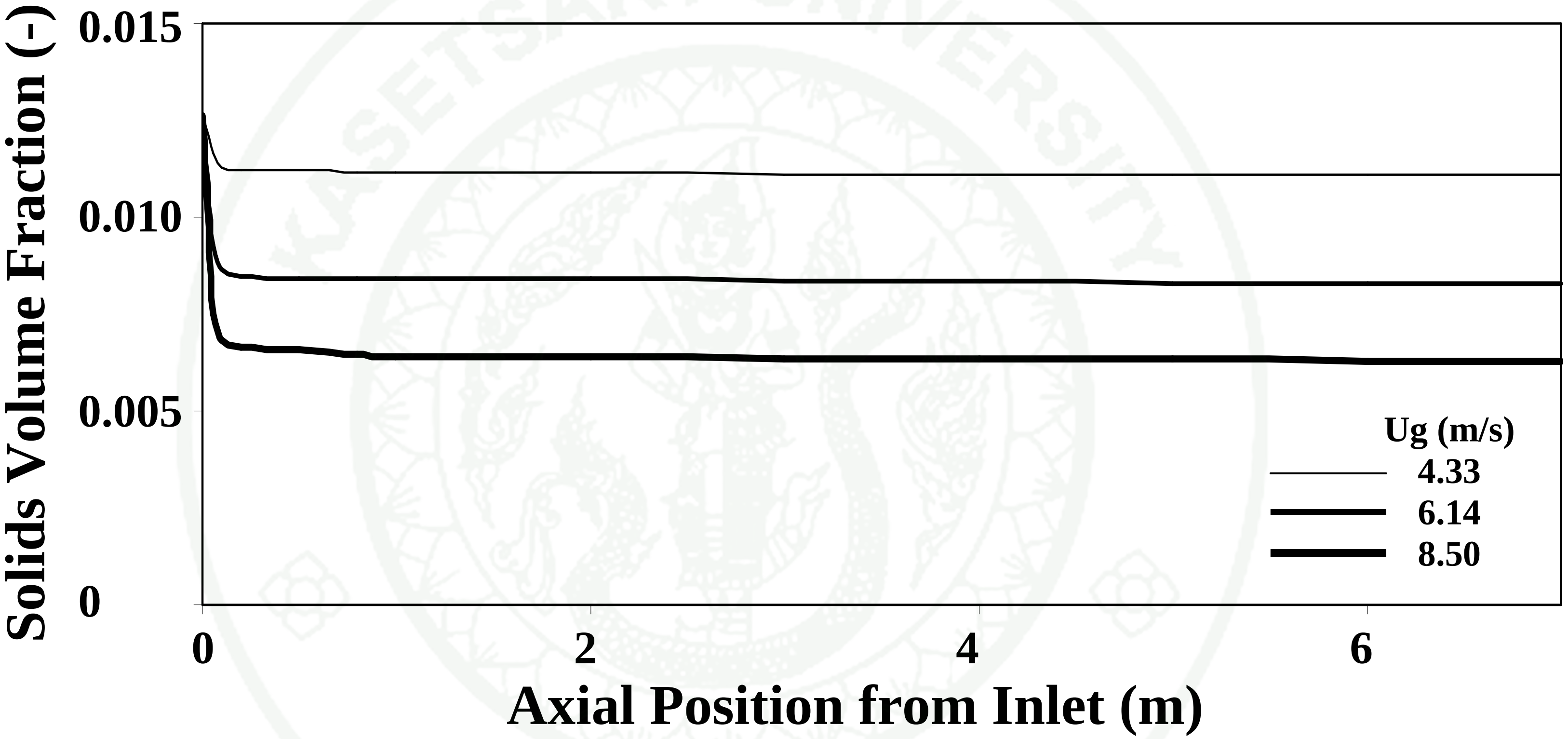

Figure 15 Effect of superficial gas velocity on the solids volume fraction in the axial direction at the solids circulation rate of 70 kg/m^2s.

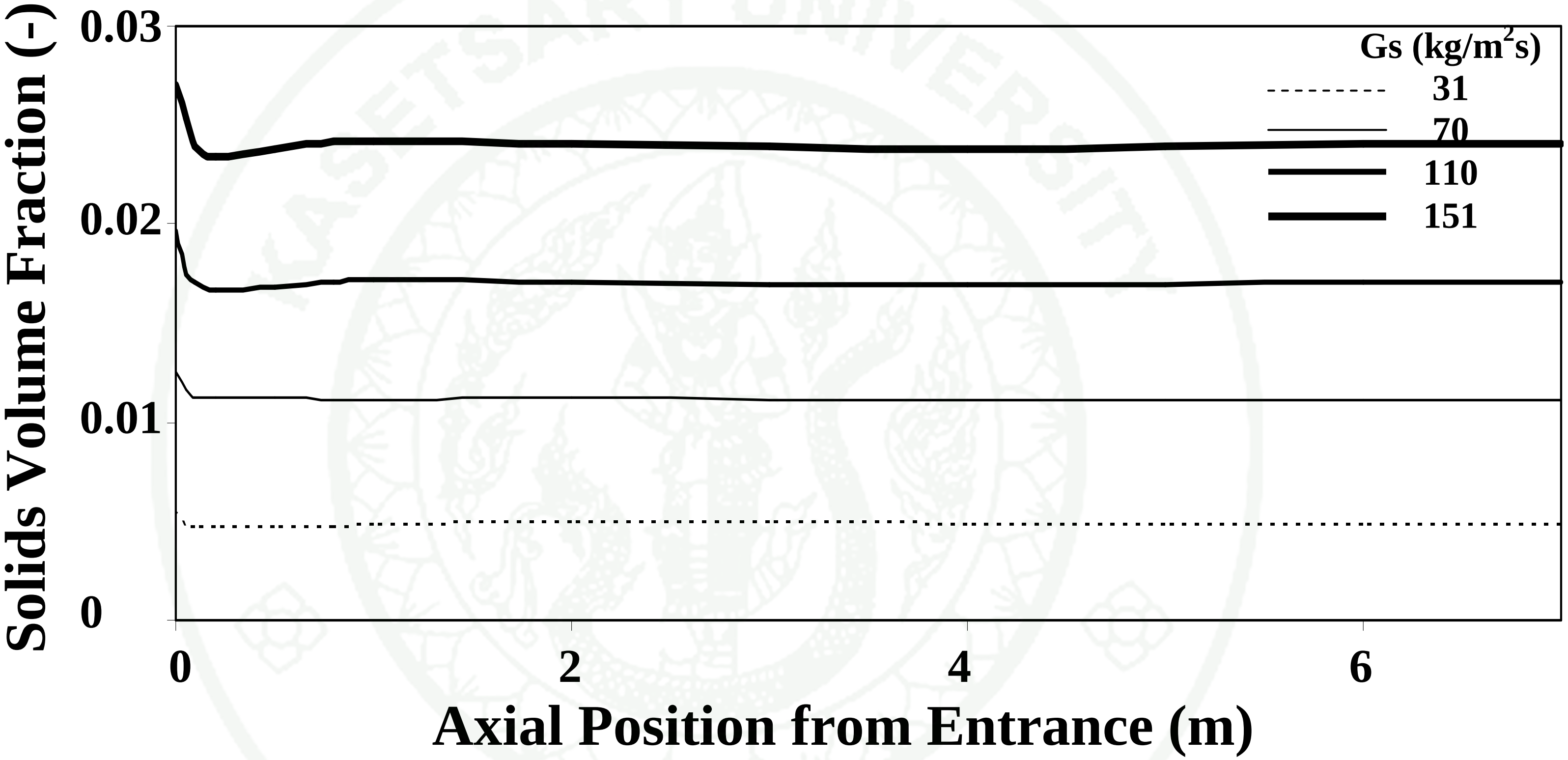

Figure 16 Effect of solids circulation rate on the solids volume fraction in the axial direction.

The effects of superficial gas velocity and solids circulation rate on the radial distributions of gas and solids velocities in the developed region are shown in Figures 17-19. The radial distributions of gas and solids velocities at various superficial gas velocities show the same trends, velocity profiles slowly increase in the center region and form a peak near the wall region as shown in Figure 17. As expected, gas and solids velocities in the fully developed region significantly increases with superficial gas velocity. According to high solids density peak near the wall region at lower superficial gas velocity (see Figure 13), gas and solids velocities are low in the center region and are high near the wall region, which can be clearly seen in Figure 18. The effect of solids circulation rate on the radial distributions of gas and solids velocities is shown in Figure 19. Due to high density peak at high solids circulation rate, both gas and solids velocities profiles show less uniform in the radial direction, which can be found in the experimental study (Qian *et al.*, 2004).

Figure 20 shows the effect of the superficial gas velocity on the axial distributions of the axial solids and gas velocities. The axial gas velocity profiles are almost constant along the downer height. The solids velocity of all cases show the profile according to the flow development in the reactor as described above. In addition, the solids velocity increases with the superficial gas velocity. Figure 21 shows the axial profiles of gas and solids velocities at various solids circulation rates. At low solids circulation rate, the gas velocity is almost constant along the downer reactor length. According to cluster formation at high solids circulation rate, this cluster drags both gas and solids to flow downward with high velocity. Therefore, both gas and particle velocities increase with increasing solids circulation rate. In addition, the developing region tends to increase with solids circulation rate.

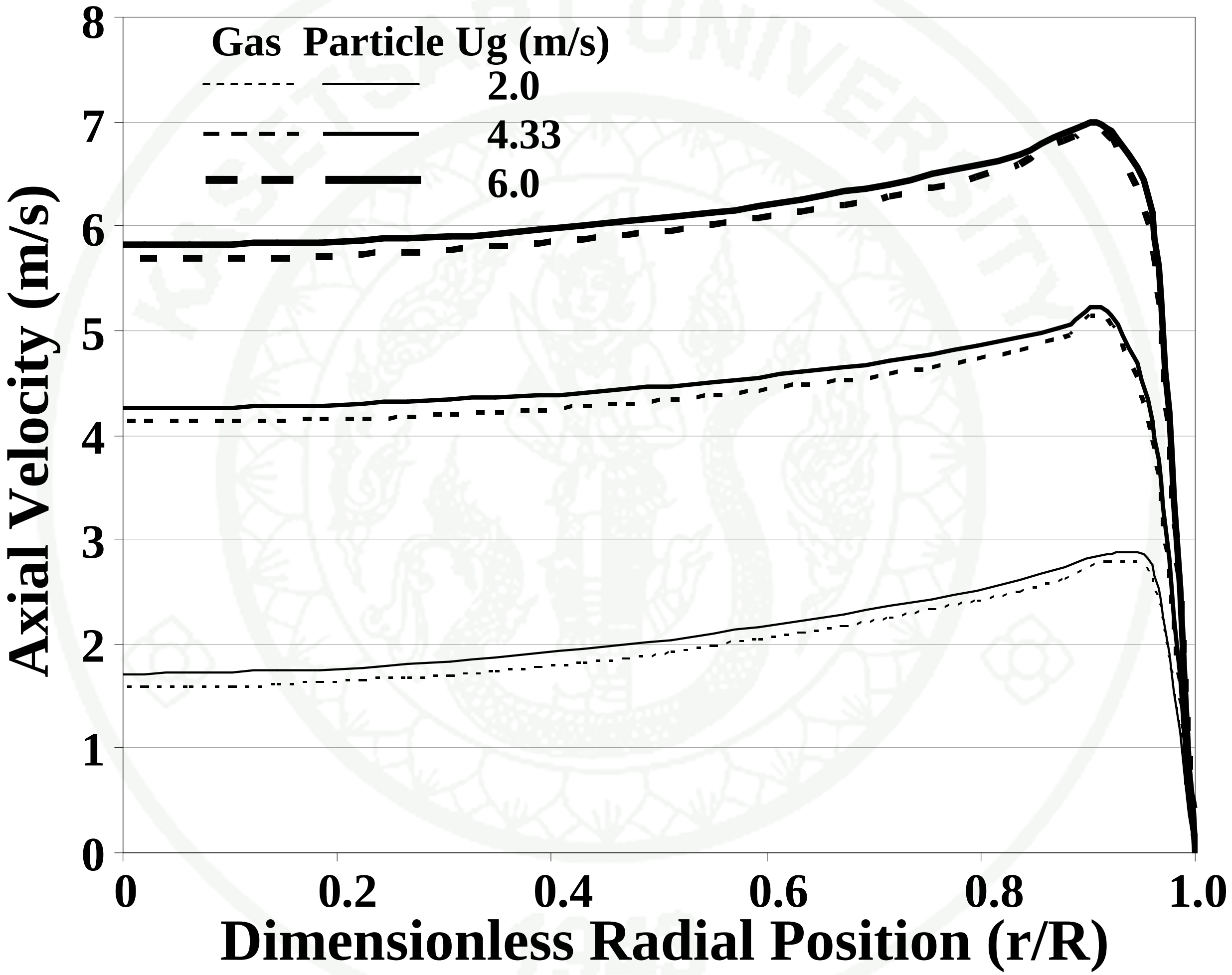

Figure 17 Effect of superficial gas velocity on the axial gas and solids velocities in the radial direction at the solids circulation rate of 31 kg/m^{2}s.

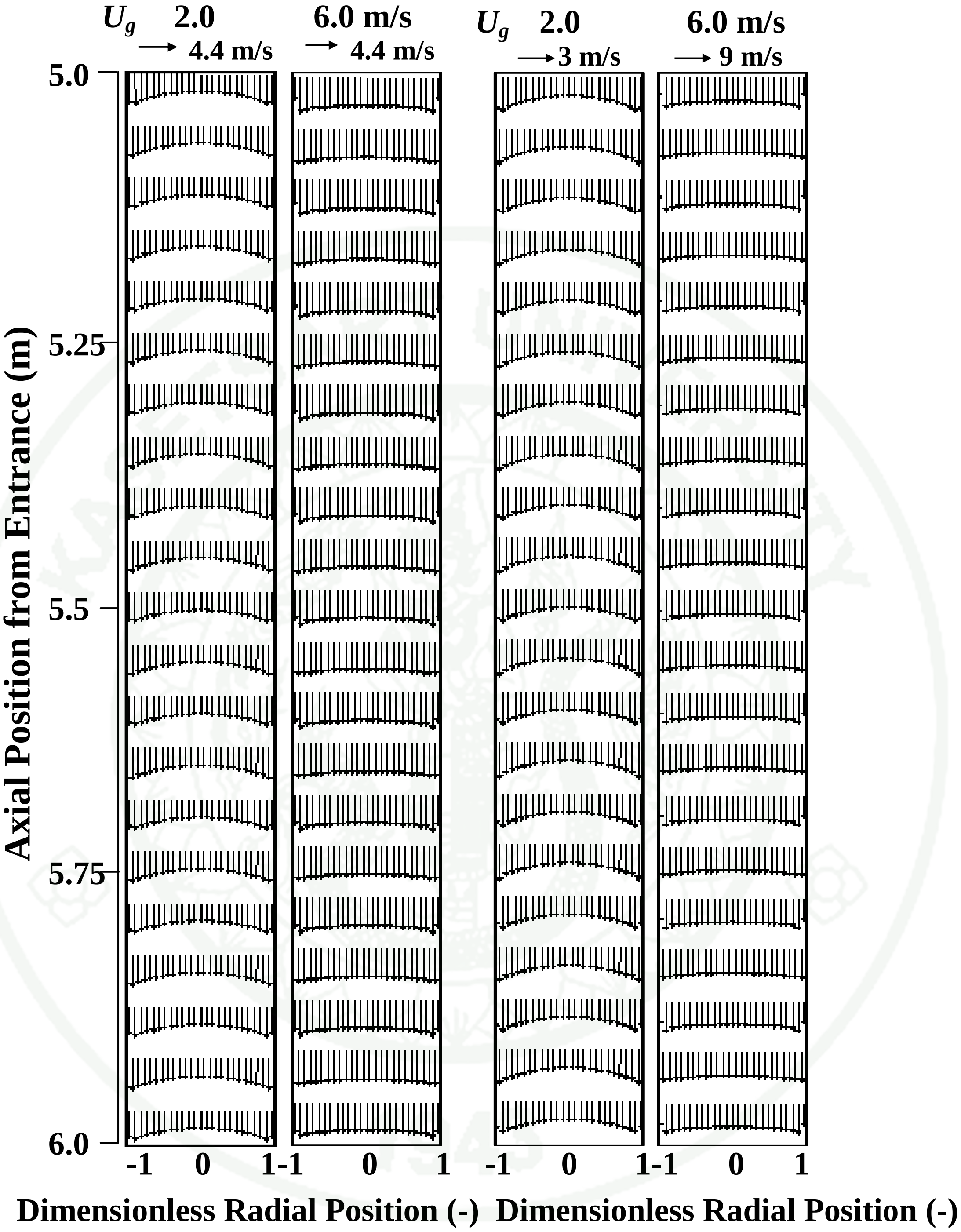

(a) Solids velocity (b) Gas velocity

Figure 18 Solids and gas velocities vector plots in the downer at the solids circulation rate of 31 kg/m^{2}s.

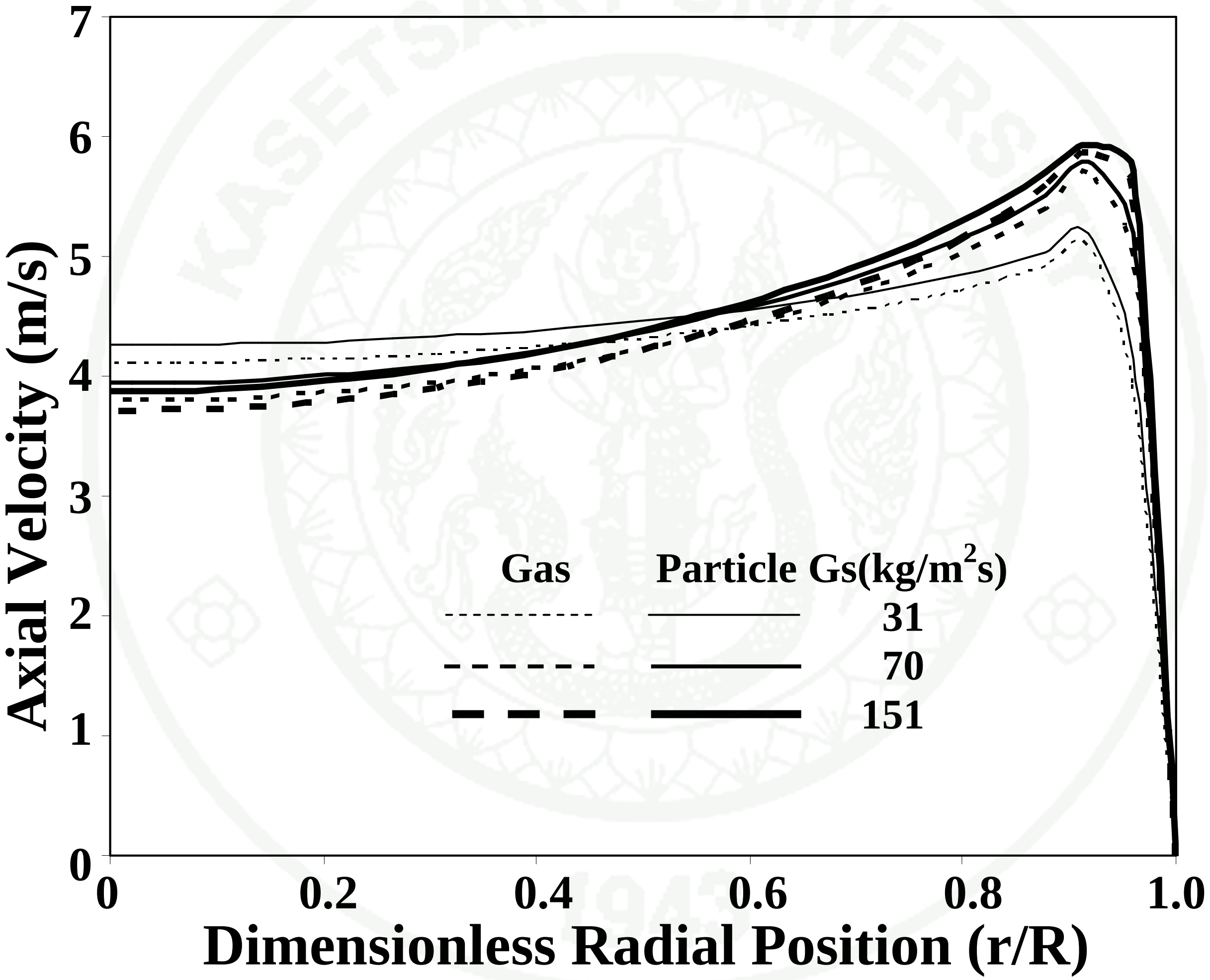

Figure 19 Effect of solids circulation rate on the gas and solids velocities distributions in the radial direction.

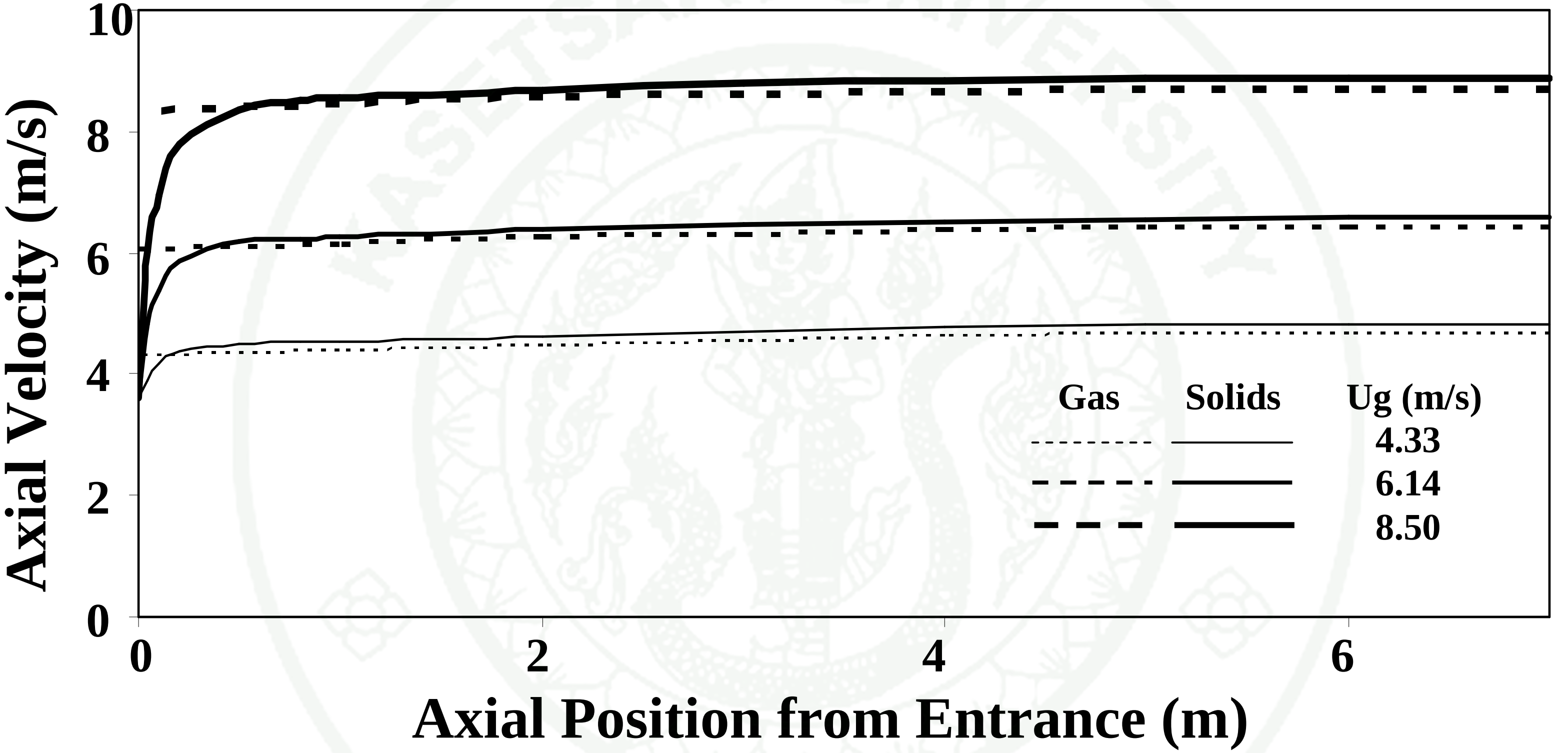

Figure 20 Effect of superficial gas velocity on the axial gas and solids velocities distribution in the axial direction at the solids circulation rate of 70 kg/m^{2}s.

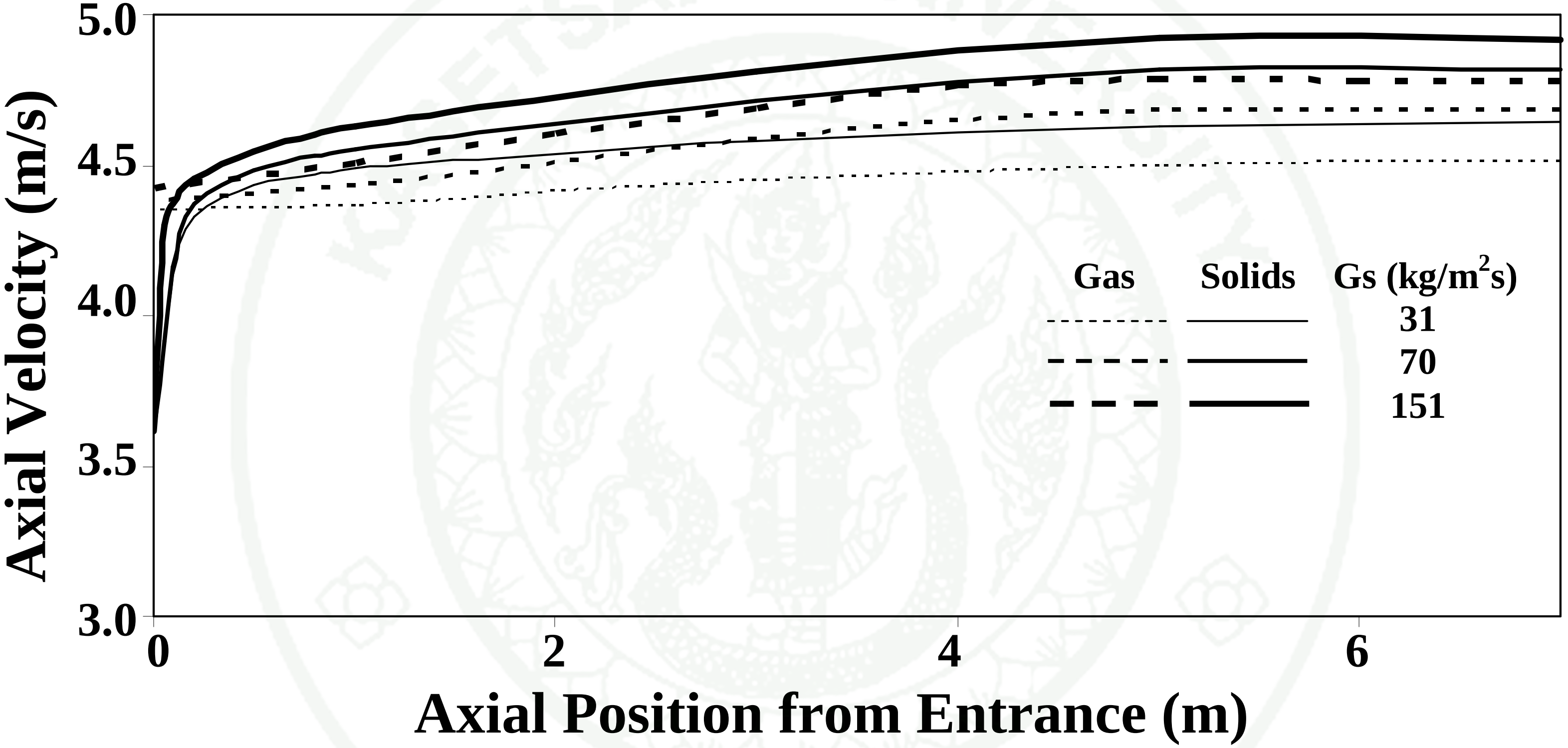

Figure 21 Effect of solids circulation rate on the axial gas and solids velocities distributions in the axial direction.

1.1.2 Effect of particle properties on the hydrodynamics behavior

Figure 22 presents the effect of particle size on the radial distribution of solids volume fraction. This figure shows that, solids volume fraction profiles insignificantly change with particle size, especially in the center region. In addition, smaller particle tends to agglomerate near the wall as a result of a high density peak tends to appear close to the wall. Figure 23 shows the effect of particle density on the radial distribution of solids volume fraction. As can be seen, increasing particle density leads to a lower solids volume fraction in the system with more uniform in the radial direction.

The particle size significantly affects the axial distribution of the solids volume fraction as shown in Figure 24. The axial distributions of solids volume fraction at various particle sizes show the same profiles which rapidly decreases near the inlet region and remains constant thereafter. A larger particle tends to decrease the solids volume fraction in the system. The effect of particle density on the solids volume fraction distribution is shown in Figure 25. A heavier particle tends to decrease the solids volume fraction in the system with a more uniform distribution in an axial direction.

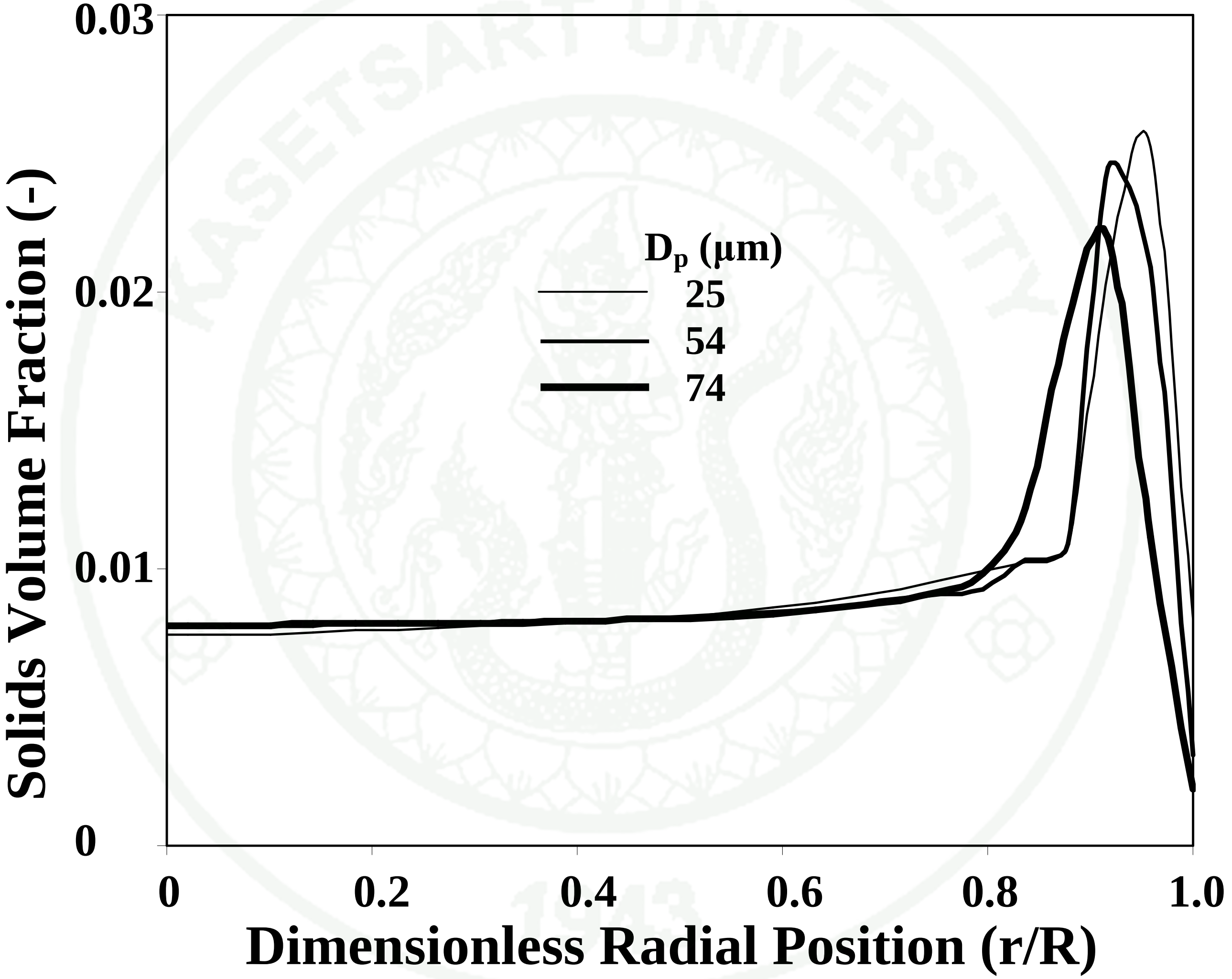

Figure 22 Effect of particle diameter on the solids volume fraction distribution in the radial direction.

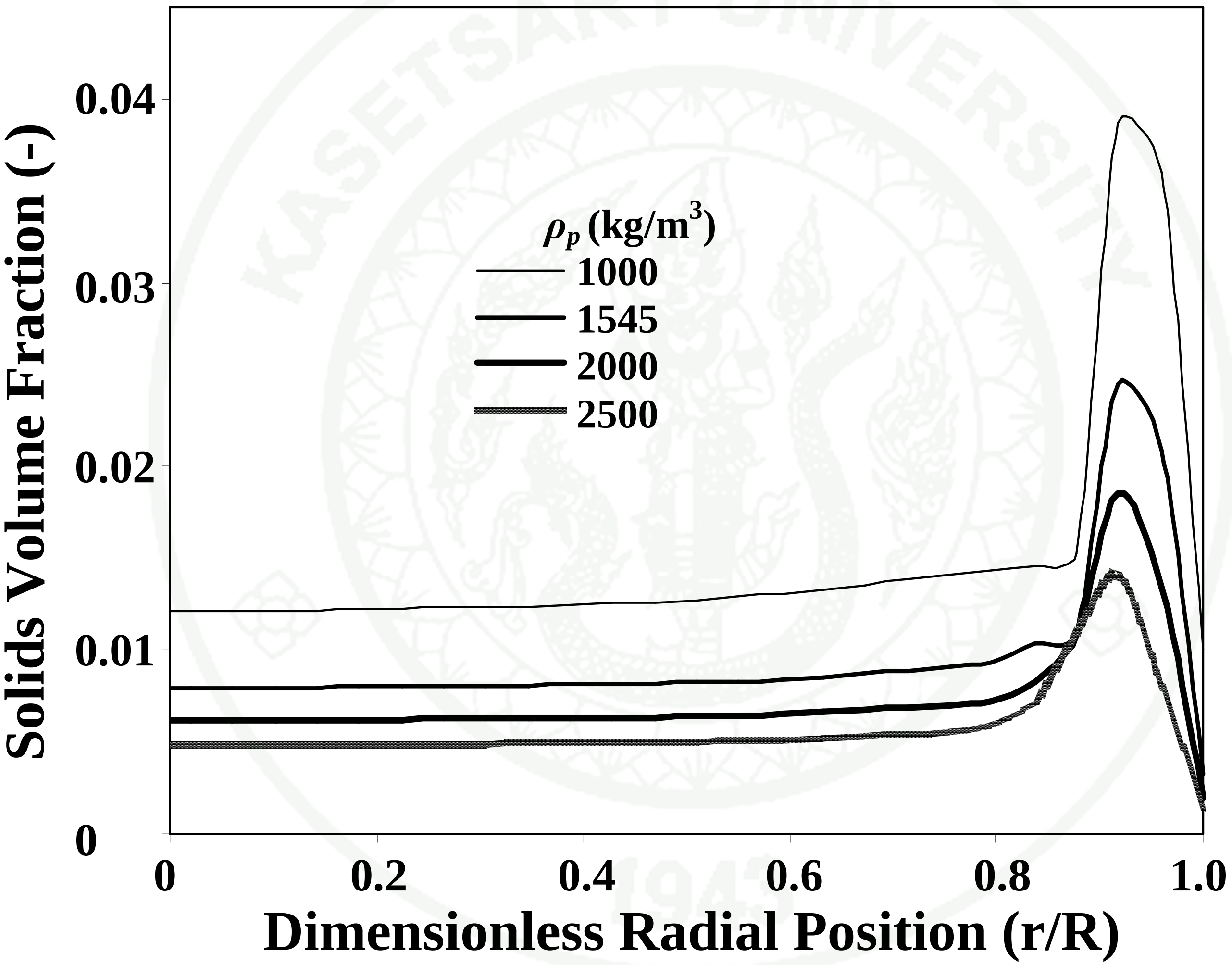

Figure 23 Effect of particle density on the solids volume fraction distribution in the radial direction.

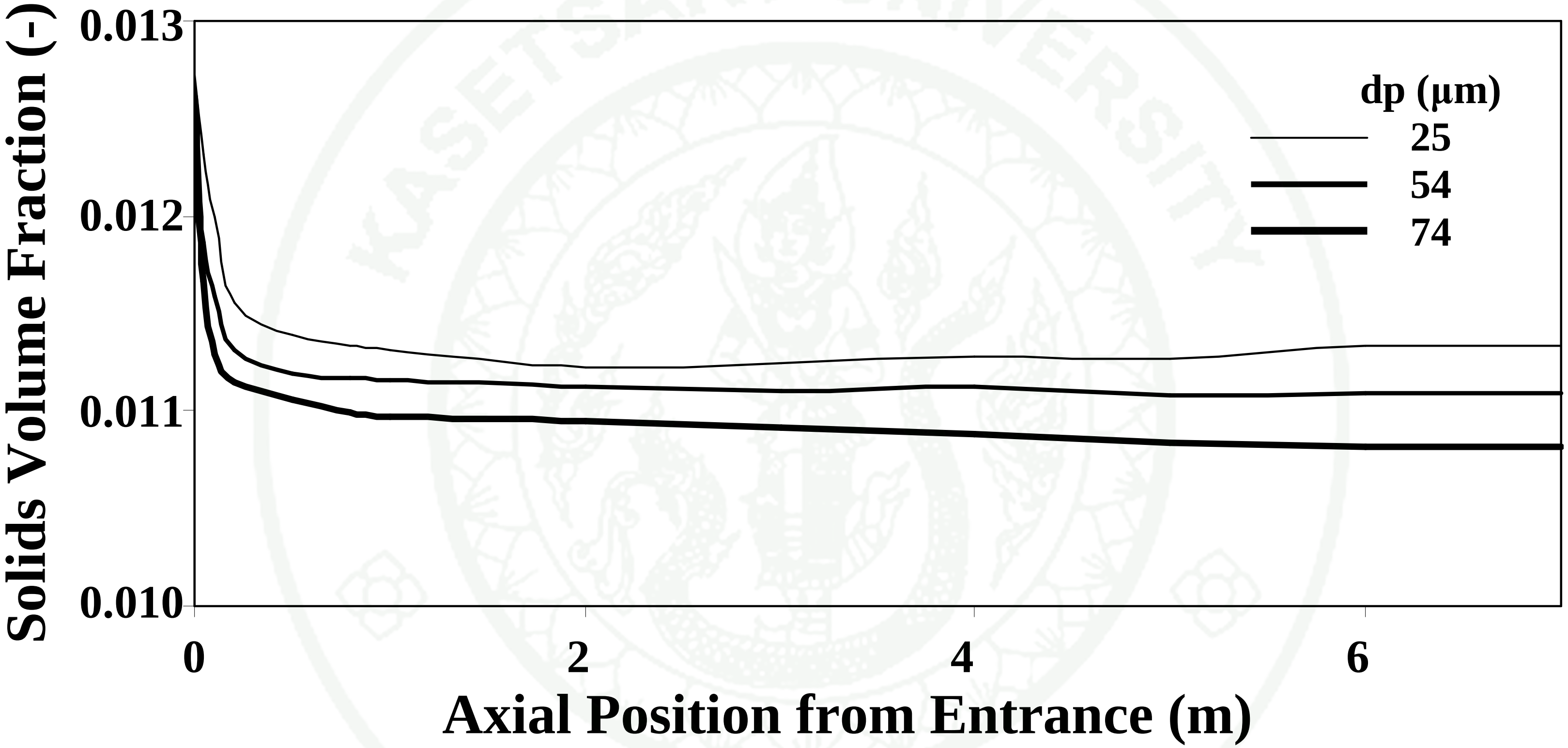

Figure 24 Effect of particle diameter on the solids volume fraction distribution in the axial direction.

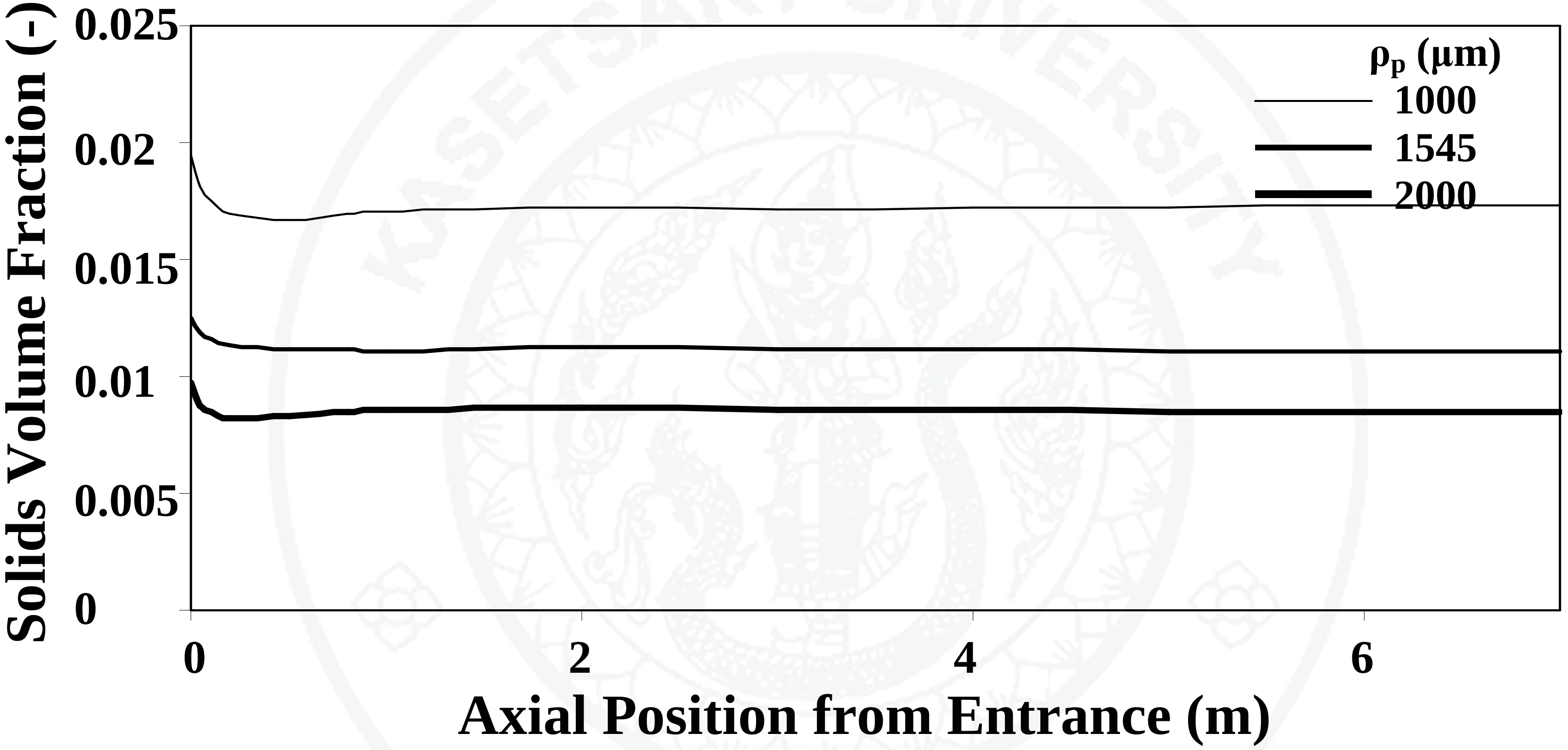

Figure 25 Effect of particle density on the solids volume fraction distribution in the axial direction.

The effects of particle size and particle density on the gas and solids velocities in the fully developed region show in Figures 26 and 27, respectively. These figures show a slowly increasing of gas and solids velocities in the center region with a high velocity peak near the wall region. However, increasing particle density and/or particle size leads to more uniform gas and solids velocities profiles. Smaller particle and/or lighter particle tend to agglomerate near the wall region as shown in Figures 22 and 23. This high particle agglomeration causes high gas and particle velocities in the near wall region, as result in less uniformity of gas and solids velocities in lateral direction.

Figure 28 shows the effect of particle size on the gas and particle velocities distribution in the axial direction. It was found that the particle velocity profiles of all cases significantly increase near the inlet section and slightly increase until reach the constant at the fully developed region. The gas velocity slightly increases along the reactor height. At any axial position, the particle velocity increases with particle size because larger particle tends to increase the gravitational force and decrease the frictional force between gas and particle. In contrast, the gas velocity decreases with increasing particle size because of low solids volume fraction in the system. The particle density shows less effect on axial distribution of particle velocity as shown in Figure 29. However, lighter particle tends to increase the gas velocity especially in the fully developed region. The reason is that lighter particle prone to accumulate to form a high density peak near the wall region as can be seen in Figure 23. Gas and particle in the zone were accelerated to flow downward. This high gas velocity in this region leads to increasing of cross-sectional average of gas velocity in the system.

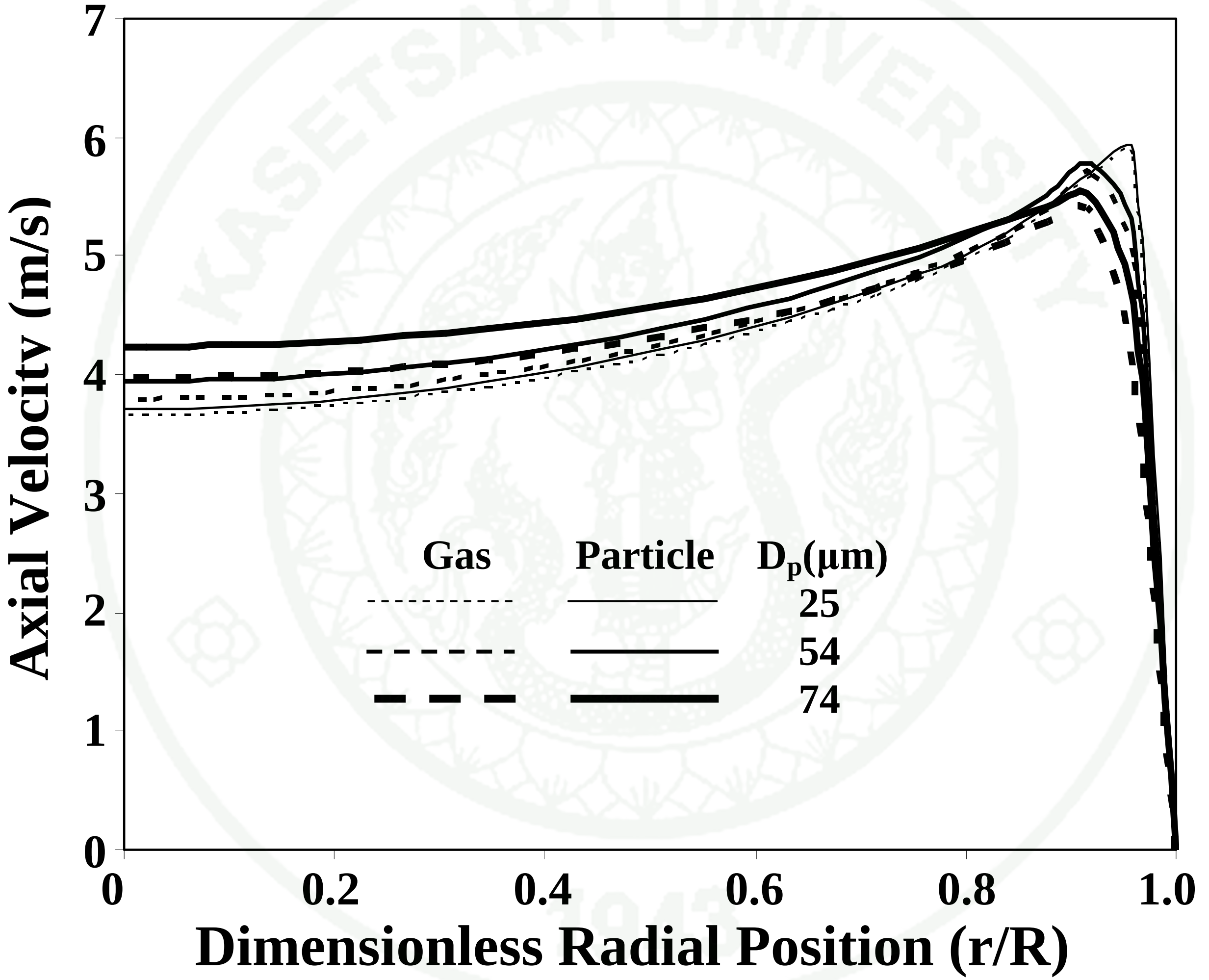

Figure 26 Effect of particle diameter on the axial gas and solids velocities distributions in the radial direction.

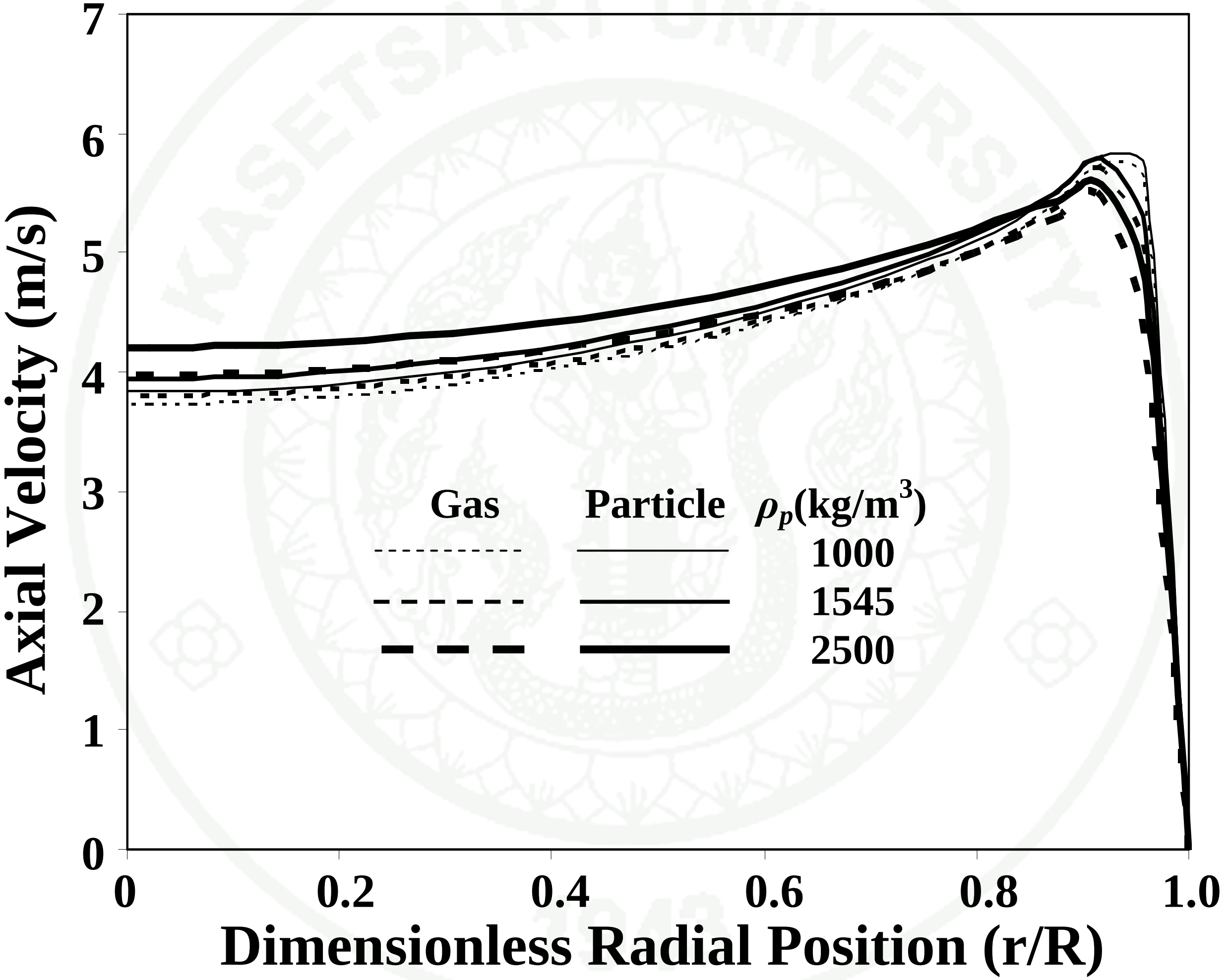

Figure 27 Effect of particle density on the gas and solids velocities distributions in the radial direction.

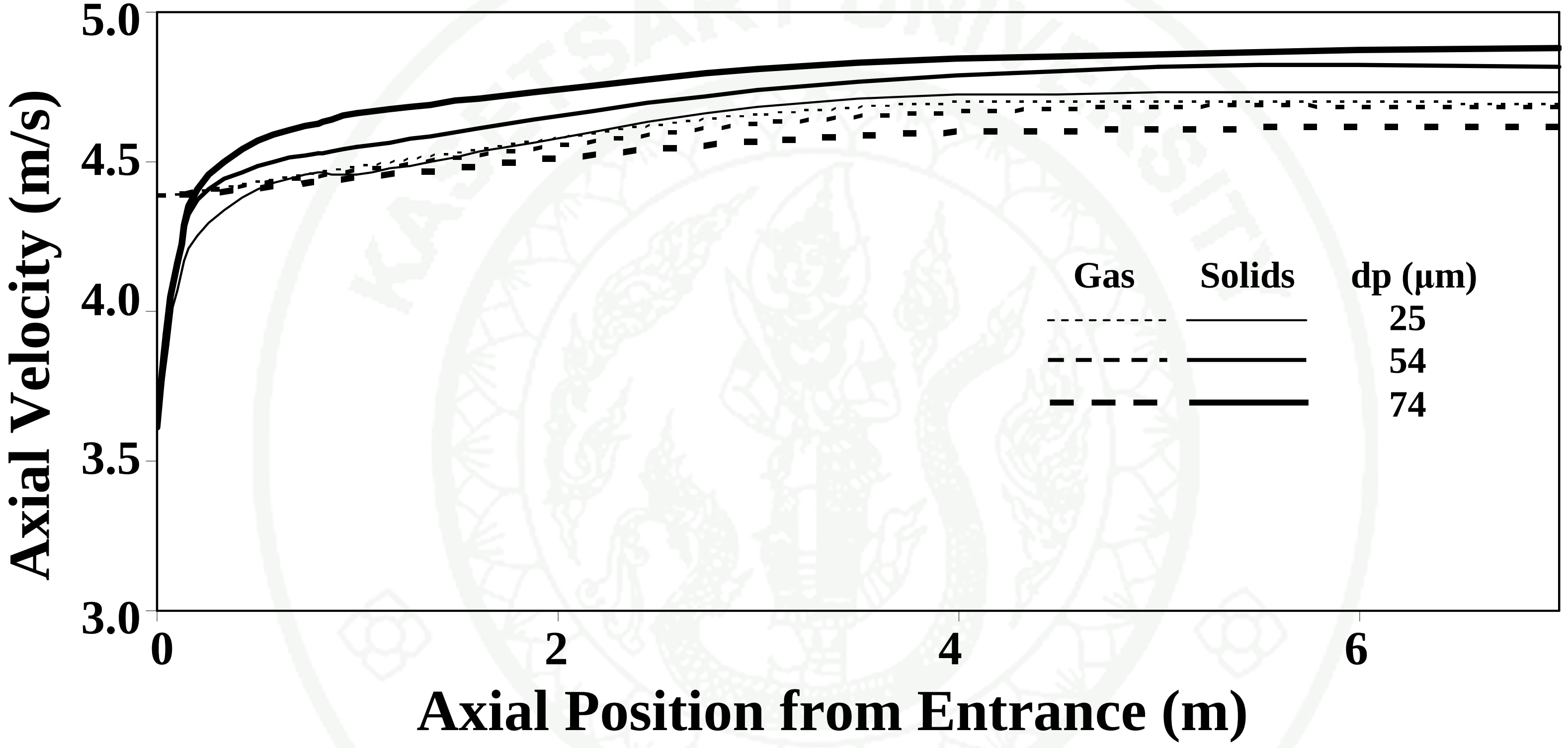

Figure 28 Effect of particle diameter on the axial gas and solids velocities distributions in the axial direction.

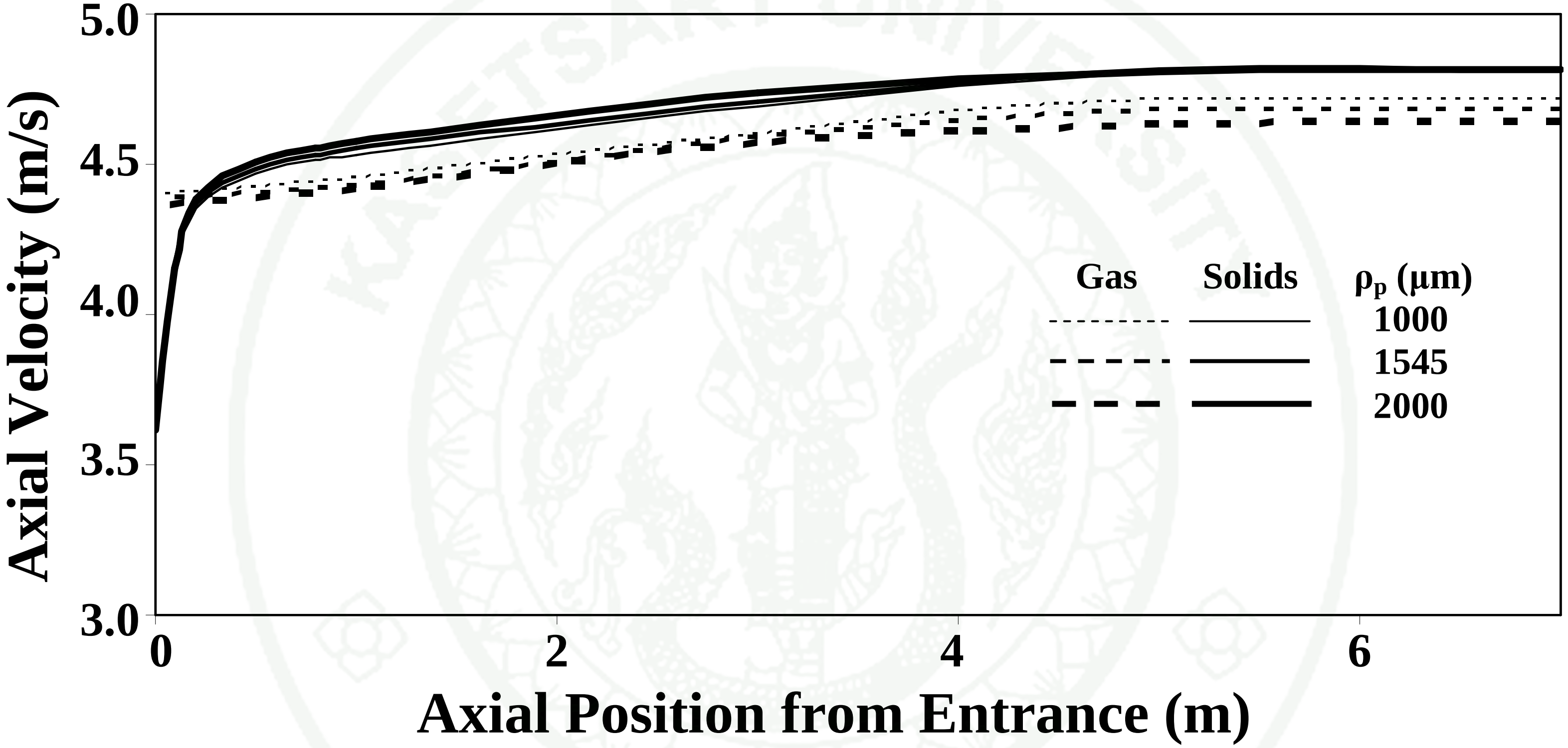

Figure 29 Effect of particle density on the axial gas and solids velocities distributions in the axial direction.

1.1.3 Comparison of hydrodynamics behavior between experimental data and model prediction

The lateral profiles of time-averaged solids volume fraction and time-averaged axial particle velocity in the fully developed region were compared with the available data. Figure 30 shows the effect of operating conditions on the solids volume fraction and the axial particle velocity. The marker represents the experimental results obtained from Wang *et al.* (1992). The dashed line denotes the simulation results of the two-fluid model obtained from Cheng *et al.* (1999) and the solid line signifies the simulation results of this study. The simulation results of this study show a satisfactory level of agreement with the experimental results and the previously obtained simulation data. This simulation captures the expected flow behavior in the downer, with an almost uniform solids volume fraction in the core region with a high peak in the proximity of the wall. Thus, it is evident that the axial mixing parameters obtained from this model also have credibility. Therefore, this information can be further used to evaluate for the accuracy of reactor performance prediction and good reactor design.

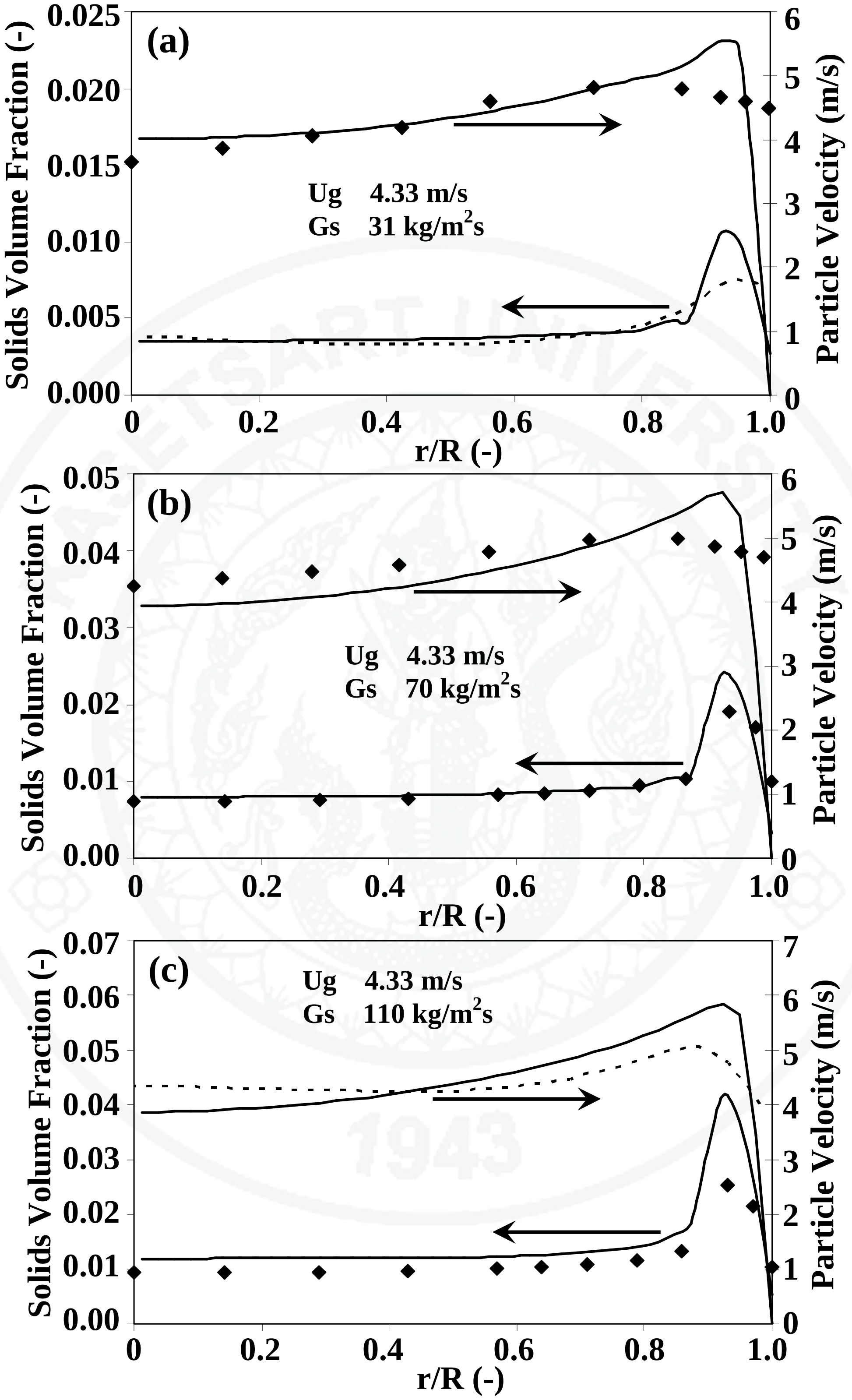

Figure 30 Effect of solids circulation rate on the solids volume fraction and the axial particle velocity (◆ = Wang *et al.*, 1992; – – – = Cheng *et al.*, 1999; —— = This work).

1.2 Axial gas and solids mixing in a downer reactor

1.2.1 Charecteristics of RTD

Figures 31 (a) and (b) show the typical RTD curves obtained from the CFD simulation results and the axial dispersion model for gas and solids phases, respectively. Gas and solids RTD curves show single narrow peak curves, which have been observed in the course of experiments (Bang *et al.*, 1999; Brust and Wirth, 2004; Wei *et al.*, 1994a). Moreover, the gas RTD curve is narrower than that of the solids RTD. This implies that the gas phase flow behavior approximates an ideal plug flow, with higher gas Peclet number. A peak height of gas RTD curve shows less sensitivity than those of solids RTD curves at varied superficial gas velocities. The RTD curves based on CFD simulation and the axial dispersion model were fitted together. A good normalization was confirmed by the unity areas under RTD curves of all cases in Figure 31, as shown in Table 15. A good agreement of RTD curves calculated on the basis of the CFD simulation and the analytical solution of the axial dispersion model indicates that the system is representative in terms of an overall Peclet number. Thus the Peclet number was used as a mixing parameter.

1.2.2 Effect of operating condition on the gas and solids mixing

Several studies have revealed that the operating conditions (i.e., superficial gas velocity, solids circulation rate) significantly affect the flow behavior in a downer reactor. Thus, this section shows the effects of superficial gas velocity and solids circulation rate on the axial mixing of gas and particle phases in such a reactor type.

Figure 32 shows the effect of superficial gas velocity on the axial gas and solids Peclet numbers. It was found that, gas and solids Peclet numbers are increased at increased superficial gas velocity. This effect is more remarkable at a low solids circulation rate at which both gas and solids Peclet numbers significantly increase with superficial gas velocities. This trend can also be observed in experimental studies (Brust and Wirth, 2004). At higher superficial gas velocity, more uniform flow in the lateral direction was found, as shown in Figures 13, 17, and 18. At any superficial gas velocity, the radial distribution of solids volume fraction is

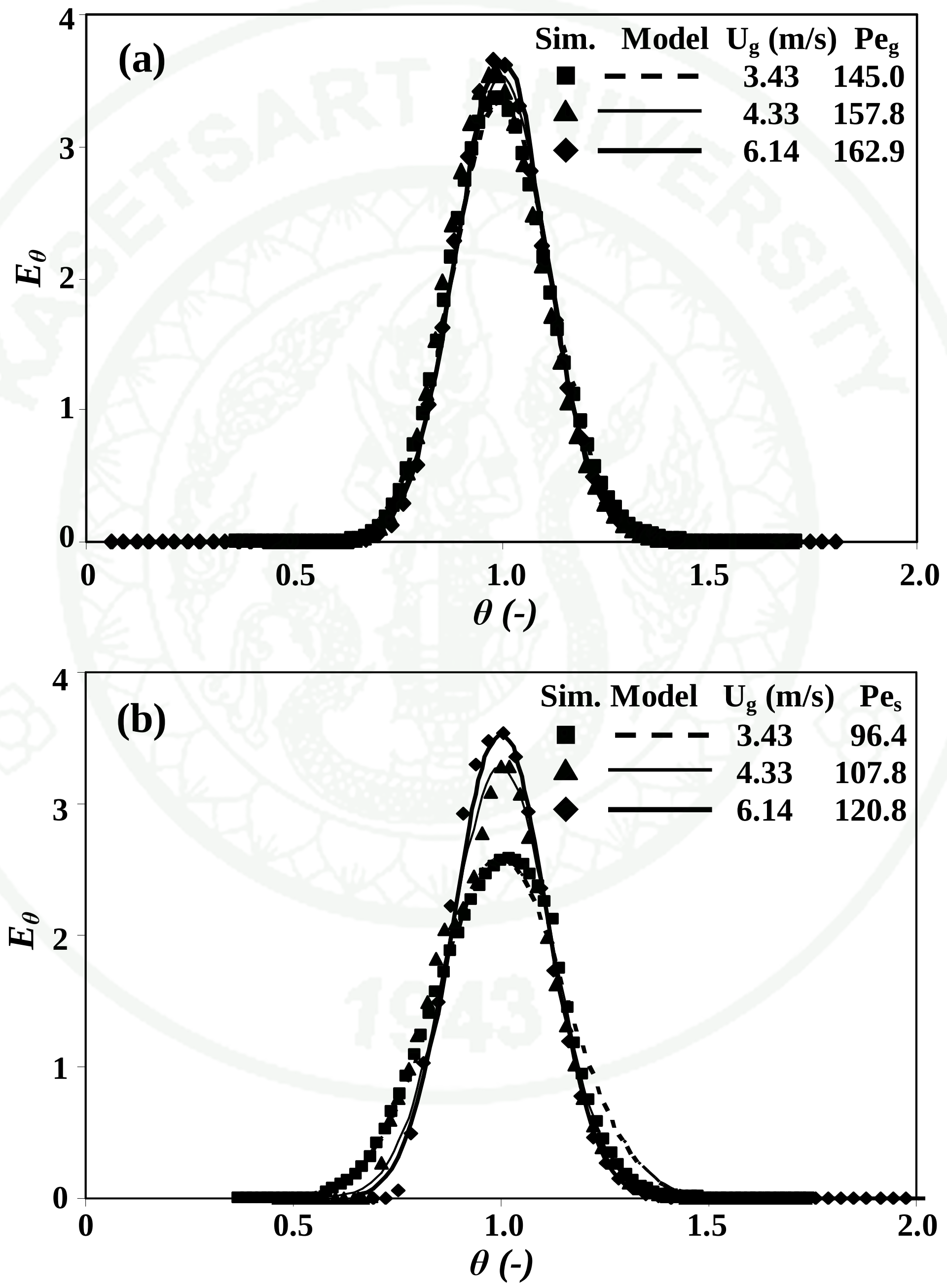

Figure 31 Typical RTD curves in a downer reactor at the solids circulation rate of 70 kg/m^{2}s: (a) gas phase; (b) solids phase.

Table 15 Area under E_θ curve.

Ug (m/s)	Area Under Curve ($\int E_\theta d\theta$)			
	Gas Phase		Solids Phase	
	Simulation	Model	Simulation	Model
3.43	1.00000	0.99980	0.96517	0.99977
4.33	1.00000	0.99980	1.00000	0.99979
6.14	1.00000	0.99980	1.00002	0.99792

almost uniform in the center region, with a density peak near the wall. The density peak of particle near the wall region, leads to high gas and solids velocities in this region because of a reduction of the effective drag force acting on gas and solids particle. The almost uniform flow in the center region causes the flow behavior in this region to approach plug flow behavior, meanwhile an axial velocity peak near the wall region causes the gas and particle from the upper layer to flow forward to mix with gas and particles in the lower layer. At a higher superficial gas velocity, smaller axial gas and particle velocity peaks cause a lower axial mixing near the wall region. Therefore, the gas and solids back-mixing is reduced, resulting in higher Peclet numbers at high superficial gas velocity.

Figure 33 shows the effect of solids circulation rate (Gs) on the axial gas and solids Peclet numbers. Axial Peclet number decreases with increased solids circulation rate. Lower values of Peclet numbers for both gas and solids phases at higher Gs are due to less uniform gas and solids flow behavior in the radial direction (see Figures 14 and 19). At low solids circulation rate, the solids volume fraction is significantly more uniform in the radial direction, which agrees with a previous study (Li *et al.*, 2004). This more uniform solids volume fraction leads to more uniform gas and solids velocities in the radial direction (see Figure 19). Therefore, the axial mixing of both gas and solids phases increases with increasing solids circulation rate. Thus increasing solids circulation rate causes the decreasing Peclet numbers.

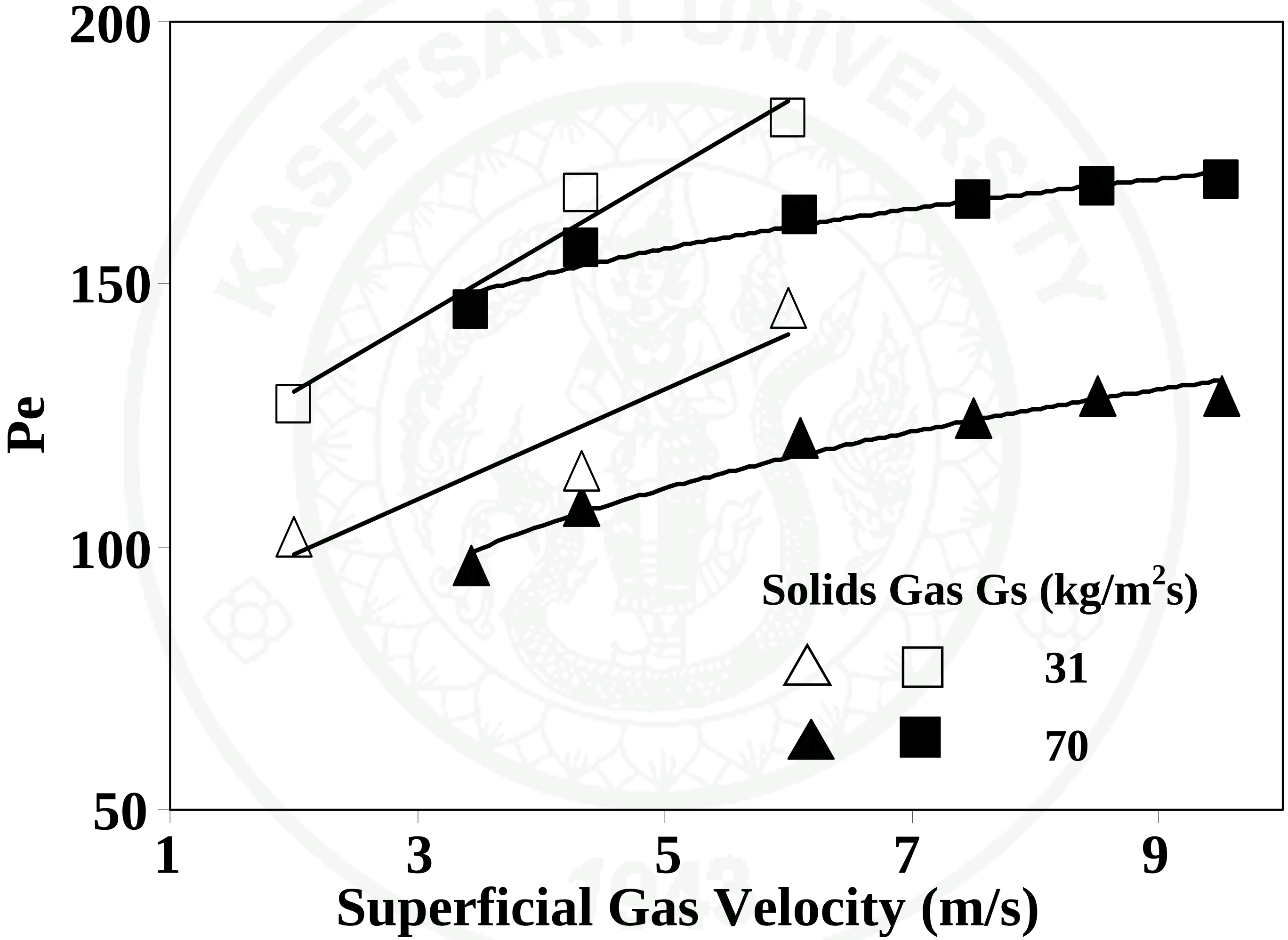

Figure 32 Effect of superficial gas velocity on the solids and gas Peclet numbers.

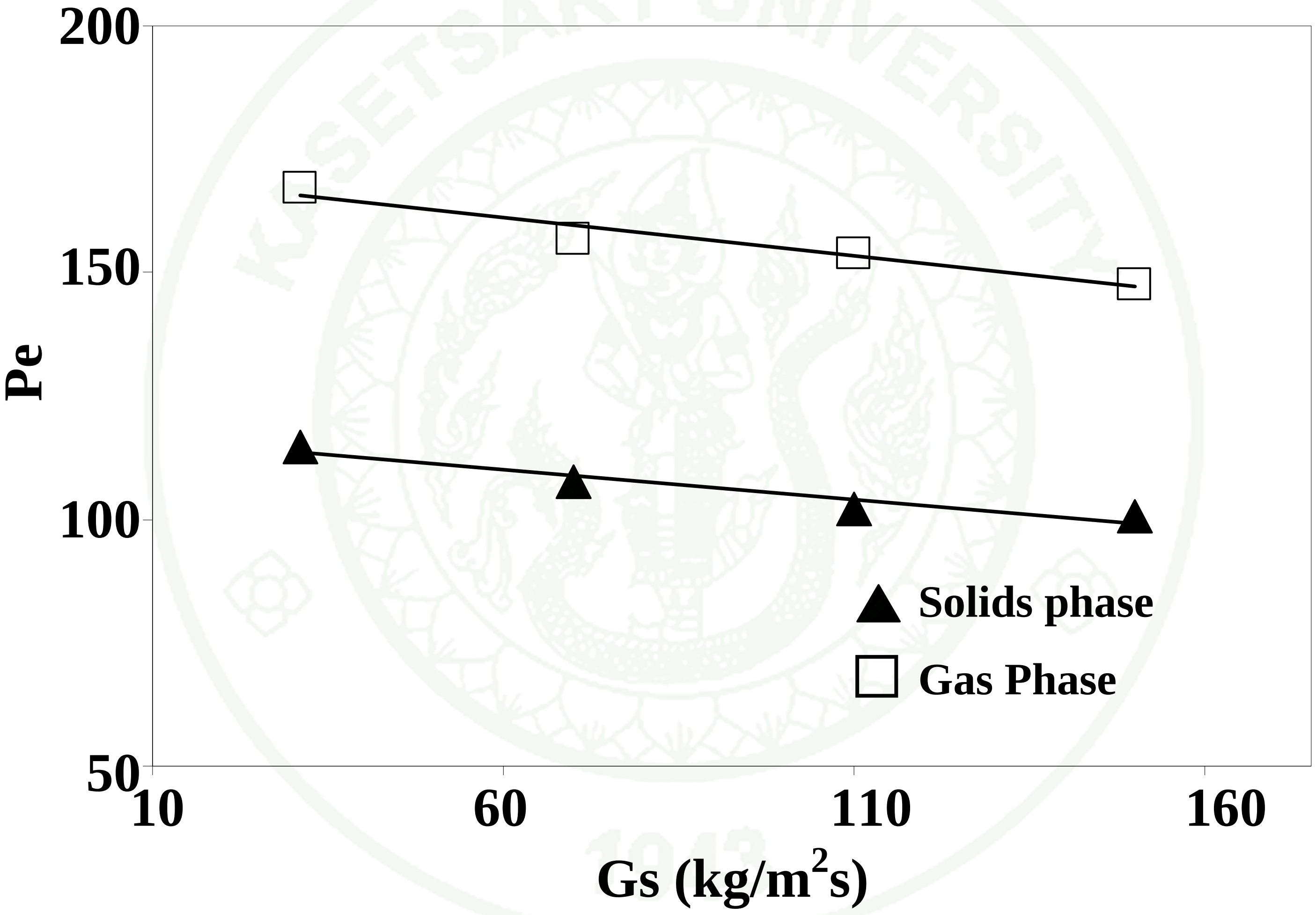

Figure 33 Effect of solids circulation rate on the solids and gas Peclet numbers.

1.2.3 Effect of particle properties on the gas and solids mixing

Figure 34 shows the effect of particle diameter on the gas and solids mixing. The Peclet numbers of gas and solids phases slightly increase with the particle diameter. In a system with large particles, more uniformity of gas and particle movements was found, as shown in Figure 26, leading to less axial mixing of gas and solids in the downer. However, the particle size has more effect on the gas mixing than on the solids mixing.

The effect of the particle density on the gas and solids mixing is shown in Figure 35. The gas and solids Peclet numbers tend to increase with the particle density. At the given Gs, the solids volume fraction is dramatically decreased when the particles are heavier (see Figure 23). In addition, denser particles cause more uniform gas and solids velocities and solids volume fraction in the radial direction as shown in Figure 27, leading to less back-mixing of gas and solids phases in the downer reactor.

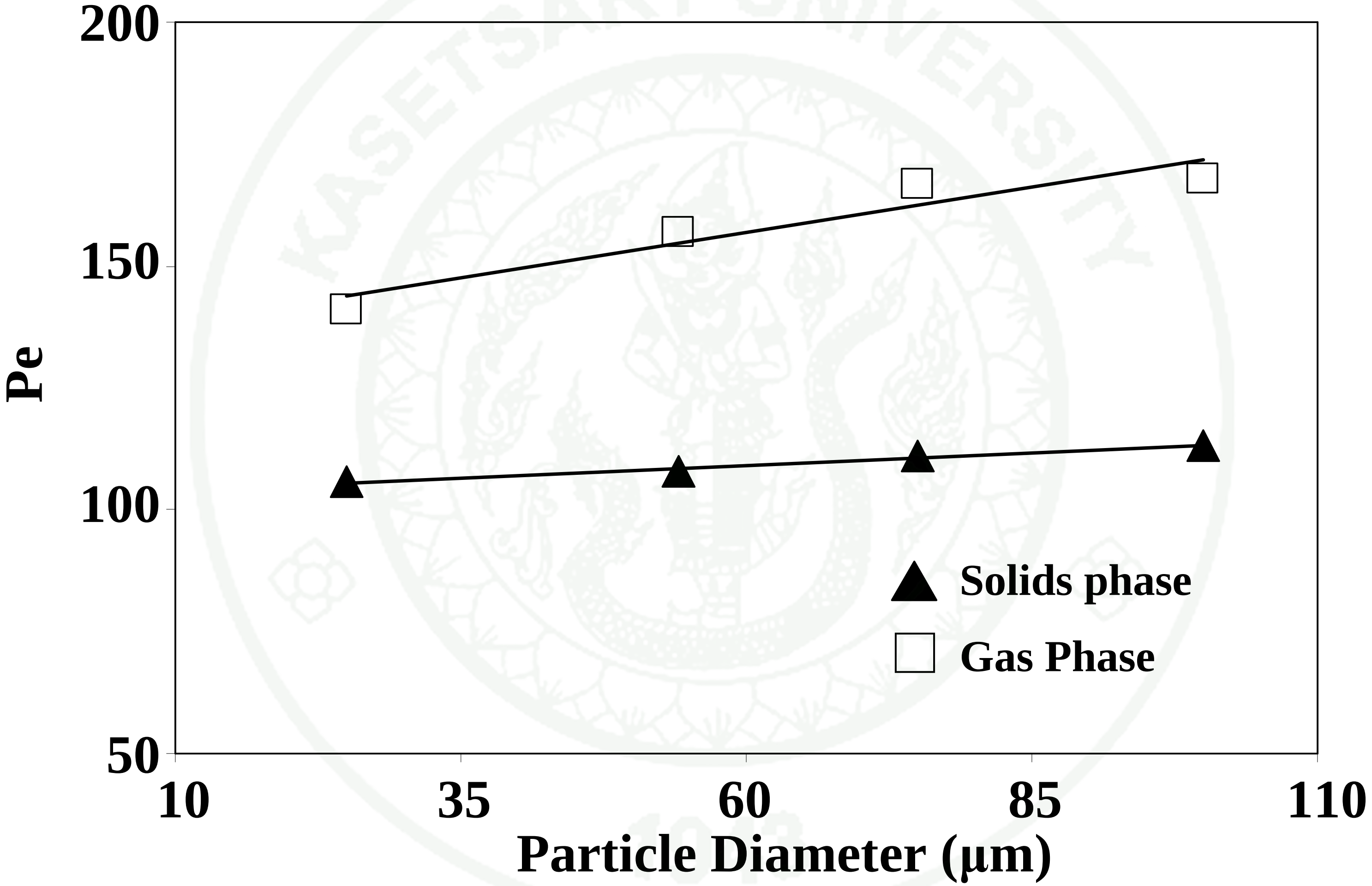

Figure 34 Effect of particle diameter on the solids and gas Peclet numbers.

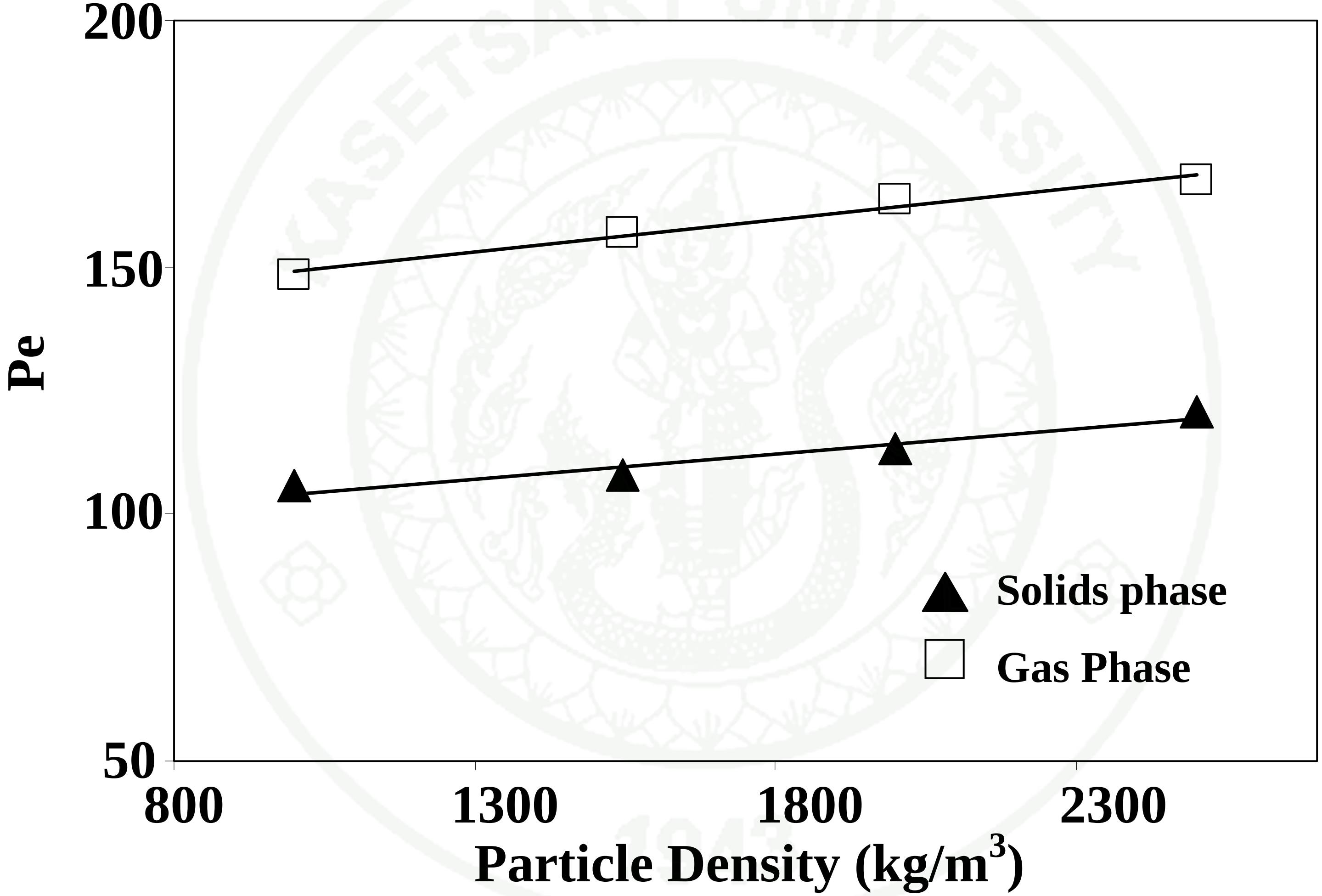

Figure 35 Effect of particle density on the solids and gas Peclet numbers.

1.2.4 Comparison of Peclet number of correlations and simulation results

In order to validate the simulation results, the axial solids Peclet number based on such simulation results was compared with the experimental data obtained from Huang *et al.* (2006), Wei *et al.* (1994b), and Yang (2001) and the correlation proposed by Wei *et al.* (1994b) as shown in Figure 36. It is evident that the axial solids Peclet number in the present work and previous studies are in a comparable range. Thus it can be concluded that the axial Peclet number based on CFD simulation has credibility and the virtual tracer method becomes a useful tool for the design of downer reactors.

A correlation for calculation of the solids Peclet number as a function of Reynolds number and bed voidage was proposed by Wei *et al.* (1994b):

$$Pe_s = \frac{8.93X10^{-7}\,\mathrm{Re}_s}{\alpha_s} + 101 \tag{84}$$

where Re_s is solids Reynolds number, which can be defined as follows:

$$\mathrm{Re}_s = \frac{\rho_g U_s D_T}{\mu} \tag{85}$$

where ρ_g denotes the gas density, U_s the superficial particle velocity, D_T the downer diameter, and μ the gas viscosity. The correlation for predicting the axial solids Peclet number obtained from this study is,

$$Pe_s = \frac{1.76X10^{-6}\,\mathrm{Re}_s}{\alpha_s} + 100 \tag{86}$$

Unfortunately, there is no correlation to calculate the axial gas Peclet number available in the literature. Thus, the gas Peclet number correlation based on this study is proposed as follows:

$$Pe_g = \frac{8.49X10^{-7}\,\mathrm{Re}_s}{\alpha_s} + 152 \tag{87}$$

In addition, correlations for the axial solids and gas Peclet numbers based on the operating conditions were proposed. Dimensionless groups of variables based on the operating conditions and the physical properties of the gas and solids phases were determined using dimensional analysis. Correlations based on these dimensionless parameters were obtained by linear regression:

$$Pe_s = 44\left(\frac{\rho_g U_g d_p}{\mu_g}\right)^{0.048}\left(\frac{G_s}{\rho_g U_g}\right)^{-0.083}\left(\frac{\rho_p - \rho_g}{\rho_g}\right)^{0.14} \tag{88}$$

$$Pe_g = 49\left(\frac{\rho_g U_g d_p}{\mu_g}\right)^{0.133}\left(\frac{G_s}{\rho_g U_g}\right)^{-0.075}\left(\frac{\rho_p - \rho_g}{\rho_g}\right)^{0.13} \tag{89}$$

Figure 37 and Table 16 show a comparison of the Peclet numbers from these proposed correlations and the simulation results, where the correlations were fitted with the simulation results. Thus these proposed correlations can be used for predicting the axial gas and solids mixing in the downer reactor.

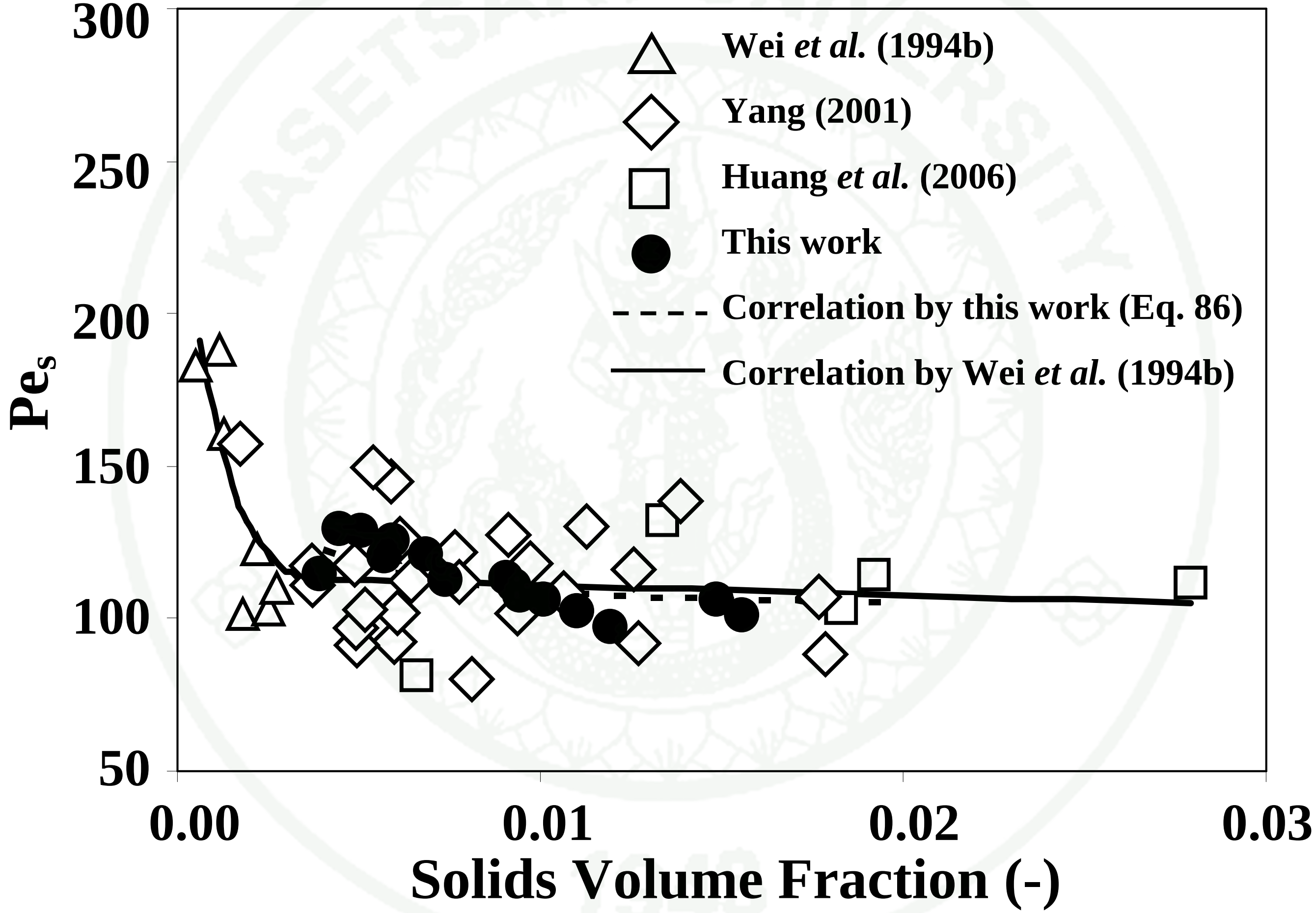

Figure 36 Comparison of the simulated solids Peclet numbers with literature data.

Table 16 Comparison of simulated Peclet number with the correlations.

Simulation case	Pe_s					Pe_g				
	Simulation	**Correlation (Eq. 86)**	**%error**	**Correlation (Eq. 88)**	**%error**	**Simulation**	**Correlation (Eq. 87)**	**%error**	**Correlation (Eq. 89)**	**%error**
The effect of Ug (m/s)										
3.43	96.43	105.16	-9.06	106.64	-10.59	145.00	154.46	-6.52	145.30	-0.21
4.33	107.81	108.14	-3.06	109.95	-1.98	156.84	155.88	+0.61	152.51	+2.76
6.10	120.81	115.62	+4.30	115.02	+4.79	162.92	159.45	+2.13	163.79	-0.53
7.50	124.74	121.96	+2.23	118.18	+5.26	165.35	162.47	+1.74	170.98	-3.40
8.50	128.75	129.18	-3.34	120.14	+6.69	164.45	165.92	-0.89	175.50	-6.72
9.50	128.73	134.60	-4.56	121.91	+5.30	160.00	168.50	-5.31	179.61	-12.26
The effect of G_s (kg/m^2s)										
31	114.60	119.15	-3.97	117.67	-2.68	167.30	161.14	+3.68	162.09	+3.11
70	107.81	108.14	-0.31	109.95	-1.98	156.84	155.88	+0.61	152.51	+2.76
110	102.13	107.40	-5.16	105.89	-3.68	154.00	155.53	-0.99	147.44	+4.26
150	100.59	105.12	-4.50	103.19	-2.58	147.67	154.44	-4.58	144.06	+2.44
The effect of d_p (μm)										
25	105.72	107.85	-2.01	105.96	-0.23	141.08	155.74	-10.39	137.63	+2.45
54	107.81	108.14	-0.31	109.95	-1.98	156.85	155.88	+0.618	152.51	+2.77
75	110.89	108.43	+2.21	111.71	-0.74	166.77	156.02	+6.44	159.34	+4.46
100	113.14	108.87	+3.77	113.26	-0.12	168.01	156.23	+7.01	165.57	+1.45
The effect of ρ_p (kg/m^3)										
1 000	105.72	104.99	+0.69	103.46	+2.14	148.44	154.38	-4.00	143.85	+3.09
1 545	107.81	108.14	-0.31	109.95	-1.98	156.85	155.88	+0.62	152.51	+2.77
2 000	113.14	110.51	+2.32	113.99	-0.75	163.62	157.01	+4.04	157.90	+3.50
2 500	120.81	113.62	+5.95	117.61	+2.65	167.48	158.50	+5.36	162.70	+2.85

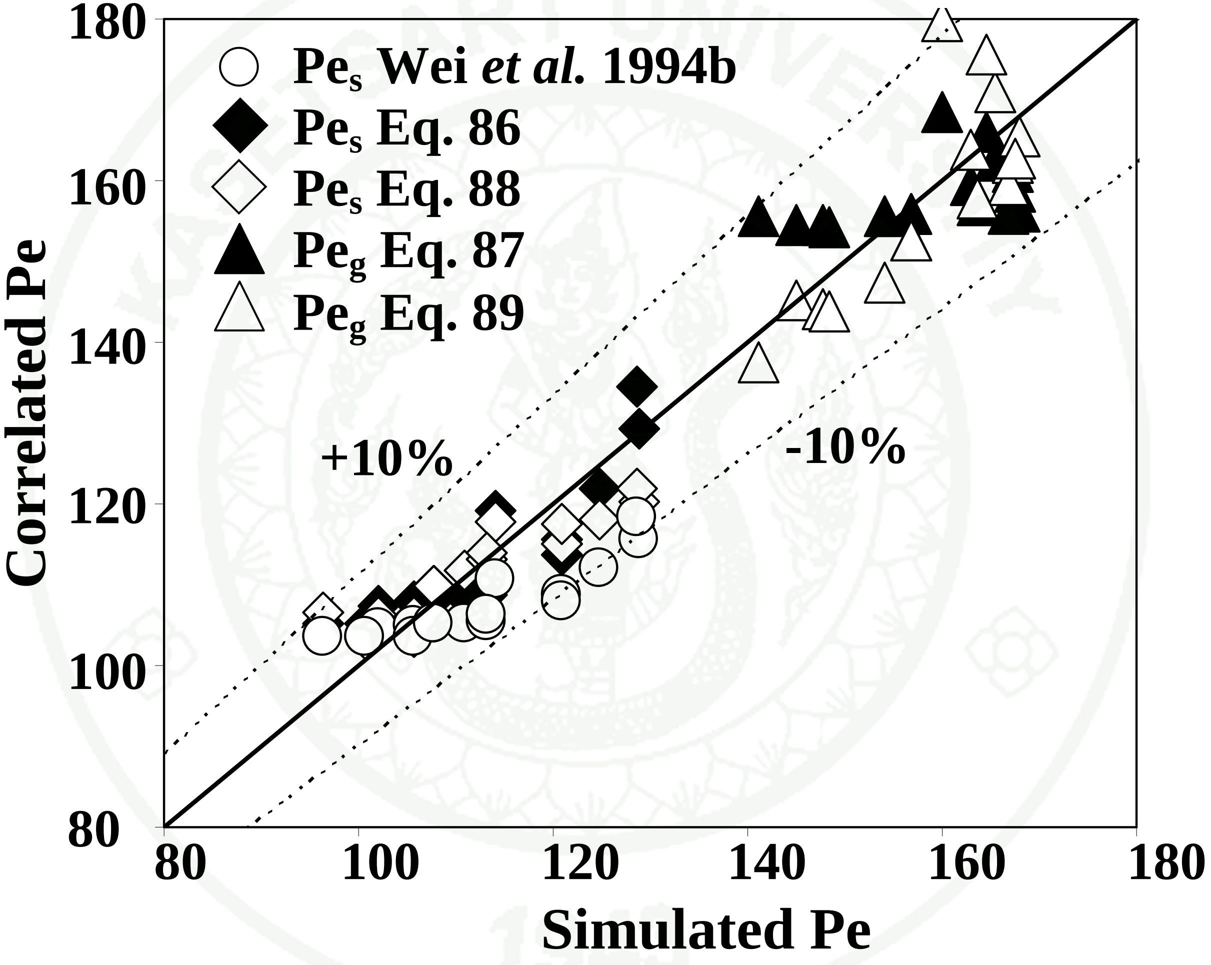

Figure 37 Comparison of the simulated Peclet numbers with the proposed correlation.

2. Flow behavior and CO_2 removal performance in a circulating fluidized bed reactor

It is now well-known that carbon dioxide (CO_2) is the main greenhouse gas which significantly effects on global warming. Thus many countries such as USA, China etc., are paying more attention to reduce CO_2 emission. One of the main sources of CO_2 emission is the coal-fired power plant. Therefore several methods have been developed to remove CO_2 from flue gas releasing from this system such as oxy-combustion (Chui *et al.*, 2003) and liquid scrubbing method such as amine-based system (Jassim and Rochelle, 2006; Oyenekan and Rochelle, 2006). However, these methods are costly. Moreover, the DOE NETL website and recent literature (Holt, 2000; Jassim and Rochelle, 2006) show that the energy consumption for capturing CO_2 from flue gases using liquid amine scrubber, is 15 to 30% of the power plant. This is due to the fact that the minimum energy for separation of CO_2 from flue gases, 7.3 KJ/gmol CO_2, is already about one third of the energy required for separation using aqueous amines (Oyenekan, 2007). Moreover for a conventional coal fired power 329 MWe plant (Holt, 2000), there are 4 absorber columns, 8.8 m diameter and 24 m high and the stripper with a diameter of 4.9 m and a height of 22.9 m. The steam requirement is 552 million kg/hr at 0.3 MPa. The diameters are large due to large flue gas emissions. The heights are large due to the use of aqueous amines with low sorption rates and low diffusion coefficients of CO_2 in the liquids.

Recently, CO_2 capture process using a regenable solids sorbent has been developed (Fang *et el.*, 2009; Nelson *et al.*, 2009; Park *et al.*, 2009). The primary economic analysis (Green *et al.*, 2005) indicated that the CO_2 capture using solids sorbent is more cost effective than the amine-based process. In addition, many solids sorbents have been developed such as solid potassium carbonate sheets (Onischak and Gidaspow, 1972; Gidaspow and Onischak, 1975) and the sodium carbonate pellets (Gupta and Fan, 2002; Nelson *et al.*, 2009). These high sorption rates of solids sorbent might be reduced the size of CO_2 capture unit.

Fluidized bed reactors have been used for CO_2 capture using solids sorbents (Fang *et al.*, 2009; Nelson *et al.*, 2009; Park *et al.*, 2009; Chalermsinsuwan *et al.*, 2010) because of its continuous particle handling ability and its good mass- and heat-transfer characteristics. The solids sorption fluidized bed reactor usually operates in fast fluidization regime with high gas velocity due to large amount of flue gas was released from power plant. The flow structure of fast fluidized bed reactor exhibits core-annular flow with low solids concentration at the center and high solids concentration near wall region. The low solids concentration in the center causes low chemical conversion in this zone. In addition the fluidized bed with side solids feed inlet, the solids concentration is less uniform in the radial direction (Chalermsinsuwan *et al.*, 2009a). Most of solids particles are accumulated near the solids feed inlet. Gas by-passing usually occurs near the wall which opposite to the solids feed inlet (Khongprom *et al.*, 2008). A circulating fluidized bed (CFB) with bottom U section has been constructed at IIT (Kashyap, 2010), which the gas/solids mixture flows from the U tube into the riser. Our research groups have also modeled the CFB using our kinetic theory and multiphase flow theory and codes. By feeding the particles through the center, rather than through the side wall as in conventional CFBs, we can reduce the undesirable core-annular flow regime.

The objective of this study is to develop the two-fluid model based on kinetic theory of granular flow for CO_2 capture using solids sorbent fluidized bed. The effect of solids feed inlet on the hydrodynamics and CO_2 capture performance in the riser was addressed. Moreover, the hydrodynamics and reactor performance in the riser and the downer reactors were also studied.

2.1 The comparison of hydrodynamics behavior between the riser with bottom solids feed inlet and the riser with side solids feed inlet (CFB system)

2.1.1 Solids volume fraction

Figure 38 shows the distributions of solids volume fraction in the riser with bottom solids feed inlet and CFB systems at 5 and 20 sec. The solids volume fraction distribution in the riser with bottom solids feed inlet is more uniform than that in the riser of the CFB. The downward flow of gas and particles near the wall region creates a small bubble in this zone of the riser with bottom solids feed inlet. In the riser of the CFB, at 5 sec., the core-annular flow, which a low solids volume fraction in the center and a dense region near the wall, can be observed. At 20 sec., the solids volume fraction is high near solids feed inlet region and very low solids volume fraction on the opposite to the solids feed inlet side. This leads to gas by-passing in this low solids region. Figure 39 shows the time-averaged solids volume fraction distribution in the axial direction. It is confirmed that the solids volume fraction in the riser with bottom solids feed inlet is much more uniform both in the axial and the radial positions, while the profiles in the riser section of the CFB show asymmetric profile, which is usually observed from the experiments (Tertan and Gidaspow, 2004). In the riser section of the CFB, the solids volume fraction is high near the right wall (solids feed side) especially in the bottom section. At the upper section of the reactor, the solids distribution becomes more uniform in the radial direction.

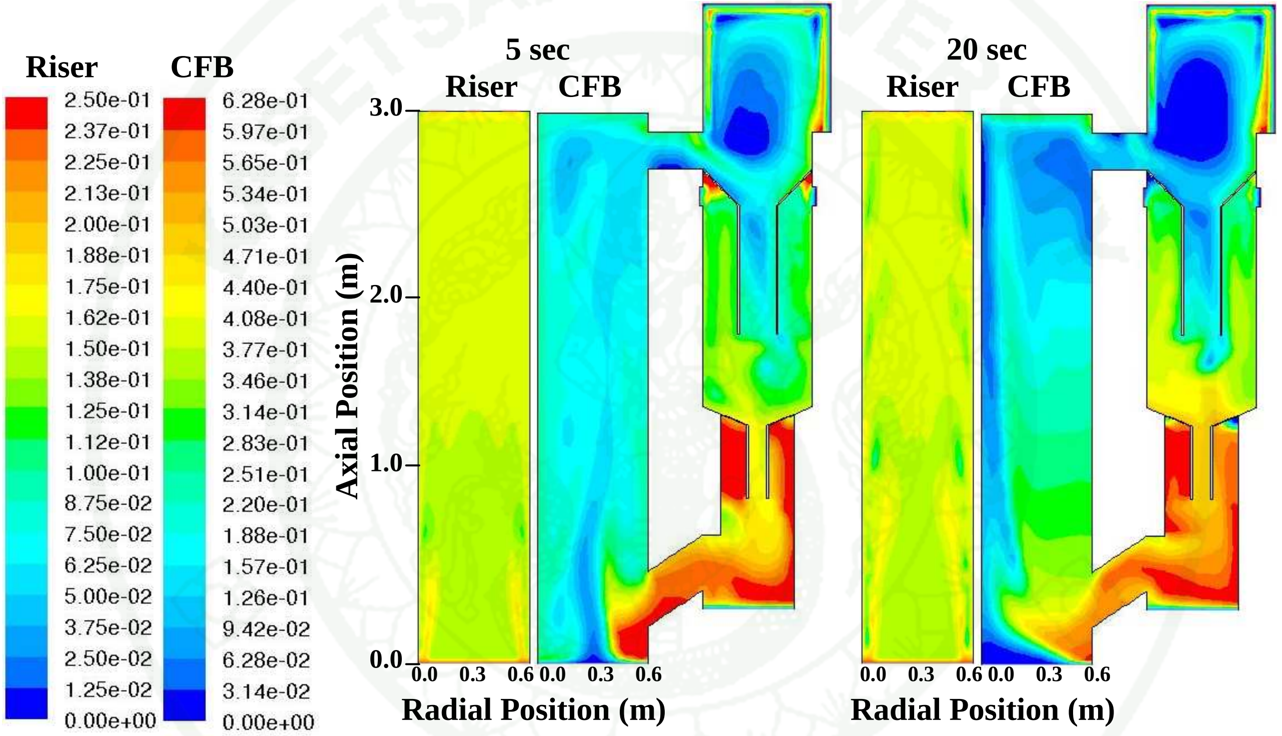

Figure 38 Distributions of solids volume fraction in the riser with bottom feed inlet and the CFB system.

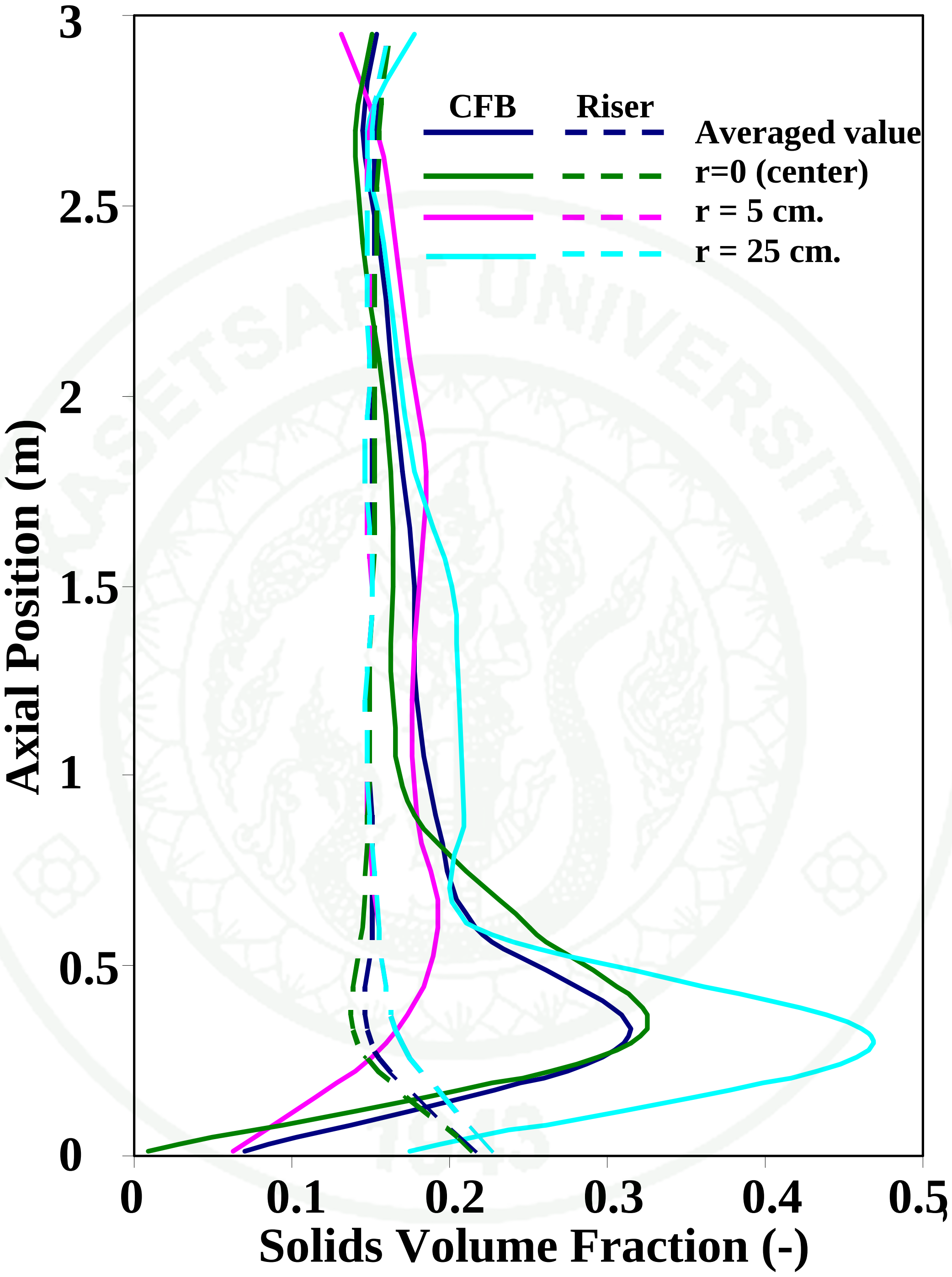

Figure 39 Time-averaged solids volume fraction distributions in the axial direction of the riser with bottom solids feed inlet and the riser of the CFB.

2.1.2 Solids and gas velocities

Figure 40 shows the solids velocity vector plot (Figure 40 (a)) and gas velocity vector plot (Figure 40 (b)) at 5 and 20 sec. It can be seen that the solids and gas velocities in the riser with bottom solids feed inlet show more symmetric than those in the riser of the CFB system. Moreover, it can be observed the down flow of both solids and gas velocities near wall region of the riser with bottom solids feed inlet. In the riser of the CFB, solids and gas flow upward with high velocity in the lean region and flow downward in the dense region. Figures 41 (a) and (b) show the radial distribution of the time-averaged axial solids and gas velocities in the riser with bottom solids feed inlet and the riser of the CFB. The profile in the riser with bottom solids feed inlet show more symmetry. Solids sorbent and gas flow upward in the center region and flow downward near the wall. The axial velocity profiles in the riser of the CFB show a strong asymmetry. The solids and gas flows upward in the left side of the reactor and flows downward in the right side of the reactor. Figures 42 (a) and (b) show the radial velocities of solids and gas phases. The radial solids and gas velocities in the riser with bottom solids feed inlet are much smaller than those in the riser of the CFB. High radial solids and gas velocities at 0.6 and 2.4 m height of the riser of the CFB are due to solids feed inlet and outlet effects, respectively.

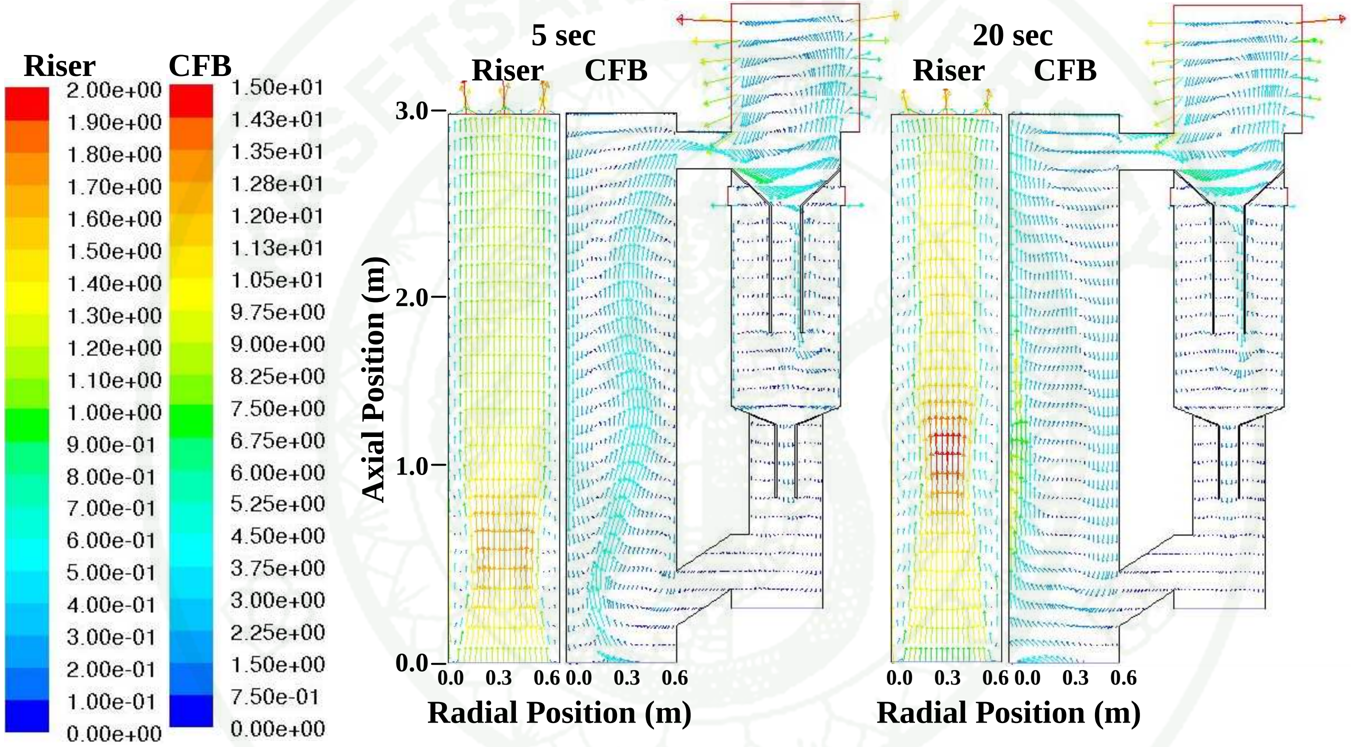

(a)

Figure 40 Velocity vector plots (a) solids phase and (b) gas phase in the riser with bottom solids feed inlet and the CFB system.

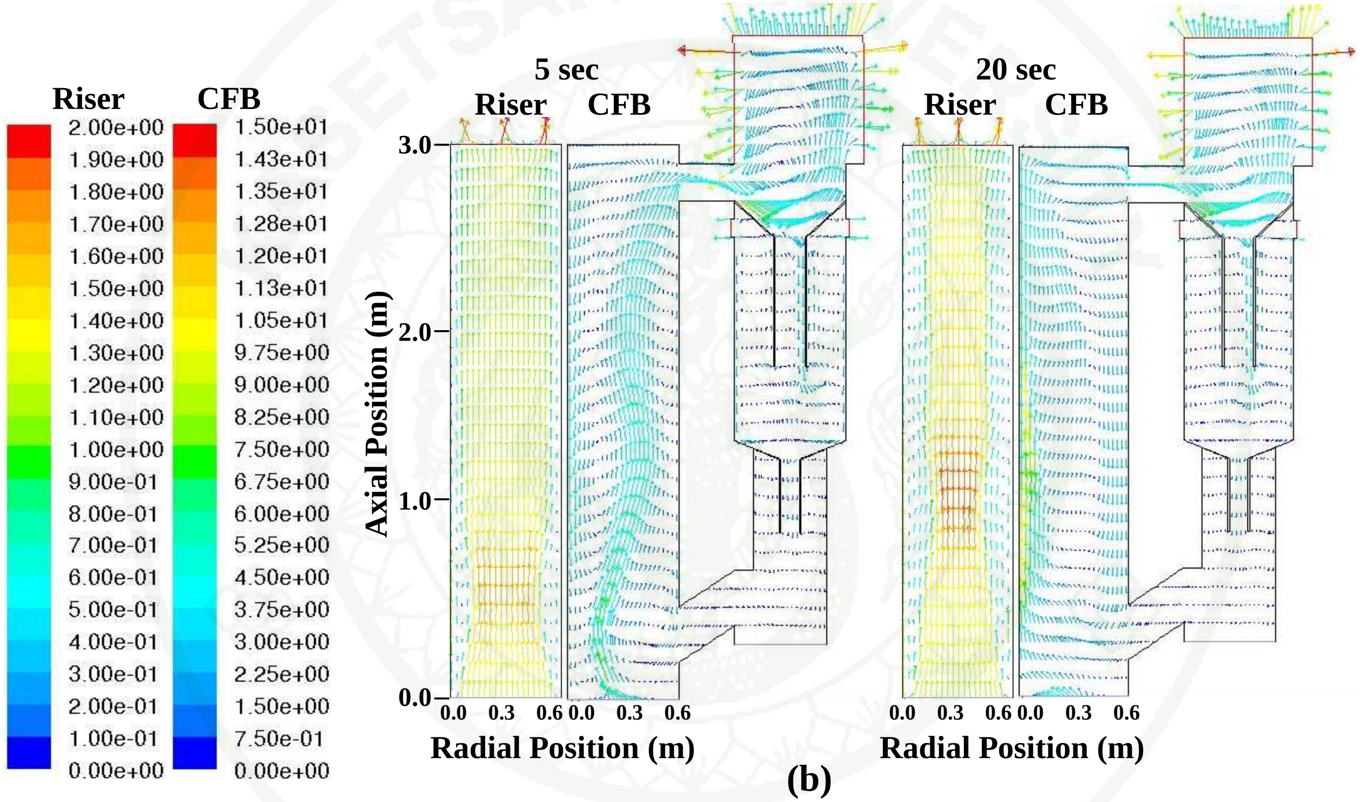

Figure 40 (Continued).

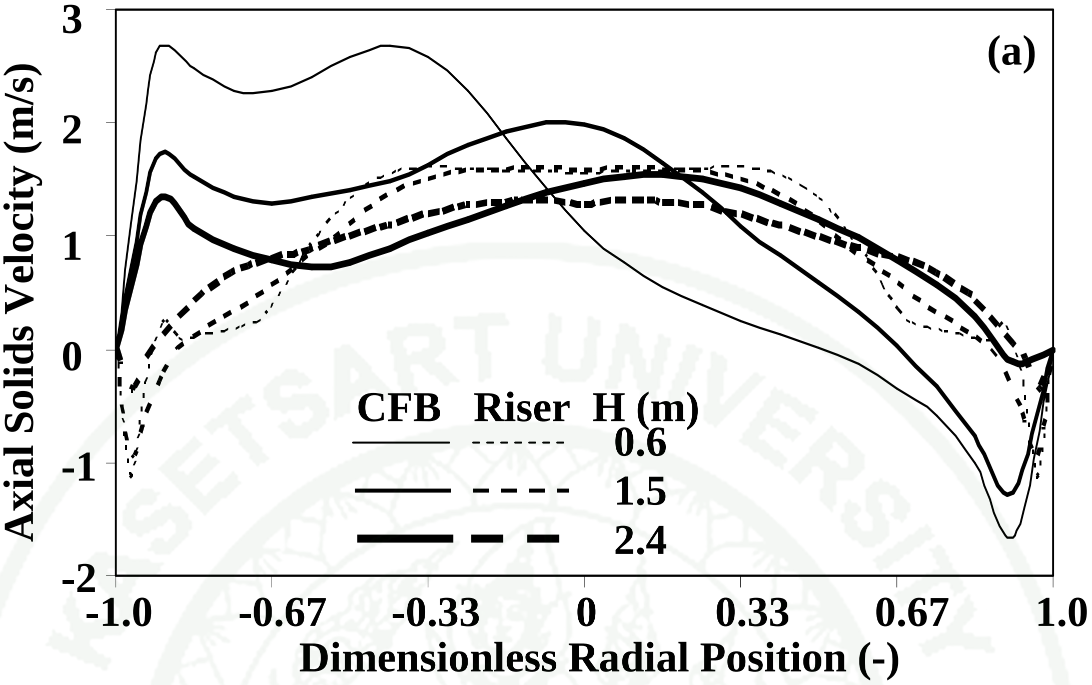

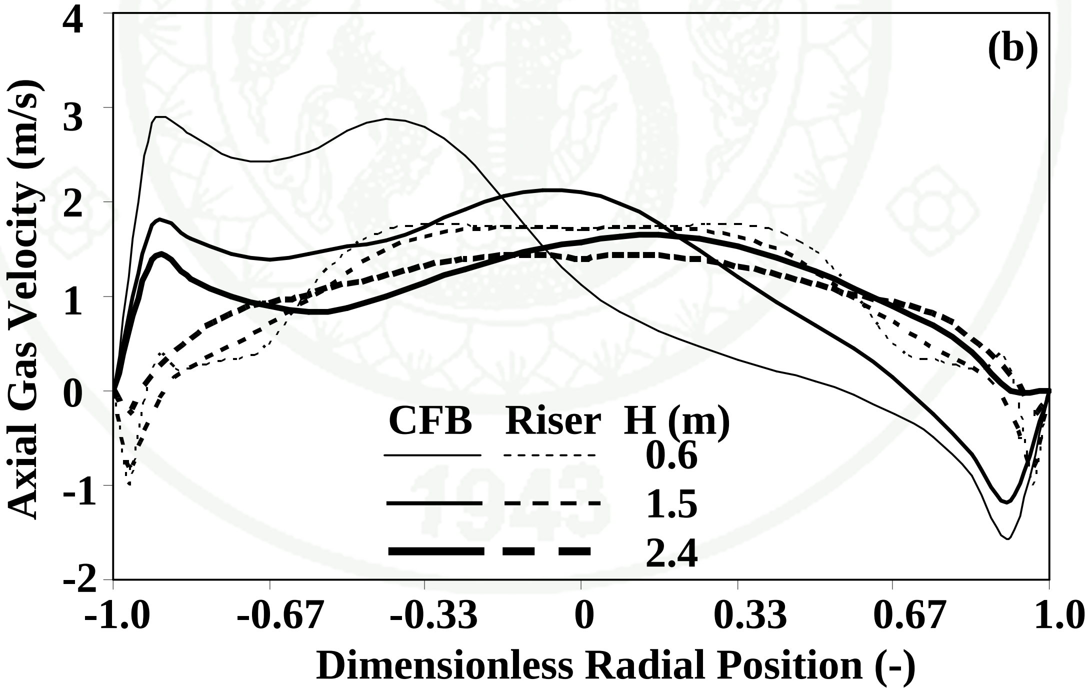

Figure 41 Radial distributions of the time-averaged axial velocity of (a) solids phase and (b) gas phase in the riser with bottom solids feed inlet and the riser of the CFB at various heights.

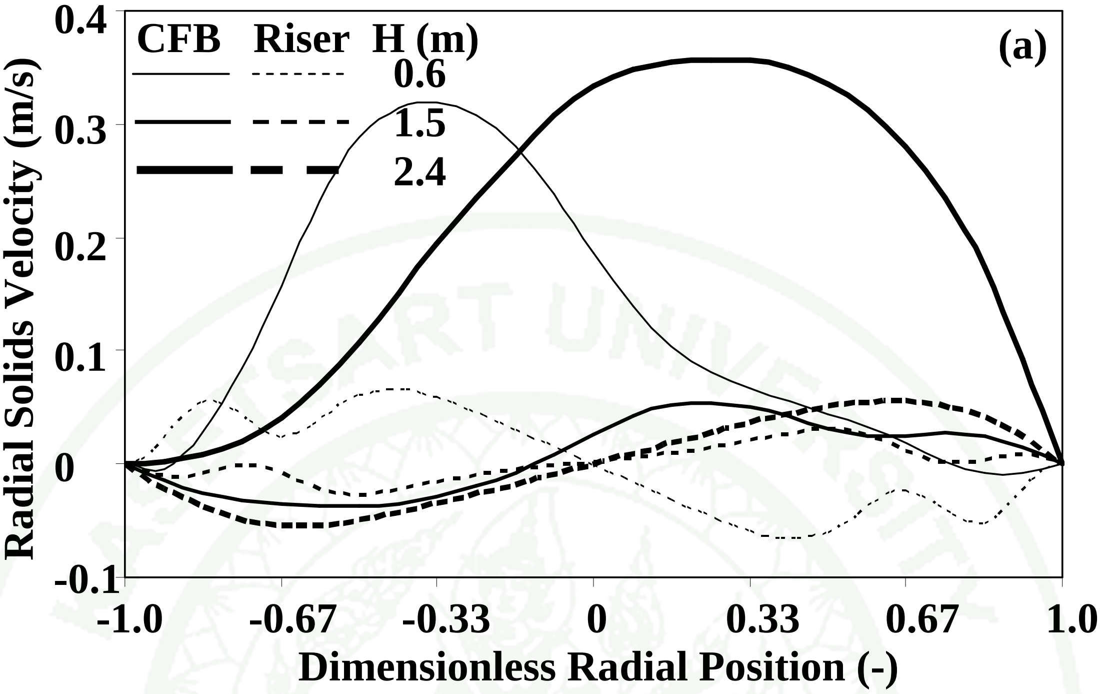

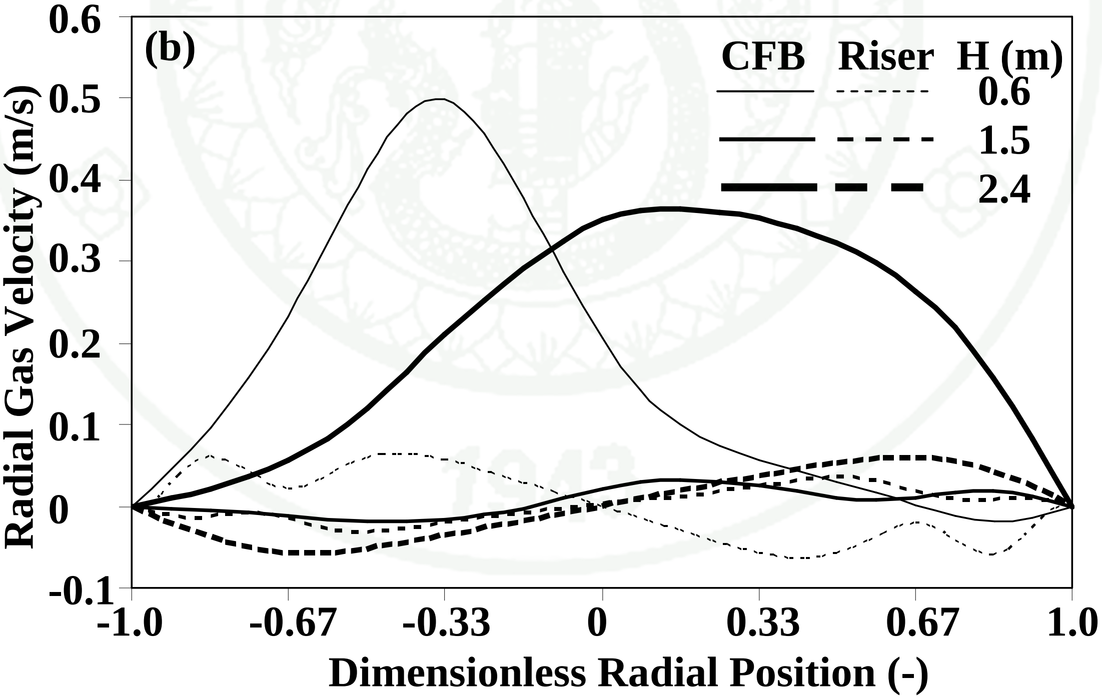

Figure 42 Radial distributions of the time-averaged radial velocity of (a) solids phase and (b) gas phase in the riser with bottom solids feed inlet and the riser of the CFB at various heights.

2.1.3 Granular temperature

Figures 43 (a) and (b) show the turbulent granular temperature in the riser with bottom solids feed inlet and the riser of the CFB, respectively. The granular temperature in the riser of the CFB is about 2 orders of magnitude higher than those in the riser with bottom solids feed inlet. Moreover, the granular temperature in the riser of CFB is much higher in the left zone of the rector. This is because of low solids concentration in this region with gas by-passing. Thus solids particles velocity is more fluctuate in this region. The granular temperature in the riser with bottom solids feeding is almost uniform in the core region with high peak near the wall. This high peak due to a small eddy was occurred in this region. Figure 44 shows the comparison of the granular temperature obtained from this simulation with the literature review (Kashyap *et al.*, 2008). The results obtained from this study show the same order of the magnitude with the published data. Hence, our calculations have credibility.

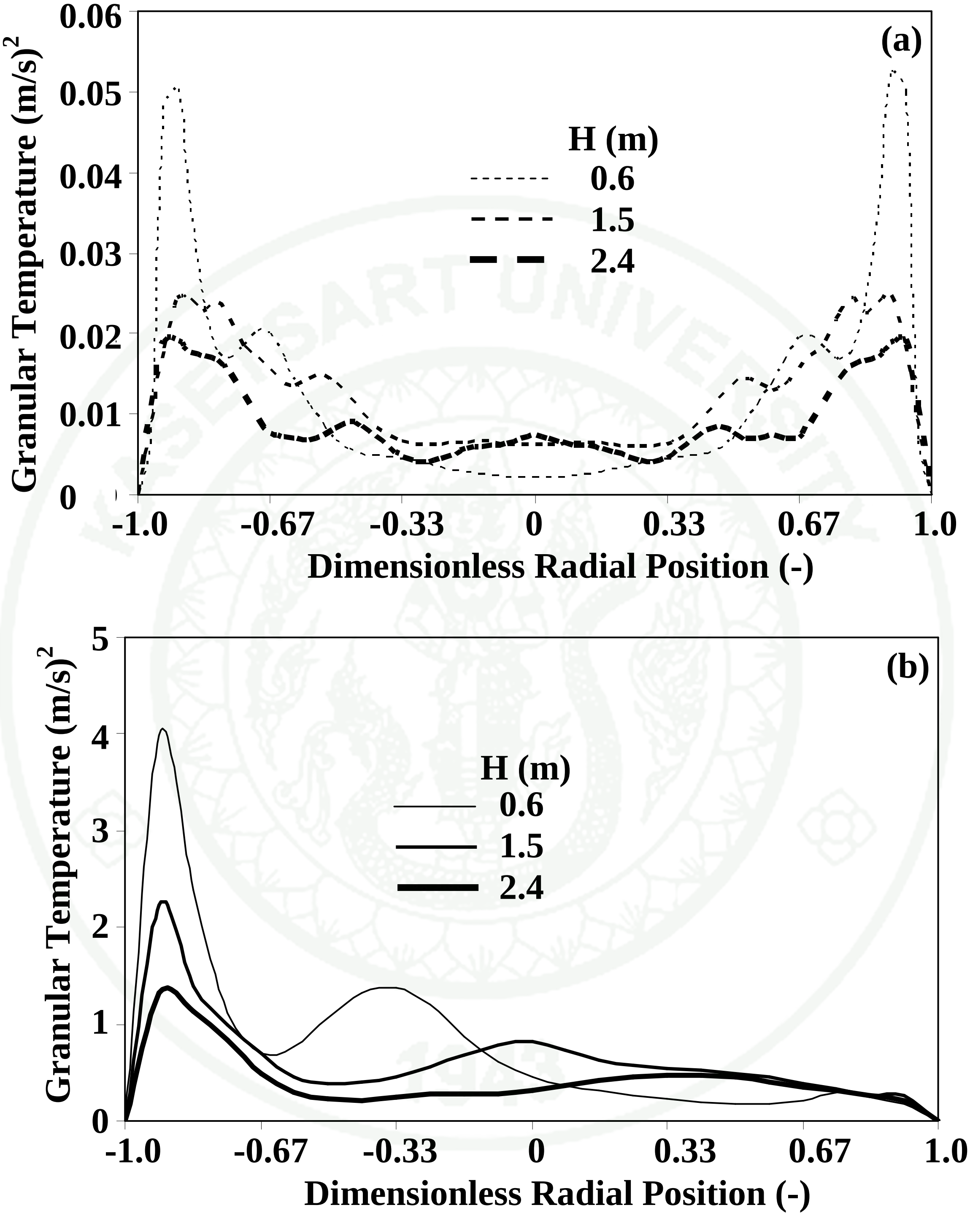

Figure 43 Radial distribution of the granular temperature (a) in the riser with bottom solids feed inlet (b) in the riser of the CFB.

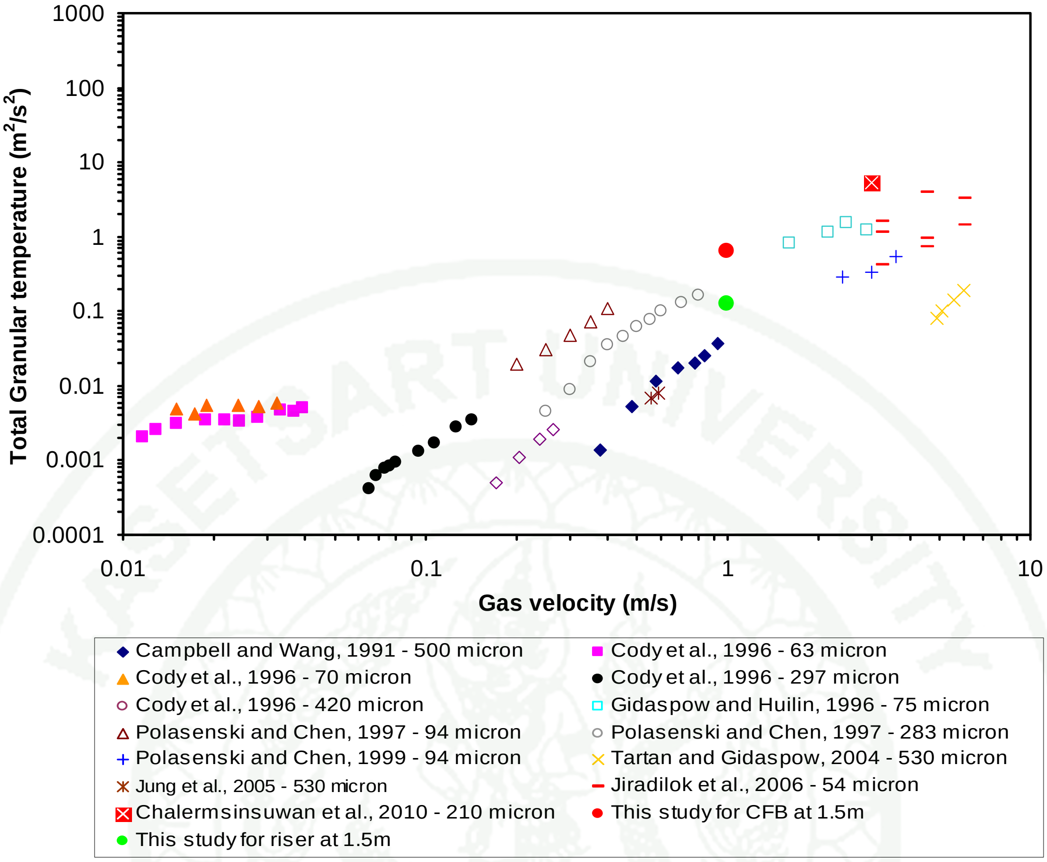

Figure 44 Comparison of the total granular temperatures obtained from this study with the literature values.

2.1.4 Effect of hydrodynamics behavior on the CO_2 removal performance

Figure 45 shows the contour of CO_2 mass fraction (Figure 45 (a)) and H_2O mass fraction (Figure 45 (b)) in the riser with bottom solids feed inlet and in the CFB loop. The profiles of CO_2 and H_2O mass fraction show the same pattern but different order of magnitude. The CO_2 and H_2O mass fractions in the riser with bottom solids feed inlet decrease along the reactor height. In the riser of the CFB, the mass fractions of CO_2 and H_2O are high in the by-passing region. This by-passing causes low conversion of CO_2 removal. According to a symmetry of solids volume fraction in the riser with bottom solids feed inlet, the radial profile of the CO_2 mass fraction in this riser is much more symmetry than that in the riser of the CFB as shown in Figure 46. At 0.6 and 1.5m, the CO_2 mass fraction in the center region of the riser with bottom solids feed inlet is higher than that in the riser of CFB because of high solids volume fraction in the bottom region of the riser of the CFB leading to high reaction rate. The CO_2 mass fraction near the wall zone of the riser with bottom solids feed inlet is low due to high gas back mixing because of eddy effect. The CO_2 mass fraction in the left region of the riser of the CFB is high due to gas by-passing in this region.

Figure 47 shows the axial distributions of the CO_2 mass fraction and CO_2 removal. The CO_2 mass fraction profile dramatically decreases in first 0.5 m both in riser of the CFB and the riser with bottom solids feed inlet. After that the CO_2 mass fraction slowly decreases due to low reaction rate. The profile of CO_2 mass fraction in the riser of the CFB shows a peak of low mass fraction at 0.3 m because most of CO_2 was absorbed due to very high solids volume fraction in this region. Conversely, the profile of percent CO_2 removal increases along the axial direction. In the bottom section of the reactor, the percent removal in the riser with bottom solids feed inlet is lower than those in the riser of the CFB. After 1 m height, the percent removal in the riser with bottom solids feed inlet is higher than that in the riser of the CFB because of no gas by-passing.

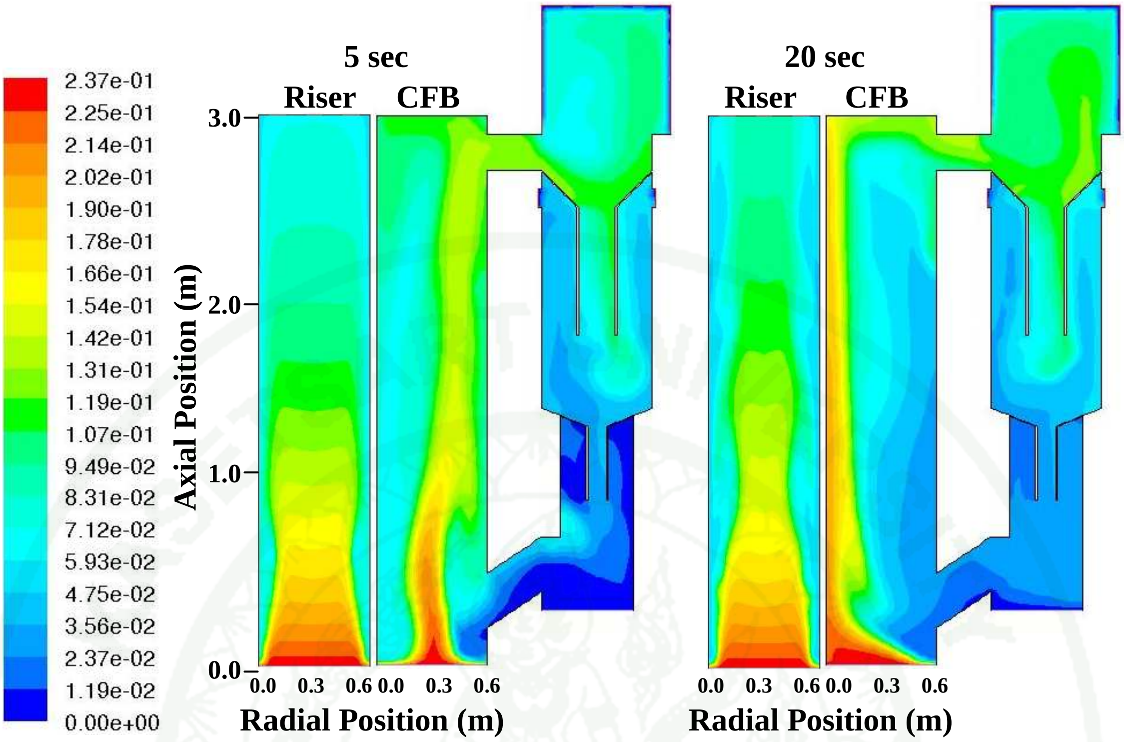

(a)

Figure 45 Contours of species mass fraction at 5 and 20 sec. (a) CO_2 mass fraction and (b) H_2O mass fraction, in the riser with bottom solids feed inlet and in the CFB.

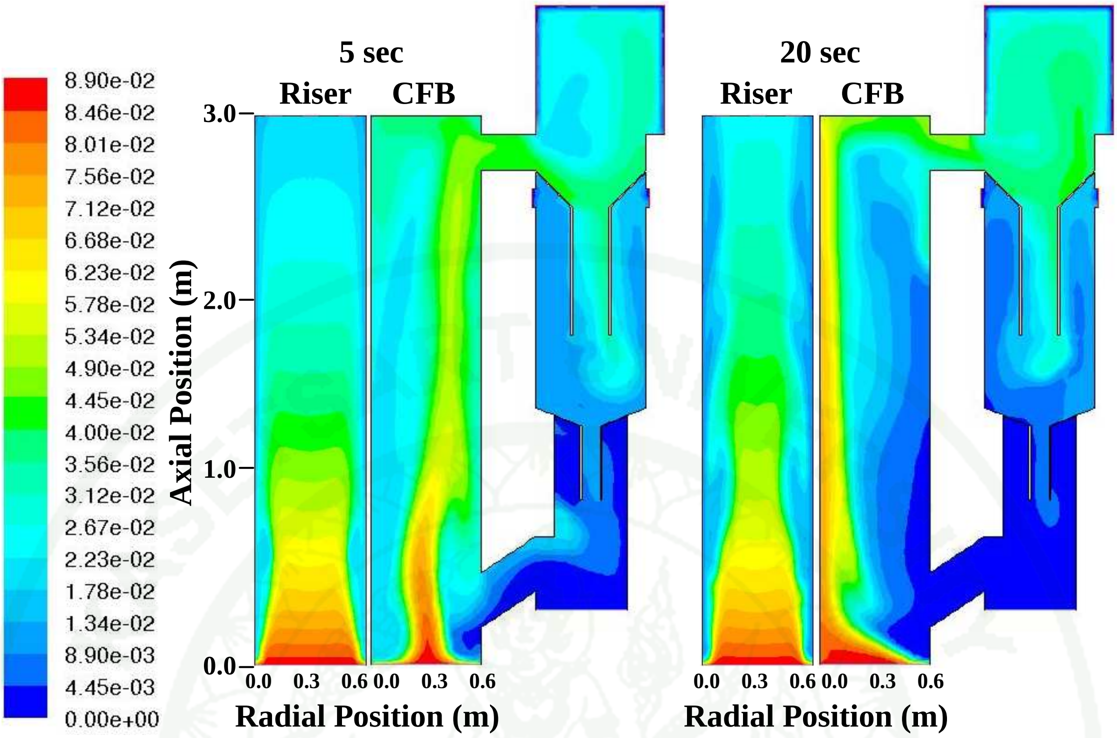

(b)

Figure 45 (Continued).

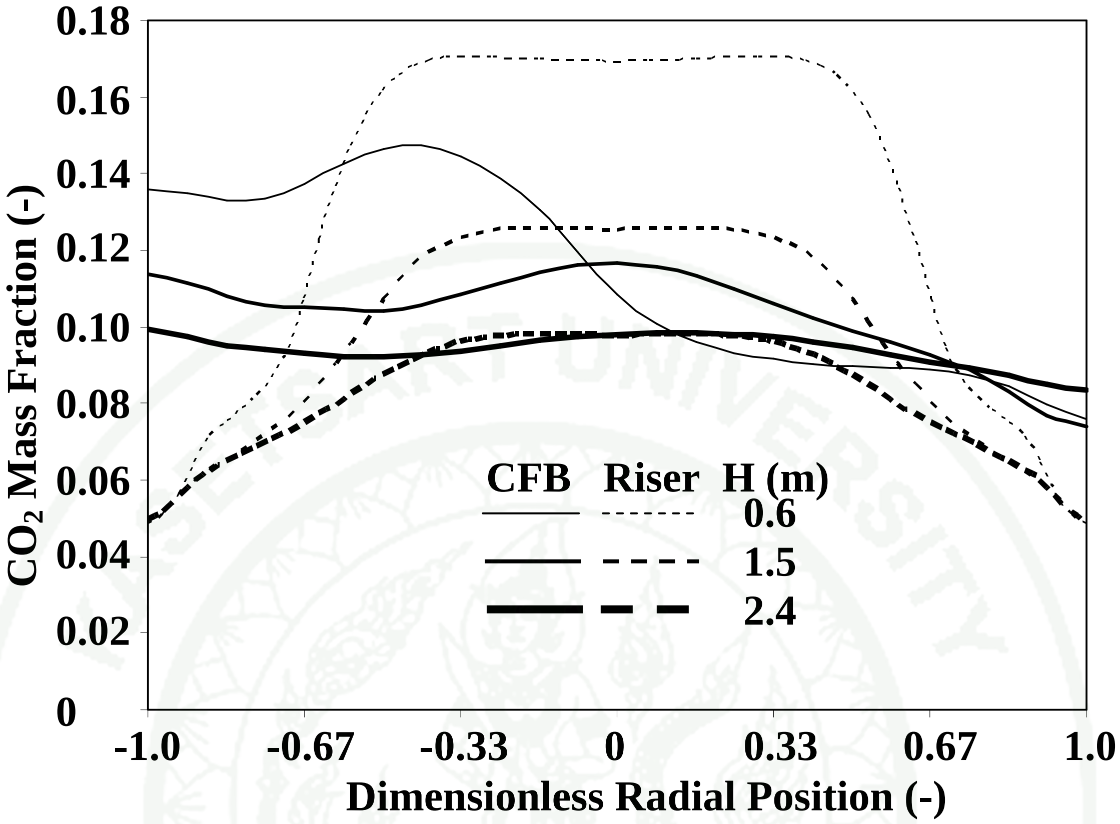

Figure 46 CO_2 mass fraction distribution in the radial direction in the riser with bottom solids feed inlet and in the riser of the CFB systems at various heights.

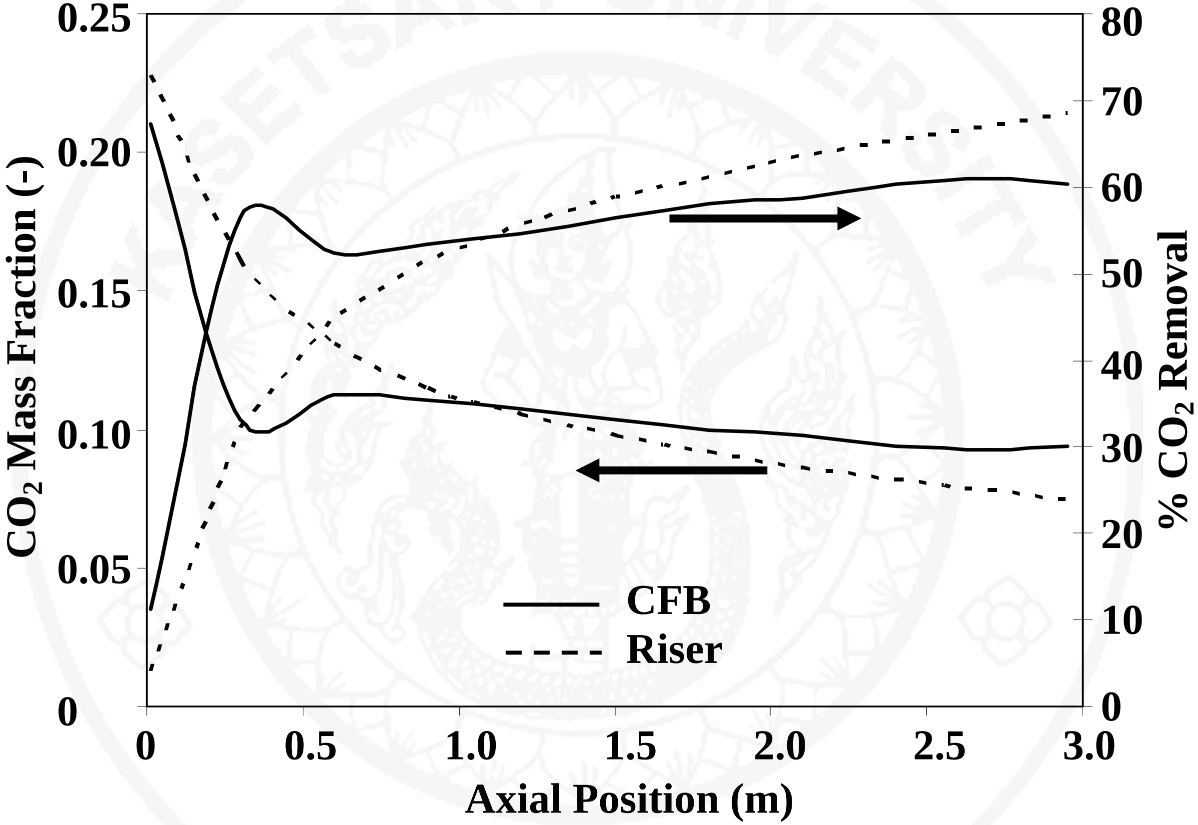

Figure 47 CO$_2$ mass fraction and percent removal of CO$_2$ profiles in the riser with bottom solids feed inlet and in the riser of the CFB.

2.1.5 Effect of the reactor height

The effect of the reactor height was further studied in the riser with bottom solids feed inlet. Figure 48 shows the CO_2 mass fraction and percent CO_2 removal in axial direction at various reactor heights. Most of CO_2 was absorbed in the first meter height. The outlet percent removals of CO_2 are 77, 81 and 83 of the rector height of 3, 4 and 5 m, respectively. In order to get 95% CO_2 removal, the reactor should be very tall. Thus the new reactor design is needed to achieve 95% CO_2 removal with short reactor. Figure 49 shows the effect of reactor height on the solids volume fraction distribution in the axial direction. It can be seen that the reactor exhibits less effect on solids volume fraction profile in the system.

Although reactor height shows less effect on the solids volume fraction distribution in the riser but high amount of solids particles inventory in a high riser, which directly produces high pressure drop in the system. The approximated pressure drop in the system can be calculated from the manometer formula (Gidaspow, 1994). This formula is the simplification form of the mixture momentum balance with the assumptions of fully developed flow, no wall shear and solid stress. Thus the pressure drop is balanced by the weight of the bed:

$$-\frac{dP}{dy} = g(\rho_g \alpha_g + \rho_s \alpha_s) \tag{90}$$

Since $\rho_s \gg \rho_g$ then equation above becomes

$$-\frac{dP}{dy} = g\rho_s \alpha_s \tag{91}$$

A comparison of pressure drop obtained from this simulation and calculated from Eq. (91) is shown in Figure 50. The simulated pressure drops are closed to the calculated pressure drop. As expected, increasing the reactor height is

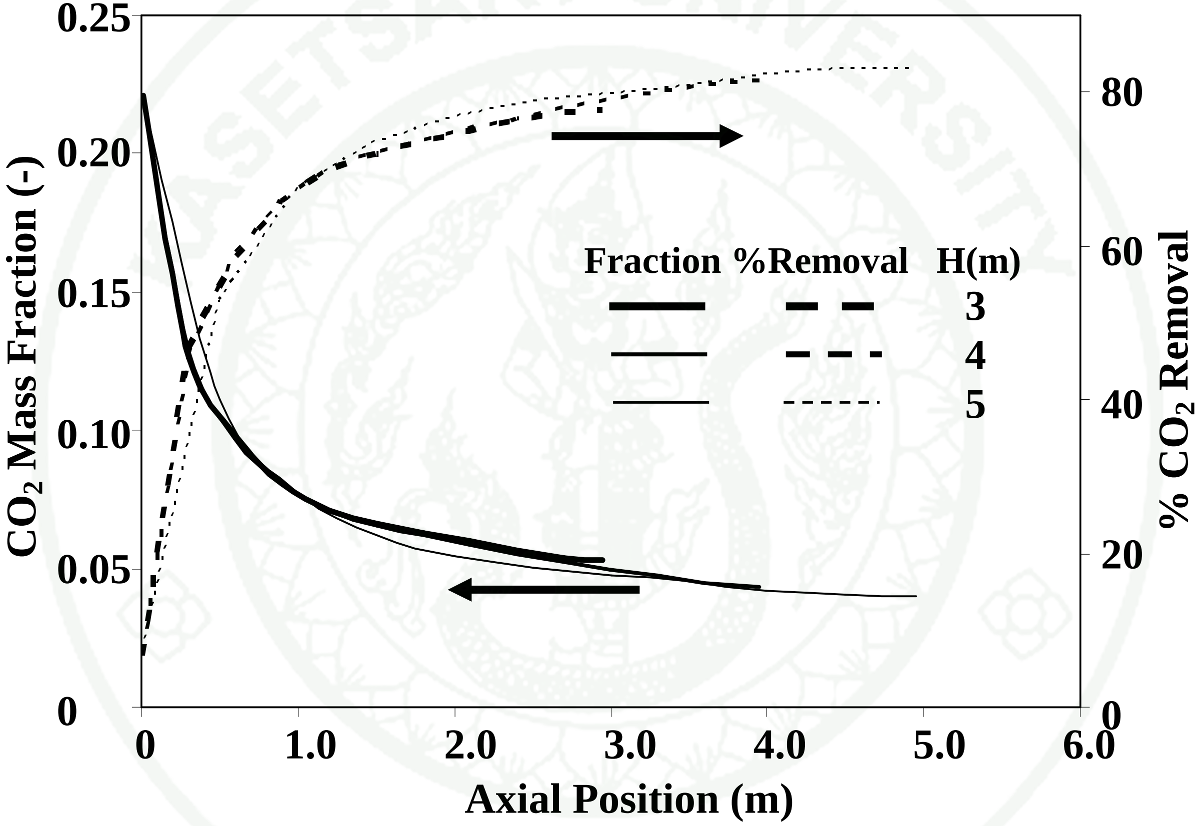

Figure 48 Effect of reactor height on the CO$_2$ mass fraction and percent removal of CO$_2$ in the riser with bottom solids feed inlet.

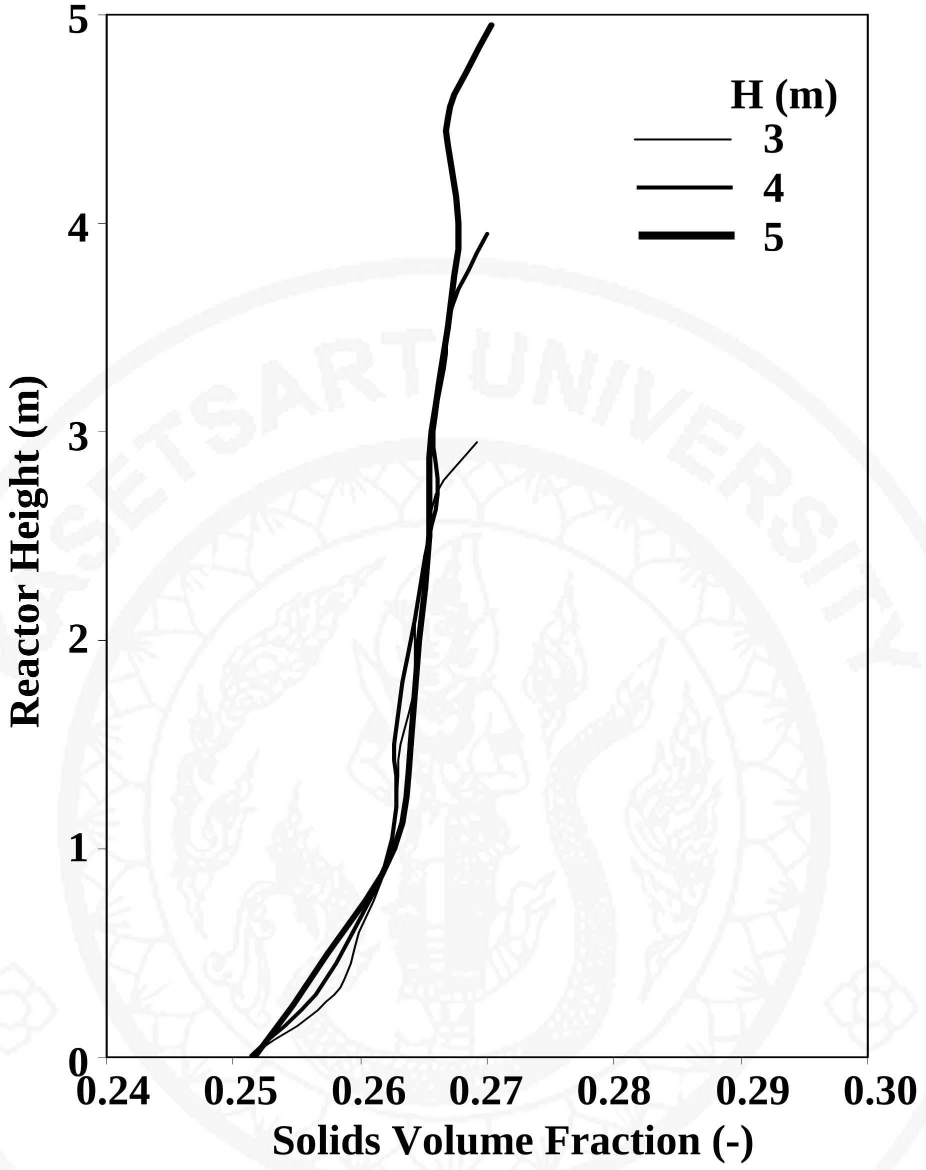

Figure 49 Effect of reactor height on the axial distribution of the solids volume fraction in riser with bottom solids feed inlet.

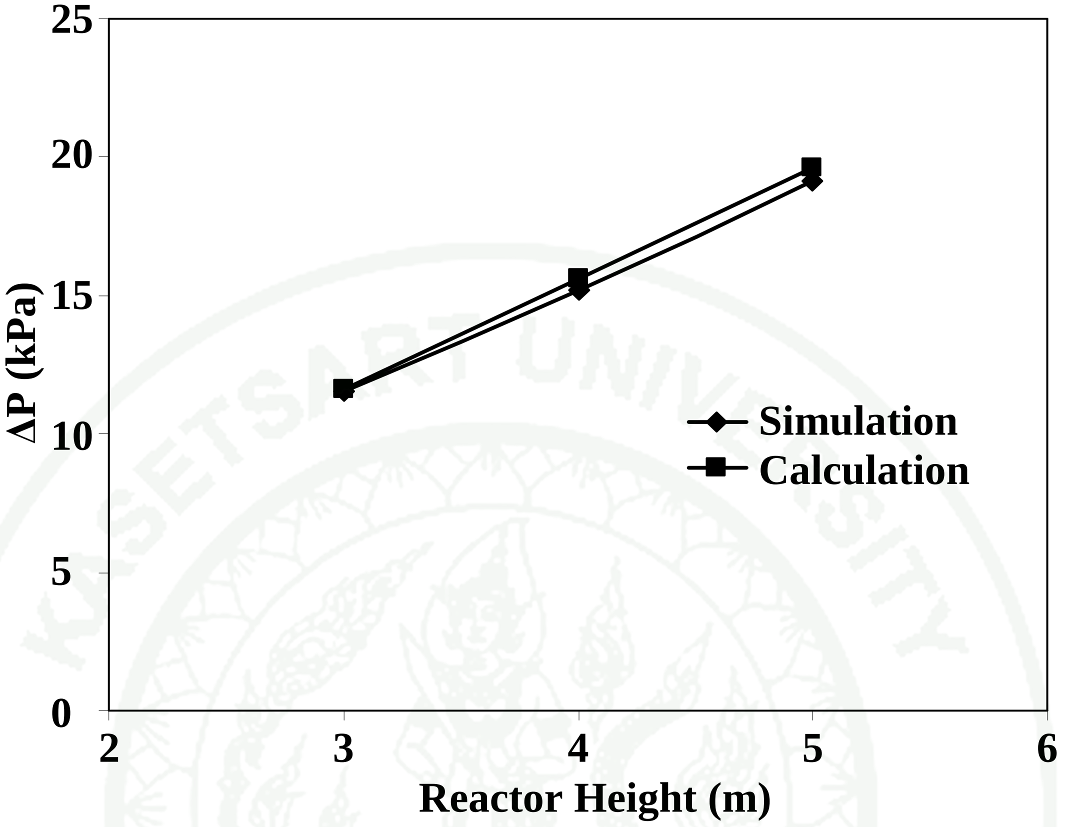

Figure 50 Effect of reactor height on the pressure drop across a riser with bottom solids feed inlet.

significantly increased pressure drop due to high solids particle inventory in the system.

2.2 Comparison of hydrodynamics behavior and CO_2 capture performance between a downer and a riser reactors

2.2.1 Solids volume fraction distribution

Figures 51 and 52 show the contour plot of solids volume fraction distribution in the downer and the riser reactors, respectively at various operating time. The solids volume fraction in the downer reactor exhibits much more uniform throughout the reactor as compared with the riser reactor. In the downer reactor, the solids volume fraction distribution is uniform in the center region with a small dense peak near the wall region. According to both gas and solids particle flow with the same direction as the gravity in the downer, leads to less axial mixing. Thus the flow in the downer reached the steady state condition within a short operating time. In the riser reactor, the solids volume fraction distribution is very non-uniform throughout the system. It can also be observed the large particle cluster formation near the wall region. This large particle cluster resists the up flow of both gas and solids particles.

The axial distributions of the cross-sectional averaged solids volume fraction in the downer and the riser reactors were shown in Figure 53. The solids volume fractions both in the downer and the riser reactors rapidly decrease and reach a constant value within a short distance from the inlet. After that the solids volume fraction profiles remain constant until exit from the reactor. In addition, the solids volume fraction in the downer is lower than that in the riser.

Figure 54 shows the lateral distribution of solids volume fraction in the downer and the riser reactors at various axial positions. It was found that the radial profiles of the solids volume fraction both in the downer and the riser show the same trends which an almost uniform in the center region and a high particle density peak near the wall region. Moreover, the high density peak in the riser is larger than that in the downer because of a large particle cluster formation near the wall region of the riser as shown in Figure 52.

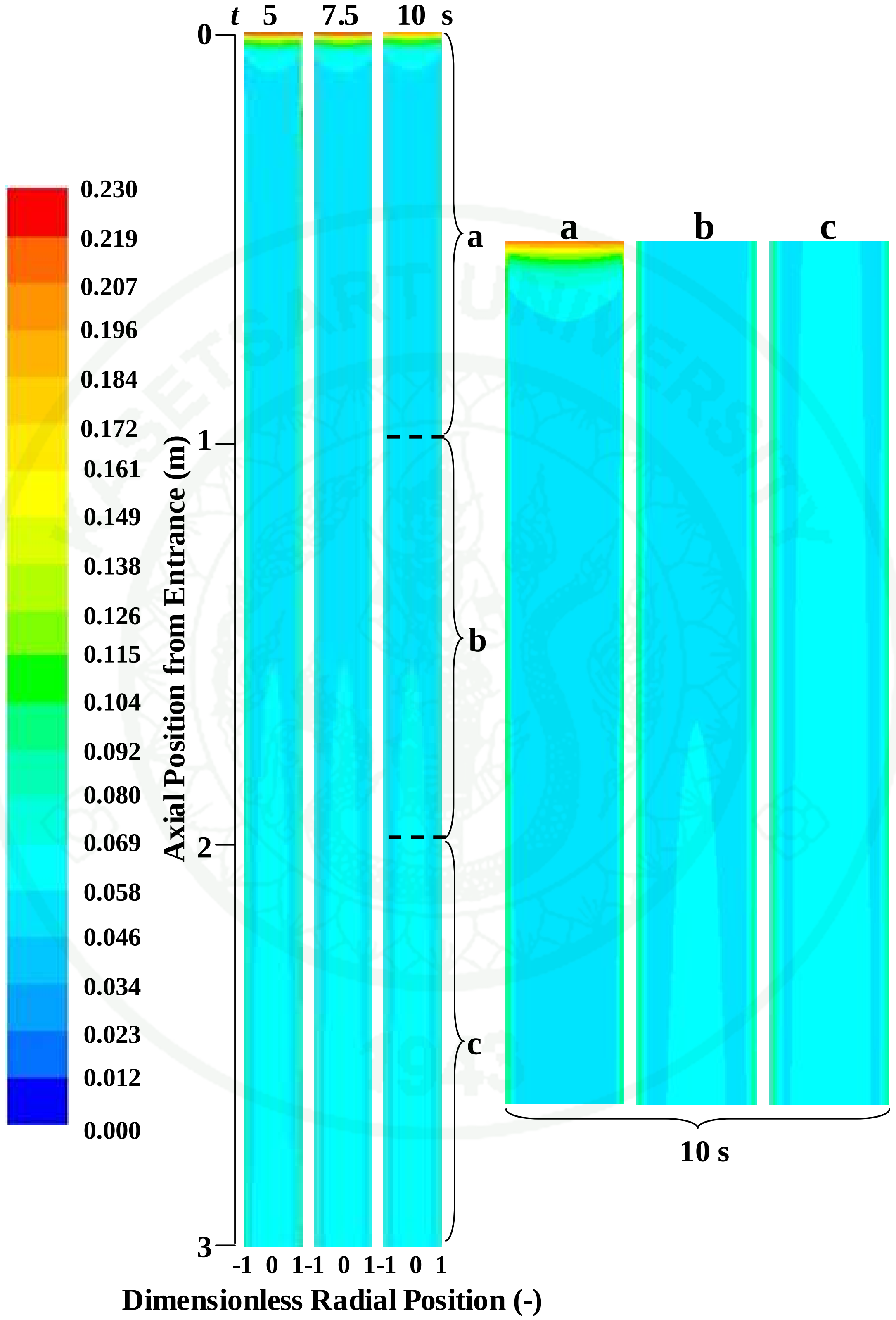

Figure 51 Contour of solids volume fraction in the downer reactor at the superficial gas velocity of 1.5 m/s and the solids circulation rate of 200 kg/m^{2}s.

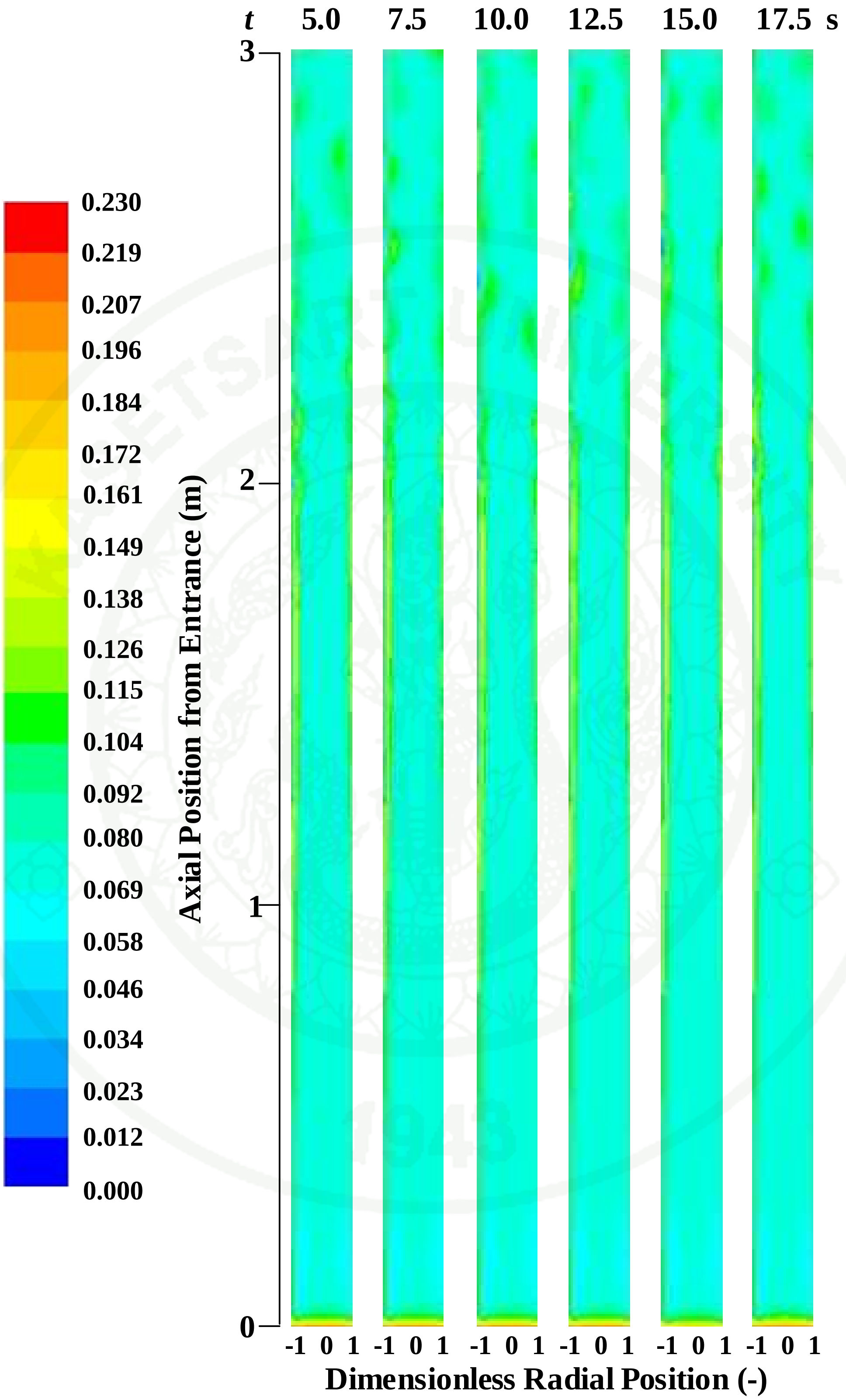

Figure 52 Contour of solids volume fraction in the riser reactor at the superficial gas velocity of 1.5 m/s and the solids circulation rate of 200 kg/m^2s.

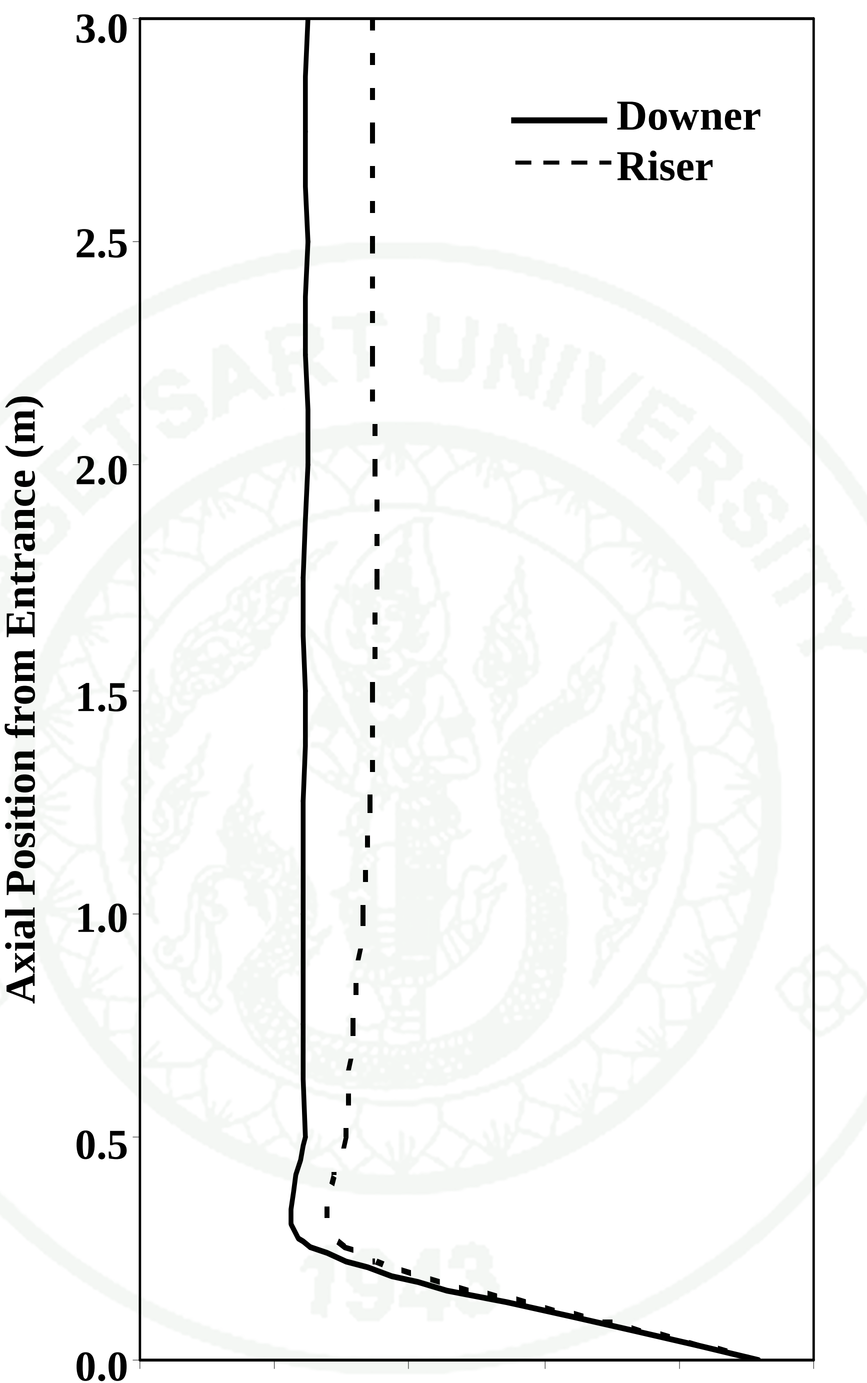

Figure 53 Axial distribution of the cross-sectional averaged CO_2 mass fraction in the downer and the riser reactors at the superficial gas velocity of 1.5 m/s and the solids circulation rate of 200 kg/m^{2}s.

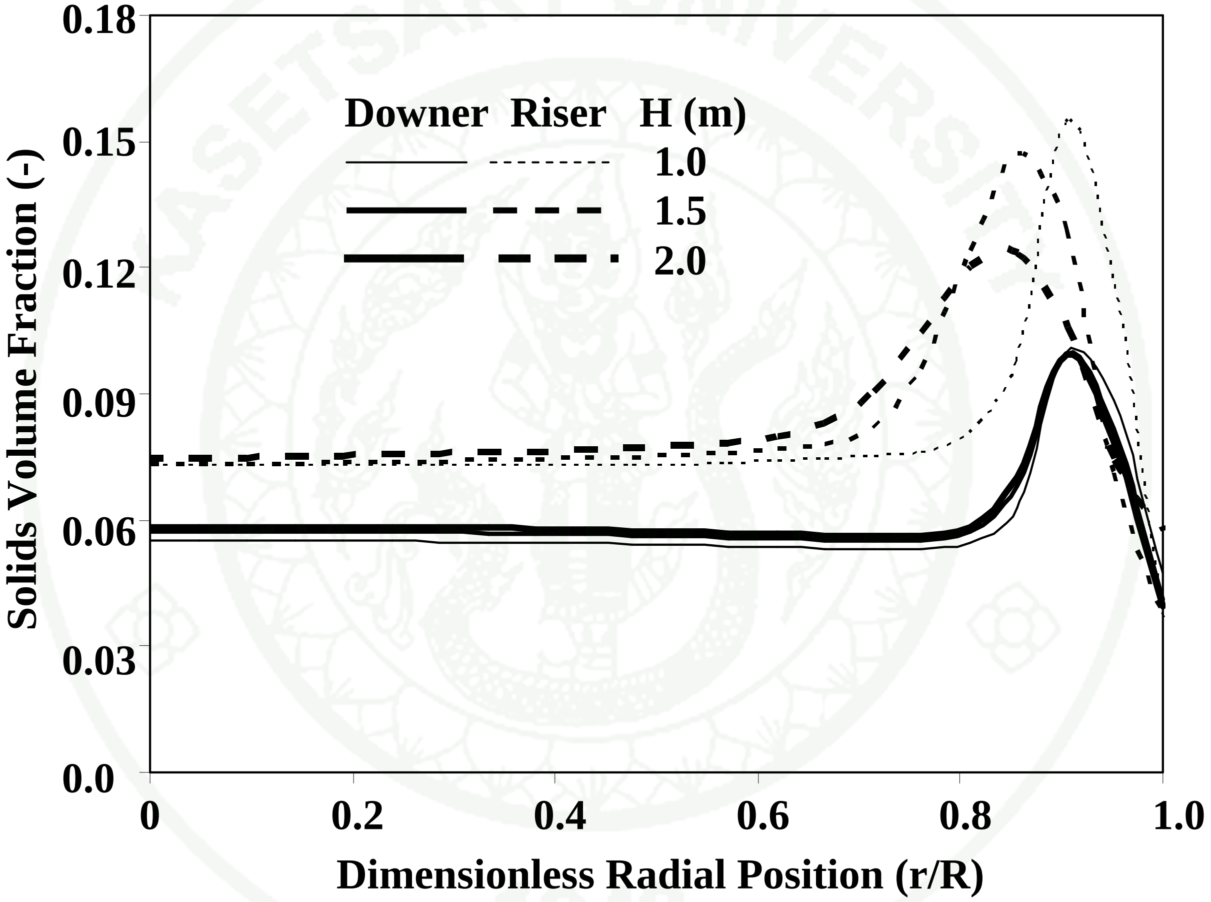

Figure 54 Radial distribution of the solids volume fraction in the downer and the riser reactors at the superficial gas velocity of 1.5 m/s and the solids circulation rate of 200 kg/m^{2}s.

2.2.2 Solids and gas velocity

Gas and solids velocity vector plots in the downer and the riser are shown in Figures 55 and 56, respectively. In the downer, both gas and solids velocity vectors are almost uniform in the inlet region. Gas and solids velocities further developed to form a constant velocity in the core region with a high velocity near the wall region in the middle and the outlet sections of the downer reactor. Near the inlet region of the riser, gas and solids particle velocities are also uniform in the system. In the upper section where the large particle cluster was formed, both gas and solids particles movements were deviated from the main flow as shown in Figure 56.

Figures 57 and 58 show the radial profiles of solids and gas velocities, respectively. In the downer reactor, gas and solids velocity profiles slowly increase from the center toward the wall and form a high velocity peak near the wall with consistency with Figure 55. In the riser, the radial profiles of gas and solids velocities show a parabolic profile which the maximum velocity at the center. The velocities tend to decrease near the wall region because the large particle cluster in this region resists the upward flow of gas and particles. Therefore, the parabolic velocity profiles of gas and particle phases can be obtained.

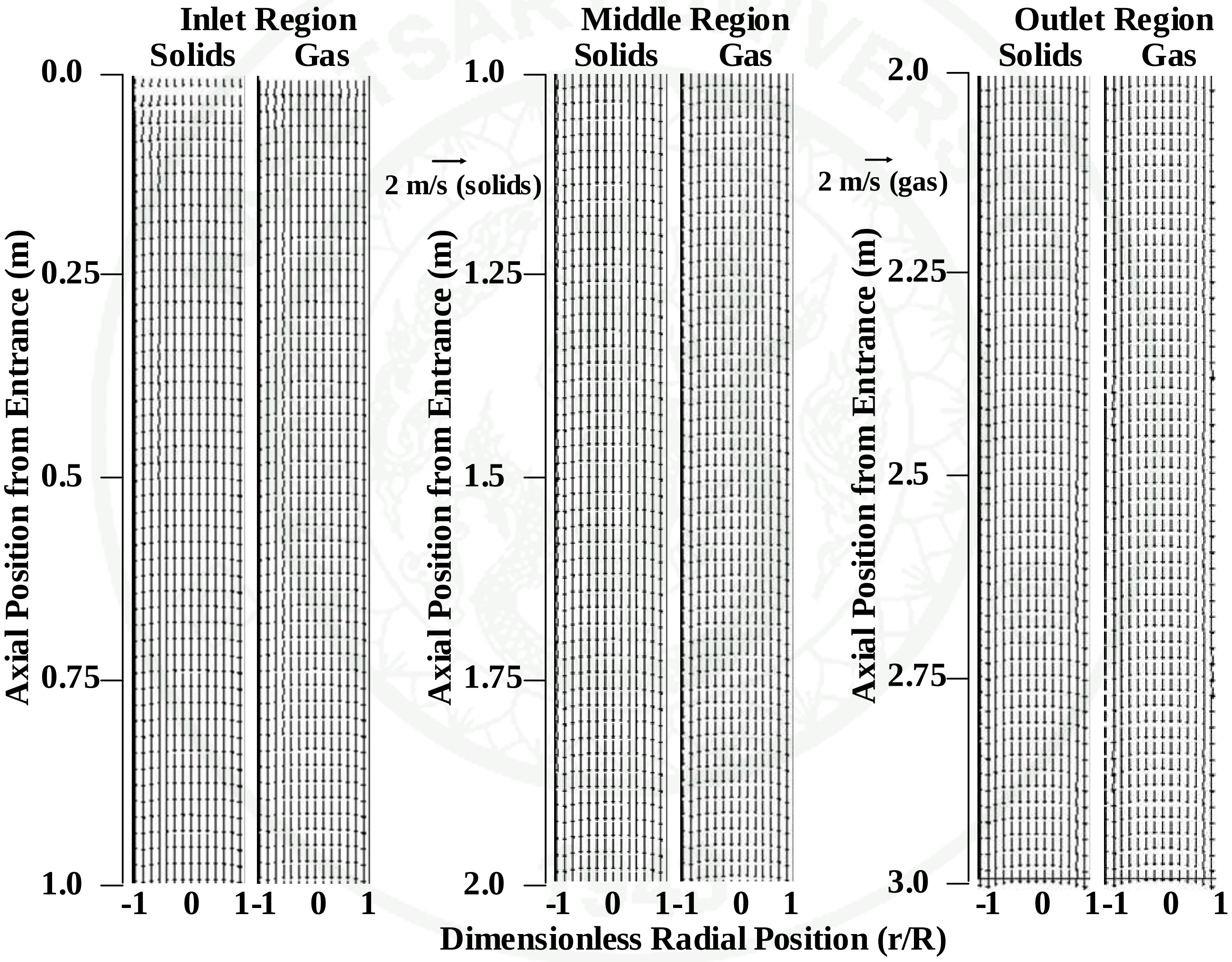

Figure 55 Gas and solids velocity vector plots in the downer reactor at 10 s, Ug = 1.5 m/s, and Gs = 200 kg/m^{2}s.

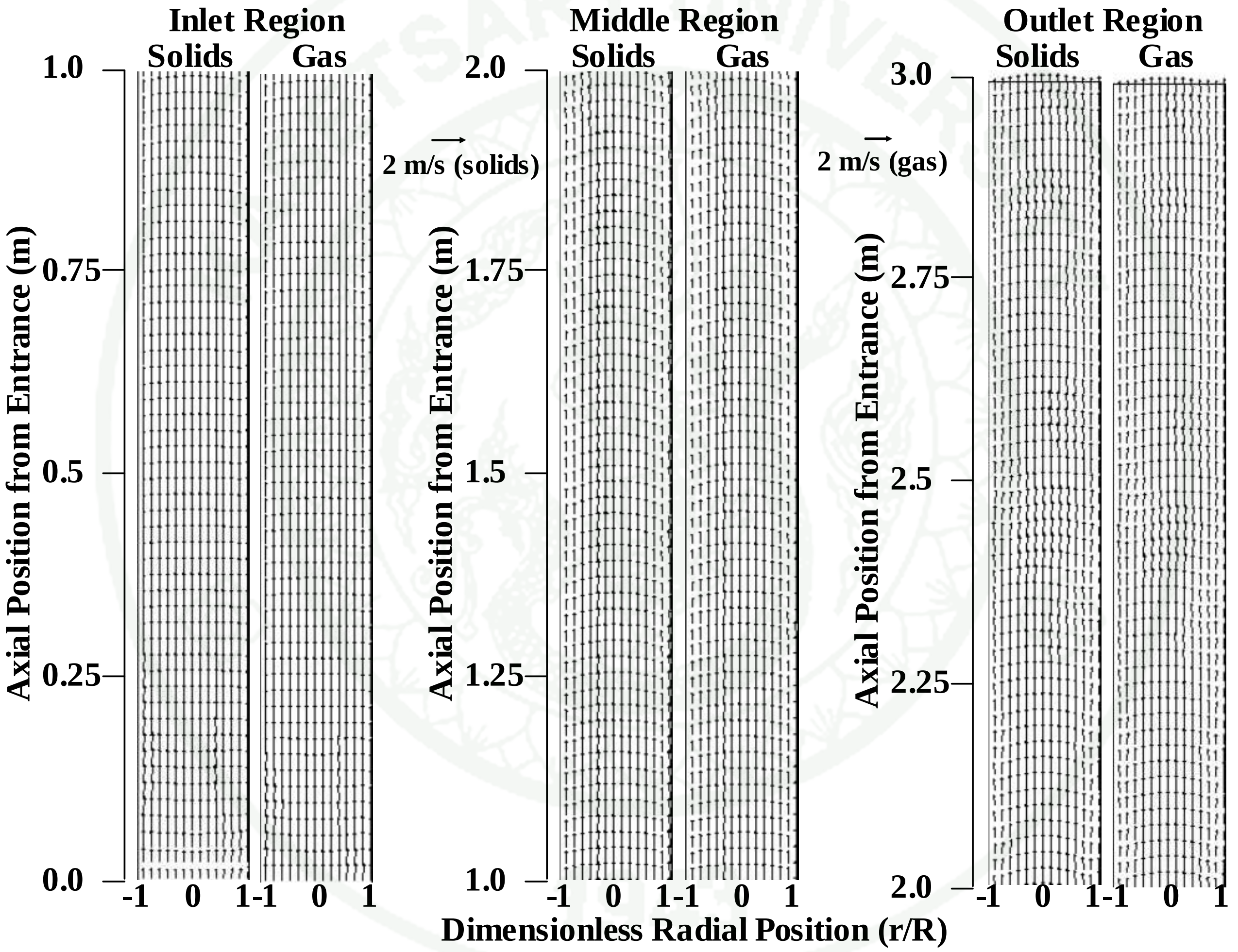

Figure 56 Gas and solids velocity vector plots in the riser reactor at 17 s, Ug = 1.5 m/s, and Gs = 200 kg/m^{2}s.

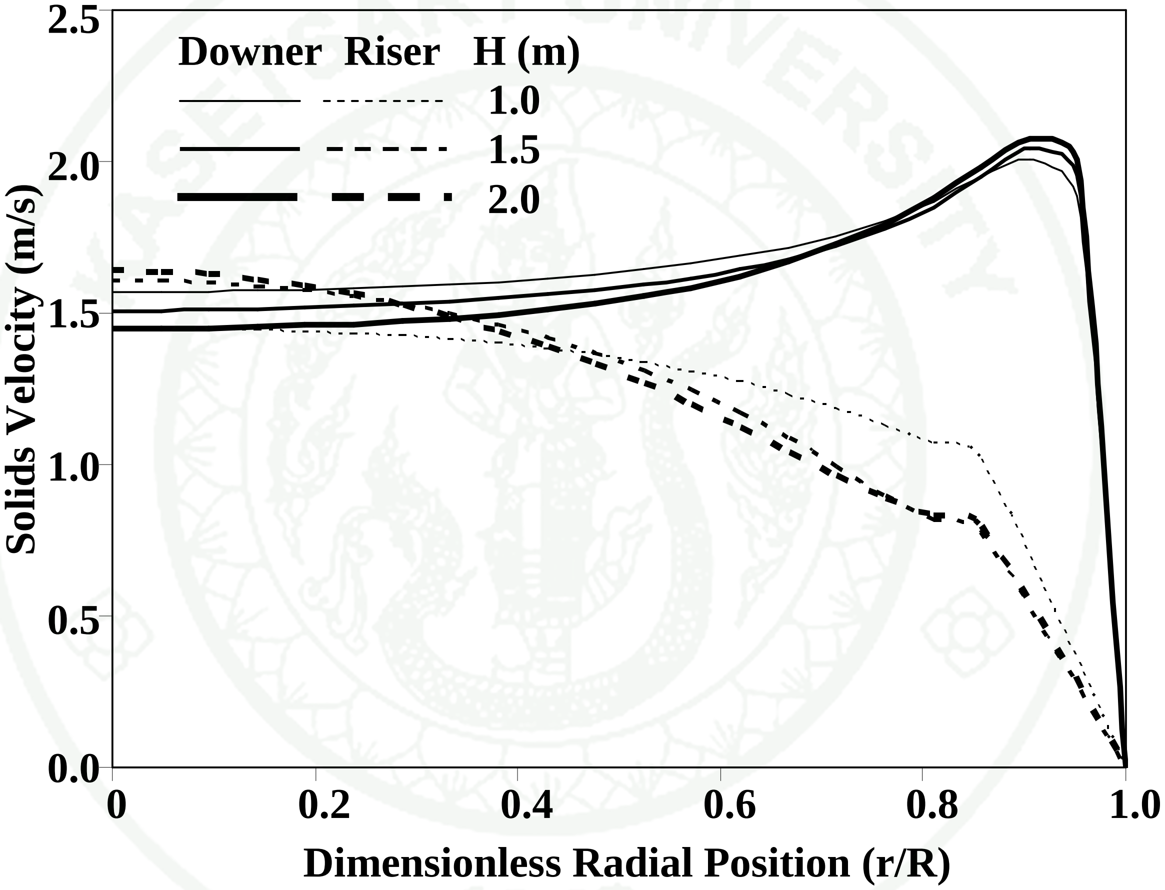

Figure 57 Radial distribution of the solids velocity in the downer and the riser reactors at the superficial gas velocity of 1.5 m/s and the solids circulation rate of 200 kg/m^{2}s.

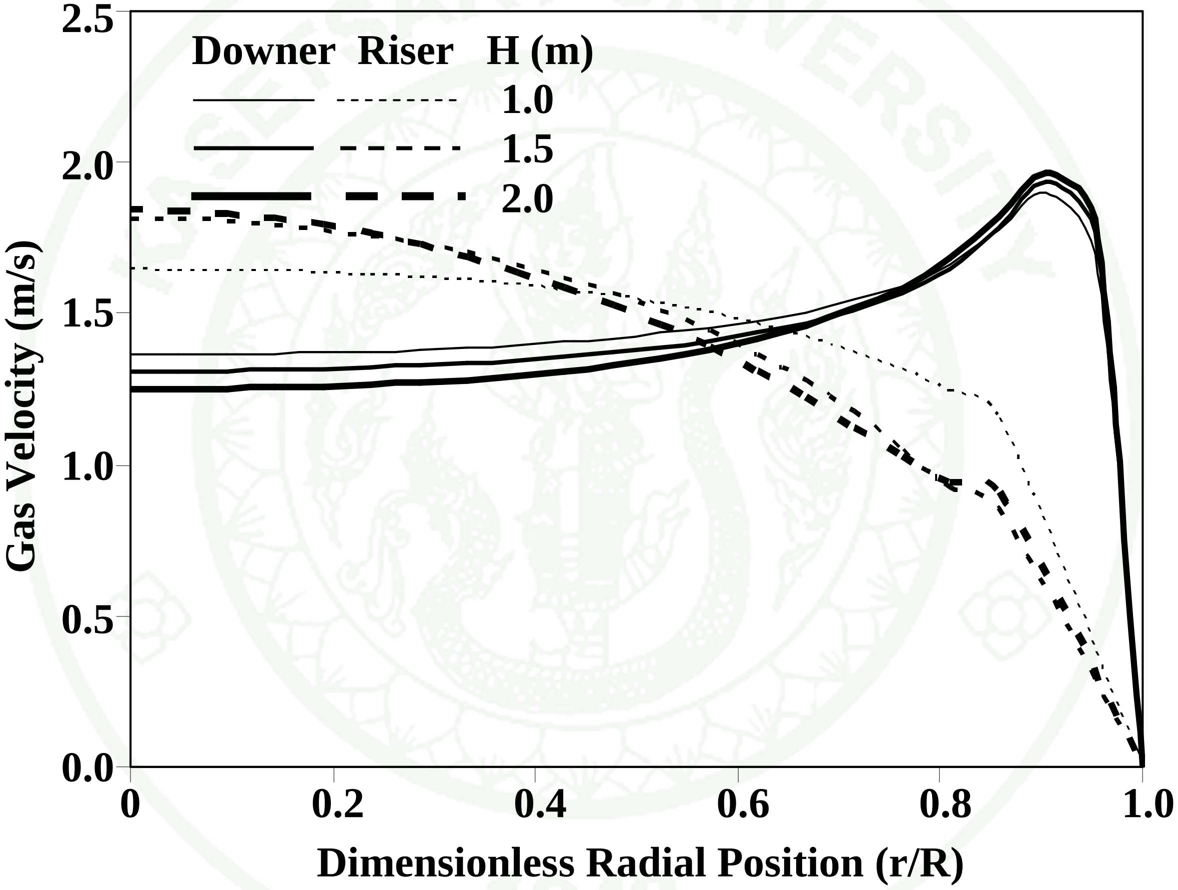

Figure 58 Radial distribution of the gas velocity in the downer and the riser reactors at the superficial gas velocity of 1.5 m/s and the solids circulation rate of 200 kg/m^2.

2.2.3 Comparison of CO_2 removal performance in the downer and the riser reactors

Figures 59 and 60 show the contours of CO_2 mass fraction distribution in the downer and the riser reactors, respectively. In the downer, the CO_2 mass fraction decreases along the reactor height. According to low solids volume fraction in the downer, thus the mass fraction profile seem be to strongly depends on the velocity distribution. As can be seen in Figure 59, near the inlet section, the mass fraction profile shows almost uniform in radial direction because the velocities are uniform in this zone (see Figures 55). Further down the reactor, the CO_2 mass fraction is high near the wall region because of high gas and solids velocities. On the other hand, the CO_2 mass fraction distribution in the riser depends on solids mass fraction and velocity distribution in the system. Near the inlet of the riser, the CO_2 mass fraction distribution is almost uniform because of a uniform solids fraction in this region as shown in Figure 52. The mass fraction profile further develops to form a parabolic distribution with a higher CO_2 mass fraction in the center region because of high gas velocity and a low CO_2 mass fraction near the wall because of high solids fraction and low gas and solids velocities.

Figure 61 show the lateral distribution of CO_2 mass fraction at various axial positions in the downer and the riser reactors. It was found that the radial distribution in the downer reactor is more uniform than that the riser reactor at any axial positions. Near the wall region of the downer, the influent of high reaction rate due to high solids volume fraction in this region on the CO_2 mass fraction was reduced by the low residence time because of high gas and solids velocities. These two effects lead to a uniform CO_2 mass fraction near the wall region. In the riser, the mass fraction near the inlet is uniform in the radial direction. At 1.5 m, the radial profile of CO_2 mass fraction shows less uniform corresponding to the non uniformity of solids fraction and gas velocity distribution in this region. Low CO_2 mass fraction near the wall region is the results from high solids fraction with low gas and solids velocities. At 2.5 m, the mass fraction profile becomes a more uniform in the radial direction.

Figure 62 shows the axial profile of the cross-sectional averaged CO_2 mass fraction and % CO_2 removal. The axial profile of CO_2 mass fraction in the downer and the riser shows the same trend, which the mass fraction dramatically decreases near the inlet section because of high reaction rate. Thereafter, the mass fraction profile slowly decreases until exit the reactor. In contrast, the % CO_2 removal rapidly increases in the inlet section and slowly increases further the reactor length. According to high solids fraction in the riser, the CO_2 removal efficiency in the riser is higher than that in the downer.

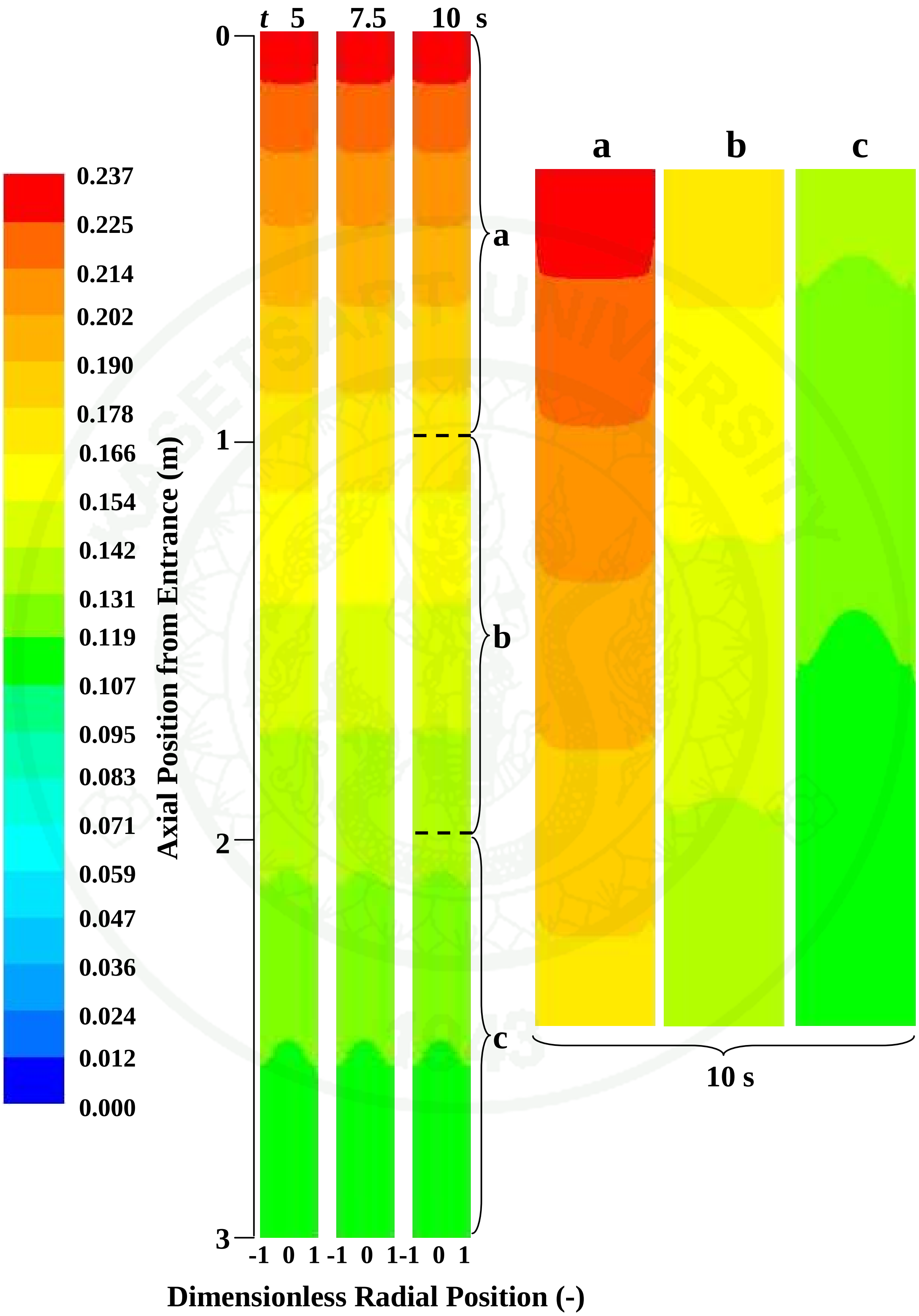

Figure 59 Contour of CO_2 mass fraction in the downer reactor at the superficial gas velocity of 1.5 m/s and the solids circulation rate of 200 kg/m^2s.

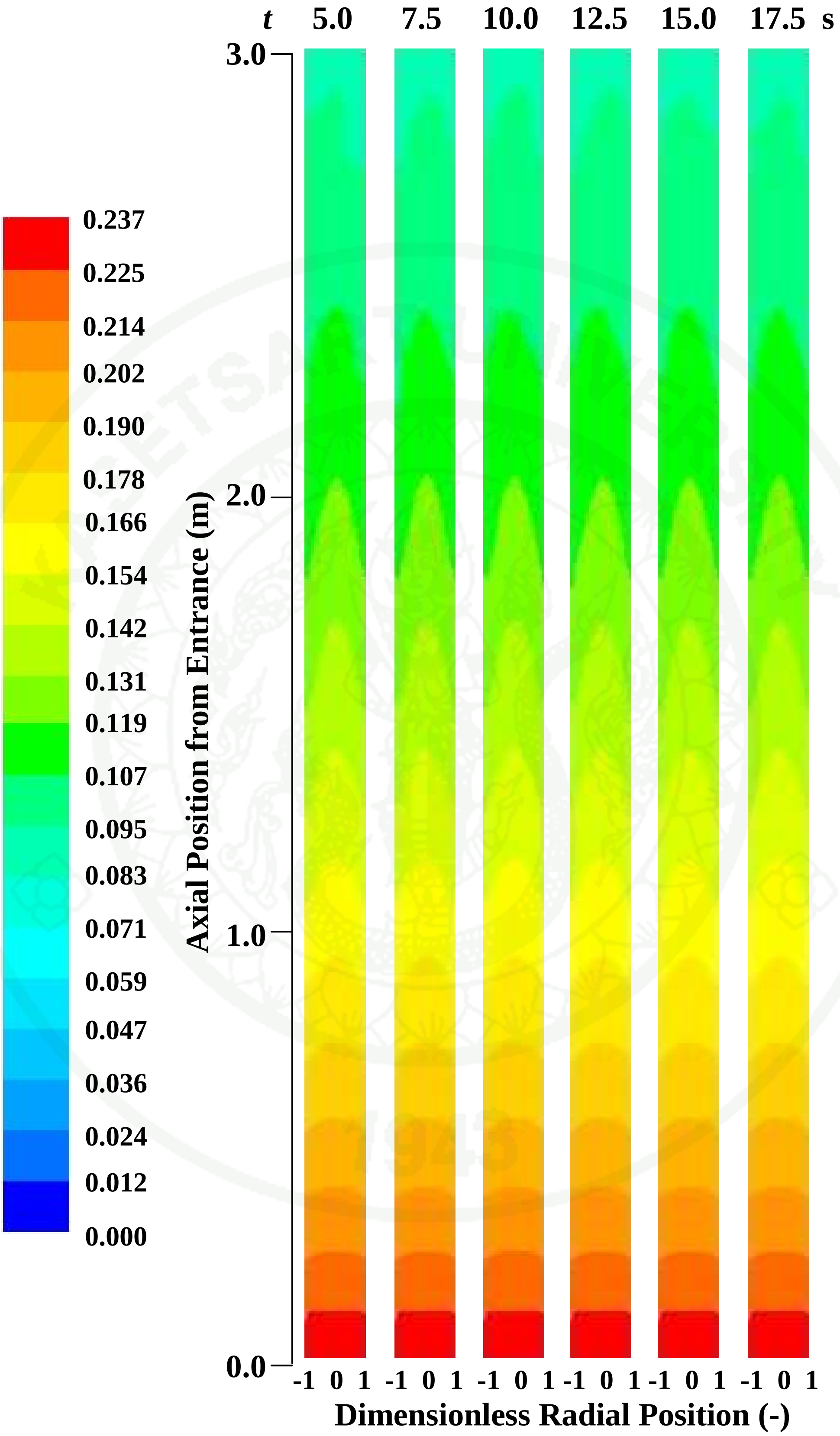

Figure 60 Contour of CO_2 mass fraction in the riser reactor at the superficial gas velocity of 1.5 m/s and the solids circulation rate of 200 kg/m^2s.

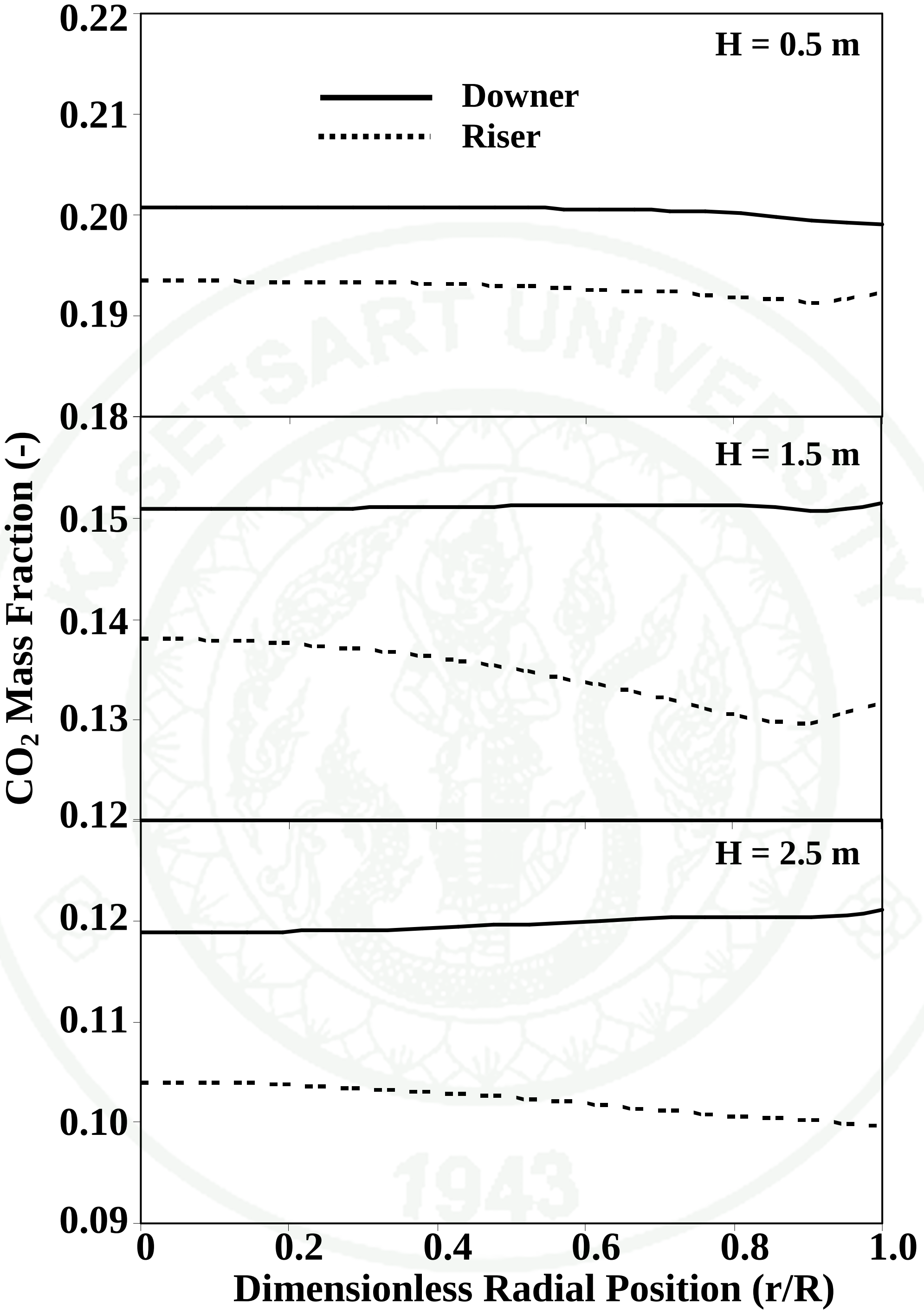

Figure 61 Radial distribution of the CO_2 mass fraction in the downer and the riser reactors at the superficial gas velocity of 1.5 m/s and the solids circulation rate of 200 kg/m^{2}s.

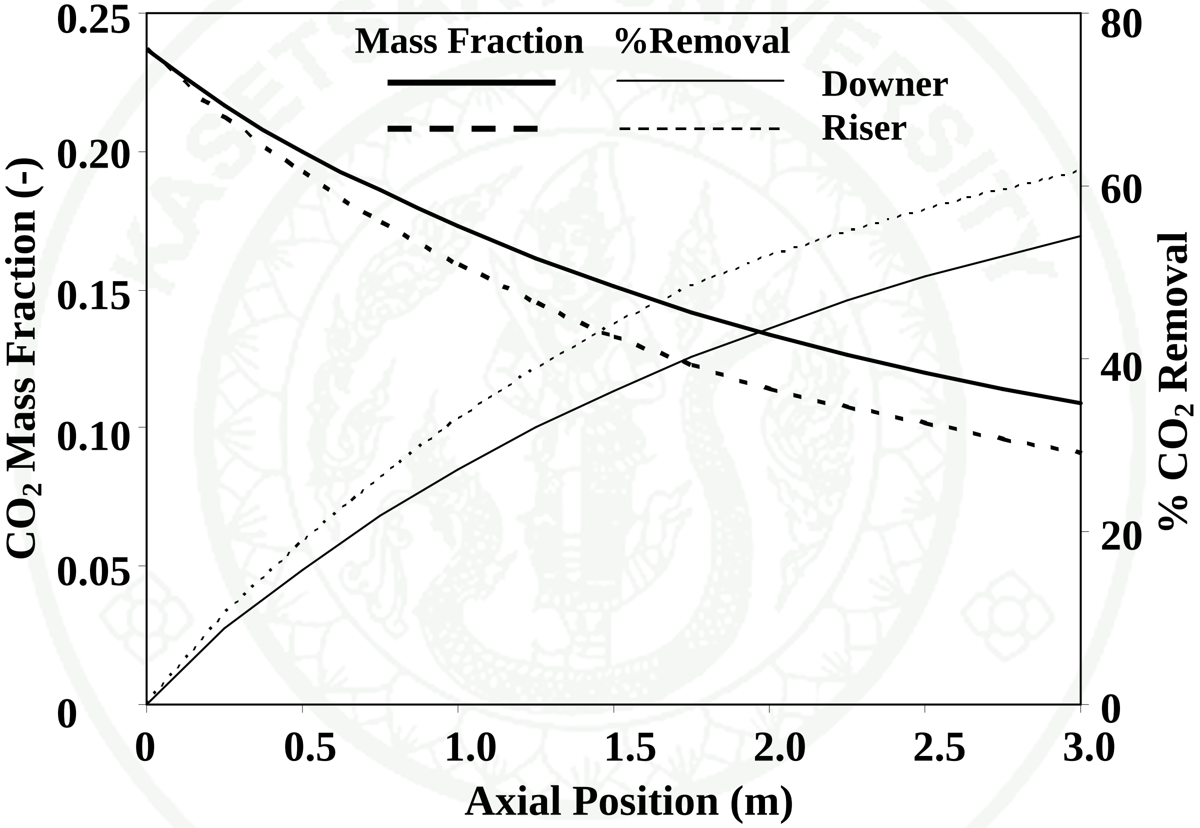

Figure 62 Axial distributions of the CO$_2$ mass fraction and the percent removal of CO$_2$ in the downer and the rise at the superficial gas velocity of 1.5 m/s and the solids circulation rate of 200 kg/m^{2}s.

2.2.4 Effect of operating conditions on the CO_2 removal performance in the downer and the riser reactors

Figure 63 shows the effect of superficial gas velocity on the radial profile of the solids volume fraction at 1.5 m in the downer and the riser. It was found that the radial profiles of both in the downer and in the riser show an almost uniform in the center region with a high density peak near the wall region. Increasing the superficial gas velocity reduces this peak height with a narrower peak distribution. A high density peak in the riser is larger than that in the downer. According to a more uniform of solids volume fraction in the downer, the radial distribution of CO_2 mass fraction in the downer is more uniform than that in the riser as shown in Figure 64. A high density peak near the wall of the riser leads to low CO_2 mass fraction in that region.

The axial profiles of the solids volume fraction at various superficial gas velocities are shown in Figure 65. The axial profiles of both in the downer and the riser show the same trends with rapidly decreases near the inlet region and approach a constant further the column. Increasing superficial gas velocity significantly decreases the solids volume fraction both in the downer and the riser. At a given superficial gas velocity the solids volume fraction in the riser is higher than that in the downer. Figure 66 shows the effect of superficial gas velocity on the axial distribution of the CO_2 mass fraction and % CO_2 removal. The axial profiles both in the riser and in the downer show the same trends which the CO_2 mass fraction significantly decreases near the inlet section due to high solids fraction. After that, the CO_2 mass fraction slowly decreases due to low reaction rate in this region. At low superficial gas velocity, the CO_2 mass fraction is very low because of high solids volume fraction and high gas residence time in the system. Conversely, the percent of CO_2 removal sharply increases near the inlet section and gradually increases thereafter. At any given superficial gas velocity, the CO_2 mass fraction in the riser is lower than that in the riser due to high solids fraction in the system.

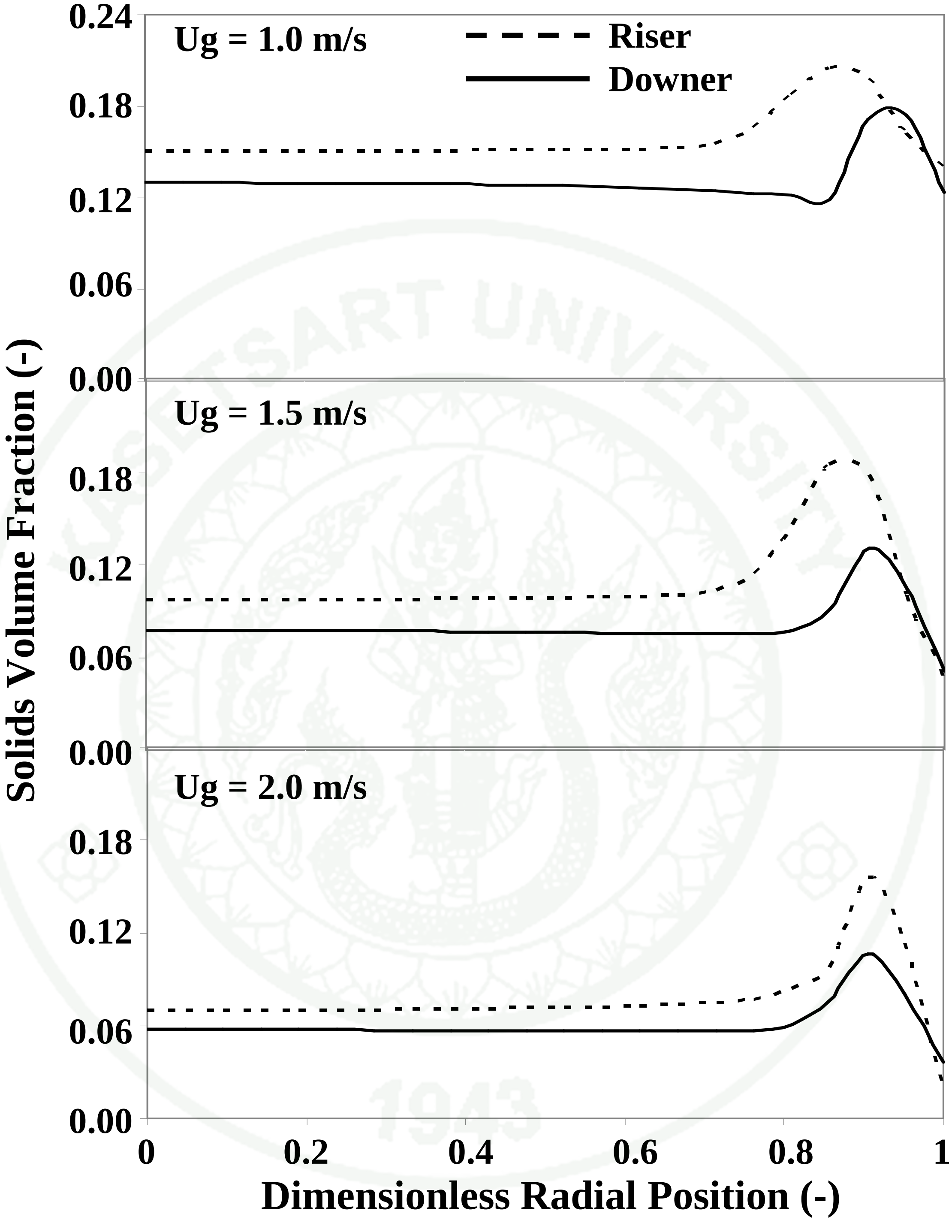

Figure 63 Effect of superficial gas velocity on the radial distribution of the solids volume fraction in the downer and the riser reactors.

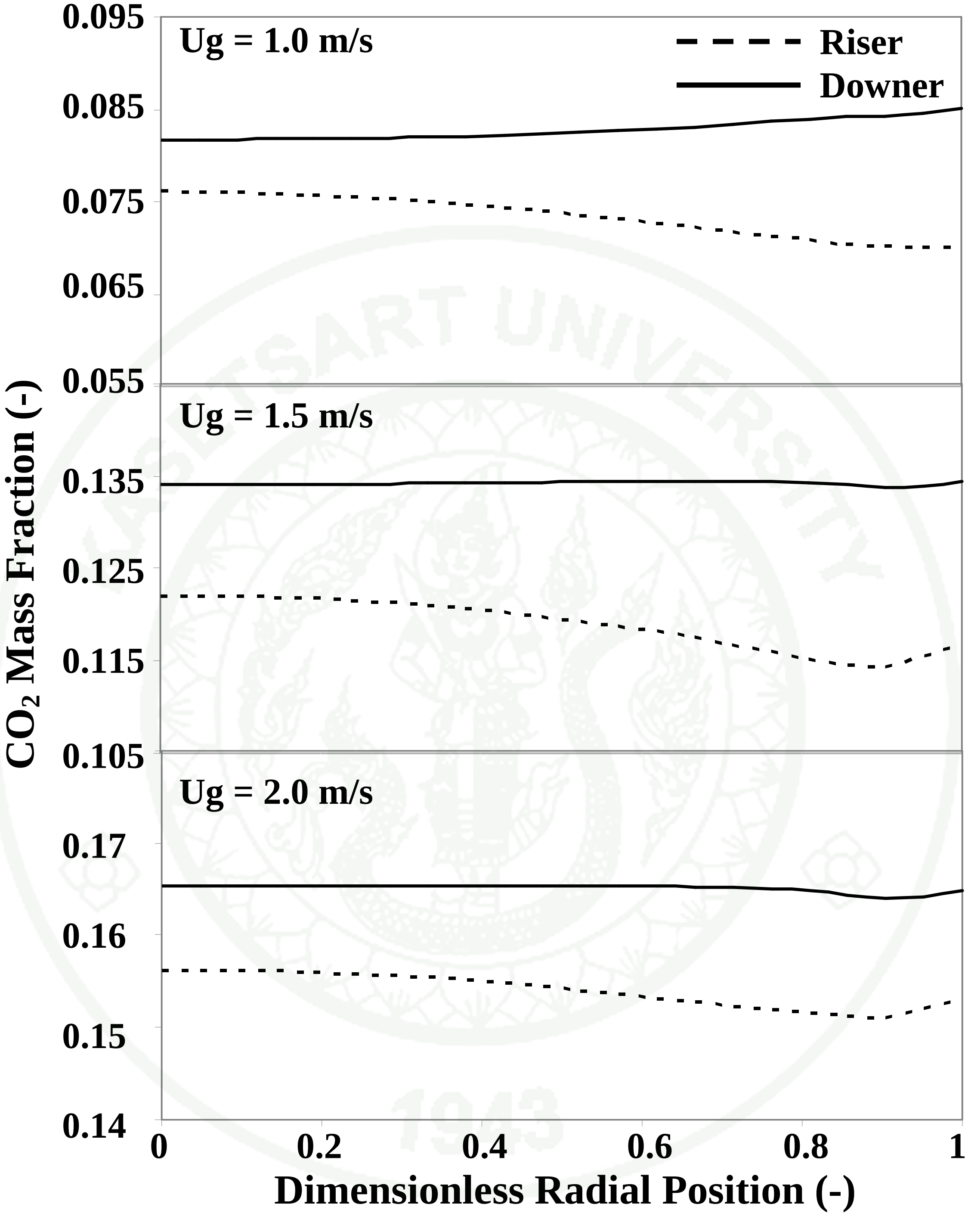

Figure 64 Effect of superficial gas velocity on the radial distribution of the CO_2 mass fraction in the downer and the riser reactors.

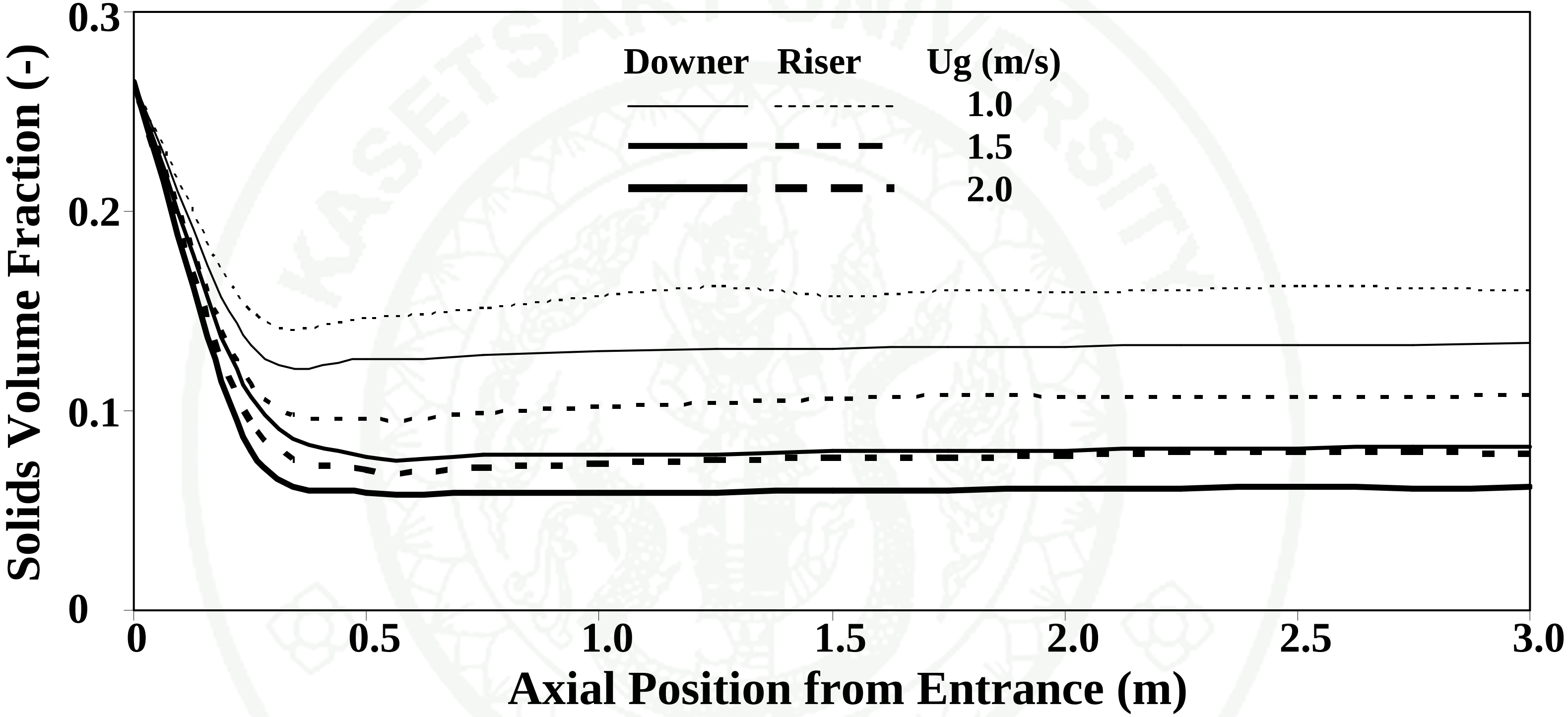

Figure 65 Effect of superficial gas velocity on the axial distribution of the solids volume fraction in the downer and the riser reactors.

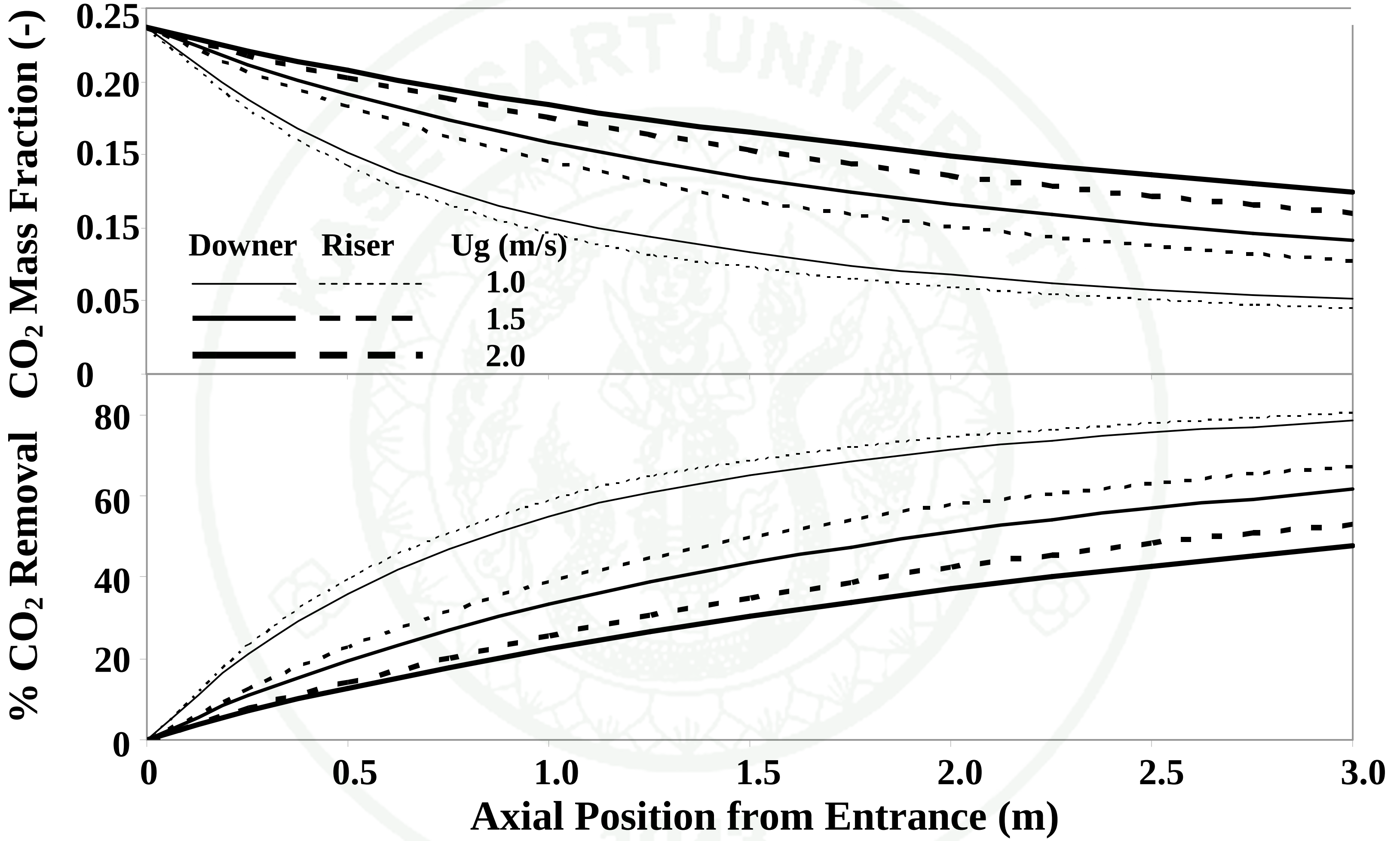

Figure 66 Effect of superficial gas velocity on the axial distributions of the CO$_2$ mass fraction and percent CO$_2$ removal in the downer and the riser reactors.

The solids circulation rate significantly affect to the solids fraction and CO_2 distribution in the system. Figure 67 shows the effect of the solids circulation rate on the radial distribution of the solids fractions in the downer and in the riser. As expected, the solids fraction both in the riser and in the downer increases with solids circulation rate. The density peak height increases as increasing the solids circulation rate. In addition, the radial distribution of solids volume fraction in the riser reactor show less uniform with a higher solids fraction peak. This non uniformity in the radial direction of the riser leads to a less uniform of CO_2 mass fraction in the lateral direction as shown in Figure 68.

Figure 69 shows the effect of solids circulation rate on the axial distribution of solids volume fraction. It was found that the solids volume fraction both in the riser and in the downer significantly increases with Gs. According to high solids fraction in the system as increases Gs, the CO_2 mass fraction significantly decreases with increasing Gs (see Figure 70). This leads to remarkably increasing the CO_2 removal efficiency.

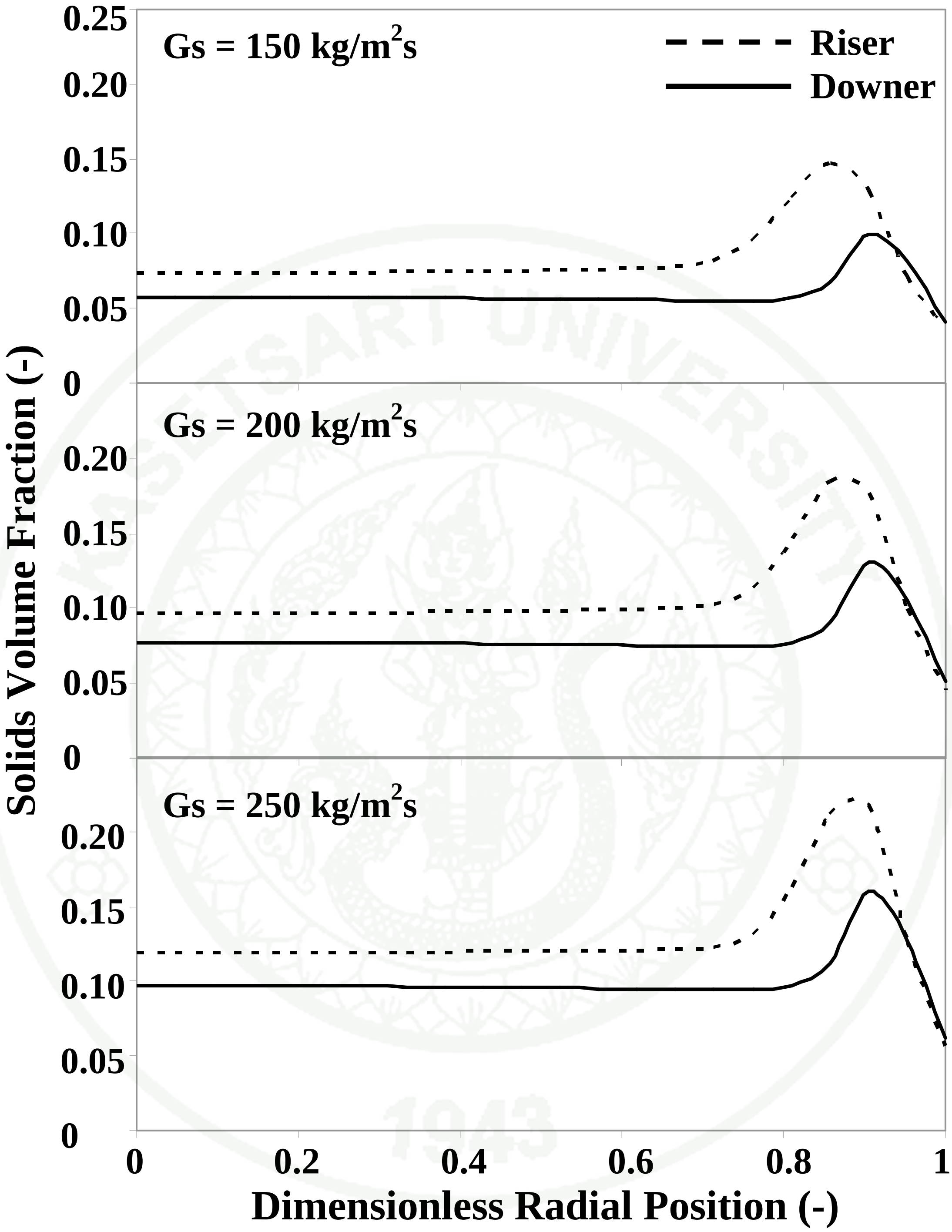

Figure 67 Effect of solids circulation rate on the radial distribution of the solids volume fraction in the downer and the riser reactors.

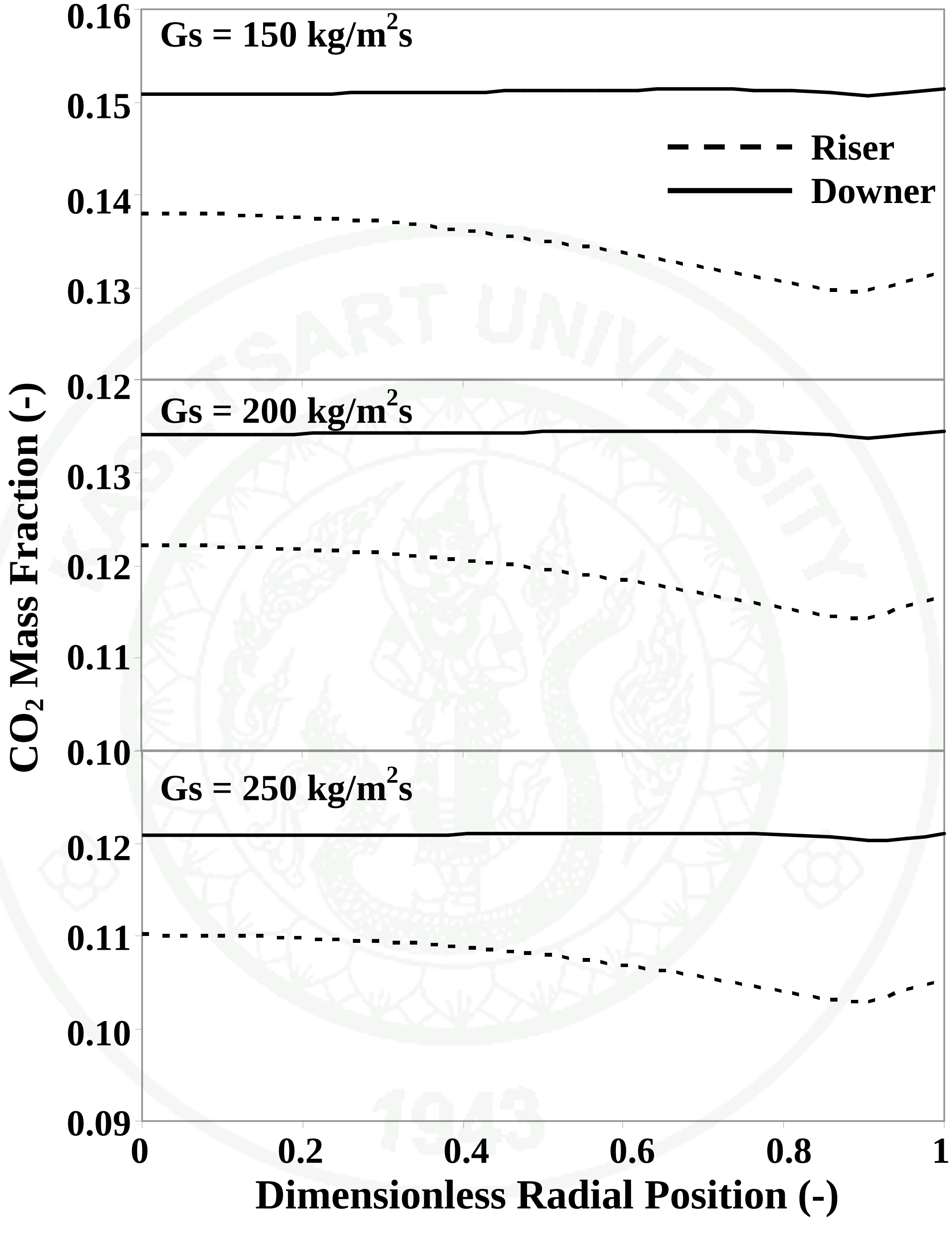

Figure 68 Effect of solids circulation rate on the radial distribution of the CO$_2$ mass fraction in the downer and the riser reactors.

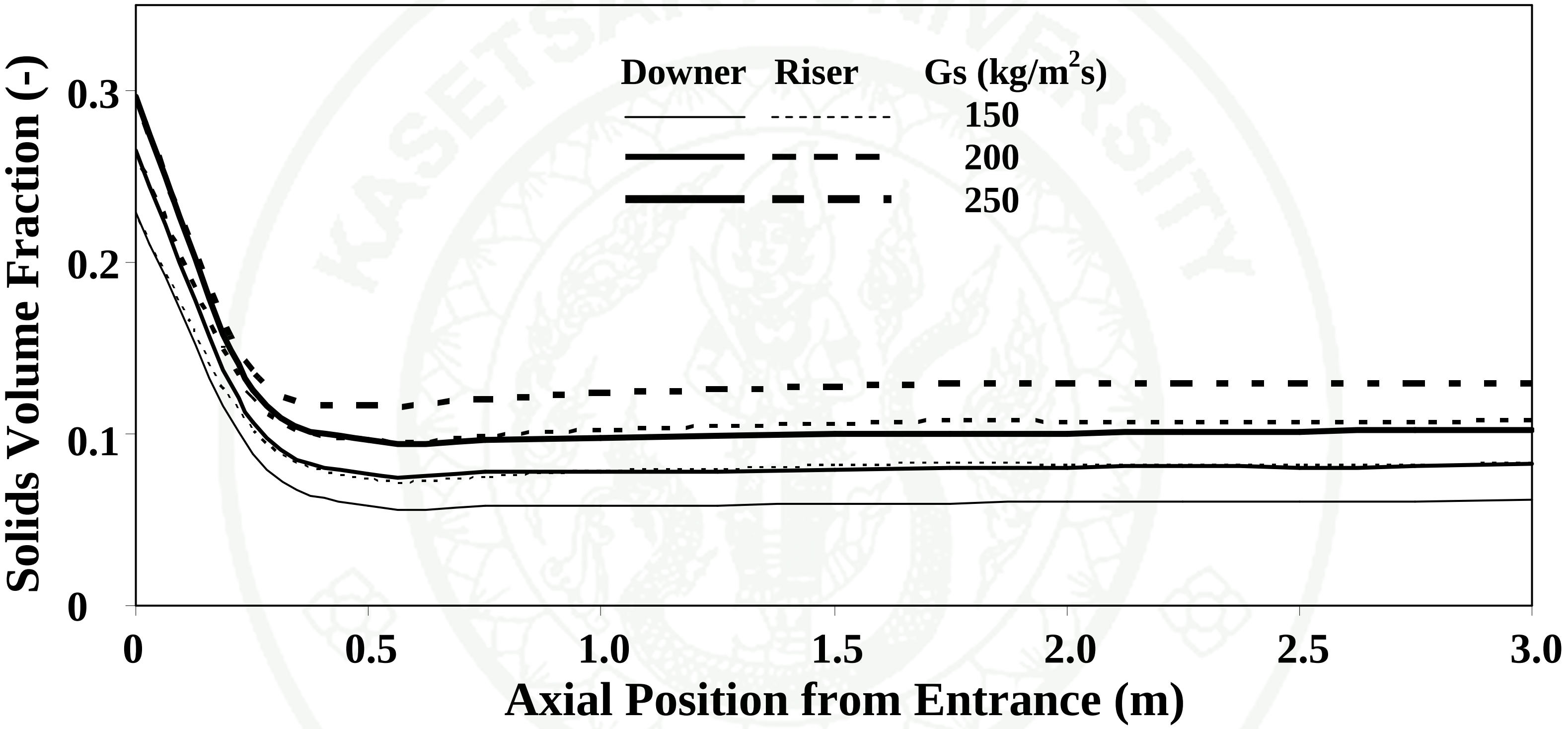

Figure 69 Effect of solids circulation rate on the axial distribution of the solids volume fraction in the downer and the riser reactors.

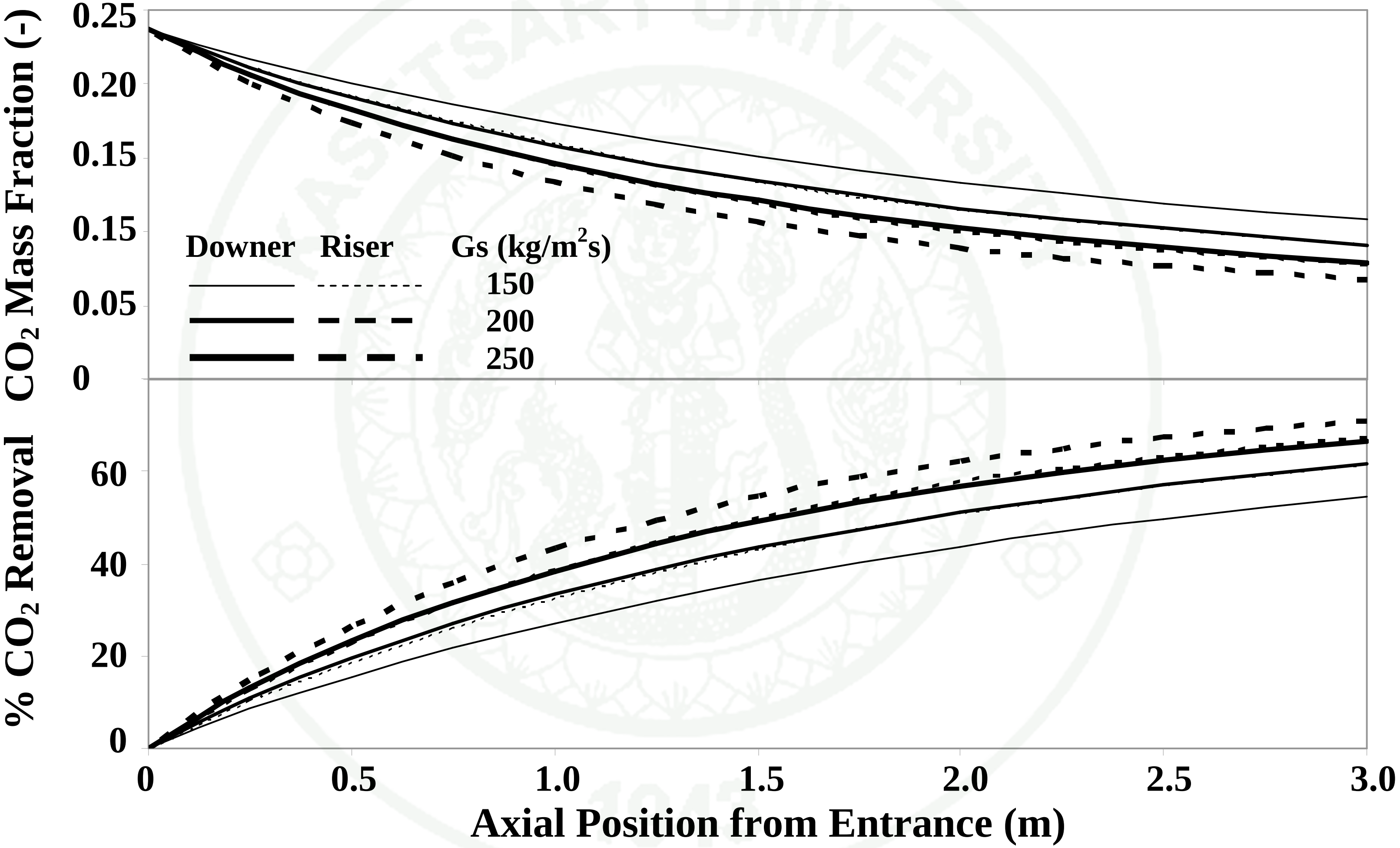

Figure 70 Effect of solids circulation rate on the axial distributions of the CO_2 mass fraction and percent CO_2 removal in the downer and the riser reactors.

2.2.5 Effect of particle properties on the CO_2 removal performance in the downer and the riser reactors

The effect of particle size on the radial distribution of the solids volume fraction in the downer and the riser is shown in Figure 71. A small particle tends to accumulate near the wall of both the downer and the riser. The particle tends to form a high density peak near the wall region as increasing the particle size especially in the riser reactor. A large difference of the solids volume fraction distribution in the radial direction between the downer and the riser can be observed in case of larger particle size. This large difference of solids volume fraction leads to a large difference of CO_2 mass fraction (see Figure 72). At small particle, the CO_2 mass fraction difference between in the downer and the riser is less due to the solids volume fraction is almost the same.

Figure 73 shows the effect of particle size on the axial distribution of solids volume fraction. In the downer, the solids volume fraction tends to decrease with increasing particle size. Inversely, the solids volume fraction in the riser increases with particle density. Figure 74 illustrates the axial profiles of the CO_2 mass fraction and the %CO_2 removal for difference particle size. It was found that the particle size shows less effect to the CO_2 mass fraction and % CO_2 removal both in the riser and the downer. A larger particle size tends to slightly decrease the CO_2 mass fraction in the riser. In contrast, the CO_2 mass fraction gradually decreases when operate with small particle in the downer reactor.

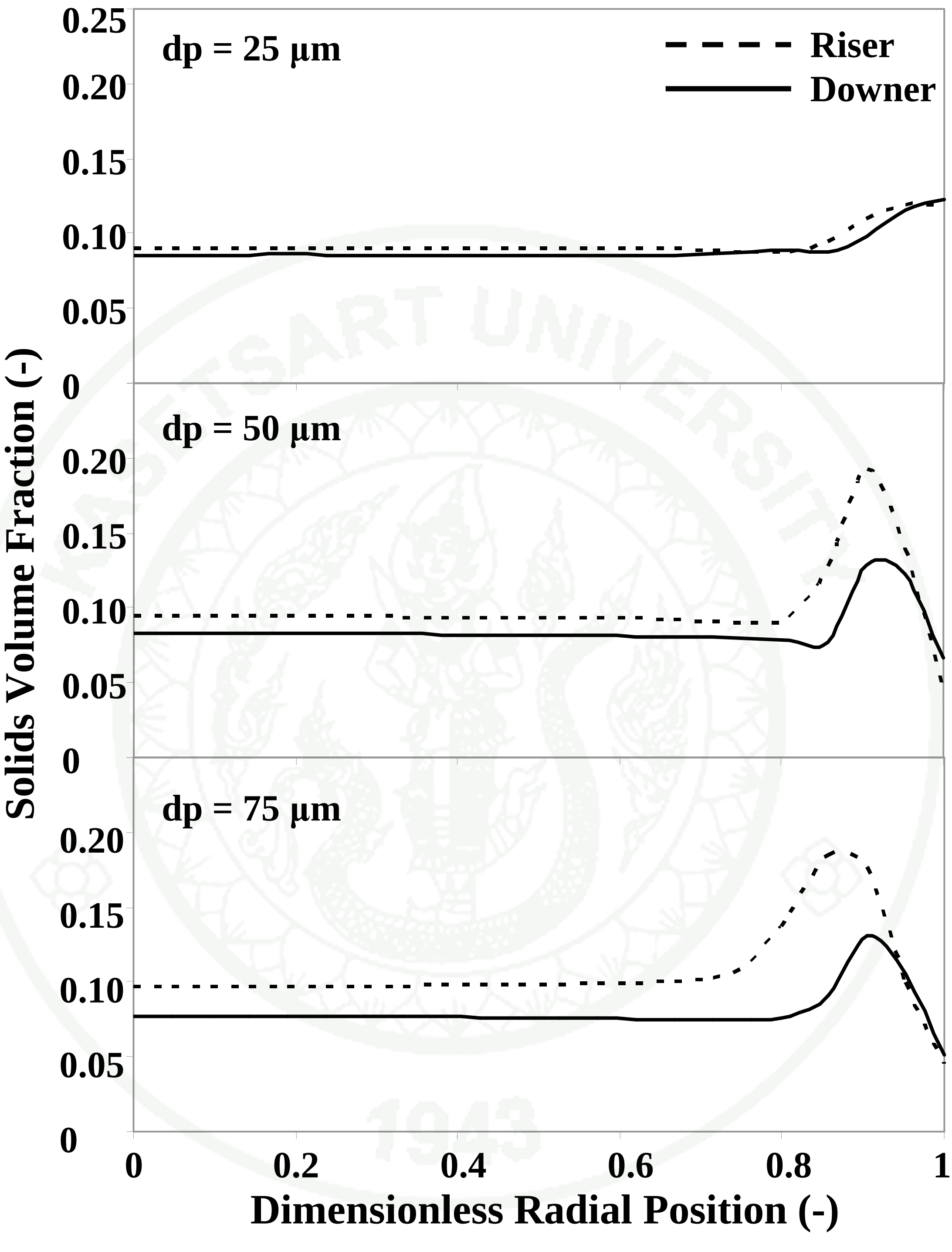

Figure 71 Effect of particle size on the radial distribution of the solids volume fraction in the downer and the riser reactors.

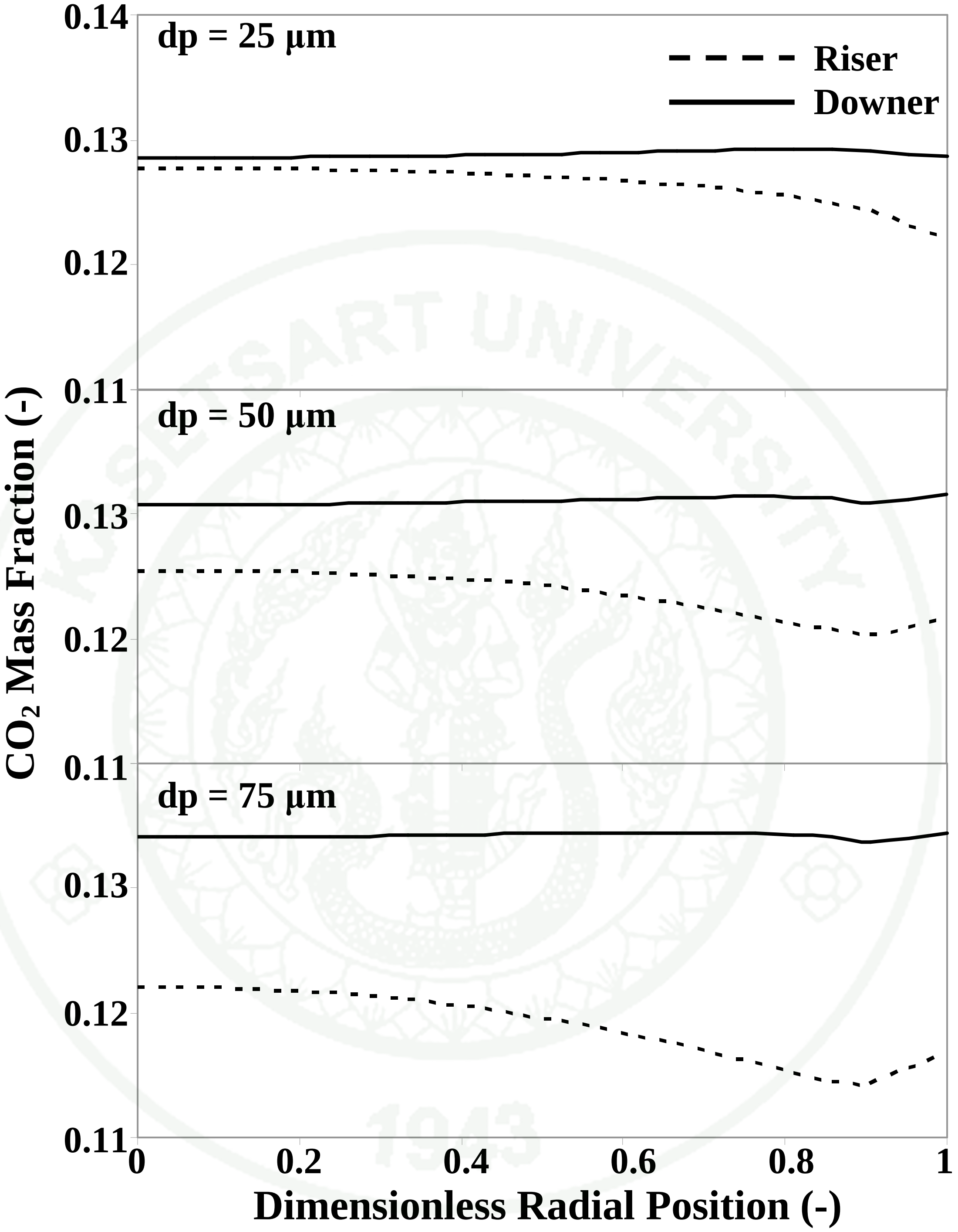

Figure 72 Effect of particle size on the radial distribution of the CO_2 mass fraction in the downer and the riser reactors.

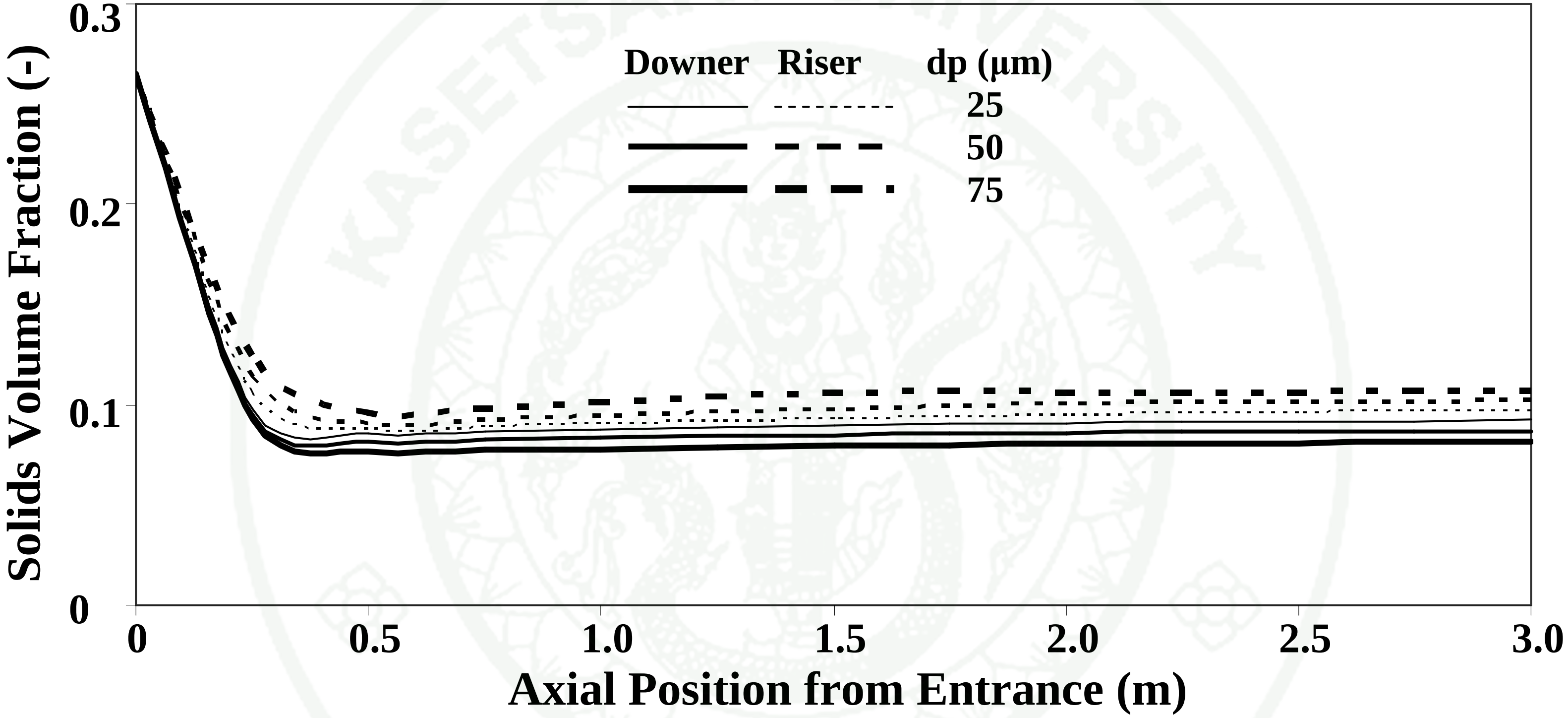

Figure 73 Effect of particle size on the axial distribution of the solids volume fraction in the downer and the riser reactors.

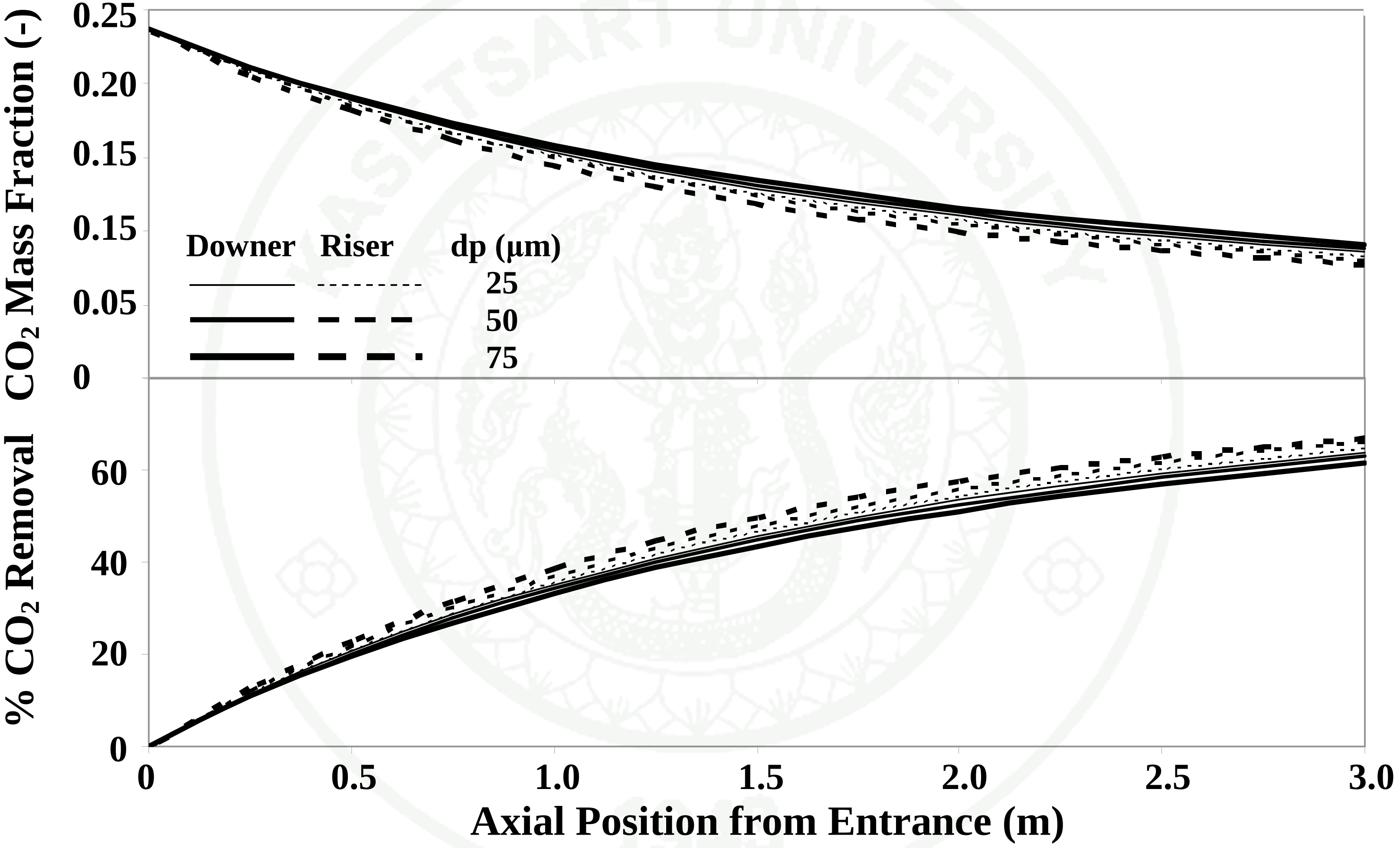

Figure 74 Effect of particle size on the axial distributions of the CO$_2$ mass fraction and the percent CO$_2$ removal in the downer and the riser reactors.

The radial distribution of the solids fraction at various difference particle densities is shown in Figure 75. The radial distribution of the solids fraction both in the downer and the riser shows a uniform distribution in the core region with a high density peak near the wall region. This high density peak tends to decrease as increasing the particle density. In addition, the peak near the wall of the riser is larger than that of the downer. The high density peak near the wall region causes a low CO_2 mass fraction in this region especially in the riser reactor (see Figure 76).

The effect of particle density on the axial profile of the solids fraction both in the downer and the riser is shown in Figure 77. As can be seen, a heavier particle tends to significantly decrease the solids fraction both in the downer and the riser. This leads to a remarkable increasing of CO_2 mass fraction in these reactors as shown in Figure 78. In addition, the solids volume fraction in the downer is lower than in the riser. Thus the CO_2 removal efficiency in the riser is higher than that in the downer.

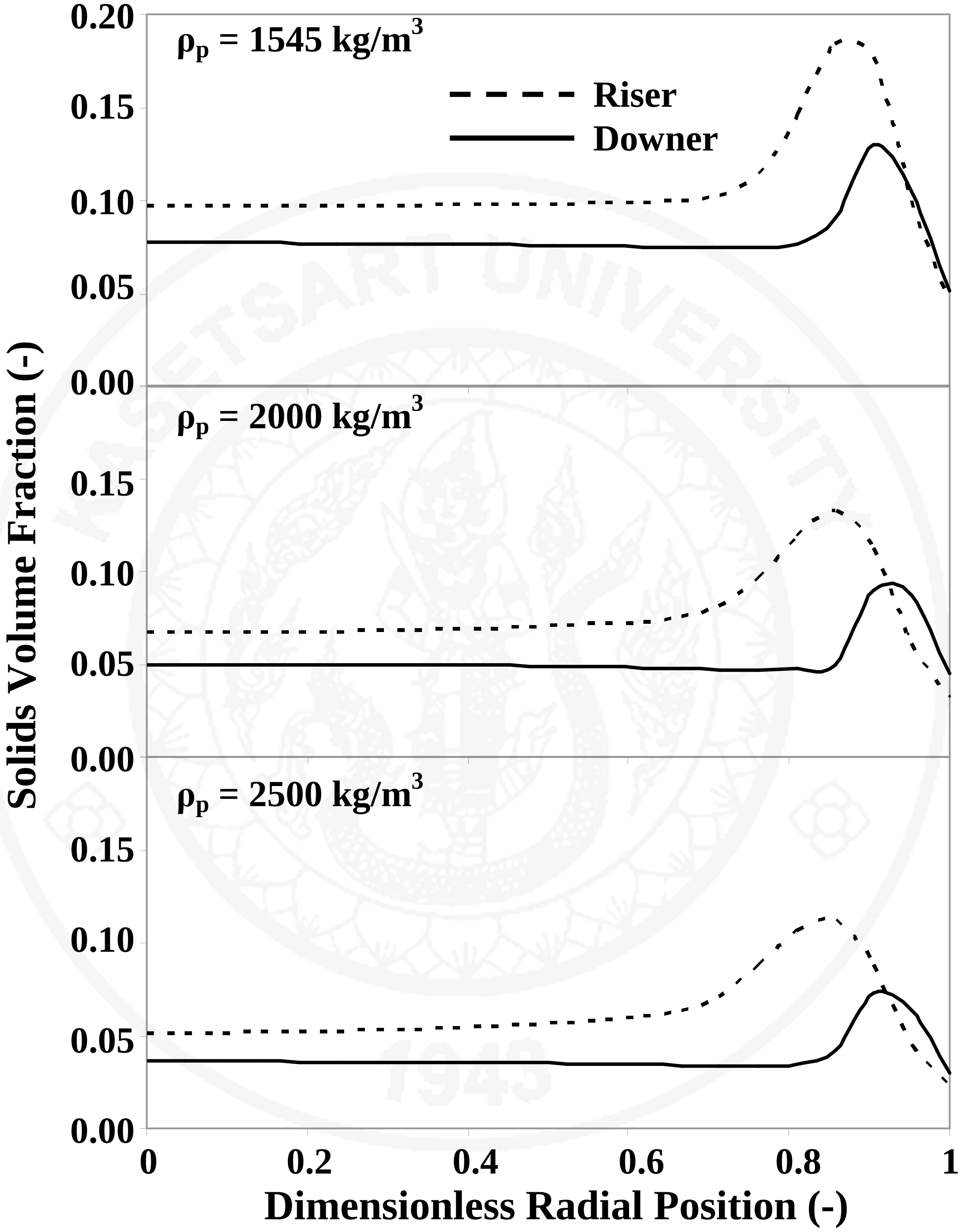

Figure 75 Effect of particle density on the radial distribution of the solids volume fraction in the downer and the riser reactors.

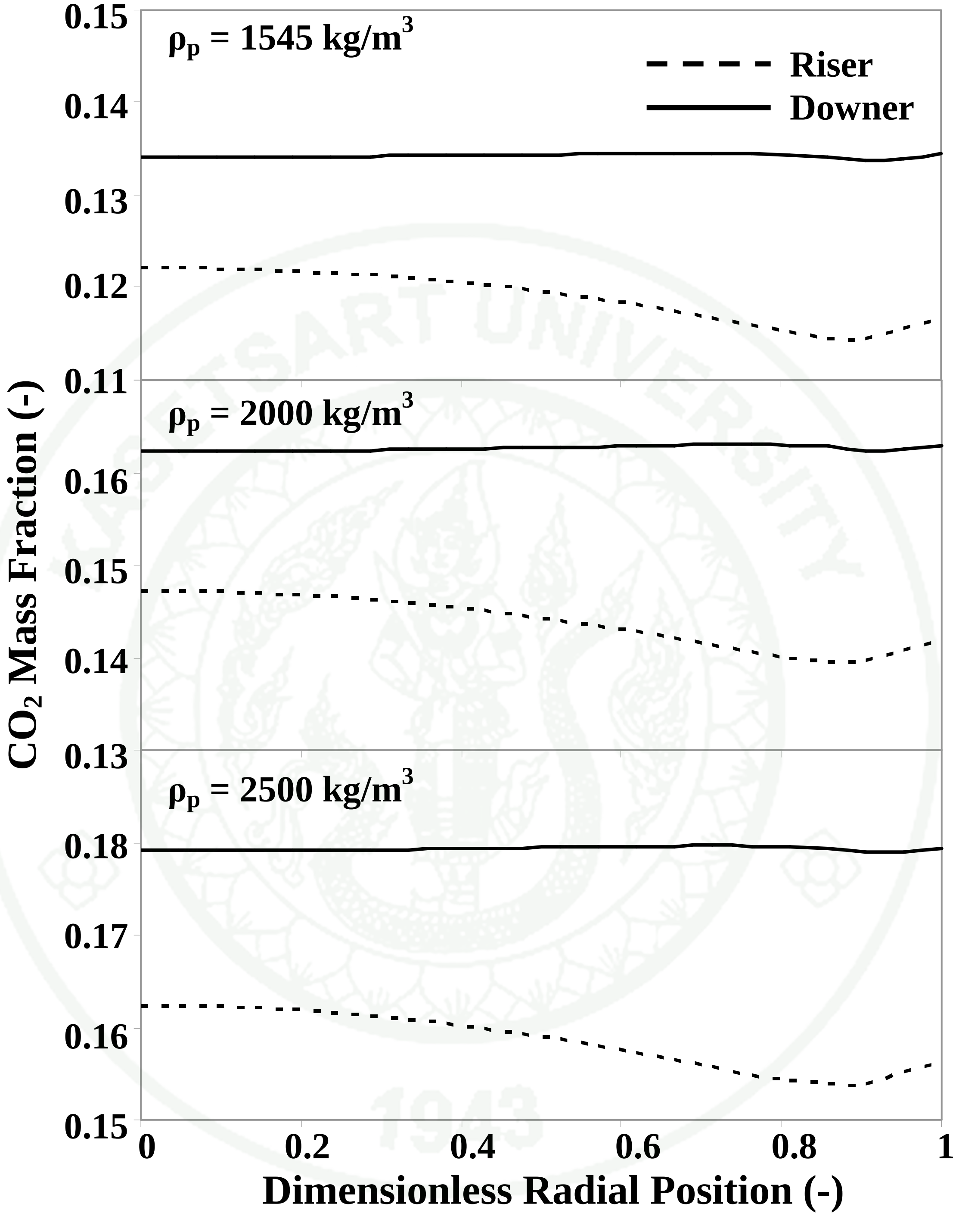

Figure 76 Effect of particle density on the radial distribution of the CO_2 mass fraction in the downer and the riser reactors.

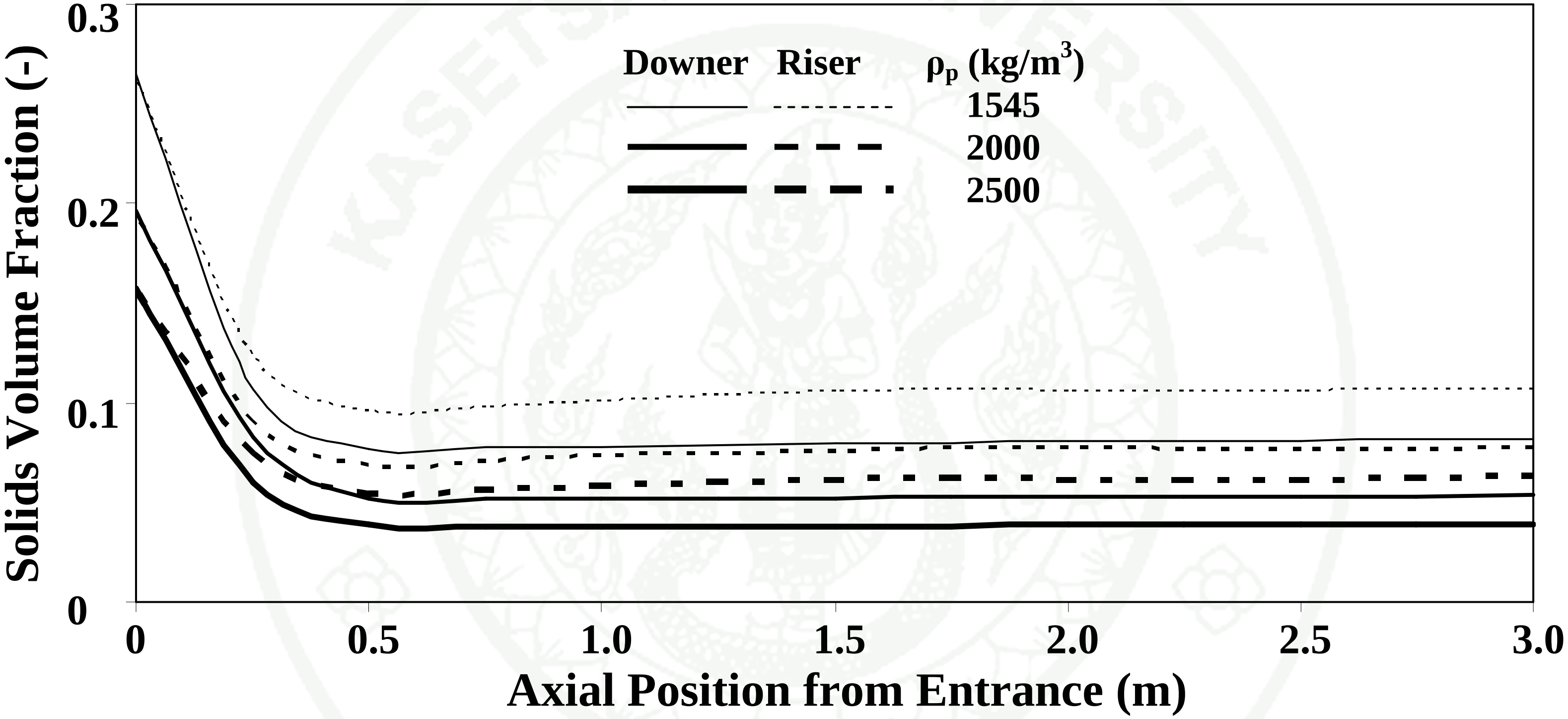

Figure 77 Effect of particle density on the axial distribution of the solids volume fraction in the downer and the riser reactors.

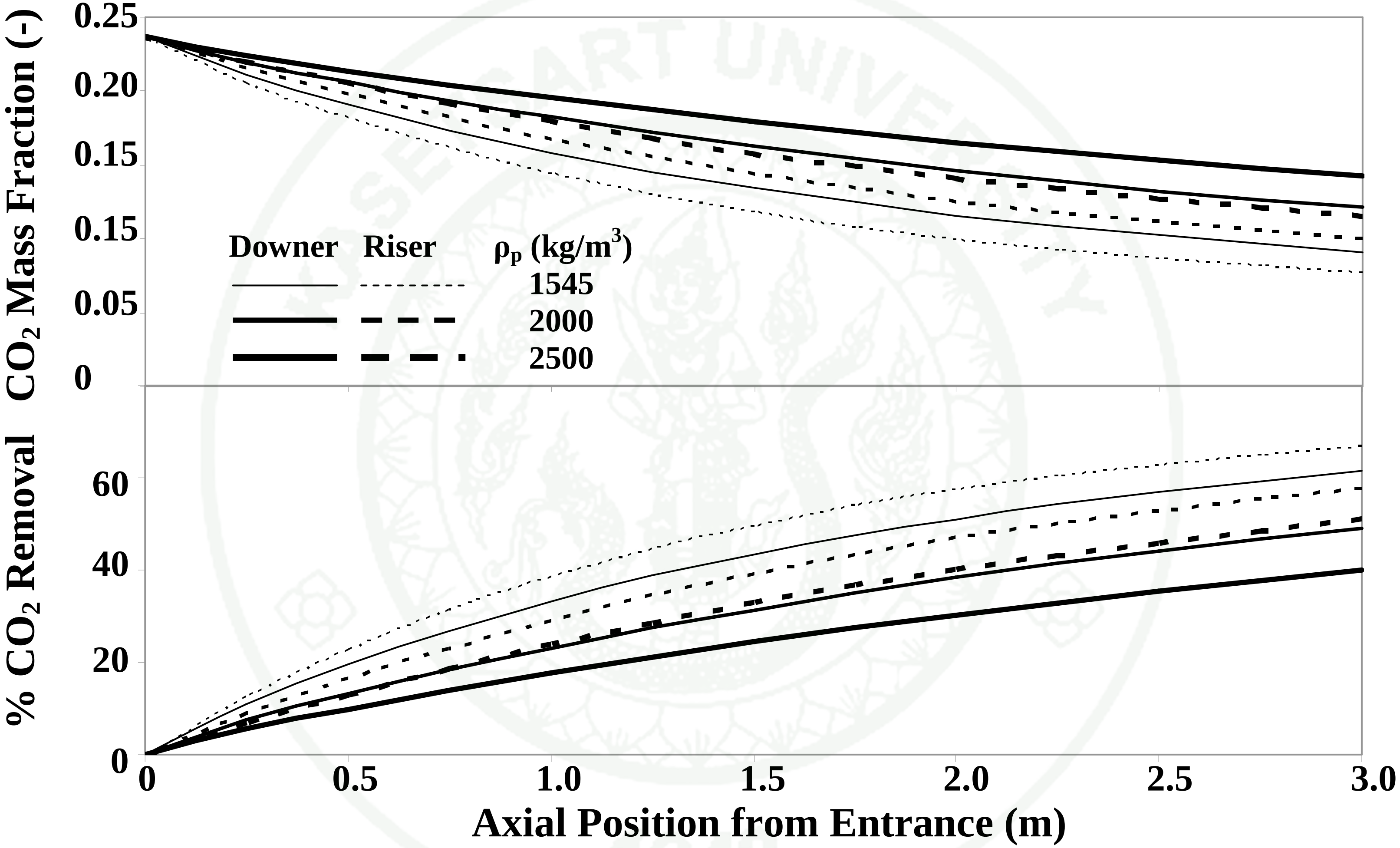

Figure 78 Effect of particle density on the axial distributions of the CO$_2$ mass fraction and the percent CO$_2$ removal in the downer and the riser reactors.

3. DEM modeling and simulation for catalytic cracking of heavy oil in a downer reactor

3.1 Hydrodynamics behavior and temperature and species distributions in a downer reactor

The developed DEM model can be predicted the local hydrodynamics behavior such as solids volume fraction, velocity, temperature, and species concentration of gas and solids phases. This section presents the distributions of particle, temperature, and species concentration in the downer. The radial and axial profiles of hydrodynamics, temperature, and species concentration are also illustrated below.

3.1.1 Distributions of particle, temperature, and concentration

The distributions of particle and gas temperatures in the downer as a function of time are shown in Figure 79. The simulation was performed at the superficial gas velocity of 5 m/s and the solids circulation rate of 65 kg/m^{2}s. The color scales represent various values of temperature. The left and right panels of each pair show the temperature in solids and gas phases, respectively. The catalyst particles and reactant gas were fed to the reactor with the same temperature of 673 K. The reaction took place on the catalyst surface when reactant gas and catalyst particles were in contact. The catalytic cracking is an endothermic reaction. Therefore, the temperature of both gas and solids phases decreased along the reactor length. In addition, this figure also provides the information of the particle distribution in the reactor. It was found that the particle distribution was almost uniform throughout the reactor. It cannot be observed the large particle cluster because of a low solids circulation rate in this study. The details of particle movements in a downer were explained by Limtrakul *et al*. (2008).

Figure 80 illustrates the distribution of the heavy oil mass fraction in solids phase (left side) and that in gas phase (right side) as a function of time under the same operating condition for Figure 79. When the catalysts were in contact with reactant gas, the catalytic cracking reaction was occurred leading to low heavy oil mass fraction especially in solids phase. The heavy oil mass fraction both in solids and gas phases decreases along the reactor height as it cracked to the products.

3.1.2 Radial profiles of solids holdup, velocity, temperature, and concentration

The radial distributions of solids volume fraction and axial gas and solids velocities at various axial positions are shown in Figure 81. It was found that the solids volume fraction and the axial velocities profiles are almost uniform in the lateral direction. However, more radial variation of solids volume fraction can be observed near the inlet region due to feeding effect. The uniform solids fraction results in the uniformities of gas and solids velocities in the radial direction. The uniform radial distributions of the particle and flows affect the heat and mass transfer in the system. This leads to the almost uniform distributions of temperature and heavy oil mass fraction in the radial direction at any axial positions. These uniform radial profiles of gas and solids temperatures in the downer have been observed in pilot plant experiments (Liu *et al.*, 2008) and simulation studies (Wu *et al.*, 2009). With low solids loading, the uniform radial profiles of momentum, heat and mass transfer are reasonable. Thus, it can be concluded that the flow behavior in the downer is approaching plug flow behavior (Limtrakul *et al.*, 2008; Zhao *et al.*, 2010a). However, a large variation of radial distribution of gas product concentration has been reported when operation was at high solids circulation rate (Liu *et al.*, 2008).

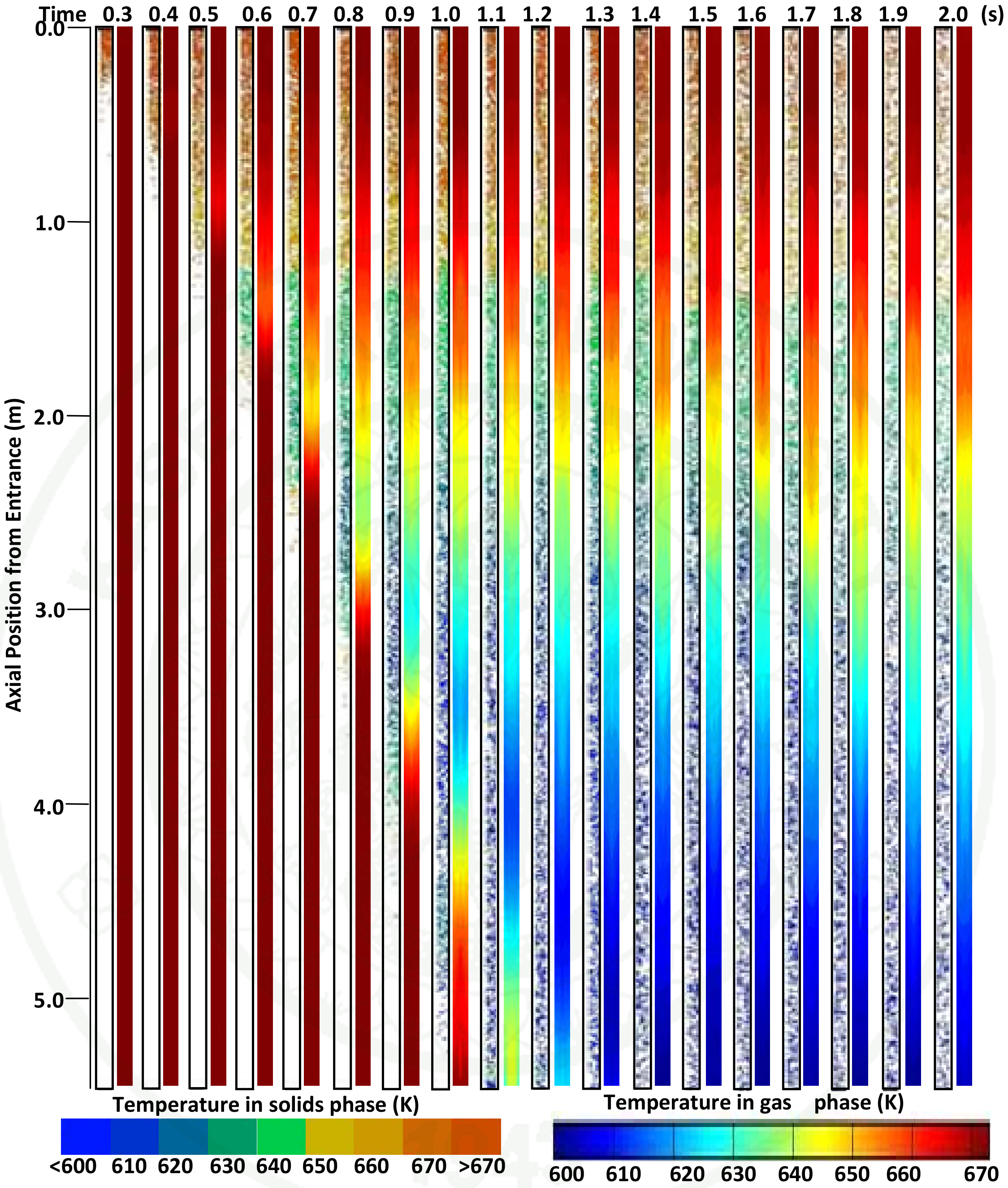

Figure 79 Particle movements and temperature distributions in particle phase (left side) and gas phase (right side) as a function of time, at the superficial gas velocity of 5 m/s, the solid circulation rate of 65 kg/m^{2}s, and the gas and solids inlet temperatures of 673 K.

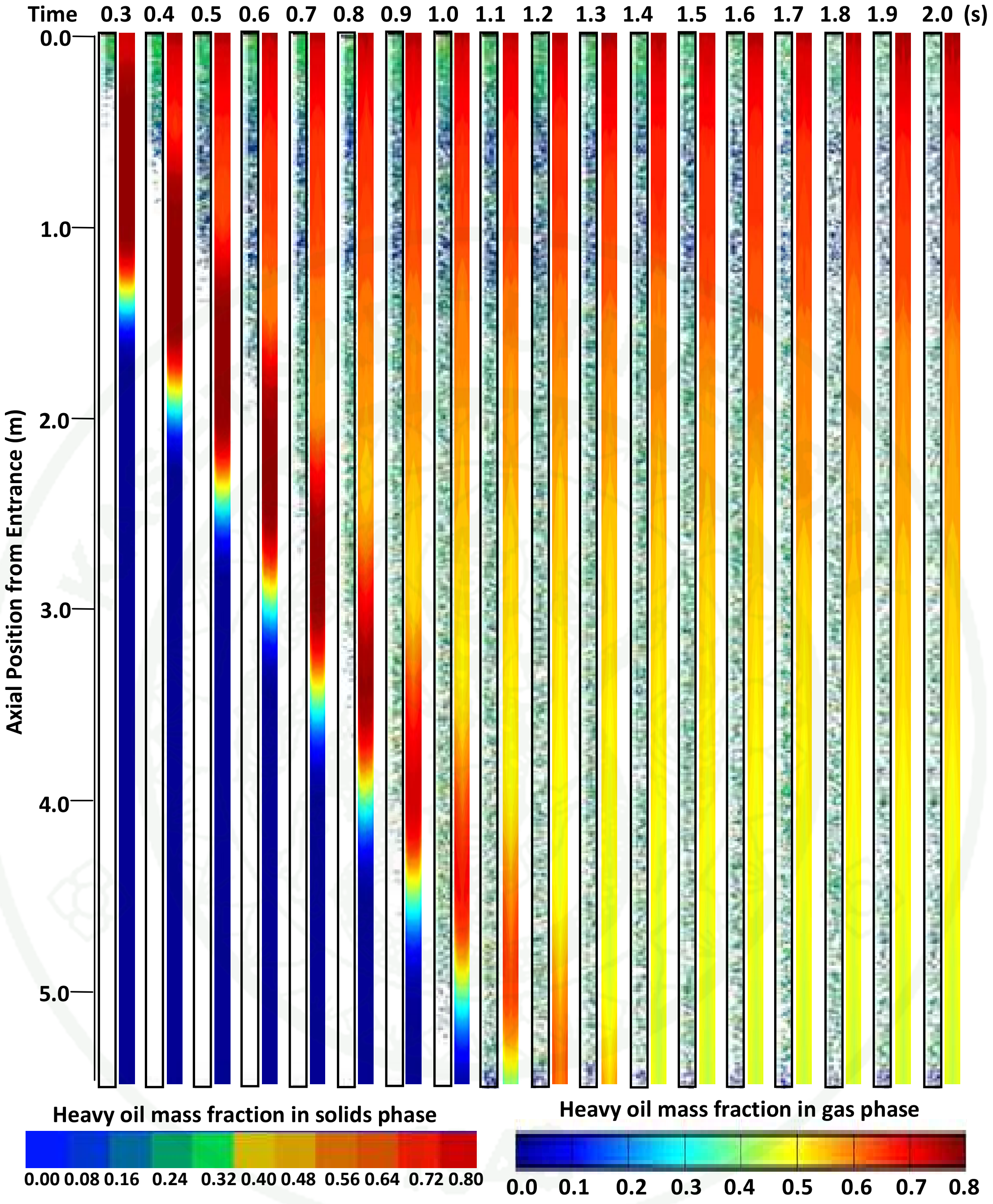

Figure 80 Particle movements and heavy oil mass fraction in particle phase (left side) and gas phase (right side) as a function of time, at the superficial gas velocity of 5 m/s, the solid circulation rate of 65 kg/m^{2}s, and the gas and solids inlet temperatures of 673 K.

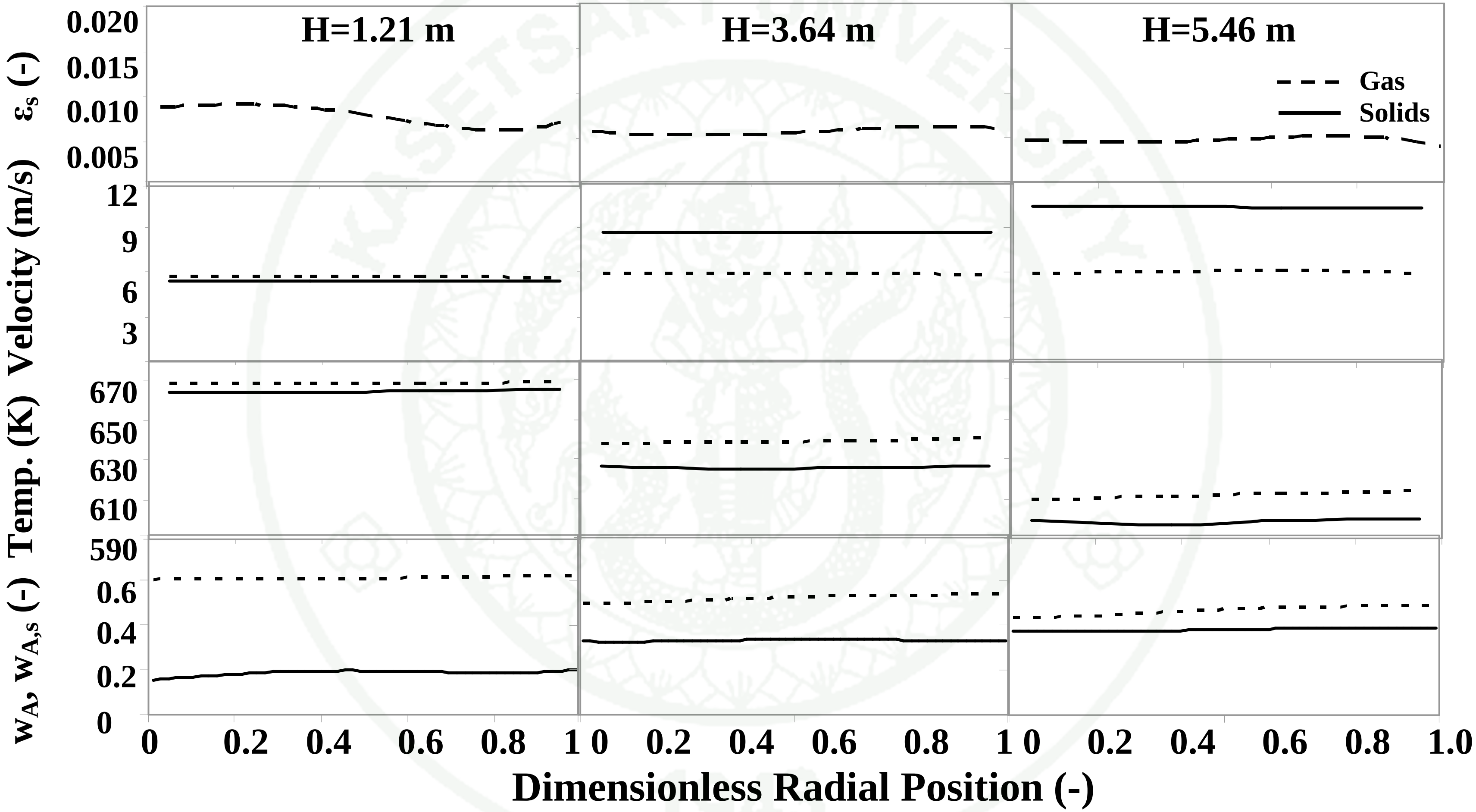

Figure 81 Radial distributions of the solids volume fraction, axial gas and solids velocities, temperature, and heavy oil mass fraction in gas phase (w_A) and in solids phase ($w_{A,s}$) at Ug 5 m/s, Gs 65 kg/m^{2}s, and the gas and solids inlet temperatures of 673 K.

3.1.3 Axial profiles of solids holdup, velocity, temperature, and concentration

The axial profile of solids volume fraction in the reactor obtained from the cross-sectional averaged values is shown in Figure 82. The solids volume fraction dramatically decreases within 2-3 m from the inlet. In this region, the particles are accelerated by gravitational force and drag force due to high gas velocity. Thus the particle velocity rapidly increases cause the rapid decreasing in solids volume fraction in this region. Further down the column, when the particle velocity is higher than gas velocity, the drag force becomes the resistance to particle movement. This result in slowly increases particle velocity, which leads to gradually decreases of solids volume fraction in the system. This axial profile of solids volume fraction in a downer reactor can be also observed by many investigators (Zhang and Zhu, 2000; Bolkan *et al.*, 2003b; Limtrakul *et al.*, 2008).

Near the inlet region, both gas and solids temperatures are high and almost the same according to the same feed temperature of both phases. These high gas and solids temperatures and high solids volume fraction in this region lead to high reaction rate. This results in a dramatic decreasing of heavy oil mass fraction in gas phase. Further down the column where the solids volume fraction gradually decreases, the temperatures of both phases decrease along the axial direction due to the effect of endothermic cracking reaction. These lead to slightly decreasing of the heavy oil mass fraction in gas phase because of a low reaction rate.

In addition, it can be observed large concentration difference between gas and solids phases especially near the inlet region. The explanation is that the reaction rate on the catalyst surface is high in this region because of a high temperature. Therefore, the rate of heavy oil consumed due to the cracking reaction is higher than the rate of heavy oil transfer from the bulk gas to the catalyst surface. This indicates that the overall mass transfer in the system was limited by the mass transfer between phases. Near the outlet, the concentration difference between phase decreases because of low reaction rate in this region. The mass transfer rate is higher in this region. In addition, the particle temperature was lower than gas temperature because the endothermic reaction occurred on the catalyst surface except in the feed region where the same feed temperatures of solids and gas phases were made. A large temperature difference between phases can be found further down the column. According to fast reaction of catalytic cracking, the rate of energy consuming due to the endothermic cracking reaction on the catalyst surface is higher than the rate of energy transfer from the bulk gas to the catalyst surface. This indicates that the overall heat transfer in the system was controlled by the energy transfer between phases. For this reason, the temperature difference between phases is high.

The general trends of feed and products distributions and the conversion along the downer reactor length can be seen in Figure 83. The mass fraction of heavy oil decreases along the reactor length. In the inlet section, the disappearance rate of heavy oil is higher than the exit region because of high solids volume fraction and temperature in this region. Thus, the conversion dramatically increases in the inlet region and gradually increases further down the column. In the aspect of gasoline distribution, it was found that the gasoline mass fraction rapidly increases in the first section and then slightly increases further down the column. This is because of the slow cracking rate further down the column due to low solids volume fraction and low temperatures of gas and solids phases with less heavy oil remained in the system. The gas mass fraction is lower than the gasoline mass fraction along the reactor length because of lower reaction rate constants (k_2' and k_4') for mechanism of lumped gas formation. However, a very small amount of coke can be observed.

In summary, the radial variation of the hydrodynamics behavior is less significant than that the variation in the axial direction. This indicates that the flow behavior in the downer is close to ideal plug flow. The axial profile of solids volume fraction shows a rapidly decreases near the inlet region and eventually approach a constant within 2-3 m from the inlet. The axial temperature profiles of both gas and solids phases decrease along the reactor height with an almost uniform distribution in radial direction. The axial distribution of heavy oil mass fraction shows a higher variation than that the radial distribution. The heavy oil mass fraction

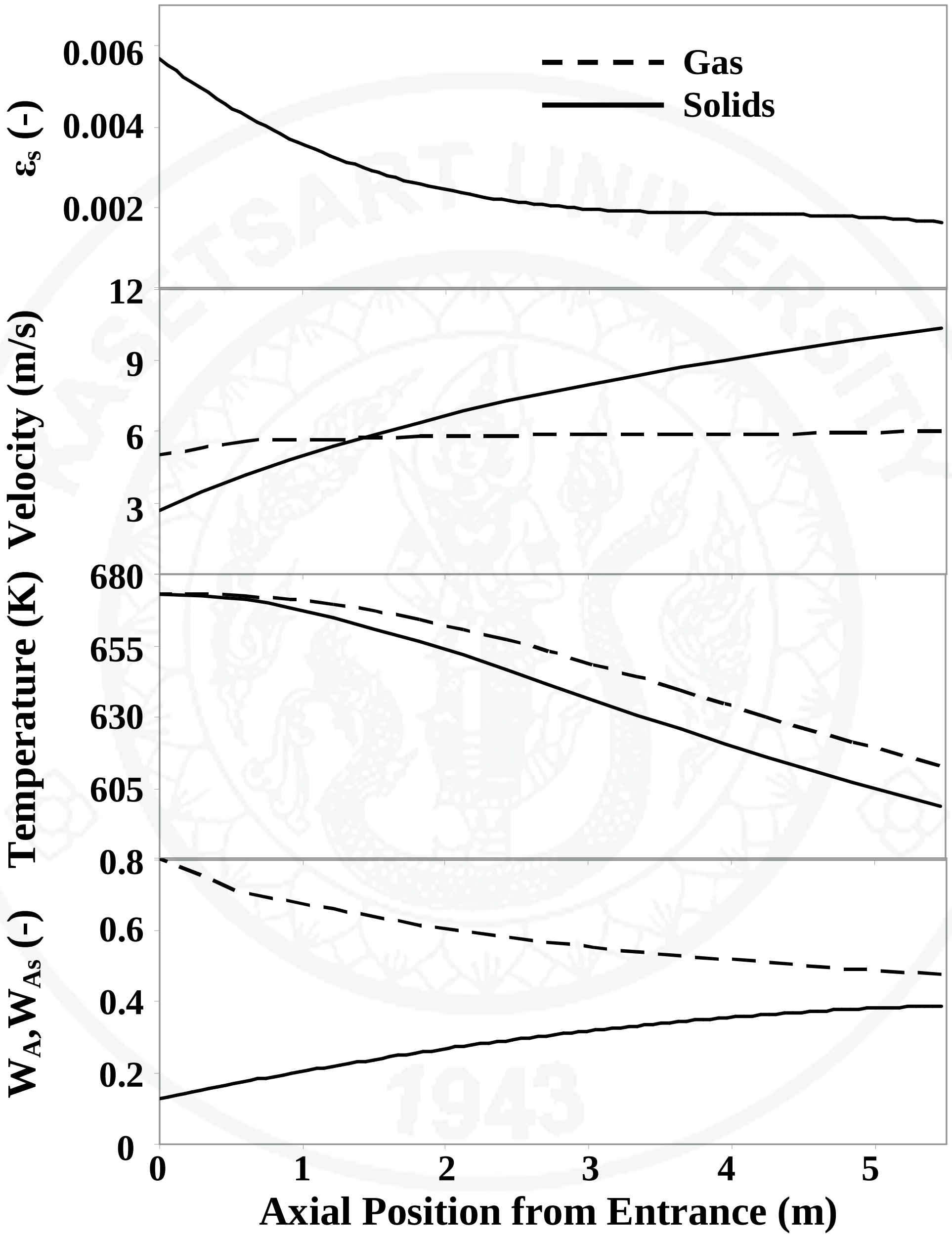

Figure 82 Axial distributions of the solids volume fraction, axial gas and solids velocities, temperature of gas and catalyst, and heavy oil mass fraction in the downer reactor, at the superficial gas velocity of 5m/s, the solids circulation rate of 65 kg/m^{2}s, and the gas and solids inlet temperatures of 673 K.

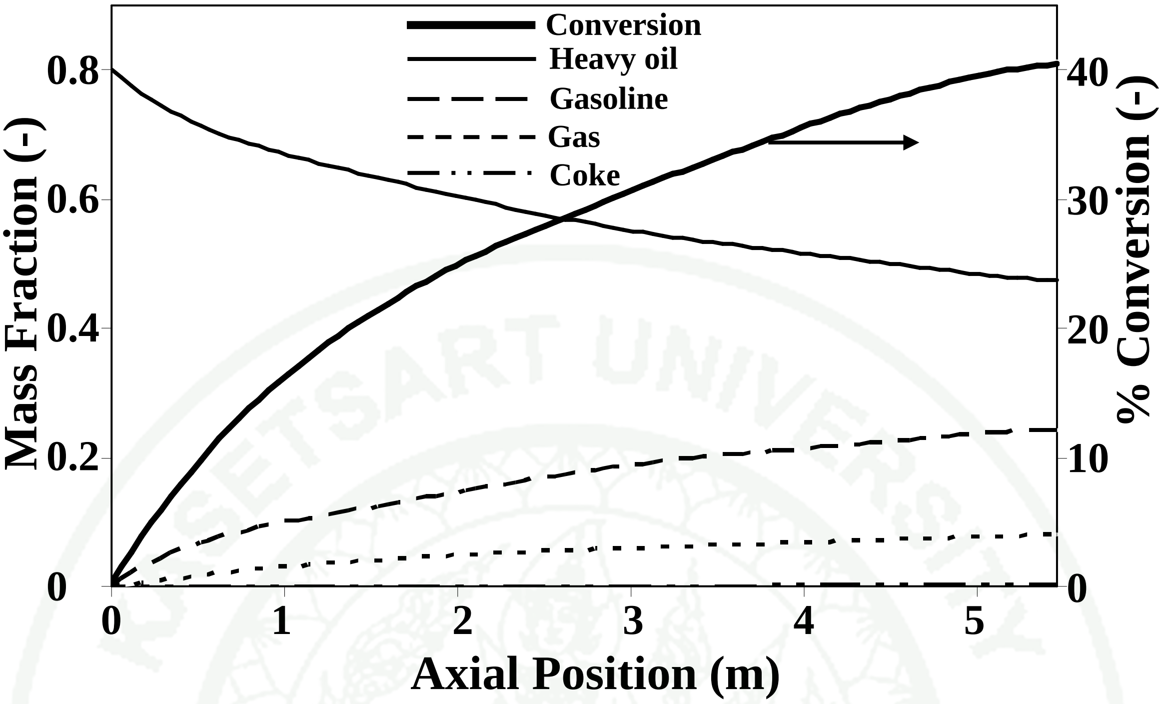

Figure 83 Axial distributions of feed and products mass fractions and the conversion in the downer reactor, at the superficial gas velocity of 5 m/s, the solids circulation rate of 65 kg/m^{2}s, and the gas and solids inlet temperatures of 673 K.

dramatically decreases near the inlet and gradually decreases further down the column due to low cracking reaction because of low solids volume fraction and low gas and solids temperatures. According to the radial profile uniformities of the solids fraction, velocity, temperature, and concentration, the further studies will be focused on the axial variation.

3.2 Effect of inlet feed temperature on the reactor performance

The effect of feed temperature on the temperature and products mass fraction distributions is shown in Figures 84 and 85, respectively. The temperature distributions of all cases show the same trend which the temperature of both phases is high in the inlet section and decreases further down the column according to the endothermic reaction occurring along the reactor length. At high inlet temperature, the temperatures in gas and solids phases rapidly decrease due to high endothermic reaction rate. This leads to lower outlet temperature. However, a large temperature difference between phases can also be observed at high inlet feed temperature. Increasing inlet feed temperature has less effect on heat transfer coefficient but significantly increase the energy consumption rate due to high endothermic cracking reaction. Thus both gas and solids temperatures are much decreased with a larger temperature difference at higher feed temperature. The feed temperature significantly affects the heavy oil mass fraction as shown in Figure 85. At high inlet temperature, high amount of heavy oil was crack to the products leading to low heavy oil mass fraction in the system. In the respect of gasoline distribution, the gasoline mass fraction increases with inlet temperature but with less effect at high inlet temperature when the temperature changes from 673 to 723 K. Note that the gasoline mass fraction does not significantly increase where the gas lump mass fraction significantly increases. The explanation is that the gasoline product undergoes further cracking to form gaseous products at high inlet temperature (723 K). As shown in Figure 85, the gasoline mass fraction distributions are almost the same at 673 and 723 K, while gas mass fractions significantly increase as inlet temperature increased.

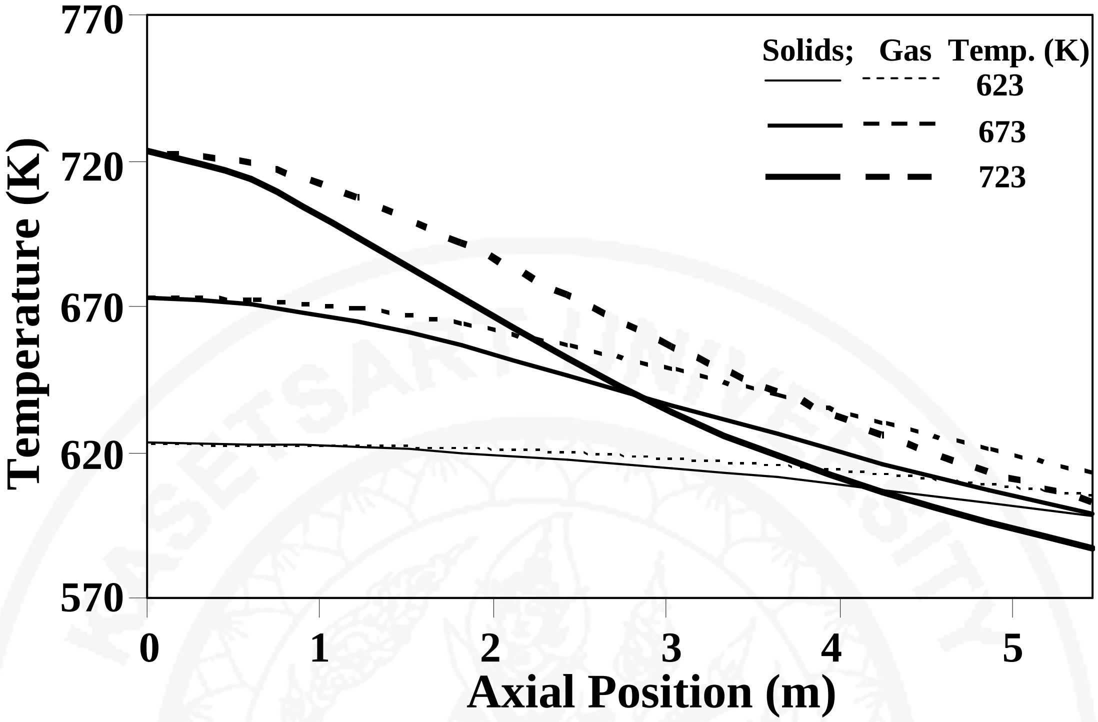

Figure 84 Effect of inlet fed temperature on the axial distributions of the gas and catalyst temperatures at the constant superficial gas velocity of 5 m/s and the solids circulation rate of 65 kg/m^2s.

3.3 Effect of solids circulation rate on the reactor performance

The effect of the solids circulation rate (Gs) on the temperature distribution is illustrated in Figure 86. At high Gs, the temperatures both in gas and solids phases significantly decrease along the reactor length leading to very low gas and solids temperatures at the outlet. The reason is that the solids fraction in the system increases with Gs (Wang *et al.,* 1992; Yang *et al.,* 1998; Zhang *et al.,* 1999; Cao and Weinstein, 2000; Zhang *et al.,* 2000; Liu *et al.,* 2001; Li *et al.,* 2004; Nova *et al.,* 2004; Limtrakul *et al.,* 2008; Vaishali *et al.,* 2008;). Therefore, at high Gs, more heavy oil can be cracked on the catalyst surface leading to rapidly decreases of gas and solids temperatures. At low Gs, the gas and solids temperatures slightly decrease along the reactor height because of low solids fraction in the system. In addition, at low Gs, the outlet temperature difference between phases tends to increase due to high reaction rate on the catalyst surface because of high reactant gas remained in the system (see Figure 87). Thus the solids temperature dramatically decreases near the outlet region.

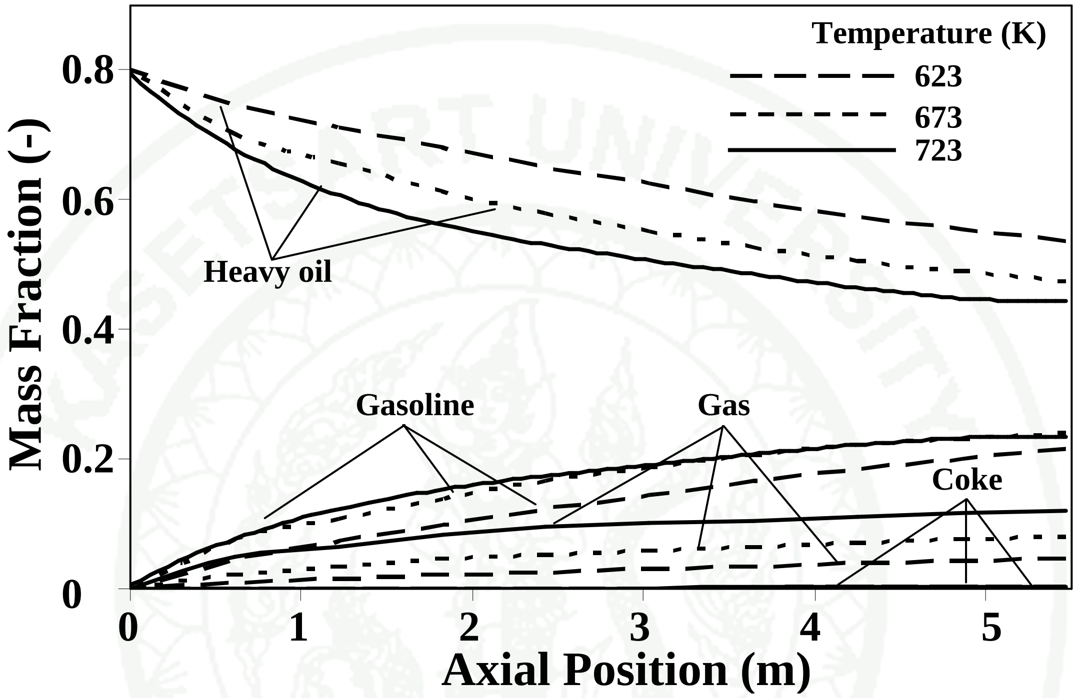

Figure 85 Effect of inlet fed temperature on the axial distributions of the feed and products mass fraction at the constant superficial gas velocity of 5 m/s and the solids circulation rate of 65 kg/m^{2}s.

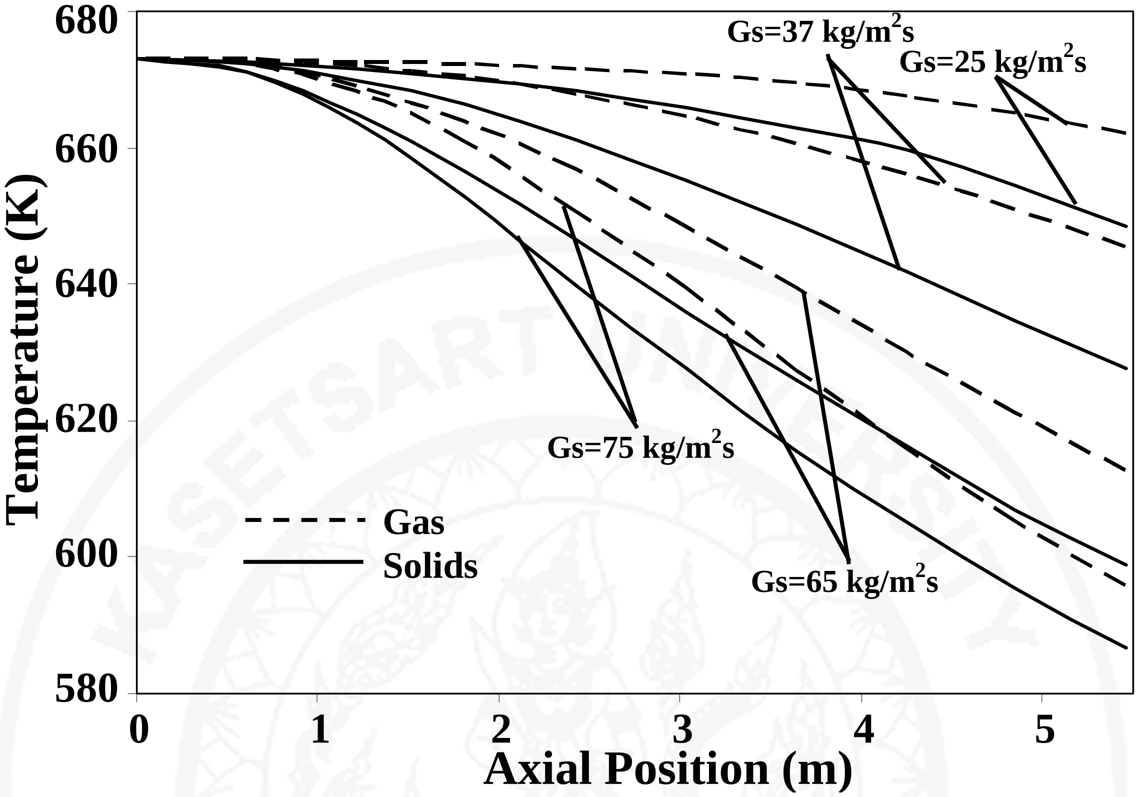

Figure 86 Effect of solids circulation rate on the axial distributions of the gas and catalyst temperatures at the constant superficial gas velocity of 5 m/s and the inlet feed temperature of 673 K.

The effect of solids circulation rate on the feed and the product distributions can be seen in Figure 87. The rate of disappearance of heavy oil increases with solids circulation rate due to the dependency of the reaction rate on the catalyst surface. At high Gs, heavy oil was mostly cracked to gasoline. Increasing of Gs remarkably increases gasoline mass fraction and slightly increases gas mass fraction in the system. Therefore, increasing Gs can be a method to overcome the limitation of inlet feed temperature increase.

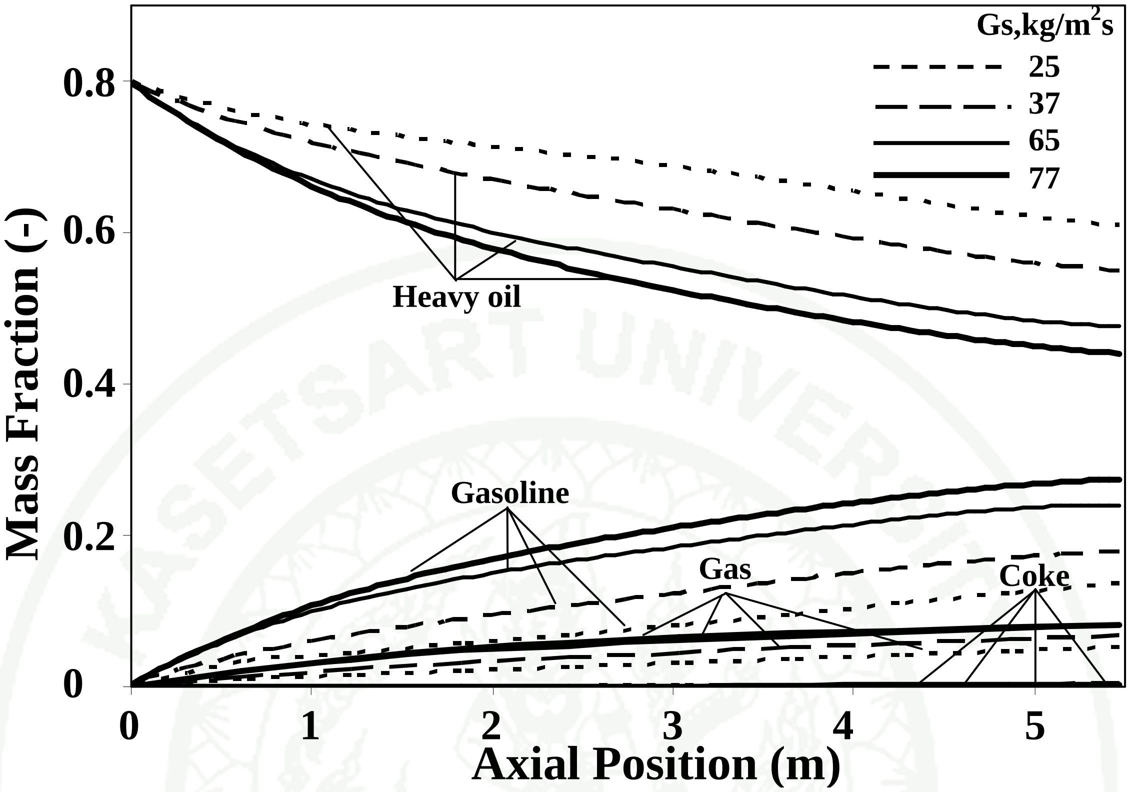

Figure 87 Effect of solids circulation rate on the axial distributions of the feed and products mass fractions at the constant superficial gas velocity of 5 m/s and the inlet feed temperature of 673 K.

3.4 Effect of inlet gas velocity on the reactor performance

The effect of inlet gas velocity on the gas and solids temperature and mass fraction distributions is shown in Figures 88 and 89, respectively. At low superficial gas velocity, the gas and solids temperatures rapidly decrease along the reactor height leading to low temperature at the outlet. The reason is that the gas residence time is high at low inlet gas velocity. In addition, the solids volume fraction increases as decreasing inlet gas velocity (Zhang *et al.,* 1999; Cao and Weinstein, 2000; Zhang *et al.,* 2000; Liu *et al.,* 2001; Bolkan *et al.,* 2003; Li *et al.,* 2004; Nova *et al.,* 2004; Vaishali *et al.,* 2008). These lead to more cracking reaction occurred in the system cause more temperature decrease. Moreover, a more cracking reaction leads to more heavy oil is cracked to the products. This results in low heavy oil mass fraction at the outlet causing a low reaction rate. This low reaction rate leads to the rate of energy transfer between phases and the rate of energy consumption due to cracking reaction are in better balanced. Therefore the outlet temperature difference between phases tends to decrease at low superficial gas velocity. Moreover, it is interesting to note that the heavy oil was mainly cracked to gasoline especially at low superficial gas velocity. At any given axial position, a decreasing inlet gas velocity leads to significantly increasing of gasoline mass fraction and slightly increasing of gas mass fraction. Moreover, less coke mass fraction was formed at various superficial gas velocities.

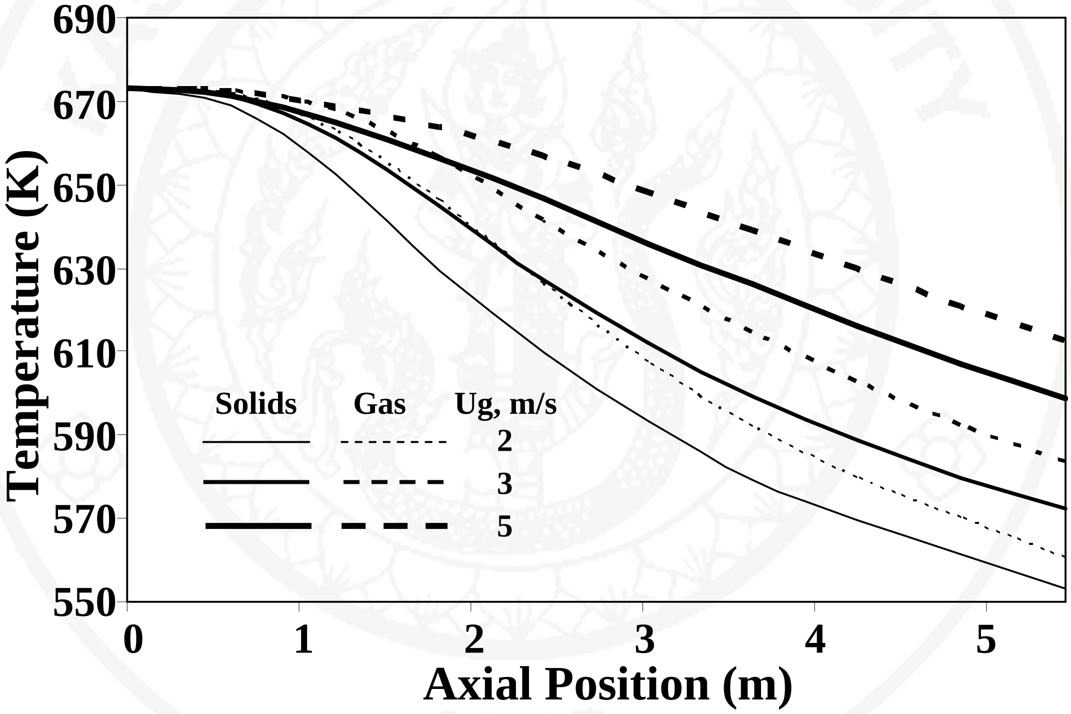

Figure 88 Effect of inlet superficial gas velocity on the axial distributions of the gas and catalyst temperatures at the constant solids circulation rate of 65 kg/m^{2}s and the inlet feed temperature of 673 K.

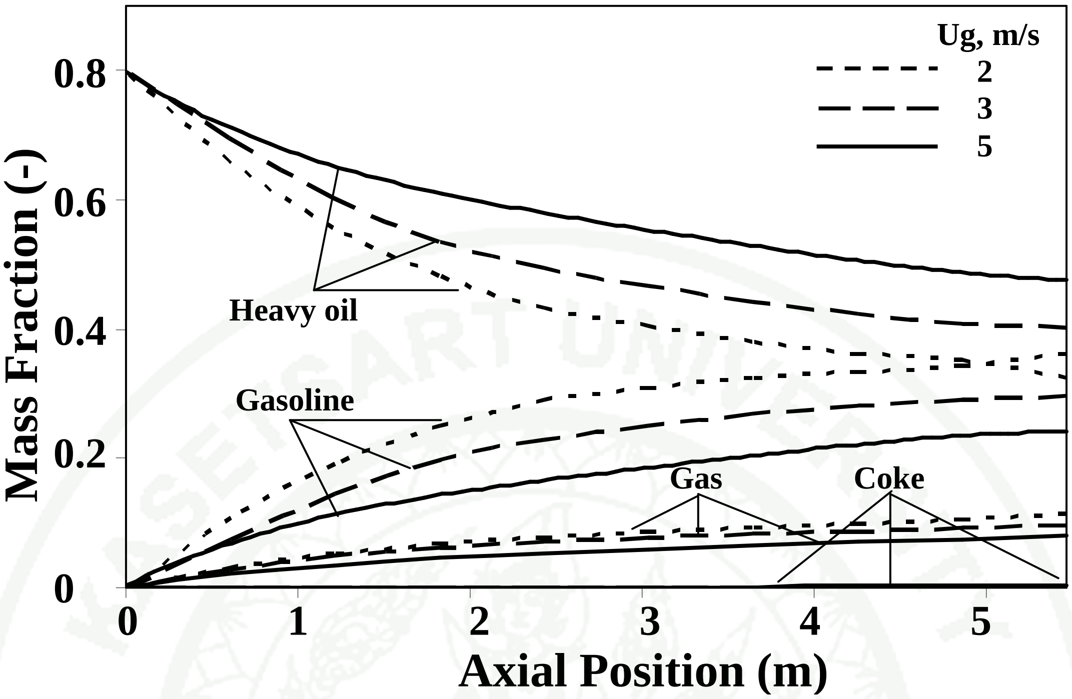

Figure 89 Effect of inlet superficial gas velocity on the axial distributions of the feed and products mass fractions at the constant solids circulation rate of 65 kg/m^{2}s and the inlet feed temperature of 673 K.

3.5 Comparison of the performance in an isothermal reactor and an adiabatic reactor

Modeling of catalytic cracking reaction was carried out in adiabatic and isothermal downer reactors. In an isothermal reactor, the energy balance is neglected and the temperature in the reactor is kept constant and equal to that of inlet temperature. In an adiabatic reactor, the temperature in the reactor can change according to the endothermic catalytic cracking reaction. The reactor temperature should reduce when the reaction progresses adiabatically. Figure 90 shows the product distributions obtained from adiabatic and isothermal cases. According to temperature reduction in the adiabatic reactor, less heavy oil was cracked than that in the isothermal reactor. Moreover, the adiabatic effect is more significant as increasing inlet temperature. At high inlet temperature, the reaction rate is high leading to dramatically decrease of bed temperature as seen in Figure 84. Thus less heavy oil was cracked especially in the outlet section.

3.6 Comparison of simulation results with ideal flow models and axial dispersion model

The cross sectional-averaged of heavy oil and product mass fraction distributions obtained from DEM model were compared with those from the axial dispersion model as shown in Figure 91. The simulations were carried out at various inlet temperatures with solids circulation rate of 65 kg/m^{2}s and superficial gas velocity of 5 m/s. The simulation results obtained from DEM are in agreement with those of axial dispersion model. However, more mass fraction difference between theses models can be observed especially the heavy oil mass fraction near the outlet section of the downer reactor. Practically, the axial mixing in the downer varies along the axial direction. The degree of axial mixing is high near the inlet region due to entrance effect and becomes less mixing further down the column. Thus the Peclet number near the inlet is lower than that near the outlet region. In this axial dispersion simulation, the Peclet number was assumed constant as 100, in the downer reactor. Near the outlet region, the lower heavy oil mass fraction obtained from the axial dispersion model indicated that the Peclet number used in the region is higher than the actual Peclet number in this region. Moreover, the performance in the downer reactor obtained from this simulation was also compared with those in ideal plug flow and ideal mixed flow downer reactors. Figure 92 shows the outlet heavy oil mass fraction in downer reactor obtained from this simulation, axial dispersion model, the ideal plug and mixed flow downer reactors. It was found that the performance obtained from the DEM model is closer to plug flow than mixed flow downer reactors. It can be concluded that the flow behavior in the downer is approaching plug flow behavior.

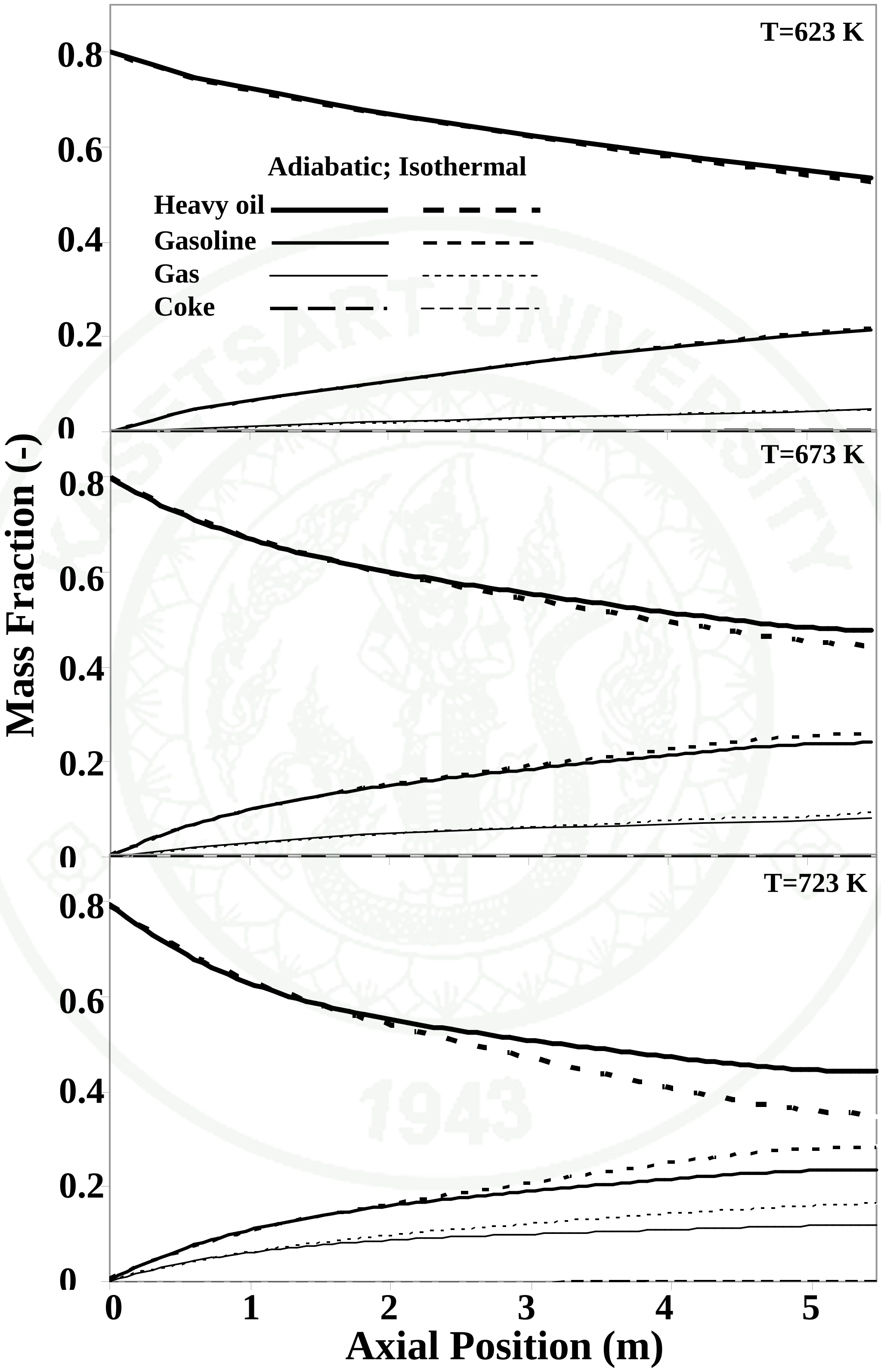

Figure 90 Comparison of feed and product distributions in adiabatic and isothermal reactors at the constant Gs = 65 kg/m^{2}s and Ug = 5 m/s.

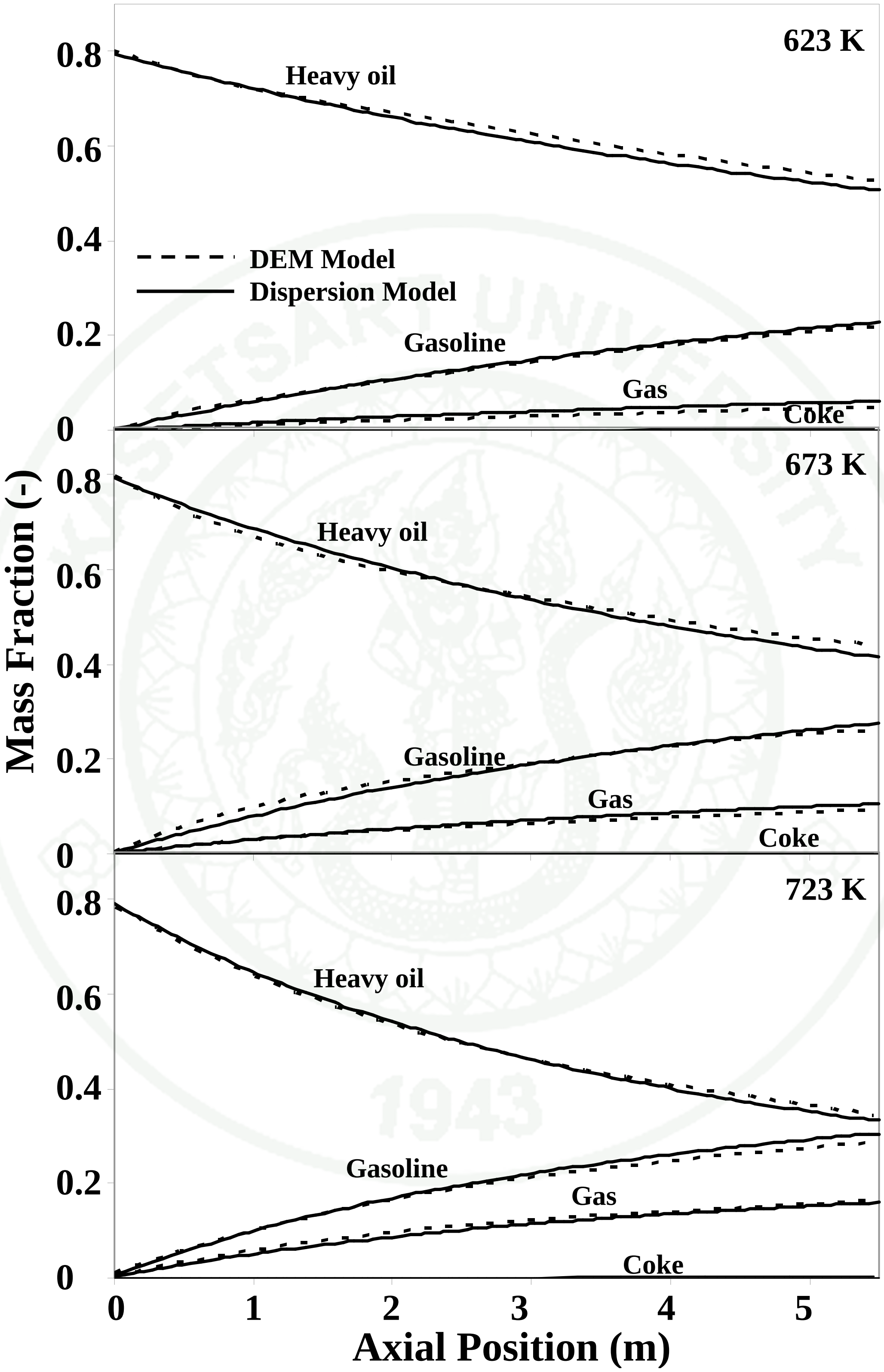

Figure 91 Comparison of species mass fraction obtained from DEM model and Axial dispersion model at the constant Gs = 65 kg/m^{2}s and Ug = 5 m/s.

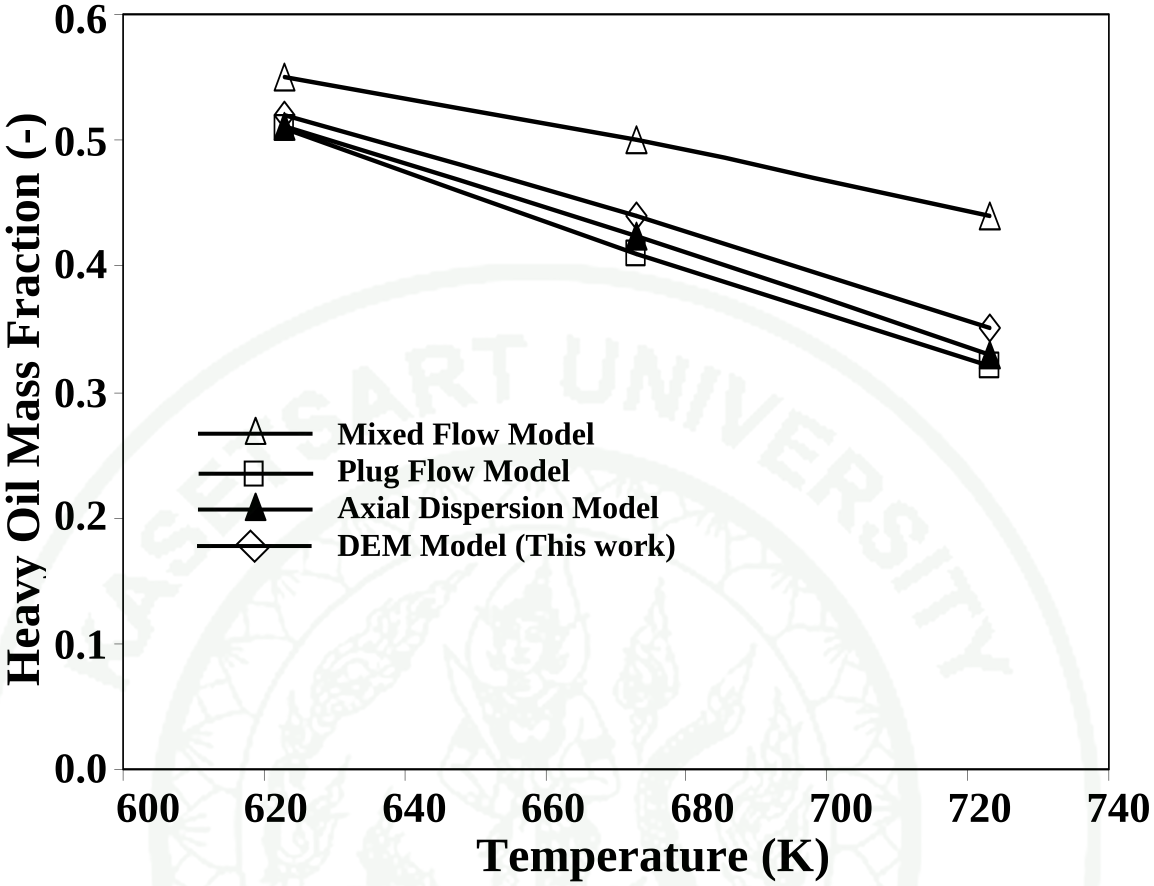

Figure 92 Comparison of outlet heavy oil mass faction in the downer reactors obtained from DEM simulation and Axial dispersion model with the performance in an ideal mixed flow and an ideal plug flow reactor.

CONCLUSION

The hydrodynamics, heat and mass transfer in a downer reactor was numerically studied. The two-fluid model and DEM model were developed for predicting the hydrodynamics, heat and mass transfer in a downer reactor. A 2-D two-fluid model based on kinetic theory of granular flow was used to simulate hydrodynamics and axial mixing of gas and solids phases. The two-fluid model was further used to predict the performance of a compact CO_2 capture fluidized bed reactor. In addition, the DEM model was developed to study the performance of a catalytic cracking downer reactor. The DEM model can predict the local behavior in the system such as velocity, holdup, temperature, and the species concentration. This detail information leads to more understanding of flow behavior and heat and mass transfer in such reactor. The conclusions of these studies are explained below:

1. Hydrodynamics and mixing behavior in a circulating fluidized bed based on the two-fluid model

1.1 Hydrodynamics behavior in a downer reactor

A two-fluid model based on kinetic theory of granular flow model captures the expected flow behavior in the downer, with an almost uniform solids volume fraction in the core region with a high peak in the proximity of the wall. Moreover, the radial distributions of solids volume fraction and gas and solids velocities are more uniform at lower solids circulation rate, in larger particle and heavier particle systems. The solids volumes fraction increases with solids circulation rate and decreasing of superficial gas velocity. In a heavier particle system, the solids volume fraction tends to decrease. Particle size has less effect on solids volume fraction.

1.2 Axial gas and solids mixing in a downer reactor

1.2.1 Gas and solids RTD curves show single narrow peaks. Both gas and solids flows approximate an ideal plug flow behavior (Pe > 100). However the gas phase flow behavior attains higher levels of attainment to ideal plug flow patterns than that of the solids phase.

1.2.2 The axial Peclet numbers for both gas and solids phases increase with increasing of superficial gas velocity and decreasing of solids circulation rate. Larger and heavier particle systems have higher axial Peclet numbers. The correlations of the axial gas and solids Peclet numbers as a function of the operating conditions and the physical properties of gas and solids particles in the system were proposed.

2. Flow behavior and CO_2 removal performance in a circulating fluidized bed reactor

2.1 The solids volume fraction distribution in the riser with upwards solids feeding at the bottom of the reactor is more uniform than that in the riser of the CFB. The CO_2 and H_2O mass fractions in the riser decrease along the reactor height without gas channeling. The CO_2 and H_2O mass fractions in the riser of the CFB are high in the area of gas channeling.

2.2 The solids volume fraction in the downer reactor exhibits much more uniform throughout the reactor as compared with the riser reactor. Large particle cluster formation is near the wall region of the riser. More uniform solids volume fraction and gas and solids velocities in the radial direction cause more uniform CO_2 mass fraction.

2.3 The conversion of CO_2 removal in the riser is higher than that in the downer because of high solids fraction with high gas and solids residence times in the riser. Both in the riser and the downer reactors, the conversions increase with increasing of Gs, decreasing of Ug and particle density. In the downer, the conversion slightly increases with decreasing of particle size, while the larger particle tends to increase the conversion in the riser.

3. Hydrodynamics, heat and mass transfer in a catalytic cracking downer reactor based on DEM model

3.1 The solids volume fraction and gas and solids velocities are almost uniform in the radial direction due to low solids circulation rate. This leads to nearly uniform temperature and heavy oil mass fraction distributions in the lateral direction.

3.3 More heavy oil was cracked to form the products at high feed temperature, increasing of solids circulation rate and decreasing of superficial gas velocity. The gasoline mass fraction increased with increasing of solids circulation rate and inlet temperature and decreasing of superficial gas velocity. However, at very high inlet temperature, the gasoline product undergoes further cracking to form more gaseous products.

3.4 The simulation results obtained from DEM model shows that the mixing in the downer is slightly higher than that obtained in the downer from axial dispersion model. In addition, the downer performance obtained from this simulation is closer to the performance of the ideal plug flow reactor than that of the ideal mixed flow reactor.

LITERATURE CITED

Abul-Hamayel, M.A., 2004. Comparison of downer and riser based fluid catalytic cracking process at high severity condition: a pilot plant study. **Pet. Sci. Technol.** 22: 475-490.

Anderson, T.B. and R. Jackson. 1967. A fluidized mechanical description of fluidized beds: equation of motion. **Ind. Eng. Chem. Fundam.** 8: 137-144.

Bai, D.R., Y. Jin, Z.Q. Yu and J.X. Zhu. 1992. The axial distribution of the crosssectionally averaged voidage in fast fluidized beds. **Powder Technol.** 71: 51–58.

______, Y. Jin, Z-Q. Yu and N-J. Gan. 1991. **Radial profiles of local solid concentration and velocity in a cocurrent downflow fast fluidized bed.** Circulating fluidized bed technology III. Pergamon Press, Toronto.

Ball, J.S. and J.X. Zhu. 2001. A preliminary study into the local solids fluxes in a downer reactor. **Powder Technol.** 114: 96-101.

Bank, J.H., Y.J. Kim, W. Namkung and S.D. Kim. 1999. Radial gas mixing characteristics in a downer reactor. **Korean J. Chem. Eng.** 16: 624-629.

Bin, Y., M.C. Zhang, B.L. Dou, Y.B. Song and J. Wu. 2003. Discrete particle simulation and visualized research of the gas-solid flow in an internally circulating fluidized bed. **Ind. Eng. Chem. Res.** 42: 214-221.

Bolkan, Y., F. Berruti, J. Zhu and B. Milne. 2003. Modeling circulating fluidized bed downers. **Powder Technol.** 4730: 1-16.

Bolkan, T.S. Pugsley and F. Berruti. 1994. Computer simulation of the performance of fluid catalytic cracking risers and downers. **Ind. Eng. Chem. Res.** 33: 3043-3052.

Boonsrirat, A. 2001. **Modeling and simulation in a fluidized bed.** M. Eng. Thesis, Kasetsart University, Thailand.

______, S. Limtrakul, Y. Tsuji, T. Kawaguch and T. Tanaka. 2001. Modeling and simulation of a catalytic gas solid fluidized bed reactor. **the 11th Chemical Engineering National Conference.** Nakornrajsrima, Thailand.

Brust, H. and K.E. Wirth. 2004. Residence time behavior of gas in a downer reactor. **Ind. Eng. Chem. Res.** 43: 5796-5801.

Campbell, C. and D. Wang. 1991. Particle pressures in gas-fluidized beds. **J. Fluid Mech.** 227: 495-508.

Cao, C., Y. Jin, Z. Yu and Z. Wang. 1994. **The gas–solids velocity profiles and slip phenomenon in a concurrent downflow circulating fluidized bed.** pp. 406-413. In A.A. Avidan ed. Circulating Fluidized Bed Technology, AIChE, New York, USA.

Chalermsinsuwan, B., P. Piumsomboon and D. Gidaspow. 2009a. Kinetic theory based computation of PSRI riser: Part I - Estimate of mass transfer coefficient. **Chem. Eng. Sci.** 64: 1195-1211.

______, ______ and ______. 2009b. Kinetic theory based computation of PSRI riser: Part II - Computation of mass transfer coefficient with chemical reaction. **Chem. Eng. Sci.** 64: 1212-1222.

______, ______ and ______. 2010. A CFD design of a carbon dioxide sorption CFB. **AIChE J.** 56:2805-2824.

Chapman, S. and T.G. Cowling. 1970. **The mathematical theory of non-uniform gases,** 3rd edition. Cambridge University Press.

Chen, H. and H. Li. 2004. Characterization of a high-density downer reactor. **Powder Technol.** 146: 84-92.

Cheng, Y., C.N. Wu, J.X. Zhu, F. Wei and Y. Jin. 2008. Downer reactor: from fundamental study to industrial application. **Powder Technol.** 183: 364-384.

______, Y. Guo, F. Wei, Y. Jin and W. Lin. 1999. Modeling the hydrodynamics of downer reactors based on kinetic theory. **Chem. Eng. Sci.** 54: 2019-2027.

Chui E. H., M. A. Douglas and Y. Tan. 2003. Modeling of oxy-fuel combustion for a western Canadian sub-bituminous coal. **Fuel** 82:1201–1210.

Cody, G., D. Goldfarb, G. Storch and A. Norris. 1996. Particle granular temperature in gas-fluidized beds. **Powder Technol.** 87: 211-232.

Cundall, P. A. and O.D.L. Strack. 1979. A discrete numerical model for granular assemblies. **Geotechnique.** 29: 47-65.

Das, A.K., E. Baudrez, G.B. Marin and G.J. Heynderickx. 2003. Three-dimensional simulation of a fluid catalytic cracking riser reactor. **Ind. Eng. Chem. Res.** 42: 2602-2617.

Davidson, J.F. and D. Harrison. 1963. **Fluidised Particles**. Cambridge University Press, Cambridge, England.

Deng, R., F. Wei, T. Liu and Y. Jin. 2002a. Radial behavior in riser and downer during the FCC process. **Chem. Eng. Process.** 41: 259-266.

Deng, R., F. Wei., Y. Jin, Q. Zhang and Y. Jin. 2002b. Experimental study of the deep catalytic cracking process in a downer reactor. **Ind. Eng. Chem. Res.** 41: 6015-6019.

Ding, J. and D. Gidaspow. 1990. A bubbling fluidization model using kinetic theory of granular flow. **AIChE. J.** 36: 523-538.

Ergun, S. 1952. Fluid flow through packed columns. **Chem. Eng. Prog.** 48: 89-94.

Fang, F., Z.S. Li and N.S. Cai. 2009. Continuous CO_2 capture from flue gases using a dual fluidized bed reactor with calcium-based sorbent. **Ind. Eng. Chem. Res.** 48, 11140-11147.

Fei, W., R. Xing, Z. Rujin, L. Guohua and J. Yong. 1997. A dispersion model for fluid catalytic cracking riser and downer reactors. **Ind. Eng. Chem. Res.** 36: 5049-5053.

Fogler, H.S. 1992. Elements of Chemical Reaction Engineering. pp. 838. *In* **Amundson, N. Ed. International Series in the Physical and Chemical Engineering.** Princeton-Hall. Englewood Cliffs, New Jersey, USA.

Fryer, C., O.E., Potter. 1976. Experimental investigation of models for fluidized bed catalytic reactors. **AIChE J.** 22: 38-47.

Gidaspow, D. 1972. Separation of gaseous mixtures by regenerative sorption on porous solids: Part I. A fluid porous solid reaction model with structural changes. In: Li NN (Eds). **Recent development in separation science - vol. II.** US:CRC Press, pp. 59-70.

______ , 1994. **Multiphase flow and fluidization: continuum and kinetic theory descriptions.** Academic Press, New York, America.

Gidaspow, D. and L. Huilin. 1996. Collisional viscosity of FCC particles in a CFB. **AIChE J.** 42: 2503-2510.

______ and M. Onischak. 1975. Process for regenerative sorption of CO_2. **US Patent** 3,865, 924, Feb 19.

Green, D., T. Nelson, B. Turk, P. Box, W. Li, A. Weber and R.Gupta. 2005. Carbon dioxide capture from flue gas using dry regenerable sorbents, **Annual report**, RTI International.

Gupta, H. and L.S. Fan. 2002. Carbonation-calcination cycle using high reactivity calcium oxide for carbon dioxide separation from flue gas. **Ind. Eng. Chem. Res.** 41: 4035-4042.

Hayashi, H., J. Taniuchi, N. Furuyashiki, S. Sugiyama, S. Hirano, N. Shigemoto and T. Nonaka. 1998. Efficient recovery of carbon dioxide from flue gases of coal-fired power plants by cyclic fixed-bed operations over K_2CO_3-on-carbon. **Ind. Eng. Chem. Res.** 37: 185-191.

Herbert, P.M., T.A. Gauthier, C.L. Briens and M.A. Bergougnou. 1995. Application of fiber optic reflection probes to the measurement of local particle velocity and concentration in gas-solid flow. **Powder Technol.** 80: 243-252.

Hirano, S., N. Shigemoto, S. Yamada and H. Hayashi. 1995. Cyclic fixed-bed operations over K_2CO_3-on-carbon for the recovery of carbon dioxide under moist conditions. **Bull. Chem. Soc. Jpn.** 68: 1030-1035.

Holt, N.A.H. 2000. Evaluation of Innovative Fossil Fuel Power Plants with CO_2 Removal", **EPRI Interim report to DOE NETL,** December.

Huang, C., Z. Qian, M. Zhang and F. Wei. 2006. Solids mixing in a down-flow circulating fluidized bed of 0.418-m in diameter. **Powder Technol.** 161: 48-52.

Jassim, M.S. and G.T. Rochelle. 2006. Innovative absorber/stripper configurations for CO_2 capture by aqueous monoethanolamine. **Ind. Eng. Chem. Res.** 45: 2465-2472.

Jiradilok, V., D. Gidaspow and R.W. Breault. 2007. Computation of gas and solid dispersion coefficients in turbulent risers and bubbling beds. **Chem. Eng. Sci.** 62: 3397-3409.

______, ______, R.W. Breault, L.J. Shadle, C. Guenther and S. Shi. 2008. Computation of turbulence and dispersion of cork in the NETL riser. **Chem. Eng. Sci.** 63: 2135-2148.

______, ______, S. Damronglerd, W.J. Koves and R. Mostofi. 2006. Kinetic theory based CFD simulation of turbulent fluidization of FCC particles in a riser. **Chem. Eng. Sci.** 61: 5544-5559.

Johnson, P.C. and R. Jackson. 1987. Frictional-collisional constitutive relations for granular materials, with application to plane shearing. **J. Fluid Mech.** 176: 67-93.

Jung, J., D. Gidaspow and I. Gamwo. 2005. Measurement of two kinds of granular temperatures, stresses, and dispersion in bubbling beds. **Ind. Eng. Chem. Res.** 44: 1329-1341.

Kaneko, Y., T. Shiojima and M. Horio. 1999. DEM simulation of fluidized beds for gas-phase olefin polymerization. **Chem. Eng, Sci.** 54: 5809-5821.

Kashyap, M. 2010. **Measurements and computation of dispersion and mass transfer coefficients in fluidized beds.** Ph.D. thesis. Illinois Institute of Technology, Chicago.

______, D. Gidaspow and M. Driscoll. 2008. Effect of electric field on the hydrodynamics of fluidized nanoparticles. **Powder Technol.** 183: 441-453.

Kato, K., C.H. Wen. 1969. Bubble assemblage model for fluidized bed catalytic reactor. **Chem. Eng. Sci.** 24: 1351-1369.

Khongprom, P., S. Limtrakul and T. Vatanatham. 2008. 3-D simulation of particle and gas flow behavior in a riser with venturi pipe inlet. **Chaing Mai J. Sci.** 35:131-140.

Kimm, N.K., F. Berruti and T.S. Pugsley. 1996. Modeling the hydrodynamics of downflow gas-solids reactors. **Chem. Eng. Sci.** 51: 2661-2666.

Kladthong, P. 2005. **Modeling and simulation of fluidized bed reactor performance for polyethylene polymerization.** M. Eng. Thesis, Kasetsart University, Thailand.

Kuipers, J.A.M., K.J. Van Duin, F.P.H. Van Beckum and W.P.M. Van Swaaji. 1992. A numerical model of gas-fluidized beds. **Chem. Eng. Sci.** 47: 1913–1924.

Kunii, D. and O. Levenspiel. 1990. Fluidized reactor models 1. for bubbling beds of fine, intermediate, and large particles 2. for the lean phase: freeboard and fast fluidization. **Ind. Eng. Chem. Res.** 29: 1226-1234.

______, and ______, 1991. **Fluidization Engineering**. 2nd ed. Butterworth-Heinemann, Boston, MA, America.

Lehner, P. and K.E. Wirth. 1999a. Characterization of the flow pattern in a downer reactor. **Chem. Eng. Sci.** 54: 5471-5483.

______ and ______ 1999b. Effects of the gas solids distributor on the local and overall solids distribution in a downer reactor. **Can. J. Chem. Eng.** 77: 199–206.

Levenspiel, O. 1999. **Chemical Reaction Engineering**. 3rd ed. John Wiley and Sons, USA

Li, S., W. Lin and J. Yao. 2004. Modeling of the hydrodynamics of the fully developed region in a downer reactor. **Powder Technol.** 145: 73-81.

Limtrakul, S., A. Boonsrirat and T. Vatanatham. 2004. DEM modeling and simulation of a catalytic gas–solid fluidized bed reactor: a spouted bed as a case study. **Chem. Eng. Sci.** 59: 5225–5231.

______, A. Chalemwattanatai, K. Ungguràwirote, Y. Tsuji, K. Toshihiro and W. Tanthapanichakoon. 2003. Discrete particle simulation of solids motion in a gas-solid fluidized bed. **Chem. Eng. Sci.** 58: 915-921.

______, N. Thanomboon, T. Vatanatham and P. Khongprom. 2008. DEM modeling and simulation of a down-flow circulating fluidized bed. **Chem. Eng. Commun.** 195: 1328-1344.

______, P. Chaisermtawan, W. Tanthapanichkoon, Y. Tsuji, T. Kawaguchi and T. Tanaka. 2002. Simulation of plug flow of particles in a pipe. pp. 89-94. **The IASTED International Conference, Modeling, Identification and Control,** Austria.

______, P. Kludthong, T. Vatanatham and P. Khongprom. 2006. DEM modeling and simulation for fluidized bed polymerization reactor. **International Conference on Modeling in Chemical and Biological Engineering Sciences, Center of Nanotechnology,** Department of Chemical Engineering and Department of Chemistry, Kasetsart University, Thailand.

Limtrakul, S., W. Rotjanavijit and T. Vathanatham. 2007. Lagrangian modeling and simulation of effect of vibration on cohesive particle movement in a fluidized bed. **Chem. Eng. Sci.** 62: 232-245.

Liu, F., F. Wei, G. Li, Y. Cheng, L. Wang, G. Luo, Q. Li, Z. Qian, Q. Zhang and Y. Jin. 2008. Study on FCC process of a novel riser-downer coupling reactor (III): Industrial trial and CFD modeling. **Ind. Eng. Chem. Res.** 47: 8582-8587.

______, ______, Y. Zheng and Y. Jin. 2006. CFD simulation of fluid catalytic cracking in downer reactors. **Chin. Particu.** 4: 160-166.

Liu, W., K.B. Luo, J.X. Zhu and J.M. Beeckmans. 2001. Characterization of high-density gas-solids downward fluidized flow. **Powder Technol.** 115: 27-35.

Lun, C.K.K., S.B. Savage, D.J. Jeffrey and N. Chepurniy. 1984. Kinetic theories for granular flow: Inelastic particles in couette flow and slightly inelastic particles in a general flow field. **J. Fluid Mech.** 140: 223-256.

Luo, B., D. Yan, Y.L. Ma, S. Barghi and J. Zhu. 2007. Characteristics of gas-solid mass transfer in a cocurrent downflow circulating fluidized bed reactor. **Chem. Eng. J.** 132: 9-15.

Ma, Y. and J.X. Zhu. 1999. Experimental study of heat transfer in a co-current downflow fluidized bed (downer). **Chem. Eng. Sci.** 54: 41-50.

Magnusson, A., Rundqvist, R., Almstedt, A.E. and Johnson, F. 2005. Dual fiber optical probe measurements of solids volume fraction in circulating fluidized bed. **Powder Technol.** 151: 19-26.

Miller, A., Gidaspow, D., 1992. Dense, vertical gas-solid flow in a pipe. **AIChE J.** 38, 1801-1815.

Mindlin, R.D. 1949. Compliance of elastic bodies in contact. **Trans. ASME** 71: A–259.

______ and H. Deresiewicz. 1953. Elastic spheres in contact under varying oblique forces. **ASME J. Appl. Mech.** 20: 327–344.

Moungrat, R., 2001. **Modeling and simulation of heat transfer in a fluidized bed.** M. Eng. Thesis, Kasetsart University, Thailand.

______, S. Limtrakul, Y. Tsuji and T. Kawaguchi. 2001. Modeling and simulation of heat transfer in a fluidized bed. pp. 272. **The 39th Kasetsart University Annual Conference,** Kasetsart Univerity, Thailand.

Nelson, T.O., L.J.I. Coleman, D.A. Green and R.P. Gupta. 2009. The dry carbonate process: Carbon dioxide recovery from power plant flue gas. **Energy Procedia** 1: 1305-1311.

Nova, S., S. Krol and H.D. Lasa. 2004. Particle velocity and particle clustering in down-flow reactors. **Powder Technol.** 148: 172-185.

Onischak, M. and D. Gidaspow. 1972. Separation of gaseous mixtures by regenerative sorption on porous solids. Part II. Regenerative Separation of CO_2. *In* **Recent Developments in Separation Science. Volume II,** Chemical Rubber Co., Cleveland, Ohio, Norman Li, editor., pp. 72-93.

Oyenekan, B.A. 2007. **Modeling of Strippers for CO_2 Capture by Aqueous Amines.** Ph.D. Thesis. University of Texas at Austin.

______ and G.T. Rochelle. 2006. Energy performance of stripper configurations for CO_2 capture by aqueous amines. **Ind. Eng. Chem. Res.** 45: 2457-2464.

Palancz, B.A. 1983. Mathematical model for continuous fluidised bed drying. **Chem. Eng. Sci.** 38: 1045-1059.

Park, S.W., D.H. Sung, B.S. Choi, J.W. Lee and H. Kumazawa. 2006. Carbonation kinetics of potassium carbonate by carbon dioxide. **J. Ind. Eng. Chem.** 12: 522-530.

Park, Y.C., S.H. Jo, C.K. Ryu and C.K. Yi. 2009. Long-term operation of carbon dioxide capture system from a real coal-fired flue gas using dry regenerable potassium-based sorbents. **Energy Procedia** 1: 1235-1239.

Partridge, B.A. and P.N. Rowe. 1966. Chemical reaction in a bubbling gas fluidized bed. **Trans. Inst. Chem. Eng.** 44: T335-T348.

Patankar, S.V. 1980. **Numerical Heat Transfer and Fluid Flow.** Hemisphere, New York.

Polashenski, W. and J. Chen. 1997. Normal solid stress in fluidized beds. **Powder Technol.** 90: 13-23.

_______ and ______ 1999. Measurement of particle stresses in fast fluidized beds. **Ind. Eng. Chem. Res.** 38: 705-713.

Promsarn, S. 2005. **The dispersion model for fluid catalytic cracking of heavy oil from waste plastic in circulating fluidized bed downer.** M.S. Thesis, Kasetsart University.

Qi, X-B., H. Zhang and J. Zhu. 2008. Solids concentration in the fully developed region of circulating fluidized bed downers. **Powder Technol.** 183: 417-425.

Qian, Z., M.H. Zhang, H. Yu and F. Wei. 2004. Radial profiles of particle velocity in a large scale CFB downer. **Int. J. Chem. Reac. Eng.** 2: A7, 1-7.

Ramachandran, P.A. and R.V. Chaudhari. 1983. **Three-phase catalytic reactors.** Gordon and breach science publishers, New York.

Reanthong, T. 2010. **Development of downflow circulating fluidized bed reactor for polypropylene cracking process.** M.S. Thesis, Kasetsart University.

Rodriguez-Rojo, S. and M.J. Cocero. 2009. Supercritical fluidized bed modeling. **J. Supercrit. Fluids** 50: 54-60.

Sinclair, J.L. and R. Jackson. 1989. Gas-particle flow in a vertical pipe with particle-particle interactions. **AIChE. J.** 35: 1473-1486.

Songip, A.R., T. Masuda, H. Kuwahara and K. Hashimoto. 1994. Kinetic studies for catalytic cracking of heavy oil from waste plastics over REY zeolite. **Energy Fuels** 8: 131-135.

Sraphet, C. 2010. **The dispersion model for fluid catalytic cracking of heavy oil from waste plastic with heat loss through the wall in circulating fluidized bed downer reactor.** M.S. Thesis, Kasetsrt University.

Syamlal, M. R-W. 1987. The particle-particle drag term in a multiparticle model of fluidization. **National Technical Information Service**, Springfield, VA.

______ and T. O'Brien T. J. 1993. MFIX Documentation: Volume 1, Theory Guide. **National Technical Information Service.** Springfield

Tartan, M. and D. Gidaspow. 2004. Measurement of granular temperature and stresses in risers. **AIChE J.** 50: 1760-1775.

Thanomboon, N. 2005. **Modeling and simulation of particle and gas movement in a down-flow circulating fluidized bed reactor.** M. Eng. Thesis, Kasetsart University, Thailand.

Toomey, R.D. and H.F. Johnstone. 1952. Gaseous fluidization of solid particles. **Chem. Eng. Progr.** 48: 220-226.

Tsuji, Y., T. Kawaguchi and T. Tanaka. 1993. Discrete particle simulation of two-dimension fluidized bed. **Powder Technol.** 77: 79-87.

______, T. Tanaka and T. Ishida. 1992. Langrangian numerical simulation of plug flow of cohesionless particles in horizontal pipe. **Powder Technol.** 71: 239-250.

Vaishali, S., S. Roy and P.L. Mills. 2008. Hydrodynamic simulation of gas-solids downflow reactors. **Chem. Eng. Sci.** 63: 5107-5119.

Wachem, B.G.M.V., J.C. Schouten, R. Krishna and Bleek, C.M.V.D. 1998. Eulerian simulations of bubbling behaviour in gas-solid fluidized beds. **Comput. Chem. Eng.** 22: s299-s306.

Wang, S., G. Liu, H. Lu, B. Yinghua, J. Ding and Y. Zhao. 2009. Prediction of radial distribution function of particles in a gas-solid fluidized bed using discrete hard-sphere model. **Ind. Eng. Chem. Res.** 48: 1343-1352.

Wang, Y., F. Wei, Z. Wang, W.Y. Jin and Z. Yu. 1998. Radial profiles of solids concentration and velocity in a very fine particle (36 um) riser. **Powder Technol.** 96: 262-266.

Wang, Z., D. Bai and Y. Jin. 1992. Hydrodynamics of concurrent downflow circulating fluidized bed (CDCFB). **Powder Technol.** 70: 271-275.

Weekman, V.W. 1968. A model of catalytic cracking conversion in fixed, moving, and fluid-bed reactors. **Ind. Eng. Chem. Process Design and Development** 7: 90–95.

______ 1969. Kinetics and dynamics of catalytic cracking selectivity in fixed bed reactors. **Ind. Eng. Chem., Process Design and Development** 8: 385.

Wei, F., J. Liu, Y. Jin and Z.Q. Yu. 1997. Hydrodynamics and mixing behaviors in the entrance region of a downer, in: M. Kwauk, J. Li (Eds.), **Circulating Fluidized Bed, vol. V,** Science Press, Beijing, pp. 122–127.

______ and J-X. Zhu. 1996. Effect of flow direction on axial solid dispersion in gas-solid cocurrent upflow and downflow systems. **Chem. Eng. J.** 64: 345-352.

______, Y. Jin, Z.Q. Yu, N.J. Gan and Z.W. Wang. 1994a. Application of phosphor tracer technique to the measurement of solids RTD in circulating fluidized bed. **J. Chem. Ind. Eng. Chin.** 2: 230-235.

______, Z. Wang, Y. Jin, Z. Yu and W. Cheng. 1994b. Dispersion of lateral and axial solids mixing in a flow concurrent downflow circulating fluidized bed. **Powder Technol.** 81: 25-30.

Wei, J. and J.C.W. Kuo. 1969. A lumping analysis in monomolecular reaction systems: analysis of the exactly lumpable system. **Ind. Eng. Chem. Fundam.** 8: 114–123.

Wen, C.Y. and Y.H. Yu. 1966. Mechanics of fluidization. **Chem. Eng. Prog. Symp. Series** 62: 100-111.

Wilke, C.R. 1950. A viscosity equation for gas mixtures. **J. Chem. Phy.** 18: 517-519.

Wu, C., Y. Cheng, Y. Ding and Y. Jin. 2010. CFD-DEM simulation of gas-solid reacting flows in fluid catalytic cracking (FCC) process. **Chem. Eng. Sci.** 65: 542-549.

______, ______ and ______ 2009. Understanding riser and downer based fluid catalytic cracking processes by a comprehensive two-dimensional reactor model. **Ind. Eng. Chem. Res.** 48: 12-26.

Yang, Y.H., 2001. **Effect of bed structure on hydrodynamics and mixing behavior in circulating fluidized bed.** Master Thesis, Tsinghua University, Beijing, China.

Yang, Y.L., J.X. Zhu, Y. Jin and Z.Q. Yu. 1998. Investigation and modeling of cocurrent downflow circulating fluidized bed (downer). **Chem. Eng. Commun.** 170: 133–157.

______, Y. Jin, Z-Q. Yu and Z-W. Wang. 1991. Particle flow-pattern in a dilute concurrent upflow and downflow circulation fluidized bed. *In* **M. Kwauk and M. Hasatani, eds. Fluidization'91, Science and technology,** Science Press, Beijing, China, pp. 66-75.

______, Y. Jin, Z.Q. Yu, Z.W. Wang and D.R. Bai. 1991. The radial distribution of local particle velocity in a dilute circulating fluidized bed, in: P. Basu, M. Horio, M. Hasatani (Eds.), **Circulating Fluidized Bed Technology, vol. III,** Pergamon Press, Toronto, pp. 201–206.

Zhang, H., J-X. Zhu and M.A. Bergougnou. 1999. Hydrodynamics in downflow fluidized beds (1): solids concentration profiles and pressure gradient distributions. **Chem. Eng. Sci.** 54: 5461-5470.

Zhang, M., Z. Qian, H. Yu and F. Wei. 2003a. The near wall dense ring in a large-scale down-flow circulating fluidized bed. **Chem. Eng. J.** 92: 161-167.

______, Z. Qian, H. Yu and F. Wei. 2003b. The solid flow structure in a circulating fluidized bed riser/downer of 0.42-m diameter. **Powder Technol.** 129: 46-52.

Zhang, M.H., K.W. Chu, F. Wei and A.B. Yu. 2008. A CFD-DEM study of the cluster behavior in riser and downer reactors. **Powder Technol.** 184: 151-165.

Zhao, Y., Y. Cheng, C. Wu, Y. Ding and Y. Jin. 2010a. Eulerian-Langrangian simulation of distinct clustering pheomena and RTDs in riser and downer. **Particuo.** 8: 44-50.

_______, Y. Ding, C. Wu and Y. Cheng. 2010b. Numerical simulation of hydrodynamics in downers using a CFD-DEM coupled approach. **Powder Technol.** 199: 2-12.

Zhu, J-X, Z-Q. Yu, Y. Jin, JR. Grace and A. Issangya. 1995. A cocurrent downflow circulating fluidized bed (downer) reactors - a state of the art review. **Can. J. Chem. Eng.** 73: 662-677.

APPENDICIES

Appendix A

Discretization of momentum, mass and heat conservation equations

The finite different method was applied to discretizing the partial differential equations. The calculation of fluid velocity and pressure from the continuity and the momentum equations is showed below.

1. The discretization of fluid motion equation

The continuity and the fluid motion equations were integrated over the control volume as shown in Figure A1.

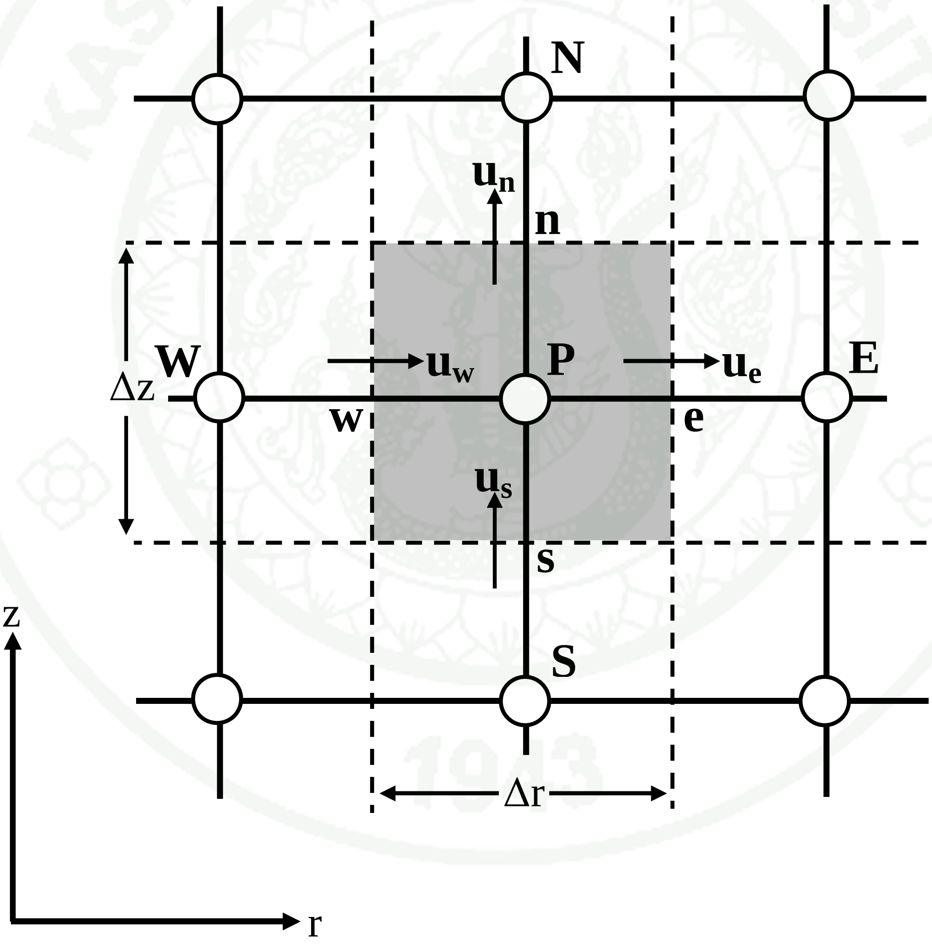

Appendix Figure A1 Control volume used in this study.

Considering the momentum equation in r direction

$$\frac{\partial(\alpha_g \rho u_r)}{\partial t} + \frac{1}{r}\frac{\partial(r\alpha_g \rho u_r u_r)}{\partial r} + \frac{\partial(\alpha_g \rho u_r u_z)}{\partial z} = -\alpha_g \frac{\partial p}{\partial r} + \beta(\bar{v}_r - u_r) \qquad \text{A-1}$$

The integration of the equation of motion in the control volume gives,

$$\int_w^e \int_s^n \int_t^{t+\Delta t} \frac{\partial(\alpha_g \rho u_r)}{\partial t} dtdzdr + \int_t^{t+\Delta t} \int_w^e \int_s^n \frac{1}{r}\frac{\partial(r\alpha_g \rho u_r u_r)}{\partial r} dzdrdt +$$
$$\int_t^{t+\Delta t} \int_w^e \int_s^n \frac{\partial\left(\alpha_g \rho u_r u_z\right)}{\partial z} dzdrdt = -\int_t^{t+\Delta t} \int_w^e \int_s^n \alpha_g \frac{\partial p}{\partial r} dzdrdt + \int_t^{t+\Delta t} \int_w^e \int_s^n \beta\left(\bar{v}_r - u_r\right) \qquad \text{A-2}$$

This equation becomes

$$\left[\left(\alpha_g \rho u_r\right)_P - \left(\alpha_g \rho u_r\right)_P^0\right]\frac{\Delta r \Delta z}{\Delta t} + J_e - J_w + J_n - J_s = -\alpha_{g,P}\left(p_E - p_P\right)\Delta z +$$
$$\beta_P\left(\vec{v}_r - \vec{u}_r\right)\Delta r \Delta z \qquad \text{A-3}$$

where

$$J_e = \frac{1}{r_P}\left(r\alpha_g \rho u_r u_r\right)_e \Delta z \qquad \text{A-4}$$

$$J_w = \frac{1}{r_P}\left(r\alpha_g \rho u_r u_r\right)_w \Delta z \qquad \text{A-5}$$

$$J_n = \left(\alpha_g \rho u_r u_z\right)_n \Delta r \qquad \text{A-6}$$

$$J_s = \left(\alpha_g \rho u_r u_z\right)_s \Delta r \qquad \text{A-7}$$

The discretization of continuity equation is shown here.

$$\frac{\partial(\alpha_g\rho)}{\partial t}+\frac{1}{r}\frac{\partial(r\alpha_g\rho u_r)}{\partial r}+\frac{\partial(\alpha_g\rho u_z)}{\partial z}=0 \qquad \text{A-8}$$

Integrate the equation of motion in the control volume,

$$\int_w^e\int_s^n\int_t^{t+\Delta t}\frac{\partial(\alpha_g\rho)}{\partial t}dtdzdr+\int_t^{t+\Delta t}\int_s^n\int_w^e\frac{1}{r}\frac{\partial(r\alpha_g\rho u_r)}{\partial r}drdzdt+\int_t^{t+\Delta t}\int_w^e\int_s^n\frac{\partial(\alpha_g\rho u_z)}{\partial z}dzdrdt=0 \qquad \text{A-9}$$

This equation becomes

$$\left[(\alpha_g\rho)_P-(\alpha_g\rho)_P^0\right]\frac{\Delta r\Delta z}{\Delta t}+F_e-F_w+F_n-F_s=0 \qquad \text{A-10}$$

where

$$F_e=\frac{1}{r_P}(r\alpha_g\rho u_r)_e\Delta z \qquad \text{A-11}$$

$$F_w=\frac{1}{r_P}(r\alpha_g\rho u_r)_w\Delta z \qquad \text{A-12}$$

$$F_n=(\alpha_g\rho u_z)_n\Delta r \qquad \text{A-13}$$

$$F_s=(\alpha_g\rho u_z)_s\Delta r \qquad \text{A-14}$$

Multiply $(u_r)_p$ with Eq. A-10 and then subtracted to Eq. A-3, this yields

$$\left(\alpha_g \rho\right)_P^0 \left[\left(u_r\right)_P - \left(u_r\right)_P^0\right]\frac{\Delta r \Delta z}{\Delta t} + \left(J_e - \left(u_r\right)_P F_e\right) - \left(J_w - \left(u_r\right)_P F_w\right) + \left(J_n - \left(u_r\right)_P F_n\right) - \left(J_s - \left(u_r\right)_P F_s\right) = -\alpha_{g,P}\left(p_E - p_P\right)\Delta z + \beta_P\left(\bar{v}_r - u_r\right)_P \Delta r \Delta z \qquad \text{A-15}$$

When the system operates at high Reynolds number, the central differencing scheme can not work quite so well. Therefore, the upwind scheme was applied for differencing the velocity in the convection term. This method follows the proper flow of information throughout the flow field.

In the upwind scheme, the velocity in r-direction $(u_r)_e$ can be calculate from the relation

$$\left(u_r\right)_e = \left(u_r\right)_P \qquad \text{when } F_e>0 \qquad \text{A-16}$$

$$\left(u_r\right)_e = \left(u_r\right)_E \qquad \text{when } F_e<0 \qquad \text{A-17}$$

Considering term $(J-(u_r)_P F)$ in Eq. A-15 for each direction (*w*,*e*,*s* and *n*) can be written in the form

$$J_e - \left(u_r\right)_P F_e = a_e\left(\left(u_r\right)_P - \left(u_r\right)_E\right) \qquad \text{A-18}$$

$$J_w - \left(u_r\right)_P F_w = a_w\left(\left(u_r\right)_W - \left(u_r\right)_P\right) \qquad \text{A-19}$$

$$J_n - \left(u_r\right)_P F_n = a_n\left(\left(u_r\right)_P - \left(u_r\right)_N\right) \qquad \text{A-20}$$

$$J_s - \left(u_r\right)_P F_s = a_s\left(\left(u_r\right)_S - \left(u_r\right)_P\right) \qquad \text{A-21}$$

where

$$a_e = \max[-F_e, 0] \qquad \text{A-22}$$

$$a_w = \max[F_w, 0] \qquad \text{A-23}$$

$$a_n = \max[-F_n, 0] \qquad \text{A-24}$$

$$a_s = \max[F_s, 0] \qquad \text{A-25}$$

Rearranging Eq. A-15 gives the form

$$a_P(u_r)_P = a_e(u_r)_E + a_w(u_r)_W + a_n(u_r)_N + a_s(u_r)_S + b_r - \alpha_{g,P}(p_E - p_P)\Delta z \qquad \text{A-26}$$

where

$$a_P = a_e + a_w + a_n + a_s + (\alpha_g \rho)_P^0 \frac{\Delta r \Delta z}{\Delta t} + \beta_P \Delta r \Delta z \qquad \text{A-27}$$

$$b_r = (\alpha_g \rho u_r)_P^0 \frac{\Delta r \Delta z}{\Delta t} + \beta_P (\bar{v}_r)_P \Delta r \Delta z \qquad \text{A-28}$$

2. The discretization of mass conservation equations

2.1 Specie A balance in solids phase

$$\frac{\partial (1-\alpha_g) w_{As}}{\partial t} = \frac{6}{d_p}(1-\alpha_g) k_g (w_A - w_{As}) - (1-\alpha_g) k_{r,A} w_{As} \qquad \text{A-29}$$

The integration of Eq. A-29 in the control volume

$$\int_{w}^{e}\int_{s}^{n}\int_{t}^{t+\Delta t}\frac{\partial\left(1-\alpha_g\right)w_{As}}{\partial t}dtdzdr=\int_{t}^{t+\Delta t}\int_{w}^{e}\int_{s}^{n}\frac{6}{d_p}\left(1-\alpha_g\right)k_g\left(w_A-w_{As}\right)dzdrdt-$$

$$\int_{t}^{t+\Delta t}\int_{w}^{e}\int_{s}^{n}\left(1-\alpha_g\right)k_{r,A}w_{As}dzdrdt \qquad \text{A-30}$$

Obtains

$$\left(1-\alpha_g\right)_P\left(w_{As}\right)_P\frac{\Delta r\Delta z}{\Delta t}-\left(1-\alpha_g\right)_P^0\left(w_{As}\right)_P^0\frac{\Delta r\Delta z}{\Delta t}=\frac{6}{d_p}k_g\left(1-\alpha_g\right)_P\left(w_A\right)_P\Delta r\Delta z$$

$$\frac{6}{d_p}k_g\left(1-\alpha_g\right)_P\left(w_{As}\right)_P\Delta r\Delta z-\left(1-\alpha_g\right)_P k_{r,A}\left(w_{As}\right)_P\Delta r\Delta z \qquad \text{A-31}$$

The rearrangement of Eq. A-31 yields,

$$\left(w_{As}\right)_P=a'\left(w_A\right)_P+b'\left(w_{As}\right)_P^0 \qquad \text{A-32}$$

where

$$a'=\frac{\frac{6}{d_p}k_g\left(1-\alpha_g\right)_P\Delta r\Delta z}{\left(1-\alpha_g\right)_P\frac{\Delta r\Delta z}{\Delta t}+\frac{6}{d_p}k_g\left(1-\alpha_g\right)_P\Delta r\Delta z+\left(1-\alpha_g\right)_P k_{r,A}\Delta r\Delta z} \qquad \text{A-33}$$

$$b'=\frac{\left(1-\alpha_g\right)_P^0\frac{\Delta r\Delta z}{\Delta t}}{\left(1-\alpha_g\right)_P\frac{\Delta r\Delta z}{\Delta t}+\frac{6}{d_p}k_g\left(1-\alpha_g\right)_P\Delta r\Delta z+\left(1-\alpha_g\right)_P k_{r,A}\Delta r\Delta z} \qquad \text{A-34}$$

Eq. A-32 can be written in the form

$$\left(w_{A,s}\right)_P = \frac{a_2}{a_1}\left(w_A\right)_P + \frac{a_3}{a_1} \tag{A-35}$$

where

$$a_1 = \left(1-\alpha_g\right)_P \frac{\Delta r \Delta z}{\Delta t} + \frac{6}{d_p} k_g \left(1-\alpha_g\right)_P \Delta r \Delta z + \left(1-\alpha_g\right)_P k_{r,A} \Delta r \Delta z \tag{A-36}$$

$$a_2 = \frac{6}{d_p} k_g \left(1-\alpha_g\right)_P \Delta r \Delta z \tag{A-37}$$

$$a_3 = \left(1-\alpha_g\right)_P^0 \left(w_{As}\right)_P^0 \frac{\Delta r \Delta z}{\Delta t} \tag{A-38}$$

and

$$k_r = k_0 \exp\left(\frac{E_a}{RT}\right) \tag{A-39}$$

2.2 Specie A balance in gas phase

$$\begin{aligned}\frac{\partial\left(\alpha_g \rho w_A\right)}{\partial t} + \frac{1}{r}\frac{\partial\left(\alpha_g r u_r \rho w_A\right)}{\partial r} + \frac{\partial\left(\alpha_g u_z \rho w_A\right)}{\partial z} &= \frac{1}{r}\frac{\partial}{\partial r}\left(r\frac{\partial\left(\alpha_g D_{A,m} \rho w_A\right)}{\partial r}\right) + \\ &\quad \frac{\partial}{\partial z}\left(\frac{\partial\left(\alpha_g D_{A,m} \rho w_A\right)}{\partial z}\right) + \frac{6}{d_p}\left(1-\alpha_g\right) k_g \rho (w_{A,s} - w_A\end{aligned} \tag{A-40}$$

Integration Eq. A-40 in the control volume gives,

$$\int_w^e\int_s^n\int_t^{t+\Delta t}\frac{\partial\left(\alpha_g\rho w_A\right)}{\partial t}dtdzdr+\int_t^{t+\Delta t}\int_w^e\int_s^n\frac{1}{r}\frac{\partial\left(\alpha_g r u_r\rho w_A\right)}{\partial r}dzdrdt+$$
$$\int_t^{t+\Delta t}\int_w^e\int_s^n\frac{\partial\left(\alpha_g u_z\rho w_A\right)}{\partial z}dzdrdt=\int_t^{t+\Delta t}\int_w^e\int_s^n\frac{1}{r}\frac{\partial}{\partial r}\left(r\frac{\partial\left(\alpha_g D_{A,m}\rho w_A\right)}{\partial r}\right)dzdrdt+$$
$$\int_t^{t+\Delta t}\int_w^e\int_n^s\frac{\partial}{\partial z}\left(\frac{\partial\left(\alpha_g D_{A,m}\rho w_A\right)}{\partial z}\right)dzdrdt+\int_t^{t+\Delta t}\int_w^e\int_s^n\frac{6}{d_p}\left(1-\alpha_g\right)k_g\rho\left(w_{As}-w_A\right)dzdrd \qquad \text{A-41}$$

Then divided by Δt

$$\left[\left(\alpha_g\rho w_A\right)_P-\left(\alpha_g\rho w_A\right)_P^0\right]\frac{\Delta r\Delta z}{\Delta t}+\frac{1}{r}\Delta z\left[\left(\alpha_g r u_r\rho w_A\right)_e-\left(\alpha_g r u_r\rho w_A\right)_w\right]+$$
$$\Delta r\left[\left(\alpha_g u_z\rho w_A\right)_n-\left(\alpha_g u_z\rho w_A\right)_s\right]=\frac{1}{r}\Delta z\left[\left(r\frac{\partial\left(\alpha_g D_{A,m}\rho w_A\right)}{\partial r}\right)_e-\left(r\frac{\partial\left(\alpha_g D_{A,m}\rho w_A\right)}{\partial r}\right)_w\right]+$$
$$\Delta r\left[\left(\frac{\partial\left(\alpha_g D_{A,m}\rho w_A\right)}{\partial z}\right)_n-\left(\frac{\partial\left(\alpha_g D_{A,m}\rho w_A\right)}{\partial z}\right)_s\right]+\frac{6}{d_p}k_g\left(1-\alpha_g\right)_P\rho\left(w_{As}-w_A\right)_P\Delta r\Delta \qquad \text{A-42}$$

Rearrangement this equation obtains the form

$$\left[\left(\alpha_g\rho w_A\right)_P-\left(\alpha_g\rho w_A\right)_P^0\right]\frac{\Delta r\Delta z}{\Delta t}+J_e-J_w+J_n-J_s=$$
$$\frac{6}{d_p}k_g\left(1-\alpha_g\right)_P\rho\left(w_{As}-w_A\right)_P\Delta r\Delta z \qquad \text{A-43}$$

where

$$J_e=\frac{1}{r}\Delta z\left[\left(r\alpha_g u_r\rho w_A\right)-\left(r\frac{\partial\left(\alpha_g D_{A,m}\rho w_A\right)}{\partial r}\right)\right]_e \qquad \text{A-44}$$

$$J_w=\frac{1}{r}\Delta z\left[\left(r\alpha_g u_r\rho w_A\right)-\left(r\frac{\partial\left(\alpha_g D_{A,m}\rho w_A\right)}{\partial r}\right)\right]_w \qquad \text{A-45}$$

$$J_n = \Delta r\left[\left(\alpha_g u_z \rho w_A\right) - \left(\frac{\partial\left(\alpha_g D_{A,m} \rho w_A\right)}{\partial z}\right)\right]_n \tag{A-46}$$

$$J_s = \Delta r\left[\left(\alpha_g u_z \rho w_A\right) - \left(\frac{\partial\left(\alpha_g D_{A,m} \rho w_A\right)}{\partial z}\right)\right]_s \tag{A-47}$$

Multiplied Eq. A-10 with $\left(w_A\right)_P$ and then substrate to Eq. A-43,

$$\begin{aligned}&\left[\left(\alpha_g \rho\right)_P^0 \left(w_A\right)_P - \left(\alpha_g \rho w_A\right)_P^0\right]\frac{\Delta r \Delta z}{\Delta t} + \left(J_e - \left(w_A\right)_P F_e\right) - \left(J_w - \left(w_A\right)_P F_w\right) + \\ &\left(J_n - \left(w_A\right)_P F_n\right) - \left(J_s - \left(w_A\right)_P F_s\right) = \frac{6}{d_p} k_g \left(1 - \alpha_g\right)_P \Delta r \Delta z \rho \left(w_{As} - w_A\right)\end{aligned} \tag{A-48}$$

Eqs. A-44 - A-47 and Eqs. A-11 – A-14 can be written in the form

$$J_e = F_e w_{A,e} - d_e' \tag{A-49}$$

$$J_w = F_w w_{A,w} - d_w' \tag{A-50}$$

$$J_n = F_n w_{A,n} - d_n' \tag{A-51}$$

$$J_s = F_s w_{A,s} - d_s' \tag{A-52}$$

and

$$d_e' = \frac{1}{r}\Delta z\left(r\frac{\partial\left(\alpha_g D_{A,m} \rho w_A\right)}{\partial r}\right)_e \tag{A-53}$$

$$d'_w = \frac{1}{r}\Delta z\left(r\frac{\partial\left(\alpha_g D_{A,m}\rho w_A\right)}{\partial r}\right)_w \tag{A-54}$$

$$d'_n = \Delta r\left(\frac{\partial\left(\alpha_g D_{A,m}\rho w_A\right)}{\partial z}\right)_n \tag{A-55}$$

$$d'_s = \Delta r\left(\frac{\partial\left(\alpha_g D_{A,m}\rho w_A\right)}{\partial z}\right)_s \tag{A-56}$$

Substituted Eqs. A-49 – A-52 into Eq. A-48 gives

$$\begin{aligned}&\left[\left(\alpha_g\rho\right)_P^0\left(w_A\right)_P-\left(\alpha_g\rho w_A\right)_P^0\right]\frac{\Delta r\Delta z}{\Delta t}+\left(F_e w_{A,e}-d'_e-\left(w_A\right)_P F_e\right)-\left(F_w w_{A,w}-d'_w-\left(w_A\right)_P F_w\right)\\&+\left(F_n w_{A,n}-d'_n-\left(w_A\right)_P F_n\right)-\left(F_s w_{A,s}-d'_s-\left(w_A\right)_P F_s\right)=\\&\qquad\qquad\frac{6}{d_p}k_g\left(1-\alpha_g\right)_P\Delta r\Delta z\rho\left(w_{As}-w_A\right)_P\end{aligned} \tag{A-57}$$

Applied upwind differencing scheme for these terms,

$$F_e w_{A,e} - F_e w_{A,P} = \max\left[-F_e,0\right]\left(w_{A,P} - w_{A,E}\right) \tag{A-58}$$

$$F_w w_{A,w} - F_w w_{A,P} = \max\left[F_w,0\right]\left(w_{A,W} - w_{A,P}\right) \tag{A-59}$$

$$F_n w_{A,n} - F_n w_{A,P} = \max\left[-F_n,0\right]\left(w_{A,P} - w_{A,N}\right) \tag{A-60}$$

$$F_s w_{A,s} - F_s w_{A,P} = \max\left[F_s,0\right]\left(w_{A,S} - w_{A,P}\right) \tag{A-61}$$

Eq. A-57 becomes

$$\left[(\alpha_g \rho)_P^0 (w_A)_P - (\alpha_g \rho w_A)_P^0\right]\frac{\Delta r \Delta z}{\Delta t} + \left(\max[-Fe,0](w_{A,P} - w_{A,E}) - d'_e\right) - \left(\max[F_w,0](w_{A,W} - w_{A,P}) - d'_w\right) + \left(\max[-F_n,0](w_{A,P} - w_{A,N}) - d'_n\right) - \left(\max[F_s,0](w_{A,S} - w_{A,P}) - d'_s\right) = \frac{6}{d_p} k_g (1-\alpha_g)_P \Delta r \Delta z \rho (w_{As} - w_A) \qquad \text{A-62}$$

Eqs. A-53 – A-56 can be written in the form

$$d'_e = \frac{1}{r}\Delta z\left(r\frac{\partial(\alpha_g D_{A,m} \rho w_A)}{\partial r}\right)_e = \frac{1}{r}\Delta z(\alpha_g D_{A,m}\rho)_e \frac{\Delta w_{A,e}}{\Delta r} = -d_e(w_{A,P} - w_{A,E}) \qquad \text{A-63}$$

$$d'_w = \frac{1}{r}\Delta z\left(r\frac{\partial(\alpha_g D_{A,m} \rho w_A)}{\partial r}\right)_w = \frac{1}{r}\Delta z(\alpha_g D_{A,m}\rho)_w \frac{\Delta w_{A,w}}{\Delta r} = -d_w(w_{A,W} - w_{A,P}) \qquad \text{A-64}$$

$$d'_n = \Delta r\left(\frac{\partial(\alpha_g D_{A,m} \rho w_A)}{\partial z}\right)_n = \Delta r(\alpha_g D_{A,m}\rho)_n \frac{\Delta w_{A,n}}{\Delta z} = -d_n(w_{A,P} - w_{A,N}) \qquad \text{A-65}$$

$$d'_s = \Delta r\left(\frac{\partial(\alpha_g D_{A,m} \rho w_A)}{\partial r}\right)_n = \Delta r(\alpha_g D_{A,m}\rho)_s \frac{\Delta w_{A,s}}{\Delta z} = -d_s(w_{A,S} - w_{A,P}) \qquad \text{A-66}$$

where

$$d_e = \frac{1}{r}\frac{\Delta z}{\Delta r}(r\alpha_g D_{A,m}\rho)_e \qquad \text{A-67}$$

$$d_w = \frac{1}{r}\frac{\Delta z}{\Delta r}(r\alpha_g D_{A,m}\rho)_w \qquad \text{A-68}$$

$$d_n = \frac{\Delta r}{\Delta z}(\alpha_g D_{A,m}\rho)_n \qquad \text{A-69}$$

$$d_s = \frac{\Delta r}{\Delta z}\left(\alpha_g D_{A,m}\rho\right)_s \tag{A-70}$$

Substituted Eqs. A-63 – A-66 into Eq. A-62, the equation becomes

$$\begin{aligned}
&\left[\left(\alpha_g\rho\right)_P^0\left(w_A\right)_P - \left(\alpha_g\rho w_A\right)_P^0\right]\frac{\Delta r\Delta z}{\Delta t} + \left(\max\left[-F_e,0\right]+d_e\right)\left(w_{A,P}-w_{A,E}\right) - \\
&\qquad \left(\max\left[F_w,0\right]+d_w\right)\left(w_{A,W}-w_{A,P}\right) + \left(\max\left[-F_n,0\right]+d_n\right)\left(w_{A,P}-w_{A,N}\right) - \\
&\qquad \left(\max\left[F_s,0\right]+d_s\right)\left(w_{A,S}-w_{A,P}\right) = \frac{6}{d_p}k_g\left(1-\alpha_g\right)_P\Delta r\Delta z\rho\left(w_{As}-w_A\right)_P
\end{aligned} \tag{A-71}$$

This equation can be written in this form

$$\begin{aligned}
&\left[\left(\alpha_g\rho\right)_P^0\left(w_A\right)_P - \left(\alpha_g\rho w_A\right)_P^0\right]\frac{\Delta r\Delta z}{\Delta t} + a_e\left(w_{A,P}-w_{A,E}\right) - a_w\left(w_{A,W}-w_{A,P}\right) + \\
&\qquad a_n\left(w_{A,P}-w_{A,N}\right) - a_s\left(w_{A,S}-w_{A,P}\right) = \frac{6}{d_p}k_g\left(1-\alpha_g\right)_P\Delta r\Delta z\rho\left(w_{As}-w_A\right)_P
\end{aligned} \tag{A-72}$$

where

$$a_e = \max\left[-F_e,0\right]+d_e \tag{A-73}$$

$$a_w = \max\left[F_w,0\right]+d_w \tag{A-74}$$

$$a_n = \max\left[-F_n,0\right]+d_n \tag{A-75}$$

$$a_s = \max\left[-F_s,0\right]+d_s \tag{A-76}$$

Substituted $w_{As,P}$ from Eq. A-32 into Eq. A-72,

$$\left[(\alpha_g\rho)^0_P (w_A)_P - (\alpha_g \rho w_A)^0_P\right]\frac{\Delta r\Delta z}{\Delta t} + a_e\left(w_{A,P} - w_{A,E}\right) - a_w\left(w_{A,W} - w_{A,P}\right) +$$

$$a_n\left(w_{A,P} - w_{A,N}\right) - a_s\left(w_{A,S} - w_{A,P}\right) = \frac{6}{d_p}k_g\left(1-\alpha_g\right)_P \Delta r\Delta z\rho\left(\frac{a_2}{a_1}w_A + \frac{a_3}{a_1} - w_A\right)_P \qquad \text{A-77}$$

Rearranged Eq. A-77 yields the form

$$w_{A,P}a_{PM} = a_e w_{A,E} + a_w w_{A,W} + a_n w_{A,N} + a_e w_{A,S} + b_A \qquad \text{A-78}$$

where

$$a_{PM} = (\alpha_g\rho)^0_P\frac{\Delta r\Delta z}{\Delta t} + (1-a')\frac{6}{d_p}k_g\left(1-\alpha_g\right)_P\Delta r\Delta z\rho\left(1-\frac{a_2}{a_1}\right) + a_e + a_w + a_n + a_s \qquad \text{A-79}$$

$$b_A = \left(\alpha_g\rho w_A\right)^0_P\frac{\Delta r\Delta z}{\Delta t} + \frac{6}{d_p}k_g\left(1-\alpha_g\right)_P\Delta r\Delta z\rho\frac{a_3}{a_1} \qquad \text{A-80}$$

2.3 Specie B balance in solids phase

$$\frac{\partial\left(1-\alpha_g\right)w_{Bs}}{\partial t} = \frac{6}{d_p}\left(1-\alpha_g\right)k_g\left(w_B - w_{Bs}\right) + \left(1-\alpha_g\right)k_{r,B}w_{As} \qquad \text{A-81}$$

Integrated the conservation equation in the control volume

$$\int_w^e\int_s^n\int_t^{t+\Delta t}\frac{\partial\left(1-\alpha_g\right)w_{Bs}}{\partial t}dtdzdr = \int_t^{t+\Delta t}\int_w^e\int_s^n\frac{6}{d_p}\left(1-\alpha_g\right)k_g\left(w_B - w_{Bs}\right)dzdrdt +$$

$$\int_t^{t+\Delta t}\int_w^e\int_s^n\left(1-\alpha_g\right)k_{r,B}w_{As}dzdrdt \qquad \text{A-82}$$

gives,

$$\left(1-\alpha_g\right)_P \left(w_{Bs}\right)_P \frac{\Delta r \Delta z}{\Delta t} - \left(1-\alpha_g\right)_P^0 \left(w_{Bs}\right)_P^0 \frac{\Delta r \Delta z}{\Delta t} = \frac{6}{d_p} k_g \left(1-\alpha_g\right)_P \left(w_B\right)_P \Delta r \Delta z - \frac{6}{d_p} k_g \left(1-\alpha_g\right)_P \left(w_{Bs}\right)_P \Delta r \Delta z + \left(1-\alpha_g\right)_P k_{r,B} \left(w_{As}\right)_P \Delta r \Delta z \qquad \text{A-83}$$

Rearranged Eq. A-83 in the form,

$$\left(w_{Bs}\right)_P = \frac{a_2}{a_4}\left(w_B\right)_P + \frac{a_5}{a_4} + \frac{a_6}{a_4}\left(w_{As}\right)_P \qquad \text{A-84}$$

where

$$a_2 = \frac{6}{d_p} k_g \left(1-\alpha_g\right)_P \Delta r \Delta z \qquad \text{A-85}$$

$$a_4 = \left(1-\alpha_g\right)_P \frac{\Delta r \Delta z}{\Delta t} + \frac{6}{d_p} k_g \left(1-\alpha_g\right)_P \Delta r \Delta z \qquad \text{A-86}$$

$$a_5 = \left(1-\alpha_g\right)_P^0 \left(w_{Bs}\right)_P^0 \frac{\Delta r \Delta z}{\Delta t} \qquad \text{A-87}$$

$$a_6 = \left(1-\alpha_g\right)_P k_{r,B} \Delta r \Delta z \qquad \text{A-88}$$

2.4 Specie B balance in gas phase

$$\frac{\partial\left(\alpha_g \rho w_B\right)}{\partial t} + \frac{1}{r}\frac{\partial\left(\alpha_g r u_r \rho w_B\right)}{\partial r} + \frac{\partial\left(\alpha_g u_z \rho w_B\right)}{\partial z} = \frac{1}{r}\frac{\partial}{\partial r}\left(r \frac{\partial\left(\alpha_g D_{B,m} \rho w_B\right)}{\partial r}\right) + \frac{\partial}{\partial z}\left(\frac{\partial\left(\alpha_g D_{B,m} \rho w_B\right)}{\partial z}\right) + \frac{6}{d_p}\left(1-\alpha_g\right) k_g \rho \left(w_{Bs} - w_B\right) \qquad \text{A-89}$$

Integrated in the control volume,

$$\begin{aligned}&\int_w^e\int_s^n\int_t^{t+\Delta t}\frac{\partial\left(\alpha_g\rho w_B\right)}{\partial t}dtdzdr+\int_t^{t+\Delta t}\int_w^e\int_s^n\frac{1}{r}\frac{\partial\left(\alpha_g r u_r\rho w_B\right)}{\partial r}dzdrdt+\\&\int_t^{t+\Delta t}\int_w^e\int_s^n\frac{\partial\left(\alpha_g u_z\rho w_B\right)}{\partial z}dzdrdt=\int_t^{t+\Delta t}\int_w^e\int_s^n\frac{1}{r}\frac{\partial}{\partial r}\left(r\frac{\partial\left(\alpha_g D_{B,m}\rho w_B\right)}{\partial r}\right)dzdrdt+\\&\int_t^{t+\Delta t}\int_w^e\int_n^s\frac{\partial}{\partial z}\left(\frac{\partial\left(\alpha_g D_{B,m}\rho w_B\right)}{\partial z}\right)dzdrdt+\int_t^{t+\Delta t}\int_w^e\int_s^n\frac{6}{d_p}\left(1-\alpha_g\right)k_g\rho\left(w_{Bs}-w_B\right)dzdrdt\end{aligned}\qquad\text{A-90}$$

And then divided by Δt

$$\begin{aligned}&\left[\left(\alpha_g\rho w_B\right)_P-\left(\alpha_g\rho w_B\right)_P^0\right]\frac{\Delta r\Delta z}{\Delta t}+\frac{1}{r}\Delta z\left[\left(\alpha_g r u_r\rho w_B\right)_e-\left(\alpha_g r u_r\rho w_B\right)_w\right]+\\&\Delta r\left[\left(\alpha_g u_z\rho w_B\right)_n-\left(\alpha_g u_z\rho w_B\right)_s\right]=\frac{1}{r}\Delta z\left[\left(r\frac{\partial\left(\alpha_g D_{B.m}\rho w_B\right)}{\partial r}\right)_e-\left(r\frac{\partial\left(\alpha_g D_{B,m}\rho w_B\right)}{\partial r}\right)_w\right]+\\&\Delta r\left[\left(\frac{\partial\left(\alpha_g D_{B,m}\rho w_B\right)}{\partial z}\right)_n-\left(\frac{\partial\left(\alpha_g D_{B,m}\rho w_B\right)}{\partial z}\right)_s\right]+\frac{6}{d_p}k_g\left(1-\alpha_g\right)_P\rho\left(w_{Bs}-w_B\right)_P\Delta r\Delta z\end{aligned}\qquad\text{A-91}$$

Rearranged this equation yields,

$$\begin{aligned}&\left[\left(\alpha_g\rho w_B\right)_P-\left(\alpha_g\rho w_B\right)_P^0\right]\frac{\Delta r\Delta z}{\Delta t}+J_e-J_w+J_n-J_s=\\&\qquad\qquad\frac{6}{d_p}k_g\left(1-\alpha_g\right)_P\rho\left(w_{Bs}-w_B\right)_P\Delta r\Delta z\end{aligned}\qquad\text{A-92}$$

where

$$J_e=\frac{1}{r}\Delta z\left[\left(r\alpha_g u_r\rho w_B\right)-\left(r\frac{\partial\left(\alpha_g D_{B,m}\rho w_B\right)}{\partial r}\right)\right]_e\qquad\text{A-93}$$

$$J_w=\frac{1}{r}\Delta z\left[\left(r\alpha_g u_r\rho w_B\right)-\left(r\frac{\partial\left(\alpha_g D_{B,m}\rho w_B\right)}{\partial r}\right)\right]_w\qquad\text{A-94}$$

$$J_n = \Delta r\left[\left(\alpha_g u_z \rho w_B\right) - \left(\frac{\partial\left(\alpha_g D_{B,m}\rho w_B\right)}{\partial z}\right)\right]_n \qquad \text{A-95}$$

$$J_s = \Delta r\left[\left(\alpha_g u_z \rho w_B\right) - \left(\frac{\partial\left(\alpha_g D_{B,m}\rho w_B\right)}{\partial z}\right)\right]_s \qquad \text{A-96}$$

Multiplied Eq. A-10 with $\left(w_B\right)_P$ and then substrate to Eq. A-92,

$$\left[\left(\alpha_g \rho\right)_P^0 \left(w_B\right)_P - \left(\alpha_g \rho w_B\right)_P^0\right]\frac{\Delta r\Delta z}{\Delta t} + \left(J_e - \left(w_B\right)_P F_e\right) - \left(J_w - \left(w_B\right)_P F_w\right) +$$
$$\left(J_n - \left(w_B\right)_P F_n\right) - \left(J_s - \left(w_B\right)_P F_s\right) = \frac{6}{d_p} k_g \left(1-\alpha_g\right)_P \Delta r\Delta z \rho\left(w_{Bs} - w_B\right)_P \qquad \text{A-97}$$

Eqs. A-11 – A-14 and Eqs. A-93 –A-96 can be written in the form

$$J_e = F_e w_{B,e} - d'_e \qquad \text{A-98}$$

$$J_w = F_w w_{B,w} - d'_w \qquad \text{A-99}$$

$$J_n = F_n w_{B,n} - d'_n \qquad \text{A-100}$$

$$J_s = F_s w_{B,s} - d'_s \qquad \text{A-101}$$

and

$$d'_e = \frac{1}{r}\Delta z\left(r\frac{\partial\left(\alpha_g D_{B,m}\rho w_B\right)}{\partial r}\right)_e \qquad \text{A-102}$$

$$d'_w = \frac{1}{r}\Delta z\left(r\frac{\partial\left(\alpha_g D_{B,m}\rho w_B\right)}{\partial r}\right)_w \qquad \text{A-103}$$

$$d'_n = \Delta r\left(\frac{\partial\left(\alpha_g D_{B,m}\rho w_B\right)}{\partial z}\right)_n \qquad \text{A-104}$$

$$d'_s = \Delta r\left(\frac{\partial\left(\alpha_g D_{B,m}\rho w_B\right)}{\partial z}\right)_s \qquad \text{A-105}$$

Substituted Eqs. A-98 – A-101 into Eq. A-97,

$$\begin{aligned}&\left[\left(\alpha_g\rho\right)_P^0\left(w_B\right)_P-\left(\alpha_g\rho w_B\right)_P^0\right]\frac{\Delta r\Delta z}{\Delta t}+\left(F_e w_{B,e}-d'_e-\left(w_B\right)_P F_e\right)-\\&\left(F_w w_{B,w}-d'_w-\left(w_B\right)_P F_w\right)+\left(F_n w_{B,n}-d'_n-\left(w_B\right)_P F_n\right)-\left(F_s w_{B,s}-d'_s-\left(w_B\right)_P F_s\right)=\\&\qquad\qquad\frac{6}{d_p}k_g\left(1-\alpha_g\right)_P\Delta r\Delta z\rho\left(w_{Bs}-w_B\right)_P\end{aligned} \qquad \text{A-106}$$

Applied upwind differencing scheme for these terms,

$$F_e w_{B,e} - F_e w_{B,P} = \max\left[-F_e,0\right]\left(w_{B,P}-w_{B,E}\right) \qquad \text{A-107}$$

$$F_w w_{B,w} - F_w w_{B,P} = \max\left[F_w,0\right]\left(w_{B,W}-w_{B,P}\right) \qquad \text{A-108}$$

$$F_n w_{B,n} - F_n w_{B,P} = \max\left[-F_n,0\right]\left(w_{B,P}-w_{B,N}\right) \qquad \text{A-109}$$

$$F_s w_{B,s} - F_s w_{B,P} = \max\left[F_s,0\right]\left(w_{B,S}-w_{B,P}\right) \qquad \text{A-110}$$

Eq. A-106 becomes

$$\left[(\alpha_g \rho)_P^0 (w_B)_P - (\alpha_g \rho w_B)_P^0\right]\frac{\Delta r \Delta z}{\Delta t} + \left(\max[-Fe,0](w_{B,P} - w_{B,E}) - d'_e\right) - \left(\max[F_w,0](w_{B,W} - w_{B,P}) - d'_w\right) + \left(\max[-F_n,0](w_{B,P} - w_{B,N}) - d'_n\right) - \left(\max[F_s,0](w_{B,S} - w_{B,P}) - d'_s\right) = \frac{6}{d_p} k_g (1-\alpha_g)_P \Delta r \Delta z \rho (w_{Bs} - w_B)_P \qquad \text{A-111}$$

Eqs. A-102 – A-105 can be written in the form

$$d'_e = \frac{1}{r}\Delta z\left(r\frac{\partial(\alpha_g D_{B,m}\rho w_B)}{\partial r}\right)_e = \frac{1}{r}\Delta z(\alpha_g D_{B,m}\rho)_e \frac{\Delta w_{B,e}}{\Delta r} = -d_e(w_{B,P} - w_{B,E}) \qquad \text{A-112}$$

$$d'_w = \frac{1}{r}\Delta z\left(r\frac{\partial(\alpha_g D_{B,m}\rho w_B)}{\partial r}\right)_w = \frac{1}{r}\Delta z(\alpha_g D_{B,m}\rho)_w \frac{\Delta w_{B,w}}{\Delta r} = -d_w(w_{B,W} - w_{B,P}) \qquad \text{A-113}$$

$$d'_n = \Delta r\left(\frac{\partial(\alpha_g D_{B,m}\rho w_B)}{\partial z}\right)_n = \Delta r(\alpha_g D_{B,m}\rho)_n \frac{\Delta w_{B,n}}{\Delta z} = -d_n(w_{B,P} - w_{B,N}) \qquad \text{A-114}$$

$$d'_s = \Delta r\left(\frac{\partial(\alpha_g D_{B,m}\rho w_B)}{\partial r}\right)_n = \Delta r(\alpha_g D_{B,m}\rho)_s \frac{\Delta w_{B,s}}{\Delta z} = -d_s(w_{B,S} - w_{B,P}) \qquad \text{A-115}$$

where

$$d_e = \frac{1}{r}\frac{\Delta z}{\Delta r}(r\alpha_g D_{B,m}\rho)_e \qquad \text{A-116}$$

$$d_w = \frac{1}{r}\frac{\Delta z}{\Delta r}(r\alpha_g D_{B,m}\rho)_w \qquad \text{A-117}$$

$$d_n = \frac{\Delta r}{\Delta z}(\alpha_g D_{B,m}\rho)_n \qquad \text{A-118}$$

$$d_s = \frac{\Delta r}{\Delta z}\left(\alpha_g D_{B,m}\rho\right)_s \qquad \text{A-119}$$

Substitute Eqs. A-112 - A-115 into Eq. A-111, the equation becomes

$$\begin{aligned}\left[\left(\alpha_g\rho\right)_P^0\left(w_B\right)_P - \left(\alpha_g\rho w_B\right)_P^0\right]\frac{\Delta r\Delta z}{\Delta t} + \left(\max\left[-F_e,0\right]+d_e\right)\left(w_{B,P}-w_{B,E}\right) - \\ \left(\max\left[F_w,0\right]+d_w\right)\left(w_{B,W}-w_{B,P}\right) + \left(\max\left[-F_n,0\right]+d_n\right)\left(w_{B,P}-w_{B,N}\right) - \\ \left(\max\left[F_s,0\right]+d_s\right)\left(w_{B,S}-w_{B,P}\right) = \frac{6}{d_p}k_g\left(1-\alpha_g\right)_P\Delta r\Delta z\rho\left(w_{Bs}-w_B\right)_P \qquad \text{A-120}\end{aligned}$$

This equation can be written in this form

$$\begin{aligned}\left[\left(\alpha_g\rho\right)_P^0\left(w_B\right)_P - \left(\alpha_g\rho w_B\right)_P^0\right]\frac{\Delta r\Delta z}{\Delta t} + a_e\left(w_{B,P}-w_{B,E}\right) - a_w\left(w_{B,W}-w_{B,P}\right) + \\ a_n\left(w_{B,P}-w_{B,N}\right) - a_s\left(w_{B,S}-w_{B,P}\right) = \frac{6}{d_p}k_g\left(1-\alpha_g\right)_P\Delta r\Delta z\rho\left(w_{Bs}-w_B\right)_P \qquad \text{A-121}\end{aligned}$$

where

$$a_e = \max\left[-F_e,0\right]+d_e \qquad \text{A-122}$$

$$a_w = \max\left[F_w,0\right]+d_w \qquad \text{A-123}$$

$$a_n = \max\left[-F_n,0\right]+d_n \qquad \text{A-124}$$

$$a_s = \max\left[-F_s,0\right]+d_s \qquad \text{A-125}$$

Substitute $w_{Bs,P}$ from Eq. A-84 into Eq. A-121,

$$\left[\left(\alpha_g \rho\right)_P^0 \left(w_B\right)_P - \left(\alpha_g \rho w_B\right)_P^0\right]\frac{\Delta r \Delta z}{\Delta t} + a_e\left(w_{B,P} - w_{B,E}\right) - a_w\left(w_{B,W} - w_{B,P}\right) +$$

$$a_n\left(w_{B,P} - w_{B,N}\right) - a_s\left(w_{B,S} - w_{B,P}\right) = \frac{6}{d_p} k_g \left(1 - \alpha_g\right)_P \Delta r \Delta z \rho \left(\frac{a_2}{a_4} w_B + \frac{a_5}{a_4} + \frac{a_6}{a_4} w_{As} - w_B\right)_P \qquad \text{A-126}$$

Rearranged Eq. A-126

$$w_{B,P} b_{PM} = a_e w_{B,E} + a_w w_{B,W} + a_n w_{B,N} + a_e w_{B,S} + b_B \qquad \text{A-127}$$

where

$$b_{PM} = \left(\alpha_g \rho\right)_P^0 \frac{\Delta r \Delta z}{\Delta t} + \left(1 - \frac{a_2}{a_4}\right)\frac{6}{d_p} k_g \left(1 - \alpha_g\right)_P \Delta r \Delta z \rho + a_e + a_w + a_n + a_s \qquad \text{A-128}$$

$$b_B = \left(\alpha_g \rho w_B\right)_P^0 \frac{\Delta r \Delta z}{\Delta t} + \left(\frac{a_5}{a_4} + \frac{a_6}{a_4} w_{As}\right)\frac{6}{d_p} k_g \left(1 - \alpha_g\right)_P \Delta r \Delta z \rho \qquad \text{A-129}$$

3. The discretization of energy conservation equation

3.1 Energy balance in solids phase

$$\frac{\partial\left(\left(1 - \alpha_g\right)\rho_s C_{ps} T_s\right)}{\partial t} = \frac{6}{d_p}\left(1 - \alpha_g\right) h\left(T - T_s\right) + \left(1 - \alpha_g\right)\left(-\Delta H\right)\left(k_{r,A} w_{As}\right) \qquad \text{A-130}$$

Integrates in the control volume,

$$\int_w^e \int_s^n \int_t^{t+\Delta t} \frac{\partial\left(\left(1 - \alpha_g\right)\rho_s C_{ps} T_s\right)}{\partial t} dt dz dr = \int_t^{t+\Delta t} \int_s^n \int_w^e \frac{6}{d_p}\left(1 - \alpha_g\right) h\left(T - T_s\right) dr dz dt +$$

$$\int_t^{t+\Delta t} \int_s^n \int_w^e \left(1 - \alpha_g\right)\left(-\Delta H\right)\left(k_{r,A} w_{As}\right) dr dz dt \qquad \text{A-131}$$

gives,

$$\left[\left(1-\alpha_g\right)\rho_s C_{ps} T_s\right]_P \frac{\Delta z \Delta r}{\Delta t} - \left[\left(1-\alpha_g\right)\rho_s C_{ps} T_s\right]_P^0 \frac{\Delta z \Delta r}{\Delta t} = \frac{6}{d_p}\left[\left(1-\alpha_g\right)hT\right]_P \Delta r \Delta z - \frac{6}{d_p}\left[\left(1-\alpha_g\right)hT_s\right]_P \Delta r \Delta z + \left(-\Delta H\right)\left[\left(1-\alpha_g\right)\left(k_{r,A} w_{As}\right)\right]_P \Delta r \Delta z \qquad \text{A-132}$$

Rearranged this equation,

$$T_{s,P} = \frac{a_{11}}{a_{13}}\left(T\right)_P + \frac{a_{12}}{a_{13}}\left(T_s\right)_P^0 + \frac{c_2}{a_{13}} \qquad \text{A-133}$$

where

$$a_{11} = \frac{6}{d_p}\left[\left(1-\alpha_g\right)h\right]_P \Delta r \Delta z \qquad \text{A-134}$$

$$a_{12} = \left[\left(1-\alpha_g\right)\rho_s C_{ps}\right]_P^0 \frac{\Delta r \Delta z}{\Delta t} \qquad \text{A-135}$$

$$a_{13} = \left[\left(1-\alpha_g\right)\rho_s C_{ps}\right]_P \frac{\Delta r \Delta z}{\Delta t} + \frac{6}{d_p}\left[\left(1-\alpha_g\right)h\right]_P \Delta r \Delta z \qquad \text{A-136}$$

$$c_2 = \left(-\Delta H\right)\left[\left(1-\alpha_g\right)\left(k_{r,A} w_{As}\right)\right]_P \Delta r \Delta z \qquad \text{A-137}$$

3.2 Energy balance in gas phase

$$\frac{\partial\left(\alpha_g \rho_g \hat{C}_{pg} T\right)}{\partial t} + \frac{1}{r}\frac{\partial\left(r\alpha_g \rho_g \hat{C}_{pg} u_r T\right)}{\partial r} + \frac{\partial\left(\alpha_g \rho_g \hat{C}_{pg} u_z T\right)}{\partial z} = \frac{1}{r}\frac{\partial}{\partial r}\left(r\alpha_g \lambda_g \frac{\partial T}{\partial r}\right) + \frac{\partial}{\partial z}\left(\alpha_g \lambda_g \frac{\partial T}{\partial z}\right) + \frac{6}{d_p}\left(1-\alpha_g\right)h\left(T_s - T\right) \qquad \text{A-138}$$

Integrated in the control volume

$$\int_s^n\int_w^e\int_t^{t+\Delta t}\frac{\partial\left(\alpha_g\rho_g\hat{C}_{pg}T\right)}{\partial t}dtdrdz+\int_t^{t+\Delta t}\int_s^n\int_w^e\frac{1}{r}\frac{\partial\left(r\alpha_g\rho_g\hat{C}_{pg}u_rT\right)}{\partial r}drdzdt+$$
$$\int_t^{t+\Delta t}\int_w^e\int_s^n\frac{\partial\left(\alpha_g\rho_g\hat{C}_{pg}u_zT\right)}{\partial z}dzdrdt=\int_t^{t+\Delta t}\int_s^n\int_w^e\frac{1}{r}\frac{\partial}{\partial r}\left(r\alpha_g\lambda_g\frac{\partial T}{\partial r}\right)drdzdt+$$
$$\int_t^{t+\Delta t}\int_w^e\int_s^n\frac{\partial}{\partial z}\left(\alpha_g\lambda_g\frac{\partial T}{\partial z}\right)dzdrdt+\int_t^{t+\Delta t}\int_s^n\int_w^e\frac{6}{d_p}\left(1-\alpha_g\right)h\left(T_s-T\right)drdzdt \qquad \text{A-139}$$

And then divided by Δt

$$\left[\left(\alpha_g\rho_g\hat{C}_{pg}T\right)_P-\left(\alpha_g\rho_g\hat{C}_{pg}T\right)_P^0\right]\frac{\Delta r\Delta z}{\Delta t}+\frac{1}{r}\Delta z\left[\left(r\alpha_g\rho_g\hat{C}_{pg}u_rT\right)_e-\left(r\alpha_g\rho_g\hat{C}_{pg}u_rT\right)_w\right.$$
$$\left.+\Delta r\left[\left(\alpha_g\rho_g\hat{C}_{pg}u_zT\right)_n-\left(\alpha_g\rho_g\hat{C}_{pg}u_zT\right)_s\right]=\frac{1}{r}\Delta z\left[\left(r\alpha_g\lambda_g\frac{\partial T}{\partial r}\right)_e-\left(r\alpha_g\lambda_g\frac{\partial T}{\partial r}\right)_w\right]+\right.$$
$$\Delta r\left[\left(\alpha_g\lambda_g\frac{\partial T}{\partial z}\right)_n-\left(\alpha_g\lambda_g\frac{\partial T}{\partial z}\right)_s\right]+\frac{6}{d_p}\Delta r\Delta z\left(1-\alpha_g\right)_P h\left(T_s-T\right)_P \qquad \text{A-140}$$

rearranged this equation,

$$\left[\left(\alpha_g\rho_g\hat{C}_{pg}T\right)_P-\left(\alpha_g\rho_g\hat{C}_{pg}T\right)_P^0\right]\frac{\Delta r\Delta z}{\Delta t}+J_e-J_w+J_n-J_s=$$
$$\frac{6}{d_p}\Delta r\Delta z\left(1-\alpha_g\right)_P h\left(T_s-T\right)_P \qquad \text{A-141}$$

where

$$J_e=\frac{1}{r}\Delta z\left[\left(r\alpha_g\rho_g\hat{C}_{pg}u_rT\right)-\left(r\alpha_g\lambda_g\frac{\partial T}{\partial r}\right)\right]_e \qquad \text{A-142}$$

$$J_w = \frac{1}{r}\Delta z\left[\left(r\alpha_g \rho_g \hat{C}_{pg} u_r T\right) - \left(r\alpha_g \lambda_g \frac{\partial T}{\partial r}\right)\right]_w \quad \text{A-143}$$

$$J_n = \Delta r\left[\left(\alpha_g \rho_g \hat{C}_{pg} u_z T\right) - \left(\alpha_g \lambda_g \frac{\partial T}{\partial z}\right)\right]_n \quad \text{A-144}$$

$$J_s = \Delta r\left[\left(\alpha_g \rho_g \hat{C}_{pg} u_z T\right) - \left(\alpha_g \lambda_g \frac{\partial T}{\partial z}\right)\right]_s \quad \text{A-145}$$

Multiply the continuity equation with $\hat{\mathrm{C}}_{\mathrm{pg}}$

$$\frac{\partial\left(\alpha_g \rho\right)}{\partial t} + \frac{1}{r}\frac{\partial\left(r\alpha_g \rho u_r\right)}{\partial r} + \frac{\partial\left(\alpha_g \rho u_z\right)}{\partial z} = 0 \quad \text{A-146}$$

Then integrates the equation of motion in the control volume

$$\int_w^e\int_s^n\int_t^{t+\Delta t} \frac{\partial\left(\alpha_g \rho_g \hat{C}_{pg}\right)}{\partial t} dtdzdr + \int_t^{t+\Delta t}\int_s^n\int_w^e \frac{1}{r}\frac{\partial\left(r\alpha_g \rho_g \hat{C}_{pg} u_r\right)}{\partial r} drdzdt + \int_t^{t+\Delta t}\int_w^e\int_s^n \frac{\partial\left(\alpha_g \rho_g \hat{C}_{pg} u_z\right)}{\partial z} dzdrdt = 0 \quad \text{A-147}$$

This equation becomes

$$\left[\left(\alpha_g \rho_g \hat{C}_{pg}\right)_P - \left(\alpha_g \rho_g \hat{C}_{pg}\right)_P^0\right]\frac{\Delta r \Delta z}{\Delta t} + F_e - F_w + F_n - F_s = 0 \quad \text{A-148}$$

where

$$F_e = \frac{1}{r_P}\left(r\alpha_g \rho_g \hat{C}_{pg} u_r\right)_e \Delta z \quad \text{A-149}$$

$$F_w = \frac{1}{r_P}\left(r\alpha_g \rho_g \hat{C}_{pg} u_r\right)_w \Delta z \qquad \text{A-150}$$

$$F_n = \left(\alpha_g \rho_g \hat{C}_{pg} u_z\right)_n \Delta r \qquad \text{A-151}$$

$$F_s = \left(\alpha_g \rho_g \hat{C}_{pg} u_z\right)_s \Delta r \qquad \text{A-152}$$

Multiply $(T)_p$ with Eq. A-148 and then subtracted to Eq. A-141, this yields

$$\begin{aligned}&\left(\alpha_g \rho_g \hat{C}_{pg}\right)_P^0 \left[(T)_P - (T)_P^0\right]\frac{\Delta r \Delta z}{\Delta t} + \left(J_e - (T)_P F_e\right) - \left(J_w - (T)_P F_w\right) + \left(J_n - (T)_P F_n\right) \\ &- \left(J_s - (T)_P F_s\right) = \frac{6}{d_p}\Delta r \Delta z\left(1-\alpha_g\right)_P h\left(T_s - T\right)_P \end{aligned} \qquad \text{A-153}$$

Eqs. A142 – A-145 and Eqs. A-149 – A-152 can be written in the form

$$J_e = F_e T_e - d'_e \qquad \text{A-154}$$

$$J_w = F_w T_w - d'_w \qquad \text{A-155}$$

$$J_n = F_n T_n - d'_n \qquad \text{A-156}$$

$$J_s = F_s T_s - d'_s \qquad \text{A-157}$$

and

$$d'_e = \frac{1}{r}\Delta z\left(r\alpha_g \lambda_g \frac{\partial T}{\partial r}\right)_e \qquad \text{A-158}$$

$$d'_w = \frac{1}{r}\Delta z\left(r\alpha_g\lambda_g\frac{\partial T}{\partial r}\right)_w \qquad \text{A-159}$$

$$d'_n = \Delta r\left(\alpha_g\lambda_g\frac{\partial T}{\partial z}\right)_n \qquad \text{A-160}$$

$$d'_s = \Delta r\left(\alpha_g\lambda_g\frac{\partial T}{\partial z}\right)_s \qquad \text{A-161}$$

Substituted Eqs. A-154 – A-157 into Eq. A-153,

$$\begin{aligned}&\left(\alpha_g\rho_g\hat{C}_{pg}\right)_P^0\left[(T)_P-(T)_P^0\right]\frac{\Delta r\Delta z}{\Delta t}+\left(F_eT_e-d'_e-(T)_PF_e\right)-\left(F_wT_w-d'_w-(T)_PF_w\right)+\\&\left(F_nT_n-d'_n-(T)_PF_n\right)-\left(F_sT_s-d'_s-(T)_PF_s\right)=\frac{6}{d_p}\Delta r\Delta z\left(1-\alpha_g\right)_Ph\left(T_s-T\right)_P\end{aligned} \qquad \text{A-162}$$

Applied upwind differencing scheme for these terms,

$$F_eT_e-F_eT_P=\max[-F_e,0](T_P-T_E) \qquad \text{A-163}$$

$$F_wT_w-F_wT_P=\max[F_w,0](T_W-T_P) \qquad \text{A-164}$$

$$F_nT_n-F_nT_P=\max[-F_n,0](T_P-T_N) \qquad \text{A-165}$$

$$F_sT_s-F_sT_P=\max[F_s,0](T_S-T_P) \qquad \text{A-166}$$

Eq. A-162 becomes

$$\begin{aligned}&\left(\alpha_g \rho_g \hat{C}_{pg}\right)_P^0 \left[(T)_P - (T)_P^0\right]\frac{\Delta r \Delta z}{\Delta t} + \left(\max[-Fe,0](T_P - T_E) - d'_e\right) - \\ &\qquad \left(\max[F_w,0](T_W - T_P) - d'_w\right) + \left(\max[-F_n,0](T_P - T_N) - d'_n\right) - \\ &\qquad\qquad \left(\max[F_s,0](T_S - T_P) - d'_s\right) = \frac{6}{d_p} h\left(1-\alpha_g\right)_P \Delta r \Delta z\left(T_s - T\right)_P \end{aligned} \quad \text{A-167}$$

Eqs. A-158 – A-161 can be written in the form

$$d'_e = \frac{1}{r}\Delta z\left(r\alpha_g k\frac{\partial T}{\partial r}\right)_e = \frac{1}{r}\Delta z\left(r\alpha_g k\right)_e \frac{\Delta T_e}{\Delta r} = -d_e\left(T_P - T_E\right) \quad \text{A-168}$$

$$d'_w = \frac{1}{r}\Delta z\left(r\alpha_g \lambda_g\frac{\partial T}{\partial r}\right)_w = \frac{1}{r}\Delta z\left(r\alpha_g \lambda_g\right)_w \frac{\Delta T_w}{\Delta r} = -d_w\left(T_W - T_P\right) \quad \text{A-169}$$

$$d'_n = \Delta r\left(\alpha_g \lambda_g\frac{\partial T}{\partial z}\right)_n = \Delta r\left(\alpha_g \lambda_g\right)_n \frac{\Delta T_n}{\Delta z} = -d_n\left(T_P - T_N\right) \quad \text{A-170}$$

$$d'_s = \Delta r\left(\alpha_g \lambda_g\frac{\partial T}{\partial r}\right)_n = \Delta r\left(\alpha_g \lambda_g\right)_s \frac{\Delta T_s}{\Delta z} = -d_s\left(T_S - T_P\right) \quad \text{A-171}$$

where

$$d_e = \frac{1}{r}\frac{\Delta z}{\Delta r}\left(r\alpha_g k\right)_e \quad \text{A-172}$$

$$d_w = \frac{1}{r}\frac{\Delta z}{\Delta r}\left(r\alpha_g k\right)_w \quad \text{A-173}$$

$$d_n = \frac{\Delta r}{\Delta z}\left(\alpha_g k\right)_n \quad \text{A-174}$$

$$d_s = \frac{\Delta r}{\Delta z}\left(\alpha_g k\right)_s \qquad \text{A-175}$$

Substitute Eqs. A-168 – A-171 into Eq. A-167, the equation becomes

$$\begin{aligned}\left(\alpha_g \rho_g \hat{C}_{pg}\right)_P^0 \left[(T)_P - (T)_P^0\right]\frac{\Delta r \Delta z}{\Delta t} &+ \left(\max\left[-Fe,0\right] + d_e\right)\left(T_P - T_E\right) - \\ &\left(\max\left[F_w,0\right] + d_w\right)\left(T_W - T_P\right) + \left(\max\left[-F_n,0\right] + d_n\right)\left(T_P - T_N\right) - \\ &\left(\max\left[F_s,0\right] + d_s\right)\left(T_S - T_P\right) = \frac{6}{d_p} h\left(1-\alpha_g\right)_P \Delta r \Delta z \left(T_s - T\right)_P\end{aligned} \qquad \text{A-176}$$

This equation can be written in this form

$$\begin{aligned}\left(\alpha_g \rho_g \hat{C}_{pg}\right)_P^0 \left[(T)_P - (T)_P^0\right]\frac{\Delta r \Delta z}{\Delta t} + a_e\left(T_P - T_E\right) - a_w\left(T_W - T_P\right) + a_n\left(T_P - T_N\right) - \\ a_s\left(T_S - T_P\right) = \frac{6}{d_p} h\left(1-\alpha_g\right)_P \Delta r \Delta z \left(T_s - T\right)_P\end{aligned} \qquad \text{A-177}$$

where

$$a_e = \max\left[-F_e,0\right] + d_e \qquad \text{A-178}$$

$$a_w = \max\left[F_w,0\right] + d_w \qquad \text{A-179}$$

$$a_n = \max\left[-F_n,0\right] + d_n \qquad \text{A-180}$$

$$a_s = \max\left[-F_s,0\right] + d_s \qquad \text{A-181}$$

Substituted $T_{s,P}$ from Eq. A-133 into Eq. A-177

$$\left(\alpha_g \rho_g \hat{C}_{pg}\right)_P^0 \left[(T)_P - (T)_P^0\right]\frac{\Delta r\Delta z}{\Delta t} + a_e\left(T_P - T_E\right) - a_w\left(T_W - T_P\right) + a_n\left(T_P - T_N\right) - a_s\left(T_S - T_P\right) = \frac{6}{d_p} h\left(1-\alpha_g\right)_P \Delta r\Delta z\left(\frac{a_{11}}{a_{13}}(T)_P + \frac{a_{12}}{a_{13}}\left(T_s\right)_P^0 + \frac{c_2}{a_{13}} - (T)_P\right) \qquad \text{A-182}$$

Rearranged Eq. A-182

$$a_T\left(T\right)_P = a_e\left(T\right)_E + a_w\left(T\right)_W + a_n\left(T\right)_N + a_s\left(T\right)_S + c_4 \qquad \text{A-183}$$

where

$$a_T = \left(\alpha_g \rho_g \hat{C}_{pg}\right)_P^0 \frac{\Delta r\Delta z}{\Delta t} + \left(1 - \frac{a_{11}}{a_{13}}\right)\frac{6}{d_p} h\left(1-\alpha_g\right)_P \Delta r\Delta z + a_e + a_w + a_n + a_s \qquad \text{A-184}$$

$$c_4 = \left(\alpha_g \rho_g \hat{C}_{pg}\right)_P^0 (T)_P^0 \frac{\Delta r\Delta z}{\Delta t} + \left(\frac{c_2}{a_{13}} + \frac{a_{12}}{a_{13}}\left(T_s\right)_P^0\right)\frac{6}{d_p} h\left(1-\alpha_g\right)_P \Delta r\Delta z \qquad \text{A-185}$$

Appendix B

Calculation of physical properties of mixture

1. Gas viscosity

1.1 The viscosity of a pure monatomic gas

The expression for viscosity of a pure monatomic gas is

$$\mu = 2.6693X10^{-6}\frac{\sqrt{MT}}{\sigma^2\Omega_\mu} \qquad \text{B-1}$$

where μ is the viscosity, in pascal-seconds; T the absolute temperature, in K; M the molecular weight; σ the “collision diameter,” a Lennard-Jones parameter, in Å (Angstroms); Ω_μ the “collision integral,” a Lennard-Jones parameter which varies in a relatively slow manner with the dimensionless temperature $\kappa T/\varepsilon$; κ the Boltzmann constant, 1.38X10^{-16} ergs/K; and ε the characteristic energy of interaction between molecules.

1.2 The viscosity of a gas mixture

For multi component gas mixtures at low density, Wilke (1950) has proposed this empirical formula to calculate the viscosity of this mixture:

$$\mu_{mixture} = \sum_{i=1}^{n}\frac{y_i\mu_i}{\sum y_j\phi_{ij}} \qquad \text{B-2}$$

where y_i, y_j are mole-fraction of species *i* and *j* in the mixture, and

$$\phi_{ij} = \frac{1}{\sqrt{8}}\left(1+\frac{M_i}{M_j}\right)^{-1/2}\left[1+\left(\frac{\mu_i}{\mu_j}\right)^{1/2}\left(\frac{M_j}{M_i}\right)^{1/4}\right]^2 \qquad \text{B-3}$$

where M_i, M_j are the molecular weights of species *i* and *j*, and μ_i, μ_j the viscosities of species *i* and *j*. Note that when *i*=*j*, we have $\phi_{ij}=1$.

2. Gas mass diffusivity

2.1 The gas mass diffusion for binary mixture

The Chapman-Enskog kinetic theory (Chapman and Cowling, 1970) was used for estimating the diffusion coefficient for gas pairs in the binary mixture, as shown below;

$$D_{AB} = \frac{0.001858T^{3/2}\left[\frac{1}{M_A}+\frac{1}{M_B}\right]^{1/2}}{P\sigma_{AB}^2\Omega_D} \qquad \text{B-4}$$

where D_{AB} is the mass diffusivity of *A* through *B*, in cm^2/s; *T* the absolute temperature, in K; M_A, M_B the molecular weights of *A* and *B*, respectively; *P* the absolute pressure, in atmospheres; σ_{AB} the "collision diameter," a Lennard-Jones parameter, in Angstroms; and Ω_D the "collision integral," for molecular diffusion, a dimensionless function of the temperature and of the intermolecular potential-field for one molecule of *A* and one molecule of *B*, which can be evaluated by Eq. B-5,

$$\Omega_D = \Omega_{D_o} + \frac{0.196\delta_{AB}^2}{T^*} \qquad \text{B-5}$$

where

$$\delta_{AB} = \left(\delta_A\delta_B\right)^{1/2} \qquad \text{B-6}$$

$$\delta = \frac{1.94X10^3\mu_P^2}{V_bT_b} \qquad \text{B-7}$$

where μ_P is dipole moment, debyes; V_b liquid molar volume of the specific compound at its boiling point, cm^3/g mol; T_b normal boiling point, K and

$$T^* = \kappa T / \varepsilon_{AB} \qquad \text{B-8}$$

where

$$\frac{\varepsilon_{AB}}{\kappa} = \left(\frac{\varepsilon_A}{\kappa} \frac{\varepsilon_B}{\kappa} \right)^{1/2} \qquad \text{B-9}$$

$$\varepsilon / \kappa = 1.18\left(1 + 1.3\delta^2\right)T_b \qquad \text{B-10}$$

and

$$\Omega_{D_O} = \frac{A}{\left(T^*\right)^B} + \frac{C}{\exp(DT^*)} + \frac{E}{\exp(FT^*)} + \frac{G}{\exp(HT^*)} \qquad \text{B-11}$$

with

A=1.06036

B=0.15610

C=0.19300

D=0.47635

E=1.03587

F=1.52996

G=1.76474

H=3.89411

The collision diameter, σ_{AB}, is evaluated with

$$\sigma_{AB} = \left(\sigma_A + \sigma_B\right)/2 \qquad \text{B-12}$$

with each component's characteristic length evaluated by

$$\sigma = \left(\frac{1.58V_b}{1+1.3\delta^2} \right)^{1/3} \qquad \text{B-13}$$

2.2 The gas mass diffusivity for gas mixture

Wilke (1950) has simplified the theory and has shown that a close approximation to the correct form is given by the relation

$$D_{1-mixture} = \frac{1}{y_2'/D_{1-2} + y_3'/D_{1-3} + \ldots + y_n'/D_{1-n}} \qquad \text{B-14}$$

where $D_{1\text{-}mixture}$ is the mass diffusivity for component 1 in the gas mixture; $D_{1\text{-}n}$ is the mass diffusivity for the binary pair, component 1 diffusing through component *n*; and y'_n is the mole fraction of component *n* in the gas mixture evaluated on a component-1-free basic, that is

$$y_2' = \frac{y_2}{y_2 + y_3 + \ldots + y_n} \qquad \text{B-15}$$

3. Heat capacity of gas

Heat capacity of gas for each species can be calculated from the expression

$$C_P^0 = a + bT + cT^2 + dT^3 \qquad \text{B-16}$$

The unit of C_P^0 is cal/gmol.K.

Heat capacity of gas mixture is as follow

$$\widehat{C}_P = \sum_{i=1}^{n} x_i \widehat{C}_{P,i} \qquad \text{B-17}$$

4. Thermal conductivity of gas

4.1 Thermal conductivity for pure gas

The expression for calculating thermal conductivity of pure gas is as follow

$$\lambda_i = \mu_i\left(\widehat{C}_{P,i} + \frac{5}{4}\frac{R}{M_i}\right) \qquad \text{B-18}$$

4.2 Thermal conductivity for gas mixture

The thermal conductivity for gas mixture can be evaluated from

$$\lambda = \sum_{i=1}^{n}\frac{y_i k_i}{\sum_{j=1}^{n} y_j A_{ij}} \qquad \text{B-19}$$

where the coefficient *Aij* can be written as

$$A_{ij} = \frac{1}{\sqrt{8}}\left(1+\frac{M_i}{M_j}\right)^{-1/2}\left[1+\left(\frac{g_i}{g_j}\right)^{1/2}\left(\frac{M_i}{M_j}\right)^{1/4}\right]^2 \qquad \text{B-20}$$

and

$$\frac{g_i}{g_j} = \left(\frac{\Gamma_j}{\Gamma_i}\right)\left[\frac{\exp(0.0464T_{r,i}) - \exp(-0.2412T_{r,i})}{\exp(0.0464T_{r,j}) - \exp(-0.2412T_{r,j})}\right] \qquad \text{B-21}$$

with

$$\Gamma = T_C^{1/6} M^{1/2} P_C^{-2/3} \qquad \text{B-22}$$

and

$$T_r = \frac{T}{T_C} \qquad \text{B-23}$$

where T_c and P_c are the critical temperature and pressure, respectively.

Appendix C

Calculation of stiffness coefficient and damping coefficient

1. Stiffness coefficient

The stiffness can be calculated by Hertzian contact theory when the physical properties such as Young’s modulus and Poisson ratio are known. According to the Hertzian contact theory, the relation between the normal force (F_{nor}) and displacement (δ_{nor}) is given by:

$$F_{nor} = k_{nor}\delta_{nor}^{3/2} \qquad \text{C-1}$$

In the case of two spheres of the same size, $k_{,nor}$ is expressed by:

$$k_{nor} = \frac{\sqrt{2r_p}E}{3(1-\upsilon^2)} \qquad \text{C-2}$$

In the case of contacting between a sphere particle and wall, $k_{,nor}$ is expressed by:

$$k_{nor} = \frac{\dfrac{4\sqrt{r_p}}{3}}{\dfrac{(1-\upsilon^2)}{E}.\dfrac{(1-\upsilon_w^2)}{E_w}} \qquad \text{C-3}$$

where E is the Young’s modulus and υ is the Poisson ratio of the particle. E_w is the Young’s modulus and υ_w is the Poisson ratio of the wall.

The relation between the tangential force ($F_{\tan}$) and displacement ($\vec{\delta}_t$) was derived by Mindlin (1949) and Mindlin and Deresiewicz (1953):

$$F_{\tan} = \frac{2\sqrt{2r_s}G_s}{2-\upsilon_s}\vec{\delta}_{nor}^{1/2}\vec{\delta}_{\tan} \qquad \text{C-4}$$

where G_s is the shear modulus which is related to the Young's modulus (E_s) and Poisson ratio (υ_s) by:

$$G_s = \frac{E_s}{2(1-\upsilon_s)} \qquad \text{C-5}$$

The stiffness $k_{stif,\tan}$ is given by:

$$k_{stif,\tan} = \frac{2\sqrt{2r_s}G_s}{2-\upsilon_s}\vec{\delta}_{nor,ij}^{1/2} \qquad \text{C-6}$$

In the case of contacting between sphere particle and wall, the stiffness $k_{stif,\tan}$ becomes

$$k_{stif,\tan} = \frac{8\sqrt{r_s}G_s}{2-\upsilon_s}\vec{\delta}_{nor,ij}^{1/2} \qquad \text{C-7}$$

This equation is based on the following assumptions. When considering the tangential displacement in contact between a sphere particle and wall, wall is regarded as a rigid body, because the elastic displacement of the wall in the tangential direction is much smaller than that of a sphere particle. In the normal direction, elastic displacement of the wall cannot be neglected.

2. Damping coefficient

The damping coefficient, which is the function of coefficient of restitution, is expressed by

$$\eta_{damp,nor} = 2\gamma\sqrt{mk_{stif,nor}} \quad \text{C-8}$$

$$\eta_{damp,\tan} = 2\gamma\sqrt{mk_{stif,\tan}} \quad \text{C-9}$$

and

$$\gamma = \frac{\alpha}{\sqrt{1+\alpha^2}} \quad \text{C-10}$$

$$\alpha = -(1/\pi)\ln e \quad \text{C-11}$$

where $\eta_{damp,nor}$ and $\eta_{damp,\tan}$ are the damping coefficient in the normal and tangential direction, respectively. e is the coefficient of restitution which is well know as one of the physical properties of the particles.

Appendix D

Performance equation for ideal reactors

1. Plug flow reactor

The performance equation of ideal plug flow reactor is

$$\frac{W}{F_{A0}} = \int_{X_{Ain}}^{X_{Aout}} \frac{dX_A}{-r'_A} \qquad \text{D-1}$$

where W is the weight of catalyst in the system, F_{A0} mass flow rate of species A at the inlet and X_A the conversion of heavy oil, which was defined by

$$X_A = 1 - w_A \qquad \text{D-2}$$

where w_A is mass fraction of heavy oil.

The production rate of heavy oil per unit mass of catalyst, $-r'_A$ is given by

$$-r'_A = k'_A C_{A0}^2 w_A^2 \qquad \text{D-3}$$

Eqs. D-2 and D-3 were substituted into Eq. D-1, yielding

$$\frac{W}{F_{A0}} = \int_{w_{A,in}}^{w_{Aout}} \frac{(-dw_A)}{k'_A C_{A0}^2 w_A^2} \qquad \text{D-4}$$

The integration of Eq. D-4 and rearranging gives

$$\frac{1}{w_{A,out}} = \frac{1}{w_{A,in}} - \frac{W}{F_{AO}} k'_A C_{AO}^2 \qquad \text{D-5}$$

2. Mixed flow reactor

The performance equation is

$$\frac{W}{F_{AO}} = \frac{X_{A,out} - X_{A,in}}{\left(-r'_{A,out}\right)} \qquad \text{D-6}$$

The substitution of Eqs. D-2 and D-3 into Eq. D-6 yields

$$\frac{W}{F_{AO}} = \frac{(1-w_{A,out}) - (1-w_{A,in})}{k'_A C_{AO}^2 w_{A,out}^2} \qquad \text{D-7}$$

The rearranging of Eq. D-7 is

$$\frac{W}{F_{AO}} k'_A C_{AO}^2 w_{A,out}^2 + w_{A,out} - w_{A,in} = 0 \qquad \text{D-8}$$

Appendix E

Axial Dispersion Model

A simplified one-dimensional dispersion model for two phase systems at steady state condition is used for validate the DEM. Recently, our research group (Promsarn, 2005; Reanthong, 2010; Sra-pet, 2010) has been developed the dispersion model to evaluate the performance of catalytic cracking downer reactors. The reaction occurs only in solid phase. Due to high thermal conductivity and fineness of solid, assumption of no temperature gradient in catalyst particles is assumed. The radial profiles of gas and solid flows are uniform from the hydrodynamics data of downer reactor. The energy and mass balance as well as kinetic equations under the above assumptions are:

1. Continuity Equation

The continuity equations for gas and solids phases can be given as:

For solid phase:

$$G_g = u_g \rho_g \quad \text{E-1}$$

For gas phase:

$$G_s = u_s \rho_s \quad \text{E-2}$$

where ε , u_g , u_s, G_g and G_s are void fraction, gas velocity, solids velocity, gas flux, and solids flux, respectively.

2. Mass balance equation

The reaction is considered as heterogeneous reaction, with influence of mass transfer between gas phase and solid phase. The mass balance based on the dispersion model which includes the effects of dispersion and convection in terms of Peclect number, *Pe*, was used. The dispersion model is combined with the four-lump kinetic model of heavy oil catalytic cracking. The equations explaining the mass distribution in the reactor for each phase can be written as follows:

$$\frac{1}{Pe}\frac{d^2 y_{js}}{dZ^2} - \frac{dy_{js}}{dZ} + \frac{k_{jg}aL}{u_s}\left(y_{jg} - y_{js}\right) + \frac{(1-\alpha_g)\rho_s L}{C_{A0}u_s} r_j = 0 \qquad \text{E-3}$$

$$\frac{1}{Pe}\frac{d^2 y_{jg}}{dZ^2} - \frac{dy_{jg}}{dZ} - \frac{k_{jg}aL}{u_g}\left(y_{jg} - y_{js}\right) = 0 \qquad \text{E-4}$$

where y_i is dimensionless concentration or mass fraction given by

$$y_i = \frac{C_i}{C_{A0}} \qquad \text{E-5}$$

C_{A0} is the initial concentration of gas base on kg/m^3.

The initial concentration of heavy oil in vapor phase is obtained from ideal gas:

$$C_{A0} = \frac{G_A P}{\sum_{n=A,i} G_n RT_g / M_{w,n}} \qquad \text{E-6}$$

The groups of Pe_{Ms}, Pe_{Mg}, U^*_{Mis} , U^*_{Mig} represent the dimensionless terms related to properties of gas and solid including the effect of diffusion and convection term defined as:

$$Pe_{Mg} = \frac{u_g L}{\varepsilon D_g}, U^*_{Mig} = \frac{k_{ic}aL}{u_g}, Pe_{Ms} = \frac{u_s L}{\left(1-\alpha_g\right)D_s}, U^*_{Mis} = \frac{k_{ic}aL}{u_s} \qquad \text{E-7}$$

where D_g and D_s are mass dispersion coefficients for gas and solid phase, respectively. The boundary conditions for mass balance for inlet and outlet components are:

At the inlet conditions,

At Z=0: $\frac{dy_{is}}{dZ} = Pe_{Ms}\left(y_{is}\big|_{Z=0^+} - y_{is}\big|_{Z=0^-}\right), \frac{dy_{ig}}{dZ} = Pe_{Mg}\left(y_{ig}\big|_{Z=0^+} - y_{ig}\big|_{Z=0^-}\right)$

At the outlet conditions,

At Z=1: $\frac{dy_{is}}{dZ} = 0, \frac{dy_{ig}}{dZ} = 0$

3. Energy Balance

The energy balance equations for gas and solid phases can be written as:

$$\frac{1}{Pe_{Hs}}\frac{d^2\Theta_s}{dZ^2} - \frac{d\Theta_s}{dZ} - \frac{haL}{G_s C_{ps}}\left(\Theta_s - \Theta_g\right) + \frac{(1-\varepsilon)\rho_s \Delta H_A L}{G_s C_{ps} T_{s0}} r_A = 0 \quad \text{E-8}$$

$$\frac{1}{Pe_{Hg}}\frac{d^2\Theta_g}{dZ^2} - \frac{d\Theta_g}{dZ} + \frac{haL}{G_g C_{pg}}\left(\Theta_s - \Theta_g\right) = 0 \quad \text{E-9}$$

where Θ_s, Θ_g, and Z are the dimensionless solid and gas temperature, and dimensionless length respectively, given by:

$$\Theta_s = \frac{T_s}{T_{s0}},\ \Theta_g = \frac{T_g}{T_{s0}},\ \text{and}\ Z = \frac{l}{L}$$

The characteristic temperature, T_{s0}, is catalyst temperature at inlet, while the characteristic length is the total reactor length, *L*.

The group of Pe_{Hs}, Pe_{Hg}, U^*_{Hs}, U^*_{Hg} represent the dimensionless terms relating to properties of gas and solid including the effect of heat dispersion and convection term defined as:

$$Pe_{Hg} = \frac{G_g C_{pg} L}{\varepsilon k_g}, U^*_{Hg} = \frac{haL}{G_g C_{pg}},\ Pe_{Hs} = \frac{G_s C_{ps} L}{(1-\varepsilon)k_s},\ U^*_{Hs} = \frac{haL}{G_s C_{ps}}$$

where k_g and k_s are the gas phase and solid phase heat dispersion coefficients, respectively.

The surface area of solid particles per unit volume of bed, *a* is given by

$$a = \frac{6(1-\varepsilon)}{d_s} \qquad \text{E-10}$$

The last term of the energy equation for solid phase presents the energy term due to the reaction.

The boundary conditions for solving the energy equations are:
At the inlet conditions,

At Z=0: $\frac{d\Theta_s}{dZ} = Pe_{Hs}\left(\Theta_s\big|_{Z=0^+} - \Theta_s\big|_{Z=0^-}\right)$, $\quad \frac{d\Theta_g}{dZ} = Pe_{Hg}\left(\Theta_g\big|_{Z=0^+} - \Theta_g\big|_{Z=0^-}\right)$

At the outlet conditions,

At Z=1: $\frac{d\Theta_s}{dZ} = 0$, $\quad \frac{d\Theta_g}{dZ} = 0$

The solids fraction in a gas-liquid system depends on the hydrodynamics and gas expansion in the reactor. The solid fraction in a downer reactor can be derived from slip velocity definition. The slip velocity in a downer is equal to the difference of particle velocity and gas velocity which is equal to particle free fall velocity. The slip velocity is related to the solid superficial velocity, u_s , and the gas superficial velocity, u_g , by following equation (Ramachandran and Chaudhari, 1983; Das *et al.*, 2003).

$$v_{sl} = v_t = \frac{u_s}{(1-\varepsilon)} - \frac{u_g}{\varepsilon} \qquad \text{E-11}$$

Thus the solid fraction can be derive from this equation

$$(1-\varepsilon) = 1 - \left[\frac{(v_t - u_g - u_s) + \sqrt{(u_g + u_s - v_t) + 4u_g v_t}}{2v_t} \right] \qquad \text{E-12}$$

The terminal velocity of a single particle, v_t is defined:

$$v_t = \sqrt{\frac{4gd_p(\rho_s - \rho_g)}{3\rho_g C_D}} \qquad \text{E-13}$$

Appendix F

Step for using FLUENT software

Recently, FLUENT software becomes a useful tool for solving the fluid dynamics problem because of its user friendly. The overall step for using this software is shown in Appendix Figure F1. It consists of 4 steps which are geometry creation, mesh generation, solving the problem, and posted processing. The geometry and mesh generation steps were done using Gambit software. The FLUENT software was used for solving the fluid dynamics problem and posted processing steps. The details of each step were described below.

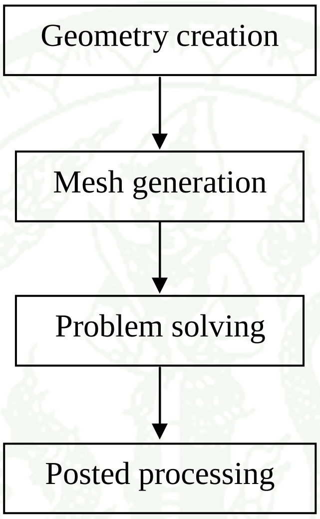

Appendix Figure F1 Flow chart for using Gambit and FLUENT software solving the CFD problem.

1. Geometry creation

The step for creating the geometry domain shows in Appendix Figure F2. The guideline to use Gambit software shows in this section.

1.1 Start Gambit software

1.2 Select solver

Solver → FLUENT 5/6

1.3 Create a point

Geometry → Vertex → Create Vertex

1.4 Create line from points

Geometry ⟶ Edge ⟶ Create Edge

1.5 Create face from edges

Geometry ⟶ Face ⟶ Form Face

1.6 Create volume from faces

Geometry ⟶ Volume ⟶ Create Volume

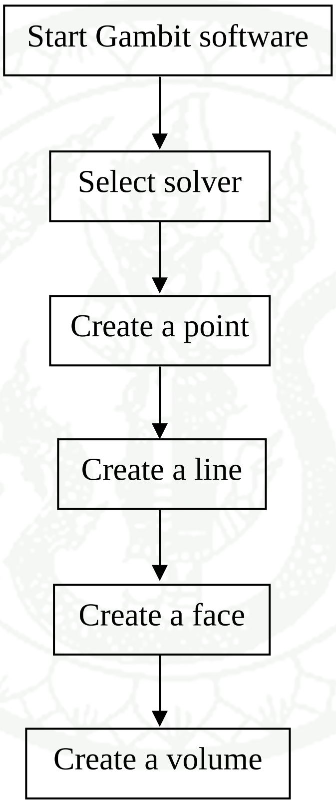

Appendix Figure F2 Flow chart for geometry creation using GAMBIT software.

2. Mesh generation

Flow chart for mesh creation using Gambit software shows in Appendix Figure F3.

2.1 Create mesh on line

Mesh ⟶ Edge ⟶ Mesh Edge

2.2 Create mesh on face

Mesh ⟶ Face ⟶ Mesh Face

2.3 Create mesh on volume

Mesh ⟶ Volume ⟶ Mesh Volume

2.4 Define boundary condition

Zones ⟶ Specify Boundary Types

2.5 Export mesh file for solving the problem by using FLUENT software

File ⟶ Export ⟶ Mesh

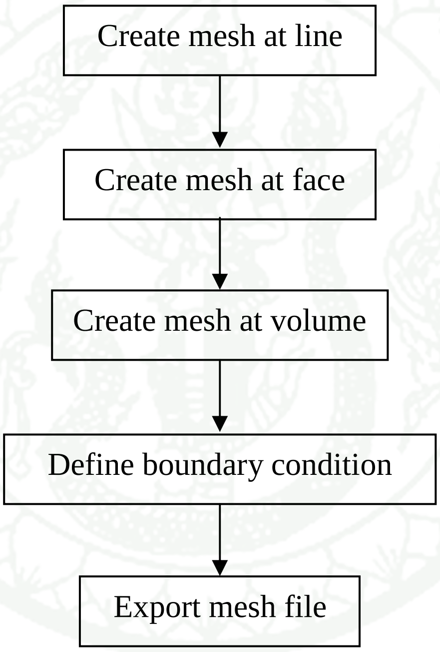

Appendix Figure F3 Flow chart for mesh creation using Gambit software.

3. Solving the problem

Appendix Figure F4 illustrates the flow chart for CFD problem solving using FLUENT software.

3.1 Start FLUENT software

3.2 Read the mesh file

File → Read → Case

3.3 Grid check

Grid → Check

3.4 Define model solver

Define → Models → Solver

3.5 Define materials

Define → Materials

3.6 Define operating condition

Define → Operating conditions

3.7 Define boundary condition

Define → Boundary conditions

3.8 Define User-Defined Functions

Define → User-Define → Functions → Compiled

3.9 Set the solution parameters

Solve → Controls → Solution

3.10 Initialize the problem

Solve → Initialize

3.11 Enable the plotting residual

Solve → Monitors → Residual

3.12 Iteration

Solve → Iterate

4. Posted processing

4.1 Display the contour plot

Display → Contours

4.2 Display the velocity vector plot

Display → Vectors

4.3 XY plot

Plot → XY Plot

4.4 Export data to Excel file

Plot → XY Plot

- Select the desired data
- Click “Write to file”
- Click “Write”

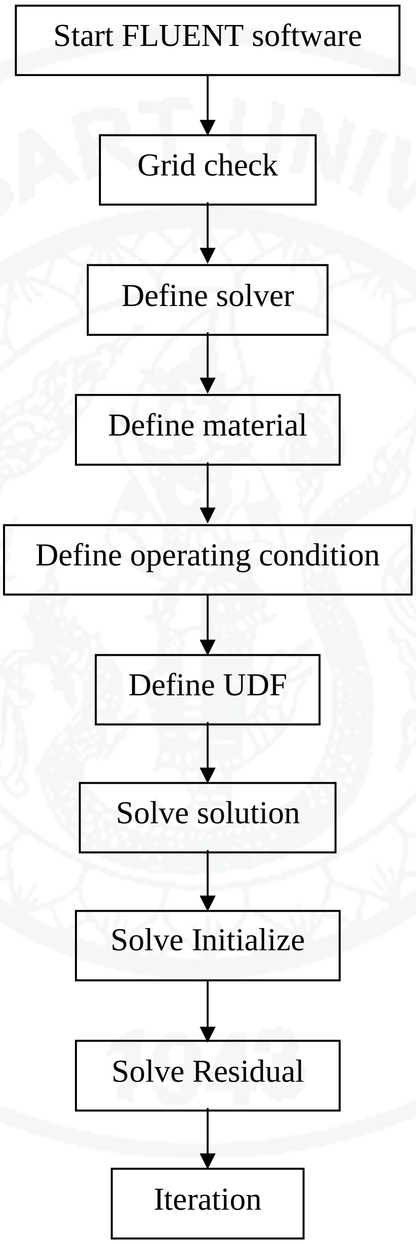

Appendix Figure F4 Flow chart for CFD problem solving using FLUENT software.

CURRICULUM VITAE

NAME : Mr. Parinya Khongprom

BIRTH DATE : Apr 08, 1978

BIRTH PLACE : Phatthalung, Thailand

EDUCATION :

YEAR	INSTITUTE	DEGREE/DIPLOMA
2001	Prince of Songkla University.	B.Eng. (Chemical-Engineering)

SCHOLARSHIP : The Royal Golden Jubilee Ph.D. Program

WORKING EXPERIENCE :

YEAR	COMPANY	POSITION
2002-2004	Bayer Thai	Shift Engineer

PUBLICATIONS

International Journal

Limtrakul, S., N. Thanomboon, T. Vatanatham and **P. Khongprom**. 2008. DEM modeling and simulation of a down-flow circulating fluidized bed. **Chem. Eng. Commun.** 195: 1328-1344.

Khongprom, P. and D. Gidaspow. 2010. Compact fluidized bed sorber for CO_2 capture. **Particu.** 8: 531-535.

Khongprom, P., A. Aimdilokwong, S. Limtrakul, T. Vatanatham and P.A. Ramachandran. Axial gas and solids mixing in a down flow circulating fluidized bed reactor based on CFD simulation. **Chem. Eng. Sci.** Submitted.

Khongprom, P., S. Limtrakul and T. Vatanatham. DEM modeling and simulation for catalytic cracking of heavy oil in a downer reactor. **Chem. Eng. J.** In Preparation.

National Journal

Khongprom, P., S. Limtrakul and T. Vatanatham. 2008. 3-D simulation of particle and gas flow behavior in a riser with venturi pipe inlet. **Chaing Mai J. Sci.** 35:131-140.

International Conference

Limtrakul, S., P. Kludthong, T. Vatanatham and **P. Khongprom**. 2006. DEM modeling and simulation for fluidized bed polymerization reactor. **International Conference on Modeling in Chemical and Biological Engineering Sciences**, Center of Nanotechnology, Department of Chemical Engineering and Department of Chemistry, Kasetsart University, Thailand.